

# **Evolution of Rocks from the Münchberg Metamorphic Complex (NE Bavaria)**

Von der Fakultät Chemie der Universität Stuttgart zur Erlangung der Würde  
eines Doktors der Naturwissenschaften (Dr. rer. nat.) genehmigte Abhandlung

Vorgelegt von

**Florian Waizenhöfer**

aus Ellwangen (Jagst)

Hauptberichter: Prof. Dr. Hans-Joachim Massonne

Mitberichter: Priv.-Doz. Dr. Elmar Buchner

Mitprüfer: Prof. Dr. Dietrich Gudat

Tag der mündlichen Prüfung: 04. Dezember 2017

Institut für Mineralogie und Kristallchemie der Universität Stuttgart

2017

# Inhaltsverzeichnis

<b>1. Abkürzungsverzeichnis</b> .....	<b>5</b>
<b>2. Zusammenfassungen</b> .....	<b>7</b>
2.1 Zusammenfassung in deutscher Sprache .....	7
2.2 Zusammenfassung in englischer Sprache .....	9
<b>3. Prolegomenon</b> .....	<b>13</b>
3.1 Motivation .....	13
3.2 Geological Frame .....	14
3.3 Analytical Section.....	26
3.3.1 Polarisation Microscope.....	26
3.3.2 Electron Microprobe .....	27
3.3.3 Mass Spectrometer.....	29
3.3.4 X-ray Fluorescence Spectrometer and Carbon Analyser .....	31
3.3.5 Verification of Analytical Techniques .....	32
<b>4. Monazite in a Variscan Mylonitic Paragneiss from the Münchberg Metamorphic Complex (NE Bavaria) records Cadomian Protolith Ages</b> .....	<b>39</b>
4.1 Introduction .....	40
4.2 Geological Setting .....	41
4.3 Analytical Procedures.....	43
4.4 Mineral Compositions and Textures.....	45
4.5 Pressure-Temperature Evolution .....	53
4.5.1 Calculation Methods .....	53
4.5.2 Results of the Calculated $p$ - $T$ Pseudosections.....	56
4.5.3 Construction of the $p$ - $T$ Path .....	59
4.6 Age Dating of Monazite .....	60
4.7 Discussion.....	63
4.7.1 $p$ - $T$ Evolution, Melting and Mylonitisation .....	63
4.7.2 Monazite Ages and Their Interpretation .....	66
4.8 Conclusions .....	69
<b>5. Contribution to the Metamorphic Evolution of Gneisses from the Münchberg Metamorphic Complex (NE Bavaria)</b> .....	<b>71</b>
5.1 Introduction .....	72
5.2 Geological Setting .....	72
5.3 Analytical Procedures.....	75

5.4 Mineral Compositions and Textures.....	77
5.5 Results of the Bulk-Rock Analyses .....	84
5.6 Pressure-Temperature Evolution .....	86
5.6.1 Calculation Methods .....	86
5.6.2 Results of the Calculated $p$ - $T$ Pseudosection of Sample 13Mm6 .....	88
5.6.3 Construction of $p$ - $T$ Paths .....	91
5.7 Age Dating of Monazite .....	95
5.8 Discussion.....	99
5.8.1 $p$ - $T$ Evolution of the Studied Samples .....	99
5.8.2 Monazite Ages and Their Interpretation .....	101
5.8.3 Protoliths of the Studied Samples .....	102
5.9 Conclusions .....	103
<b>6. Revision of the Pressure - Temperature Evolution of Eclogites from the Münchberg Metamorphic Complex, NE Bavaria (Germany).....</b>	<b>105</b>
6.1 Introduction .....	106
6.2 Geological Setting .....	107
6.3 Analytical Procedures.....	109
6.4 Mineral Compositions and Textures.....	111
6.4.1 Eclogite 13Mm1.....	113
6.4.2 Eclogite 13Mm7_2.....	120
6.4.3 Eclogite MüMa03_3c.....	122
6.5 Results of the Bulk-Rock Analyses .....	123
6.6 Pressure-Temperature Evolution .....	126
6.6.1 Calculation Methods .....	126
6.6.2 Results of the Calculated $p$ - $T$ Pseudosections.....	128
6.6.3 Construction of $p$ - $T$ Paths on the Basis of the Chemical Zonation of Garnet.....	131
6.6.4 Hints at $p$ - $T$ Conditions Before and After Garnet Growth.....	136
6.7 Discussion.....	138
6.7.1 Protoliths of the Studied Samples .....	138
6.7.2 Eclogite-facies Metamorphism of the Studied Samples .....	138
6.7.3 Early Prograde and Late Retrograde $p$ - $T$ Evolution of the Studied Samples.....	140
6.7.4 Geodynamic Consequences .....	141
6.8 Conclusions .....	142
<b>7. Argumentation.....</b>	<b>143</b>

7.1 Geodynamic Considerations .....	143
7.2 Further Outlook .....	146
<b>8. Appendix .....</b>	<b>149</b>
8.1 Eclogite MüMa12 .....	149
8.2 Additional Analyses of Eclogite Samples .....	155
8.3 Additional Analyses of Gneiss Samples .....	160
8.4 Analytical Work .....	163
<b>9. Bibliography .....</b>	<b>165</b>
<b>Danksagung.....</b>	<b>182</b>
<b>Erklärung über die Eigenständigkeit der Dissertation.....</b>	<b>183</b>

## 1. Abkürzungsverzeichnis

Ab	albite-rich plagioclase or pure albite
ACM	active continental margin
Af	alkali feldspar
Alm	almandine
Am	amphibole
An	andradite
BSE	backscattered electron(s)
Bt	biotite
C	core
Ch	chlorite
Cl	clinopyroxene
CNRS	Centre National de Recherche Scientifique
E97	Erzgebirge sample
EMP	Electron Microprobe
Ep	clinozoisite-epidote
Gr	grossular
GSB	Góry Sowie Block
Gt	garnet
Hm	hematite-rich ilmenite
I	intermediate
Im	ilmenite
Kf	K-feldspar
Ky	kyanite
LA ICP-MS	Laser ablation with an inductively coupled plasma - mass spectrometer
liquid ICP-MS	Liquid sample mass spectrometer with inductively coupled plasma
Lw	lawsonite
MLC	Mariánské Lázně Complex
MMC	Münchberg Metamorphic Complex
Mt	magnetite
Mz	monazite
N-MORB	normal mid-ocean ridge basalt

Om	omphacite
Op	orthopyroxene
Pa	paragonite
Ph	potassic white-mica
Pl	plagioclase
Py	pyrope
Qu	quartz
R	rim
REE	rare-earth element
Ru	rutile
SARM	Service d'Analyse des Roches et des Minéraux
SEM	Scanning Electron Microscope
SHRIMP	Sensitive High Resolution Ion Microprobe
Sp	spessartine
St	stilpnomelane
STZ	Saxo-Thuringian Zone
TBU	Teplá-Barrandian Unit
Tt	titanite
WGS	World Geodetic System
X(Ca)	molar fraction of the grossular (+ andradite) component in garnet
X(Mg)	molar fraction of the pyrope component in garnet
XRF	X-ray Fluorescence Spectrometer
Zr	zirconium

## 2. Zusammenfassungen

### 2.1 Zusammenfassung in deutscher Sprache

Die Dissertation „Evolution of Rocks from the Münchberg Metamorphic Complex (NE Bavaria)“ behandelt metamorphe Gesteine, hauptsächlich Eklogite und Gneise. Diese Gesteine wurden in einem Gebiet im nordöstlichen (NE) Bayern (Deutschland), der Münchberger Gneismasse (MMC), beprobt. Dort treten variszische Gesteine auf, die Hinweise auf die geodynamische Entwicklung der Plattenkollision von Laurussia und Gondwana in paläozoischer Zeit liefern. Es wurden 14 Gesteinsproben im Detail untersucht.

Um die Gesamtgesteinszusammensetzung zu bestimmen, wurde die jeweilige Probe zerkleinert und anschließend mit Hilfe einer Scheibenschwingmühle gemahlen. Das auf diese Weise erhaltene Gesteinspulver wurde entweder mit Lithiumborat, einem Gemisch aus 66 wt%  $\text{Li}_2\text{B}_4\text{O}_7$  und 34 wt%  $\text{LiBO}_2$ , im Massenverhältnis 1:10 oder 1:6 vermischt um eine Schmelztablette herzustellen oder mit dem Wachs  $\text{C}_{38}\text{H}_{76}\text{N}_2\text{O}_2$  (Massenverhältnis 4:1) vermischt um eine Tablette zu pressen. Die Schmelztablette diente der Bestimmung der Hauptelementgehalte und die Presstablette der Ermittlung der Spurenelementkonzentrationen in der jeweiligen Gesteinsprobe. Die Messungen erfolgten mit einem Panalytical PW 2400 Röntgenfluoreszenzspektrometer (XRF). Die Schmelztabletten wurden weiterhin mit einem Cetac LSX-213 Laser ablatiert. Das Ablationssystem war wiederum mit einem AGILENT SERIE 7700 Massenspektrometer mit induktiv gekoppeltem Plasma verbunden (LA ICP-MS). Zusätzlich wurden die Gesteinspulver in einer Mischung aus HF, HCl und  $\text{HNO}_3$  bei erhöhten Drücken und Temperaturen in säurefesten Behältern in einer Mikrowellenanlage gelöst. Die sich hieraus ergebenden Lösungen wurden mit einem AGILENT SERIE 7700 Massenspektrometer mit induktiv gekoppeltem Plasma (liquid ICP-MS) untersucht. Die ermittelten Gesamtgesteinszusammensetzungen wurden herangezogen um die Protolithen der Gesteine zu ermitteln. Zudem wurden diese Zusammensetzungen zur thermodynamischen Auswertung der beobachteten Minerale gebraucht.

Nach Herstellung von Gesteinsdünnschliffen der im MMC genommenen Gesteinsproben wurden diese petrographisch mit dem Polarisationsmikroskop untersucht. Es wurde eine Auswahl für weitere Untersuchungen getroffen. Diese beinhalteten die Ermittlung der chemischen Zusammensetzungen von Mineralen (hauptsächlich Silikaten) und deren chemischer Zonierung. Hierbei wurde eine CAMECA SX100 Elektronenstrahlmikrosonde (EMP) eingesetzt. Rückstreuelektronen (BSE) - Bilder wurden ebenfalls mit der EMP erzeugt um beispielsweise spezifische Texturen zu dokumentieren. Außerdem wurden mittels der EMP

die Alter der Monazite bestimmt. Aus den modifizierten Hauptelementgehalten konnten mit der Software PERPLE\_X Pseudoschnitte errechnet werden. Hieraus wurden wiederum, vor allem unter Berücksichtigung der chemischen Veränderung verschiedener Minerale mit Druck ( $p$ ) und Temperatur ( $T$ ),  $p$ - $T$  Pfade abgeleitet.

Es wurden die folgenden wichtigen Ergebnisse erzielt: Die Protolithen der Gneise stellen Grauwacken und Tonsteine, d.h. unreife Sedimente eines aktiven Kontinentalrands (ACM) mit einem starken Relief, dar, während die Protolithen der eingeschalteten Eklogite Ozeanbasalte (MORBs) sind. Die  $p$ - $T$  Pfade der Gneise, welche hauptsächlich auf den unterschiedlichen Zonierungsmustern von Granatkörnern und den variablen Si Gehalten in K-Hellglimmern basieren, sind generell im Uhrzeigersinn gerichtet. Es wurden bei den Gneisen nur sehr wenige gegen den Uhrzeigersinn gerichtete  $p$ - $T$  Pfade gefunden. Bei Drücken von ungefähr 15 kbar und Temperaturen von etwas unterhalb 700°C wurden die höchsten metamorphen Bedingungen erreicht. Auch die Eklogite zeigen im Uhrzeiger gerichtete  $p$ - $T$  Pfade. Sie erreichen ihre höchsten metamorphen Bedingungen jedoch bei höheren Drücken von 26 - 30 kbar und Temperaturen von 670 - 740 °C.

Monazitalter in Gneisen der MMC weisen eine multimodale Verteilung auf. Ältere cadomische Populationen reichen von c. 575 bis c. 455 Ma, während variszische Populationen Alter von c. 430 bis c. 340 Ma ergaben. Während die älteren Monazitpopulationen als detritische Monazite magmatischen Ursprungs aus einem cadomischen ACM gedeutet werden können, können die jüngeren anhand von Seltenerdelement (REE) - Fraktionierungen teilweise als gleichzeitig mit dem Wachstum der vorliegenden metamorphen Paragenese mit Granat angesehen werden. Monazit bildete sich somit auf dem prograden  $p$ - $T$  Pfad, am  $p$ - $T$  Maximum und dem frühen retrograden  $p$ - $T$  Pfad.

Die Unterschiede in den  $p$ - $T$  Bedingungen der Gneise und Eklogite können unter Berücksichtigung der Monazitalter wie folgt gedeutet werden: Unreife klastische Sedimente, die später zu den untersuchten Gneisen metamorphosiert wurden, lagerten sich am Nordrand Gondwanas ab. Ihr Liefergebiet waren unter anderem die magmatischen Bögen, die sich dort in (spät)cadomischer Zeit gebildet hatten. Der nördlich vorgelagerte Ozean (Rheischer Ozean) wurde in dieser Zeit subduziert. Damit näherten sich die Kontinente Gondwana und Baltica an. Die untersuchten Eklogite repräsentieren wahrscheinlich verbliebene Reste dieses einstmals ausgedehnten Ozeans. Sie wurden nach vorliegenden Literaturdaten im mittleren Devon subduziert und schließlich in einem Subduktionskanal exhumiert. Dieser Prozess dauerte bis zum Ende des Devons, wobei zeitgleich die Kollision von Gondwana und Baltica stattfand.

Dabei wurden die Kontinentalrandsedimente ebenfalls bis in größere Tiefen (40 - 50 km) versenkt und mit den bis zu diesen Tiefen exhumierten Eklogiten tektonisch vermischt. Erst in karbonischer Zeit fanden großräumige Deckenüberschiebungen statt, welche nach Literaturdaten die MMC auf niedriggrade Metamorphite aufschob. Davon kündeten die jüngeren Monazitpopulationen in den untersuchten Gneisen.

## 2.2 Zusammenfassung in englischer Sprache

The dissertation “Evolution of Rocks from the Münchberg Metamorphic Complex (NE Bavaria)” deals with metamorphic rocks, mainly eclogites and gneisses. These rocks were sampled in a Variscan area in north-eastern (NE) Bavaria (Germany), the Münchberg Metamorphic Complex (MMC), in order to find hints at the geodynamic evolution of the collision of Laurussia and Gondwana in Palaeozoic times. In detail, 14 rock samples have been studied.

For the determination of the bulk-rock composition, a piece of the particular rock sample was broken and subsequently ground with a tungsten carbide dish-and-puck mill. The obtained rock powder was either fused with lithium borate, consisting of 66 wt%  $\text{Li}_2\text{B}_4\text{O}_7$  and 34 wt%  $\text{LiBO}_2$ , in a mass ratio of 1:10 or 1:6 to prepare a glass disk or mixed with the wax  $\text{C}_{38}\text{H}_{76}\text{N}_2\text{O}_2$  (mass ratio 4:1) to press a tablet, which were analysed for major elements and some minor elements, respectively, with a Panalytical PW 2400 X-ray Fluorescence Spectrometer (XRF). The glass disks were further ablated by a Cetac LSX-213 laser connected to an AGILENT SERIE 7700 mass spectrometer with inductively coupled plasma (LA ICP-MS). Additionally, the powder samples, which were transferred into acid-resistant flasks in a microwave oven, were dissolved in a mixture of HF, HCl and  $\text{HNO}_3$  at elevated pressures and temperatures. Then, the resulting liquids were analysed by an AGILENT SERIE 7700 mass spectrometer with inductively coupled plasma (liquid ICP-MS). The determined bulk-rock compositions were used to identify the protoliths of the rocks. In addition, these compositions were employed for the thermodynamic evaluation of the observed minerals.

After the preparation of thin sections from MMC rocks, these thin sections were petrographically studied with a polarisation microscope. Promising rock samples for further research were selected. This includes the determination of chemical compositions of minerals (especially silicates) and their chemical zonation patterns. A CAMECA SX100 Electron Microprobe (EMP) was used for that. Backscattered electron (BSE) images were prepared with

the EMP, for instance, to document specific textural relations. Besides, monazite ages were determined with the EMP. Due to modified major element contents, pseudosections were calculated by the software programme PERPLE\_X. Based on that, pressure ( $p$ ) - temperature ( $T$ ) paths were derived particularly by considering chemical zonation patterns of different minerals.

The following, important results were obtained: The protoliths of the gneisses are greywackes and mudstones, which means immature sediments of an active continental margin (ACM) with a strong relief, whereas the protoliths of the intercalated eclogites are mid-ocean ridge basalts (MORBs). The  $p$ - $T$  paths of the gneisses, which are mainly based on distinct zonation patterns of garnet grains and variable Si contents in potassic white-mica, are generally clockwise. Anti-clockwise  $p$ - $T$  paths have rarely been found among gneiss samples. Peak metamorphic conditions are reached at pressures of about 15 kbar and temperatures of somewhat below 700 °C. The eclogite rocks also show clockwise  $p$ - $T$  paths. However, they reach their peak metamorphic conditions at higher pressures of 26 - 30 kbar and temperatures of 670 - 740 °C.

Monazite ages of gneisses from the MMC show a multimodal distribution. Older Cadomian populations range from c. 575 to c. 455 Ma, whereas Variscan populations have got ages from c. 430 to c. 340 Ma. While the older populations are interpreted as detrital monazite of magmatic origin from a Cadomian ACM, the younger ones can be considered, due to rare-earth element (REE) fractionations, as partly simultaneous with the growth of the metamorphic paragenesis of garnet. Therefore, monazite was formed at the prograde  $p$ - $T$  path, the  $p$ - $T$  maximum and the early retrograde  $p$ - $T$  path.

Considering the aforementioned monazite ages, the differences between the  $p$ - $T$  conditions of the gneisses and the eclogites can be interpreted as follows: Immature, clastic sediments, which were metamorphosed to the studied gneisses later on, were deposited at the northern rim of Gondwana. Magmatic arcs, which had been formed in (late) Cadomian times, acted as their provenance area. The ocean in the north (Rheic Ocean) was subducted at that time. Consequently, the continents of Gondwana and Baltica converged. The analysed eclogites probably represent remaining relicts of this formerly ample ocean. According to literature, they were subducted in Middle Devonian times and finally exhumed in a subduction channel. This process, during which the collision between Gondwana and Baltica took place, lasted until the end of the Devonian. At that time, sediments of the continental rim were also brought to greater depths (40 - 50 km) and then tectonically mixed with eclogites that were exhumed to these depths. According to literature, it was until Carboniferous times when large-scale nappe-

movements occurred that brought the MMC on top of low-grade metamorphic rocks. This is discernible by the younger monazite populations of the studied gneisses.



## 3. Prolegomenon

### 3.1 Motivation

The evolution of the Variscan orogeny in western and central Europe in Palaeozoic times is not well understood despite a century of intensive scientific studies. In the last two decades, several suggestions were presented on the timing and type of collision of Gondwana and Laurussia as well as on involved microplates from Devonian to Carboniferous times. These partly contradictory proposals include a major contribution of compressive strike-slip movements (e.g. Krohe 1996; Shelley and Bossière 2000; Keppie et al. 2010), the deep subduction of continental crust (e.g. Matte 1998; O'Brien 2000) or the long-lasting thickening of orogenic crust combined with lithospheric mantle delamination with continental crust involved (Willner et al. 2000, 2002; Massonne and O'Brien 2003; Massonne 2005). The recent detection of widespread high-pressure (HP) metamorphic rocks and even of occurrences of ultrahigh-pressure (UHP) rocks (Massonne 2001, 2003; Kotková et al. 2011) in the Variscan orogeny has motivated the prediction of the aforementioned orogenic processes. An especially interesting research area with abundant Variscan HP and UHP rocks is the Bohemian Massif (Massonne 2011) that represents the north-eastern (NE) part of the Variscan belt.

HP rocks in the Bohemian Massif, such as eclogites and garnet peridotites, are abundant (Massonne and O'Brien 2003). As pointed out by Willner et al. (2000), the age data related to HP rocks are bimodal. Ages of metamorphism between 400 and 380 Ma as well as up to 20 Ma lower ages, interpreted as cooling ages, were reported for the Münchberg Metamorphic Complex (MMC), the Zone of Erbsdorf-Vohenstrauß, the Frankenberg and Wildenfels Nappes, the Góry Sowie Block (GSB; Owl Mountains) and the Mariánské Lázně Complex (MLC). Significantly younger ages of metamorphism (345 - 340 Ma) were determined for HP rocks of the Granulitgebirge (Granulite Mountains), the Saxonian Erzgebirge (Ore Mountains), and the Šniežnik (Snowy Mountains) as well as the Gföhl Unit of southern Bohemia. At the time of the Lower Carboniferous HP metamorphism, the Devonian HP metamorphic rocks had already been exhumed to upper crustal levels.

A major debate concerning the aforementioned areas with HP and UHP rocks is related to the extent of HP and UHP metamorphism. Not all rocks of these complexes in total ("in situ" model) were necessarily exposed to HP and UHP conditions. Willner et al. (2000) and Štípská et al. (2006, 2008) have shown that specific rocks, such as eclogites, of the Bohemian Massif can have experienced significantly higher pressures than corresponding country rocks, usually mica-schists, gneisses and migmatites. Thus, eclogites, commonly forming lenses in

surrounding rocks, may have been tectonically emplaced against these rocks (“foreign” model), at least in some instances.

The MMC, as part of the Saxo-Thuringian Zone (STZ), is of special interest because it was interpreted as the leading edge of Gondwana that collided first with Laurussia during the closure of the Rheic Ocean (Kroner et al. 2010). On the other hand, it may also represent the oldest Variscan collision zone between the STZ and the Teplá-Barrandian Unit (TBU). Furthermore, it is unknown whether the “in situ” or the “foreign” model is applicable to the MMC. Eclogite rocks of the MMC were intensively studied (e.g. Matthes 1978; Franz et al. 1986; Klemd 1989; O’Brien 1993). Nevertheless, there are still lots of issues concerning HP rocks of the MMC, including their pressure ( $p$ ) - temperature ( $T$ ) evolutions. Especially for gneisses constituting the bulk of the MMC and surrounding all the eclogite bodies, no detailed studies concerning their  $p$ - $T$  evolutions have been carried out and no monazite in these rocks has been dated. Geotectonic discrimination diagrams for geochemical characterisation of the protoliths of metamorphic rocks should also be employed.

### 3.2 Geological Frame

The Variscides range from the northern part of the Bohemian Massif to the Ossa-Morena-Zone of the Iberian Peninsula via the Armorican Massif (Linnemann 2003). They were given the Latin name *Curia Variscorum*, after a region around the Bavarian city of Hof (Linnemann et al. 2010a). It was Kossmat who established the idea of Variscan orogenic zoning that is still considered to be valid today (Drost and Kroner 2003). He also proposed large-scale nappe-transport of several units inside the STZ (Linnemann et al. 2010a). As part of the Variscan orogeny, the STZ is named after the (former) German states of Saxony and Thuringia that are situated in central Europe (see Fig. 3.1). Besides, the STZ can be separated into different subareas, which are the Allochthonous and Autochthonous Domains as well as two Wrench and Thrust Zones (Fig. 3.1).

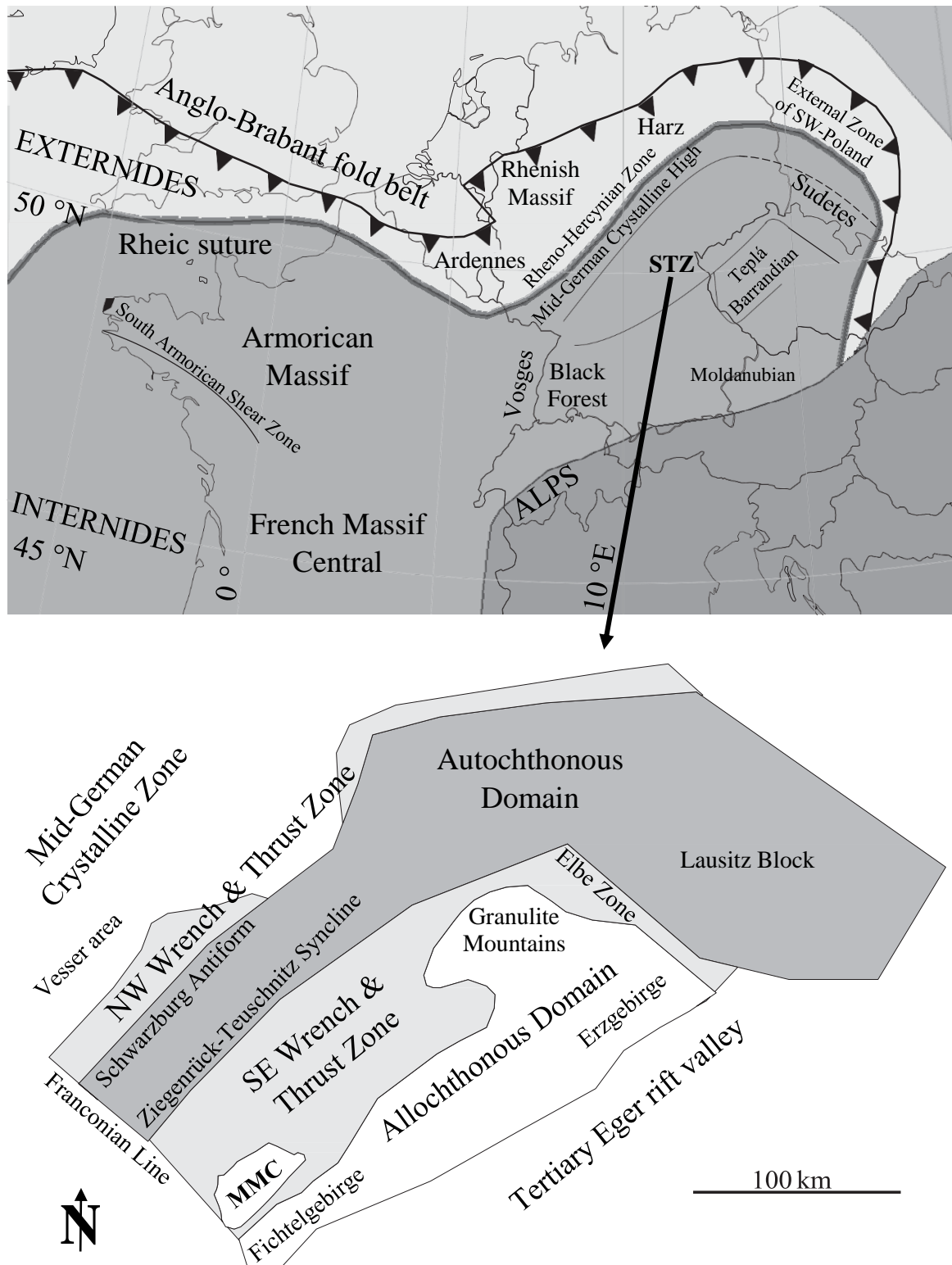


**Fig. 3.1:** Principal domains of central and western Europe (top), which contain important geological features including the Saxo-Thuringian Zone (STZ), and of the STZ itself (down) (maps are modified after Kroner et al. 2008 and 2007, respectively).

The Allochthonous Domain is made up of the Granulite Mountains, the MMC, the Fichtelgebirge and the Erzgebirge (Kroner et al. 2010). The latter is rather famous because it

contains world class ores of tin, silver, uranium, and other metals (Linnemann et al. 2010a). This study focuses on the MMC, therefore detailed geological descriptions of this area are provided in sections 4.2, 5.2, and 6.2. As the Allochthonous Domain did experience Variscan deformation and metamorphism, medium- to high-grade metamorphic rocks can be found there (Kroner et al. 2010).

Unlike the Allochthonous Domain, its Autochthonous counterpart escaped significant Variscan metamorphism and is therefore characterised by low-grade to non-metamorphosed rocks (Kroner et al. 2010). Prominent segments are the Lausitz Block, the Schwarzburg Antiform and the Ziegenrück-Teuschnitz Syncline.

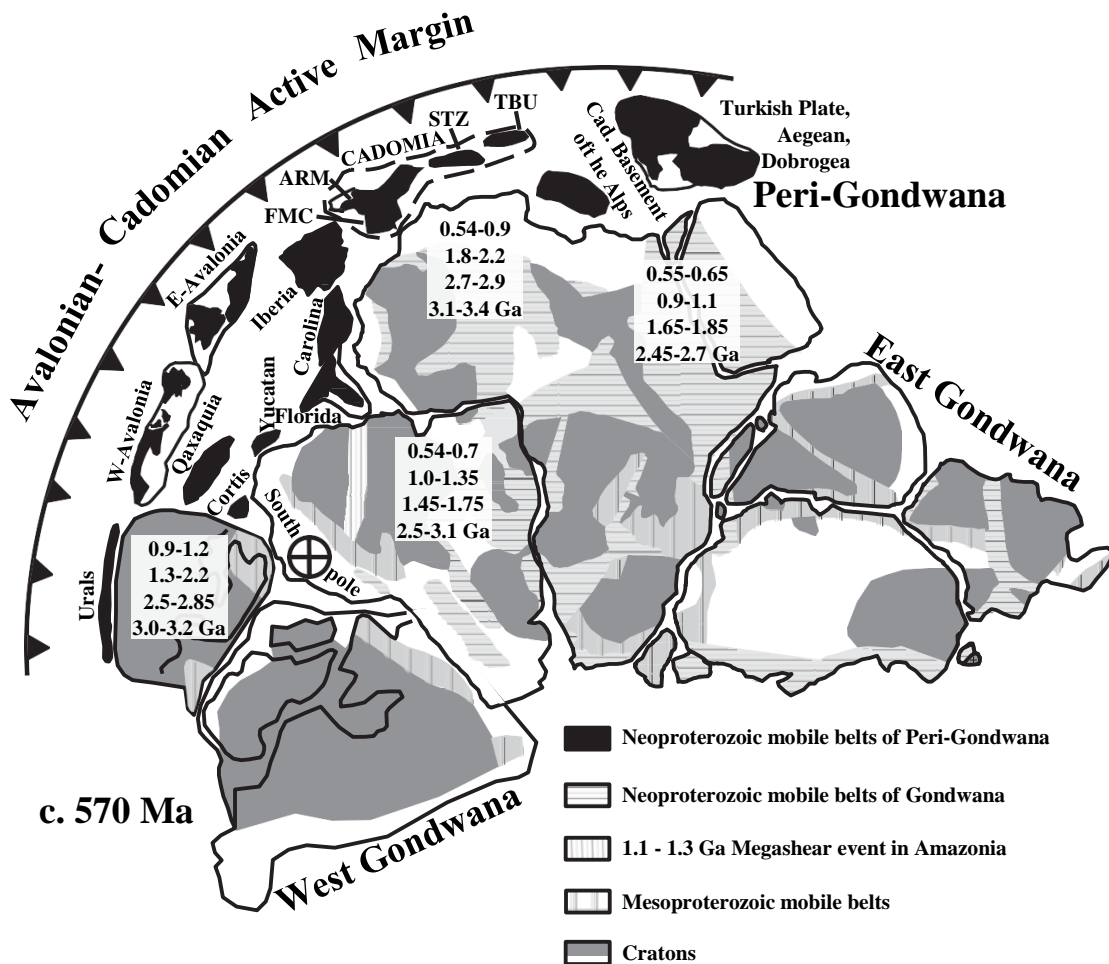


**Fig. 3.2:** Paleogeography of the Cadomian - Avalonian active margin and related major Peri-Gondwana terranes at ~570 Ma after Linnemann et al. (2007) and references therein: ARM = Armorican Massif, Cad. = Cadomian, FMC = French Massif Central, STZ = Saxo-Thuringian Zone (as part of the Bohemian Massif), TBU = Teplá-Barrandian Unit (also part of the Bohemian Massif).

Both Wrench and Thrust Zones show some lithological similarities with the Autochthonous Domain but differ in lots of peculiarities, such as remnants of an outer shelf facies. One of the most prominent distinctive features is the existence of low-grade tectono-metamorphic units in the NW/SE Wrench and Thrust Zones (Kroner et al. 2010). The Elbe Zone is considered the most prominent segment of the SE Wrench and Thrust Zone.

Moreover, it is important to mention that some zircon ages on the Gondwana continent were determined to be Proterozoic or even Archaean (see Fig. 3.2 and Linnemann et al. 2003). Furthermore, Cadomian orogenic processes occurred at the periphery of the West African Craton, being part of Gondwana, in a time range from c. 750 to 530 Ma (Linnemann et al. 2007 and references therein). In the STZ, merely younger sediments and magmatic events (590 - 530 Ma) are preserved (Linnemann et al. 2008). The Cadomian orogeny is characterised by a wide range of geotectonic events of Peri-Gondwana in Late Proterozoic and Early Cambrian times. Rocks related to the Cadomian orogeny are commonly called “Cadomian Basement” (Linnemann et al. 2010b). It was Linnemann et al. (2007, 2010b, 2010c) who reported a detailed model for the development of the Cadomian Basement in the STZ focussing on weakly to non-metamorphosed rocks, such as sediments from the Schwarzburg Unit and the Lausitz Block. According to these authors, there was a Cadomian back-arc basin (c. 590 - 560 Ma), consisting of thinned continental crust (Fig. 3.3).

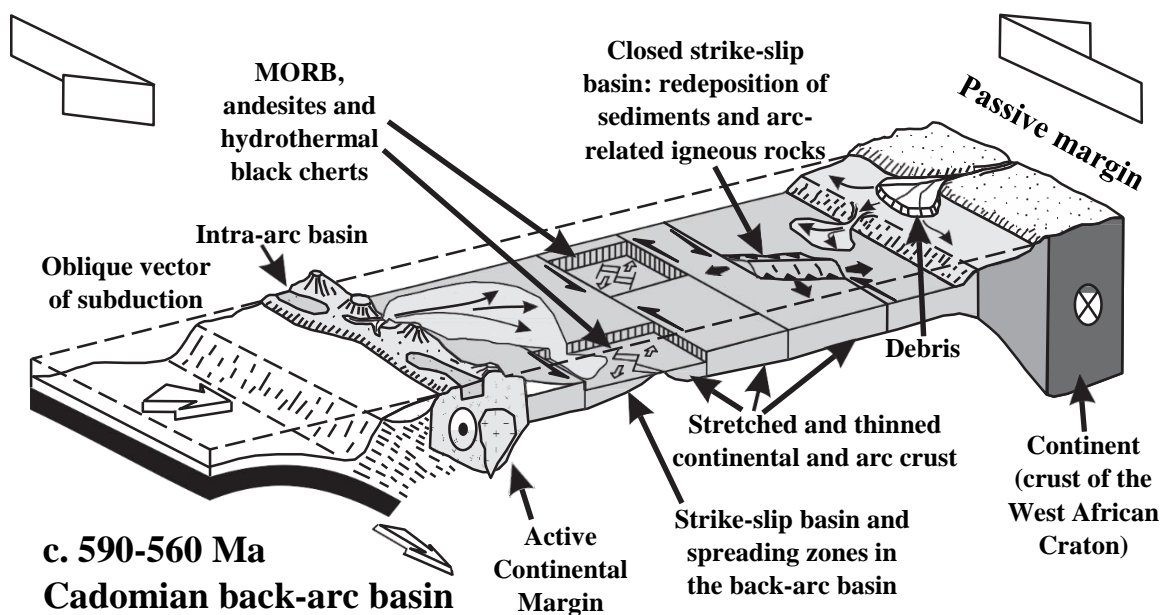


**Fig. 3.3:** Model for the plate-tectonic development of the Cadomian back-arc basin at ~590 - 560 Ma, based on data from the Saxo-Thuringian Zone (STZ) after Linnemann et al. (2007).

It was probably flanked by a continent-ward passive margin (West African Craton as part of Gondwana) in the south and an Active Continental Margin (ACM) in the north (Linnemann et al. 2000). The ACM was associated to volcanism due to continuous subduction of oceanic crust. Besides, back-arc spreading could have occurred based on the interpretation of MORBs, andesites, and hydrothermal black cherts (Buschmann et al. 2001). Debris, igneous rocks and sediments were also deposited due to a strong relief at the margin of the postulated back-arc basin. Their provenance areas were both the ACM and the passive margin.

A later stage of the Cadomian development was probably the collision of the ACM with the passive margin (Fig. 3.4), which closed the back-arc basin, formed a fold- and thrust belt, as well as a related retro-arc basin (Linnemann et al. 2007).

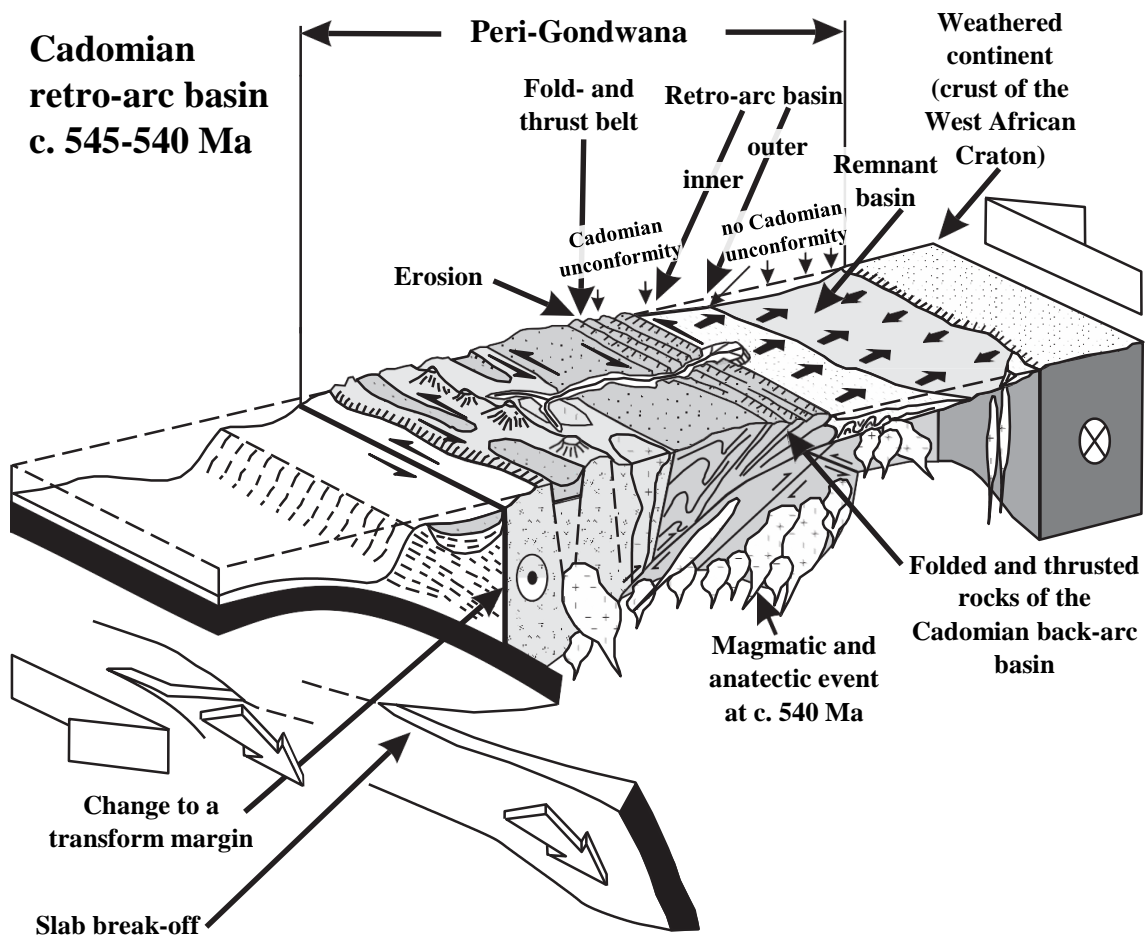


**Fig. 3.4:** Model for the plate-tectonic evolution of the Cadomian retro-arc basin between c. 545 and 540 Ma, based on data from the Saxo-Thuringian Zone (STZ) after Linnemann et al. (2007).

Later on, only the inner part of the retro-arc basin that was folded and thrust (Linnemann et al. 2007) and the remnant basin, characterised by quartzite-rich sediments, was located between the outer retro-arc basin and the passive margin (Fig. 3.4). Nevertheless, both basins should be regarded as short-lived depositional systems (Linnemann et al. 2007). At c. 540 Ma, sediments of the Cadomian Basement were intruded by plutons (Linnemann et al. 2000; Tichomirowa 2002), which could supposedly be related to slab break-off of the subducted oceanic plate. Therefore, Linnemann et al. (2010b) suggested a massive heat flow directed from the descending oceanic plate to the West African Craton.

In Cambrian times, a major change of the plate-tectonic regime occurred in the STZ (Linnemann et al. 2007). The entire Cadomian Basement was uplifted (Linnemann et al. 2010c), while asymmetric rifting started and former ACMs were largely denuded (Fig. 3.5). Due to erosional processes of both former ACMs and the cratonic hinterland, sediments were deposited in the Early and Middle Cambrian (Linnemann and Romer 2002; Buschmann et al. 2006; Geyer et al. 2008).

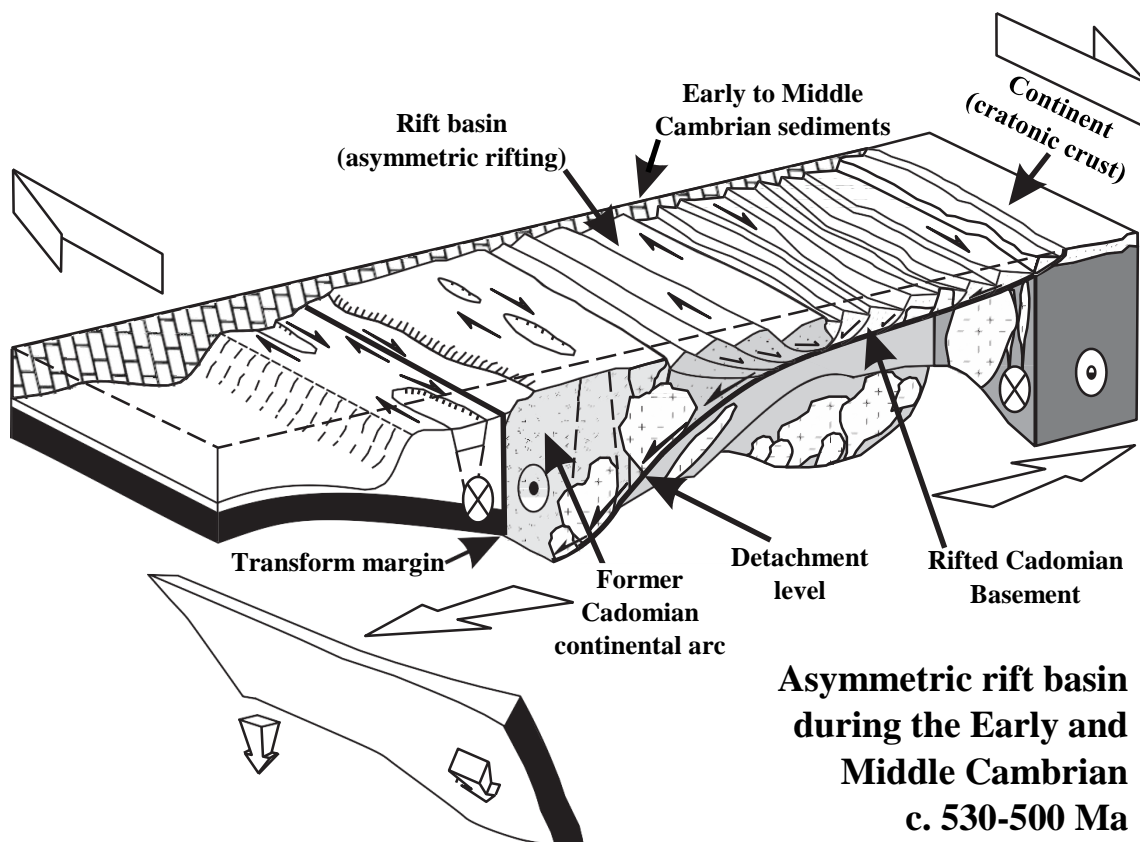


**Fig. 3.5:** Model for the formation of the asymmetric rift basin during the Lower to Middle Cambrian between c. 530 and 500 Ma in the Saxo-Thuringian Zone (STZ) after Linnemann et al. (2007).

The rift basin, which is depicted in Fig. 3.5, led to the separation of a new, small continent (name?), similar to Avalonia, from Gondwana in the Early Ordovician (Linnemann et al. 2003, 2007). One possible scenario among others is that this northward movement opened the Rheic Ocean (Fig. 3.6a). During the growth of the Rheic Ocean, the microcontinent Avalonia collided with Baltica (Linnemann et al. 2003, 2010c) and the (hypothetical) Tornquist Sea, which was part of the Iapetus Ocean, was closed in the Early Silurian (Fig. 3.6b). By the Lower Silurian, the newly formed Avalonia-Baltica plate collided with Laurentia, closing the remaining Iapetus Ocean (Walter 2014). In general, the collisions of Avalonia, Baltica, and Laurentia formed Laurussia (Linnemann et al. 2003) resulting in the Caledonian orogeny in Early Palaeozoic times (Walter 2014).

In the following, the first few steps of the breakup of the aforementioned new, small continent, which was probably located to the east of Avalonia, from Gondwana are discussed in more details. In the late Cambrian, thinning of the lithosphere and an upwelling asthenosphere, according to the imaginations of Linnemann et al. (2007, 2010c), led to the incision of an oceanic ridge (Fig. 3.7a), which was accompanied by a massive upturned heat flow (dehydration and new melts). The newly formed ocean floor is made up of (altered) MORBs. The outer Zone, the former Cadomian ACM, was characterised by a relatively thick crust, ongoing subsidence and Upper Cambrian sedimentation, whereas the inner Zone, the former Cadomian back-arc and retro-arc basins, was strongly affected by uplift as well as upwelling of the asthenosphere (Linnemann et al. 2007). This finding is rather typical for asymmetric rifting (Wernicke 1985; Coward 1986). Chemical weathering was enhanced due to the uplift of the inner Zone. In general, parts of the aforementioned new, small continent are represented by the outer Zone in Fig. 3.7a, while the inner Zone stands for the rest of Peri-Gondwana (Linnemann et al. 2007). Besides, Fig. 3.7b illustrates the further opening of the Rheic Ocean at c. 490 - 480 Ma.

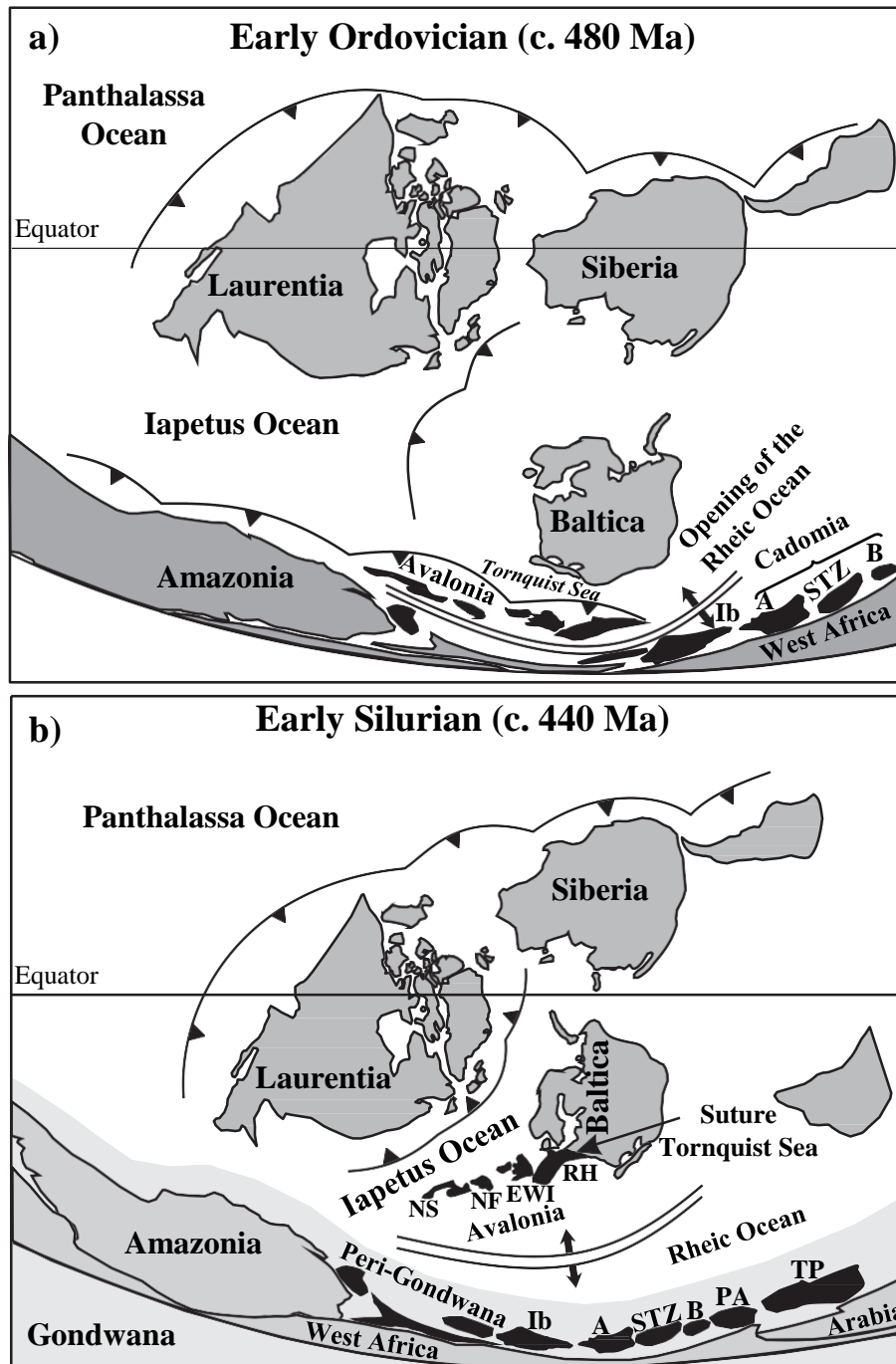


**Fig. 3.6:** Palaeogeography in the a) Early Ordovician (c. 480 Ma) and b) Early Silurian (c. 440 Ma), modified after Linnemann et al. (2010c) and references therein: A = Armorica, B = Barandian, EWI = England, Wales, Southern Ireland, NF = Newfoundland, NS = Nova Scotia, PA = Proto-Alps, RH = Rheno-Hercynian, STZ = Saxo-Thuringian Zone, TP = Turkish Plate.

Due to intensive rift-related magmatism, Early Ordovician rocks are commonly found in the STZ (Linnemann et al. 2007, 2010c). It is assumed that the Rheic Ocean was bounded by a northern (e.g. new, small continent and Avalonia) and a southern (Peri-Gondwana) passive

margin (Fig. 3.7b). Furthermore, this new, small continent formed an ACM towards the Tornquist Sea in the north (Fig. 3.6). Around c. 480 Ma, the STZ was characterised by tectonic and magmatic quiescence and monotonous shelf sedimentation (Linnemann et al. 2007).

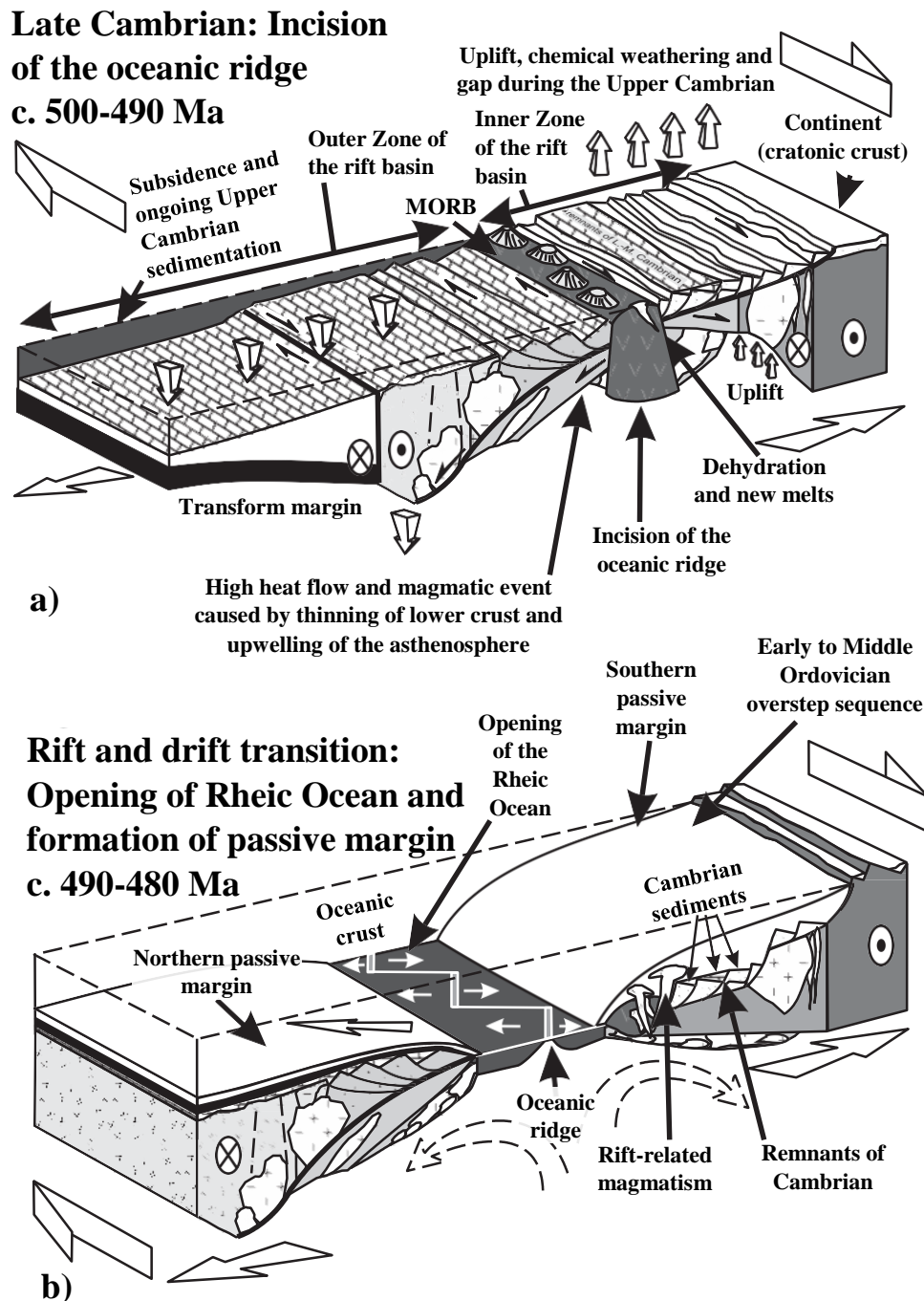


**Fig. 3.7:** Plate tectonic model for a) the opening of the Rheic Ocean during the Late Cambrian (c. 500 - 490 Ma) and b) the formation of a passive margin (c. 490 - 480 Ma) in the Saxo-Thuringian Zone (STZ) after Linnemann et al. (2007).

At c. 420 Ma, Gondwana started a north to north-westward movement (Fig. 3.8), contracting the Rheic Ocean (e.g. Linnemann et al. 2003; Arenas et al. 2014). This plate-tectonic movement finally caused the collision of Gondwana with Laurussia in the Late Devonian resulting in the formation of the Variscan orogen and thereby in the assembly of the supercontinent Pangaea (see sections 4.2, 5.2 and 6.2).

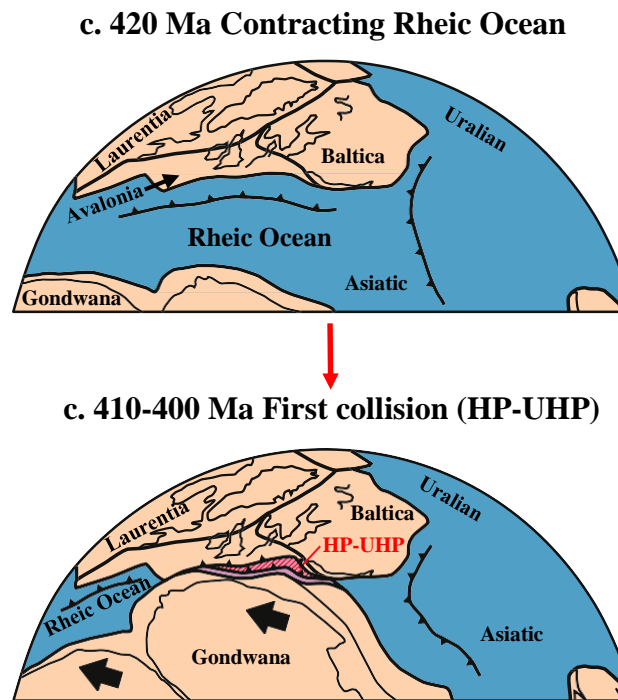


**Fig. 3.8:** Palaeogeography in the Late Silurian (top) and Early Devonian (down), modified after Arenas et al. (2014). The closure of the Rheic Ocean is illustrated.

Zeh and Will (2010) released another detailed geotectonic model for the Variscan orogeny, while studying the Mid-German Crystalline Zone (Fig. 3.9). In the Late Ordovician, Avalonia collided with Baltica (see above), after subducting oceanic crust of the Tornquist Sea (Fig. 3.9a). Later on, there was a north directed subduction of the Rheic Ocean underneath the Avalonian part of Laurussia (see also above). Therefore, an ACM could be identified on the southern margin of former Avalonia (Fig. 3.9b). In the Early Devonian, a back-arc on the southern rim of Laurussia was opened. At the same time, the Rheic Ocean was continued to be subducted (Fig. 3.9c). A few Ma later, a south directed subduction of the relic Rheic Ocean underneath Peri-Gondwana occurred. This was accompanied by an ACM on the northern margin of Peri-Gondwana (Fig. 3.9d). In the Early Carboniferous, the southern shelf of the aforementioned back-arc (see Fig. 3.9c) was subducted underneath Peri-Gondwana (Fig. 3.9e).

Later on, thrusting of continental and oceanic crust was assumed by Zeh and Will (2010) (Fig. 3.9f).

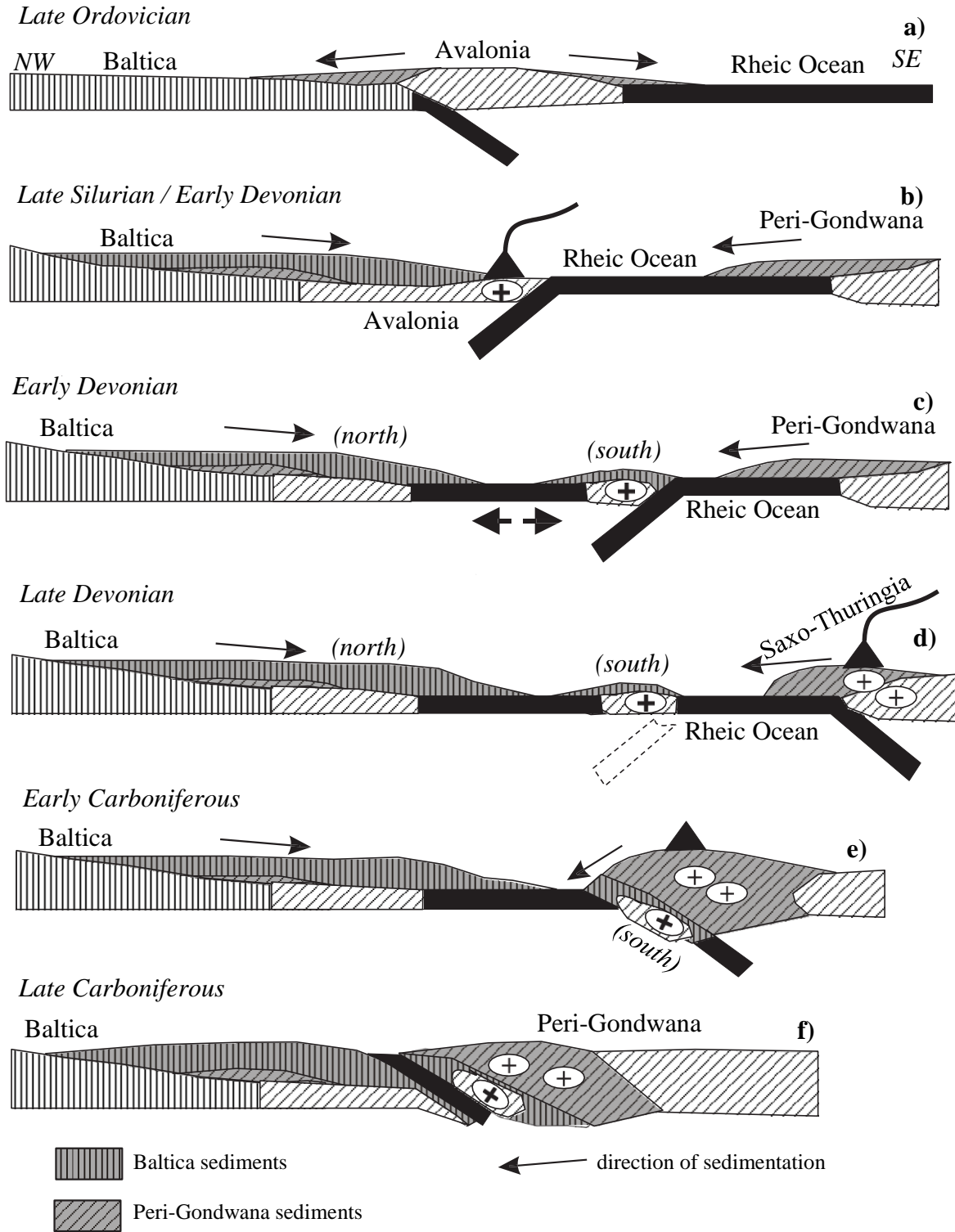


**Fig. 3.9:** Model for the formation of Pangaea, modified after Zeh and Will (2010) and references therein. From a) to f), about 150 Ma passed and the Rheic Ocean was subducted.

Beside the aforementioned models, there are other hypotheses to account for the complicated features of the Variscan orogen considering different geological aspects (e.g. Franke 2000; Franke and Stein 2000; Willner et al. 2002; Massonne 2005; Kroner et al. 2007; Rohmer and Hahne 2010; Guy et al. 2011; Nance et al. 2012; Kroner and Romer 2013; Willner et al. 2015; Franke et al. 2017). Nevertheless, it is unanimously agreed that the metamorphic rocks of the STZ were derived from Gondwana, which was located on the southern hemisphere before the formation of Pangaea (Linnemann et al. 2003).

Interestingly, there are especially two areas in the Bohemian Massif that show similarities with the MMC (see sections 3.1, 4.2, 5.2 and 6.2), the MLC in the Czech Republic (see Beard et al. 1995; O'Brien 1997; Timmermann et al. 2004; Schulmann et al. 2009) and the GSB in Poland (see O'Brien et al. 1997; Bröcker et al. 1998; Kryza and Fanning 2007), because of similar rock types,  $p$ - $T$  conditions, ages, and protoliths. For instance, O'Brien (1997) reported metamorphic conditions of  $< 19.5$  kbar and  $640 - 715$  °C, studying garnets of eclogites from the MLC. According to Beard et al. (1995), the Sm-Nd geochronology of garnet-omphacite pairs from eclogite samples yields metamorphic ages of  $377 \pm 7$  and  $367 \pm 4$  Ma. Timmermann et al. (2004) reported two age groups, namely c. 540 Ma and c. 380 Ma, after analysing eclogites and related rocks and postulated that ocean-floor basalts were probably the Cadomian protoliths of the studied eclogites in good agreement with Beard et al. (1995). Schulmann et al. (2009) explained these findings by an Early Devonian subduction of the Saxothuringian Ocean of unknown size underneath the eastern continental plate represented by the present-day Teplá-Barrandian and Moldanubian domains. According to these authors, this subduction stage was followed by a continent-continent collision. Beard et al. (1995) suggested that during this collision, which is particularly marked by the suture zone MLC, the STZ was subducted beneath the Teplá-Barrandian plate. This interpretation is in line with Kachlík (1993) and Faryad (2012).

Regarding the GSB, O'Brien et al. (1997) obtained two metamorphic events of 15 - 20 kbar, 900 - 1000 °C and 6.5 - 8.5 kbar, 775 - 910 °C. Kryza and Pin (2002) confirmed two metamorphic events, however, in the  $p$ - $T$  ranges of 9.5 - 11.5 kbar, 780 - 880 °C and 4 - 8 kbar, 600 - 780 °C. O'Brien et al. (1997) determined detrital zircon ages between  $2157.7 \pm 1.4$  Ma and  $452 \pm 22$  Ma, as well as a metamorphic zircon age of  $401.5 \pm 0.9$  Ma. Metamorphic monazite and xenotime ages of c. 380 Ma were reported by Bröcker et al. (1998). Furthermore, Rb-Sr thin-slab and mica-whole-rock dating provided metamorphic ages between 375 and 362 Ma (Bröcker et al. 1998). According to Kröner and Hegner (1998), detrital zircon ages of gneisses are 2620 - 1124 Ma, and 488 - 473 Ma. They postulated an early metamorphic zircon

age of c. 440 Ma. Kryza and Fanning (2007) suggested detrital zircon ages of c. 580 Ma, and c. 500 Ma. According to these authors, metamorphic zircon ages are c. 395 Ma, c. 384 - 370 Ma, and c. 360 Ma. Kröner and Hegner (1998) as well as Kryza and Fanning (2007) postulated that pre-Devonian ages date the protoliths of the studied rocks. For example, Kryza and Pin (2002) reported the occurrence of MORBs as one type of precursor rocks. These findings are in reasonable agreement with a Devonian collision of two continental blocks, as reported by Winchester et al. (1998), namely the STZ and the TBU. Schäfer et al. (1997) believe that this collision can be linked to the Rand-Amphibolit unit of the MMC.

### 3.3 Analytical Section

#### 3.3.1 Polarisation Microscope

In order to identify minerals in thin sections, a polarisation microscope ZEISS Axioplan was used (Fig. 3.10). Applying this microscopic technique was a necessary requirement because it allowed the selection of promising rock samples for further research.

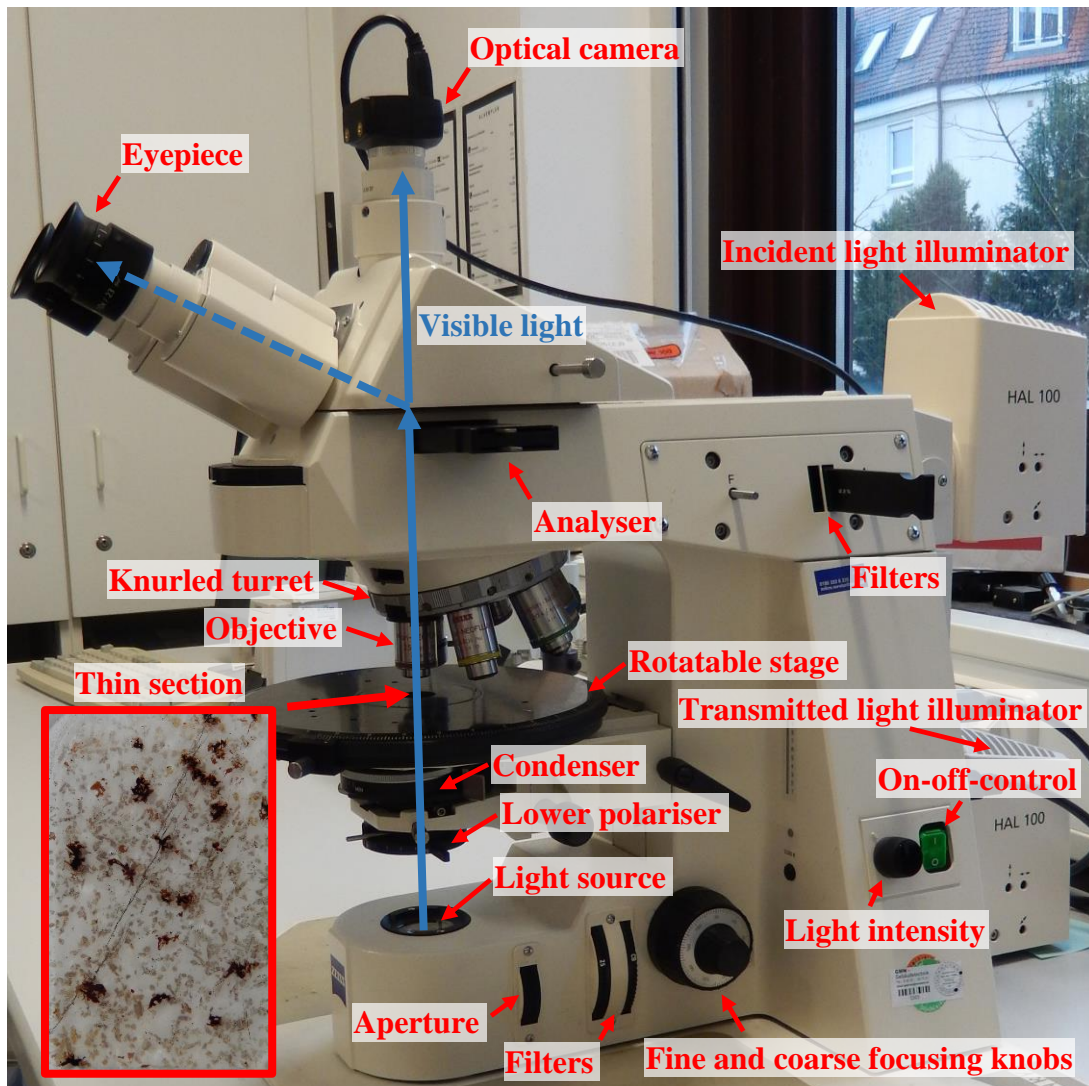


**Fig. 3.10:** Photographical image of a polarisation microscope ZEISS Axioplan, used for analysing thin sections.

In Fig. 3.10, the transmitted light path is indicated. The thin sections were placed on the rotatable stage. Then, they were studied both in plane polarised light and under crossed nicols. With the optical camera, which is connected to a computer, images could be taken. More details concerning the microscope are provided in Murphy (2001), Klein and Philpotts (2013) as well as Nesse (2013).

### 3.3.2 Electron Microprobe

A CAMECA SX100 Electron Microprobe (EMP) that was used to analyse minerals in thin sections is shown in Fig. 3.11. The EMP allows us to measure highly regioselective elemental

concentrations. The minimum spot size of the beam to analyse mineral grains in this study was 5  $\mu\text{m}$ .

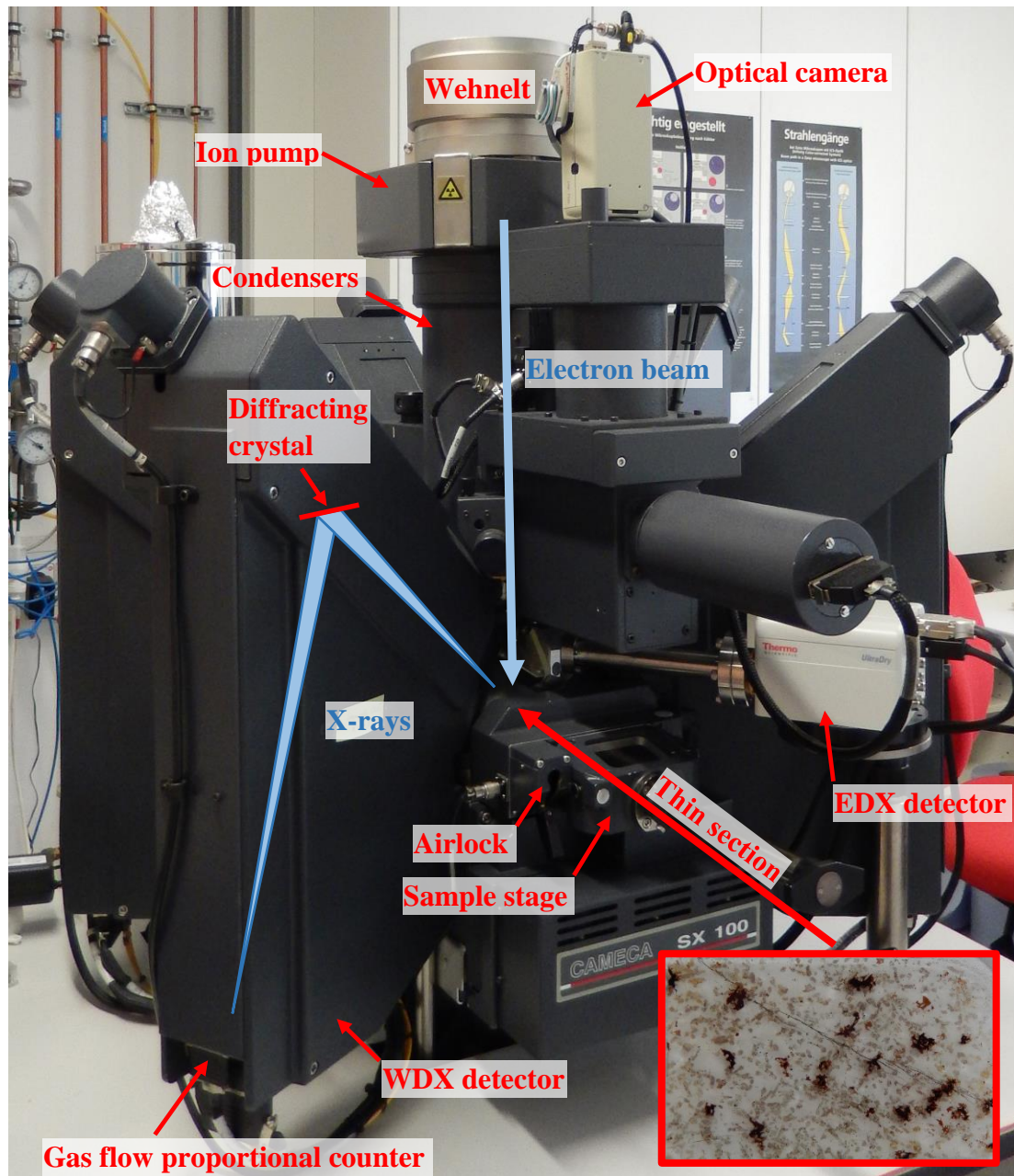


**Fig. 3.11:** Photographical image of a CAMECA SX100 Electron Microprobe (EMP), used for analysing carbon-coated thin sections: EDX = energy-dispersive X-ray, WDX = wavelength-dispersive X-ray.

First, up to two carbon-coated thin sections were transferred into the EMP via the sample stage. During this process, the airlock had to be opened and closed to prevent air from getting inside the EMP. Then, a focused electron beam was directed at the analysis area of the thin section.

Electron-matter interactions are characterised by the occurrence of Auger electrons, backscattered electrons (BSE), Bremsstrahlung, cathodoluminescence, characteristic X-ray emissions, heat, and secondary electrons (see Goldstein 2007). In this study, BSE images and characteristic X-ray emissions, which were measured by energy-dispersive (ED) and wavelength-dispersive (WD) detectors (see Fig. 3.11), were of significance. Exact procedures during and after the measurements are described in sections 4.3, 5.3 and 6.3. For calibration purposes, all standards were provided by Jarosewich (1980, 1991, 2002), Donovan et al. (2003), and P&H Developments. Further details concerning the EMP are found in Goldstein (2007) and Egerton (2010).

### 3.3.3 Mass Spectrometer

In order to obtain bulk-rock elemental concentrations of the studied samples, mass spectrometric measurements were applied (Fig. 3.12).

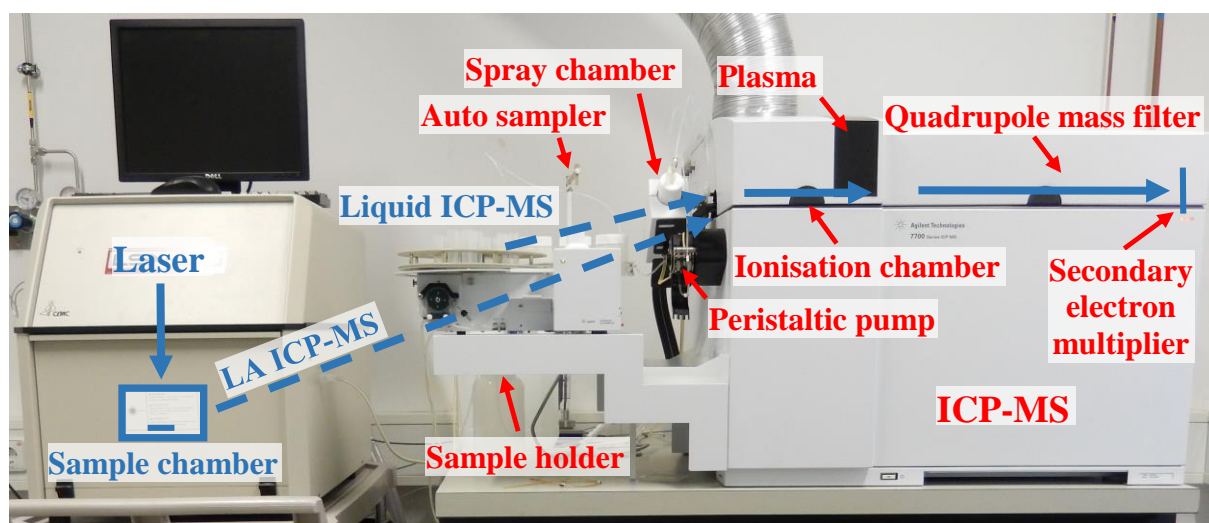


**Fig. 3.12:** Photographical image of a Cetac LSX-213 laser connected to an AGILENT SERIE 7700 mass spectrometer with inductively coupled plasma.

The equipment of Fig. 3.12 may be operated in two different modes. First, only an AGILENT SERIE 7700 mass spectrometer with inductively coupled plasma is used. This mode is called liquid ICP-MS. An auto sampler can be employed to host different sample solutions in vials. Preparation procedures of the aforementioned liquids are described in section 6.3. The sample solution is sucked into a spray chamber by a peristaltic pump. In this chamber, the solution is converted into aerosol particles. These are transferred into an ionisation chamber with an Ar

gas flow of 1000 ml/min, where they are atomised and ionised by interacting with Ar plasma. To sustain the Ar plasma itself, a plasma torch is operated at an Ar flow of 15 l/min. After that, the produced sample ions are directed to a quadrupole mass filter, where they are separated according to their mass to charge ratios ( $m/z$ ). A secondary electron multiplier detects the incoming ions and transfers the multiplied signal to a computer. For calibration purposes concerning liquid ICP-MS, four references were used, namely Multi-Element Calibration Standards-1, -3, and -4 from Agilent Technologies as well as an ICP Multi-Element Standard VI from Merck KGaA.

The second mode of operation is laser ablation ICP-MS (LA ICP-MS). A Cetac LSX-213 laser is connected to the aforementioned mass spectrometer. In this case, the output of a Nd:YAG laser with a ground wavelength of 1064 nm is quintupled to 213 nm. The total energy per laser shot is 4 - 5 mJ at a pulse length of roughly 2 - 3 ns. This laser ablates the sample, which is usually a glass disk consisting of rock powder and lithium borate (optimised, ideal mass ratio 1:6). The aforementioned lithium borate (Spektromelt) was provided by FLUXANA<sup>®</sup> GmbH & Co. KG as lithium tetraborate ( $\text{Li}_2\text{B}_4\text{O}_7$ ) : lithium metaborate ( $\text{LiBO}_2$ ) 66 wt% : 34 wt% (99.98 % purity). Preparation procedures of glass disks are described in sections 4.3, 5.3, and 6.3. A He-Ar gas mixture acts as a transport medium to transfer the ablated material of the sample to the ionisation chamber. The subsequent processes are parallel to those described about liquid ICP-MS. In general, the ideal experimental conditions are as follows:

- Laser energy  $E = 20 \%$
- Diameter of the laser beam  $d = 150 \mu\text{m}$
- Frequency of laser shots  $f = 20 \text{ Hz}$
- Overall number of laser shots per spot: 450
- Ar flow  $f_{\text{Ar}} = 800 \text{ ml/min}$
- He flow  $f_{\text{He}} = 300 \text{ ml/min}$

The following standards were used for calibration: DLH 7 and DLH 8 by P&H Developments as well as NIST 612 by the National Institute of Standards and Technology. The concentrations of the main elements of these standards had previously been determined by an EMP. An issue of the LA techniques is a potential need for correction of differences in the absolute amount of ablated material of the standard glass disk and an unknown sample, e.g. caused by distinctions in absorption and reflection properties. In order to conduct data evaluations after LA ICP-MS measurements, two possible methods, which circumvent this problem, are available. The first one, which is favoured in this study, is called "Quotienten-Methode". Measured ion intensities

are corrected for average corresponding background ion intensities. Ratios of these corrected intensities between the studied ion and a reference ion are calculated within a proper ablation time interval. Then, these ratios are averaged for every studied ion. These average ratios are used to calculate the corresponding elemental concentrations. This procedure is possible because absolute elemental concentrations of every reference are known, all sensitivity factors are provided by calibrations of the previously mentioned standards and, assuming a well known natural isotopic distribution, all isotopic abundances have been established in literature. The second method is called “Integrations-Quotienten-Methode”. After subtractions of averaged background ion intensities, whole profiles of the individual ion signal are integrated. Then, ratios of the areas between the studied ion and the reference ion are calculated. The subsequent data evaluation steps are parallel to those described about the “Quotienten-Methode”.

In all methods, involving quotient formations, the absolute elemental concentration of at least one reference element must be obtained by another source. Here, XRF results were used, except for the geostandards (see below) for which literature values were used. Considering the studied gneisses as well as the geostandards (see below), the concentrations of both Si and Ba were employed as internal references values. After separated evaluations, the two corresponding elemental concentrations of each studied element were averaged. For the data evaluation of eclogites, only the Si elemental concentrations were used. Ba could not be applied because of its low and questionable concentrations. The reasons of these disputable results are provided in section 3.3.5. Further details concerning mass spectrometry are found in Pavićević and Amthauer (2000), Budzikiewicz and Schäfer (2005), Thomas (2008) as well as Gross (2011).

### 3.3.4 X-ray Fluorescence Spectrometer and Carbon Analyser

In addition to liquid and LA ICP-MS, the X-ray Fluorescence Spectrometer (XRF) Panalytical PW 2400 provides another possibility of obtaining bulk-rock elemental concentrations of the studied samples. Generally speaking, the samples are irradiated by a primary X-ray beam, which is emitted by a Rh X-ray tube. As a result, the elements in the sample emit fluorescent X-rays with discrete energies that are characteristic of the very elements in the sample. Therefore, these elements can be identified and quantified. At the time of delivery, the XRF was calibrated with several international standards, such as a Granite (AC-E), Anorthosite (AN-G), Diorite (DR-N), Serpentine (UB-N), and Zinnwaldite (ZW-C). In this study, glass disks, consisting of rock powder and the aforementioned lithium borate (mass ratio 1:6 or 1:10), and pressed tablets, which were made of rock powder and the wax  $C_{38}H_{76}N_2O_2$  (mass ratio 4:1),

were analysed to determine main and trace elements, respectively. Changing the mass ratios had no effect on the results. The wax  $C_{38}H_{76}N_2O_2$  was provided by Merck KGaA as Hoechst wax C micropowder. Preparation procedures of glass disks and pressed tablets are described in sections 4.3, 5.3 and 6.3. More details of XRF are found in Lachance and Claisse (1995), Grieken and Markowicz (2001) as well as Brouwer (2010).

Based on the individual infrared (IR) absorption of  $CO_2$  and  $H_2O$  as oxidation products, a Carbon and Water Analyser (LECO<sup>®</sup> RC-412) was used to analyse total carbon and water contents of the studied rock powder.

### 3.3.5 Verification of Analytical Techniques

To verify the analytical methods for the determination of bulk-rock compositions, two geostandards, namely Diorite (DR-N) and Zinnwaldite (ZW-C), were treated as unknown samples. Thus, DR-N and ZW-C were analysed by liquid and LA ICP-MS as well as XRF. The results of these measurements are compared with literature data, provided by the Service d'Analyse des Roches et des Minéraux (SARM), in Tabs. 3.1 and 3.2.

In general, both literature and experimentally obtained values are in reasonable agreement in Tabs. 3.1 and 3.2. However, large standard deviations of reference elemental concentrations are frequently reported by SARM. Particularly the elemental concentrations of Cr and Ni vary to a great extent depending on the technique used to determine them (valid for DR-N and ZW-C). The reason for that is still unknown. Considering liquid ICP-MS values of Hf and Zr, it is remarkable that they are always lower than their literature counterparts and the values determined by XRF or LA ICP-MS (see Tabs. 3.1 and 3.2). A reasonable explanation for this finding (similar to section 6.5) is the resistance of zircon, which also contains larger quantities of Hf, against the used acids and, thus, was not properly solved in the liquids that were analysed by ICP-MS. By having a closer look at the liquid ICP-MS values of ZW-C, in general, it becomes evident that they are (a little) too low compared to SARM, XRF and LA ICP-MS. It is probably the undissolved residuum which was optically observed in the liquids before ICP-MS measurements that is responsible for this obvious falsification of analytical results (analogue to section 5.5). Besides, a possible source of error for XRF is the spectral overlap of X-ray emission lines of different elements. For instance, Ba concentrations may be falsified if they are below 100 ppm in the presence of larger amounts of Ti (see Tab. 3.2 and Fig. 3.13).

**Tab. 3.1:** Comparison of elemental concentrations as mass fractions in ppm (<sup>#</sup> in wt%) for the geostandard Diorite (DR-N). The values are from the Service d'Analyse des Roches et des Minéraux (SARM), a Panalytical PW 2400 X-ray Fluorescence Spectrometer (XRF), an AGILENT SERIE 7700 mass spectrometer with inductively coupled plasma (liquid ICP-MS) and a Cetac LSX-213 laser connected to the previously mentioned mass spectrometer (LA ICP-MS).

Element	SARM	XRF	liquid ICP-MS	LA ICP-MS
Si <sup>#</sup>	24.70±0.340	25.03		25.28
Al <sup>#</sup>	9.273±0.290	9.49		9.52
Fe <sup>#</sup>	6.786±0.481	7.14		6.80
Mn <sup>#</sup>	0.170±0.016	0.166		
Mg <sup>#</sup>	2.653±0.163	2.66		3.19
Ca <sup>#</sup>	5.039±0.172	5.03		4.58
Na <sup>#</sup>	2.220±0.141	2.11		1.77
K <sup>#</sup>	1.411±0.083	1.41		1.49
Ti <sup>#</sup>	0.653±0.048	0.674	0.657	0.723
P <sup>#</sup>		0.096		
As	3±0.64	4.6		
Ba	385±12	430	398	390
Bi	0.5		0.5	
Ce	46±6	47.7	44.2	43.5
Co	35±7.8	35.5		
Cr	40±10.29	26.7	33.2	58.0
Cs	6.3±1.08			6.2
Cu	50±7.18	41.7	48.7	
Dy	4.6±1.07		4.9	5.2
Er	2.5		2.8	3.1
Eu	1.45±0.19		1.5	1.4
Ga	22±4.5	14.0	23.2	
Gd	4.7±0.9		5.5	5.6
Hf	3.5±0.52		1.5	4.1
Ho	1		1.0	1.1
La	21.5±3.94	13.2	20.5	22.0
Li	40±9.8		37.0	
Lu	0.4±0.11		0.4	0.4
Mo	0.9	0.7		
Nb	7±3.08	12.2	7.1	6.6
Nd	23.5±2	22.1	23.3	26.4
Ni	15±11.05	12.7	16.6	23.1
Pb	55±11.4	54.1	54.5	48.2
Pr	5.7±0.49	6.5	5.5	5.3
Rb	73±7.62	58.4	74.6	69.8
Sc	28±3		26.7	29.7
Sm	5.4±0.56	4.8	5.1	6.5
Sr	400±49.6	363	406	409
Ta	0.6±0.17	1.1	0.7	0.6
Tb	0.77±0.3		0.8	0.8
Th	5±4.56	7.0	4.6	5.4
Tl	0.7	3.5	0.7	
Tm	0.39		0.4	0.4
U	1.5±1	0.96	1.6	1.4
V	220±34.4	201	230	220
W	130	126		
Y	26±6.96	29.4	24.8	25.5
Yb	2.5±1.33	2.9	2.6	2.9
Zn	145±16.38	127	168	
Zr	125±24.83	104	53.8	151

**Tab. 3.2:** Comparison of elemental concentrations as mass fractions in ppm (<sup>#</sup> in wt%) for the geostandard Zinnwaldite (ZW-C). The values are from the Service d'Analyse des Roches et des Minéraux (SARM), a Panalytical PW 2400 X-ray Fluorescence Spectrometer (XRF), an AGILENT SERIE 7700 mass spectrometer with inductively coupled plasma (liquid ICP-MS) and a Cetac LSX-213 laser connected to the previously mentioned mass spectrometer (LA ICP-MS).

Element	SARM	XRF	liquid ICP-MS	LA ICP-MS
Si <sup>#</sup>	25.24±0.46	25.54		24.55
Al <sup>#</sup>	9.765±0.349	10.04		9.61
Fe <sup>#</sup>	6.617±0.33	6.66		6.56
Mn <sup>#</sup>	0.751±0.077	0.749		
Mg <sup>#</sup>	0.096±0.030	0.074		0.092
Ca <sup>#</sup>	0.264±0.050	0.255		0.294
Na <sup>#</sup>	0.245±0.074	0.216		0.160
K <sup>#</sup>	6.409±0.340	6.38		6.22
Ti <sup>#</sup>	0.030±0.012	0.024	0.025	0.032
P <sup>#</sup>	0.011±0.017	0.003		
As	31±10	27.3		
Ba	52±17.4	95.9	9.0	55.0
Bi	15±4.68	23.9	14.2	
Cd	15±1.57	13.2		
Ce	97±11	99.9	67.7	92.0
Co	2±1.3	1.0		
Cr	56±15	50.2	45.5	92.9
Cs	260±49	345		217
Cu	39±10.75		34.8	
Dy	9.2±1.95		3.9	10.6
Er	6.7±1.64		3.0	8.9
Eu	0.04±0.04		0.015	0.033
Ga	99±13	91.3	96.7	
Gd	4.7±1.1		2.6	5.4
Hf	9.7±2.23		8.2	12.2
Ho	2±0.63		0.8	2.2
La	30±6.61	34.0	13.8	26.9
Li	11288±1858		10388	
Lu	2.2±0.39		1.0	2.6
Mo	4.3±1.41	3.5		
Nb	198±46	191	174	221
Nd	25±4.61	27.7	13	26.5
Ni	11±17	30.2	7.5	17.8
Pb	80±18	66.9	54.5	69.9
Pr	9.5±1.69	1.9	4.8	8.7
Rb	8500±789	7651	7460	8822
Sb	4.2±1.88	13.0		
Sc	42±7.93	35.1	12.3	46.0
Sm	6.6±0.55	4.8	3.4	7.5
Sr	17±7.22	10.9	4.3	7.4
Ta	82±8	78.8	46.3	93.0
Tb	1.2±0.3		0.6	1.4
Th	43±13	32.8	10.3	48.9
Tl	34	29.0	30.3	
Tm	1.6±0.39		0.7	1.9
U	20±8.33	15.3	13.1	19.0
V	6±4.37	2.7	1.1	5.3
W	320±55	319		
Y	33±7	63.6	13.7	34.9
Yb	14±3.08	14.1	6.8	17.7
Zn	1050±167	1035	946	
Zr	82±23.75	66.8	74.2	98.1

To illustrate this in more detail, the Intensity / kcps is plotted versus  $2\theta / ^\circ$  in Fig. 3.13. For these experiments, different samples were produced, which aimed at mimicking natural rocks: Every sample powder consisted of 1 wt%  $\text{TiO}_2$  but the elemental Ba concentration increased from 0 to 500 ppm.  $\text{Ba}(\text{NO}_3)_2$  was the most suitable Ba containing salt.  $\text{Al}_2\text{O}_3$  acted as a matrix material in the pressed tablet and, therefore, was added until the rock powder had an overall mass of 12 g. Furthermore, the wax  $\text{C}_{38}\text{H}_{76}\text{N}_2\text{O}_2$  with a mass of 3 g was added to every rock powder before the mixing and pressing processes.

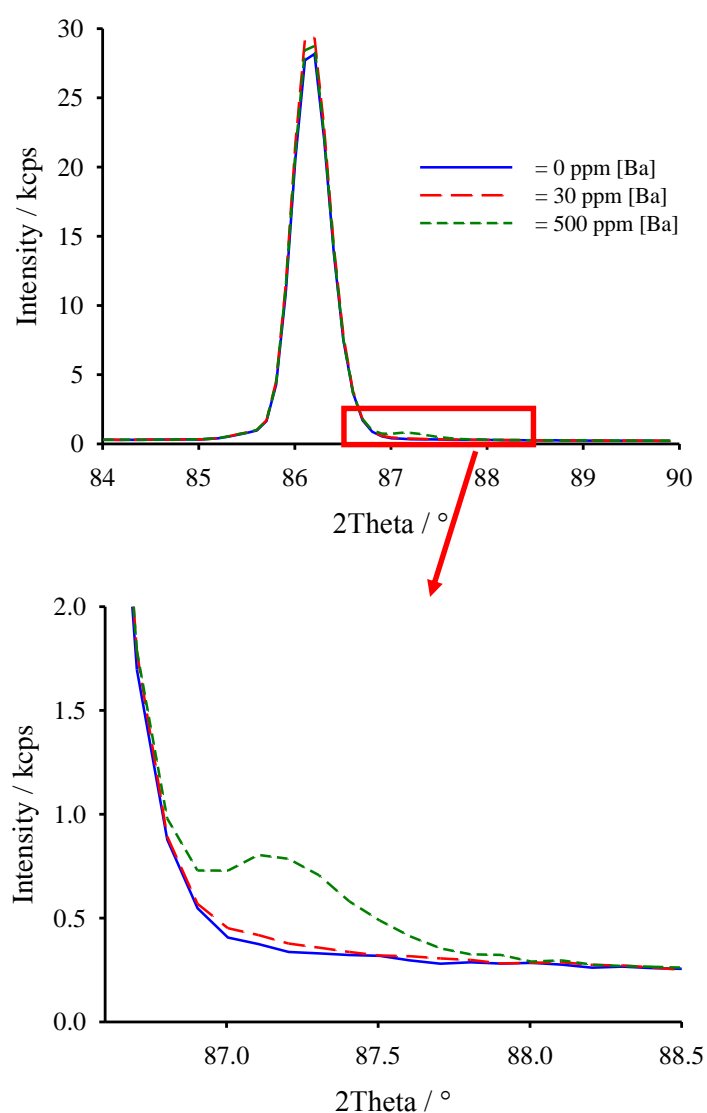


**Fig. 3.13:** Plots of Intensity / kcps versus  $2\theta / ^\circ$  for XRF measurements with different elemental Ba contents and identical  $\text{TiO}_2$  concentrations of 1 wt%.

In Fig. 3.13, there are several peaks, which are partly overlain by others (corresponding intensities in brackets):

- Ti K $\alpha$ 1 at 86.074° (100.0 %)
- Ti K $\alpha$ 2 at 86.218° (50.68 %)
- Ba L $\alpha$ 1 at 87.157° (100.0 %)
- Ba L $\alpha$ 2 at 87.527° (11.35 %)

As demonstrated, the Ba peaks are smaller than their Ti counterparts and the entire Ba signal is significantly superimposed by a huge Ti intensity. In the presence of elemental Ti, this finding explains the rather poor reliability of Ba values below 100 ppm obtained by XRF. This result has got some implications in the data evaluation of LA ICP-MS (see section 3.3.3). Due to these difficulties in dealing with Ba contents below 100 ppm (in the presence of a substantial amount of Ti), it was tried to determine the lower limit of detection for elemental Ba with XRF. Therefore, we prepared samples (pressed tablets) with different mass fractions of elemental Ba, using Ba(NO<sub>3</sub>)<sub>2</sub> again. As explained above, the TiO<sub>2</sub> contents were kept constant at 1 wt% and Al<sub>2</sub>O<sub>3</sub> was the matrix material. The measured mass fraction Ba / ppm was plotted versus the input mass fraction Ba / ppm (Fig. 3.14). For curve fitting with the computer programme SigmaPlot (version 11.0), the data point with an input mass fraction of 10 ppm and a measured mass fraction of 0 ppm was not included because of its uncertainty. The following three types of functions were tested and the given roots were calculated by the programme Wolfram Mathematica (version 11.1.1.0):

- $f_1(x) = -2.0134 + 0.7274x = 0 \rightarrow x = 2.8$
- $f_2(x) = -6.9679 + 0.8048x - 0.0001x^2 = 0 \rightarrow x = 8.7$
- $f_3(x) = -14898.1581 + 1916.6693 \ln|x + 2366.5993| = 0 \rightarrow x = 8.8$

Due to these roots and the individual experimental data points of XRF measurements in Fig. 3.14, there is reasonable evidence that the lower limit of detection of elemental Ba (in the presence of about 1 wt% TiO<sub>2</sub>) must lie between 10 and 30 ppm. In Fig. 3.14, it is also illustrated that the recovery rate of elemental Ba is not satisfactory below 100 ppm at these Ti concentrations. The comparison with Ba results in Tabs. 3.1 and 3.2 indicates that XRF results are merely reliable of Ba contents above 300 ppm.

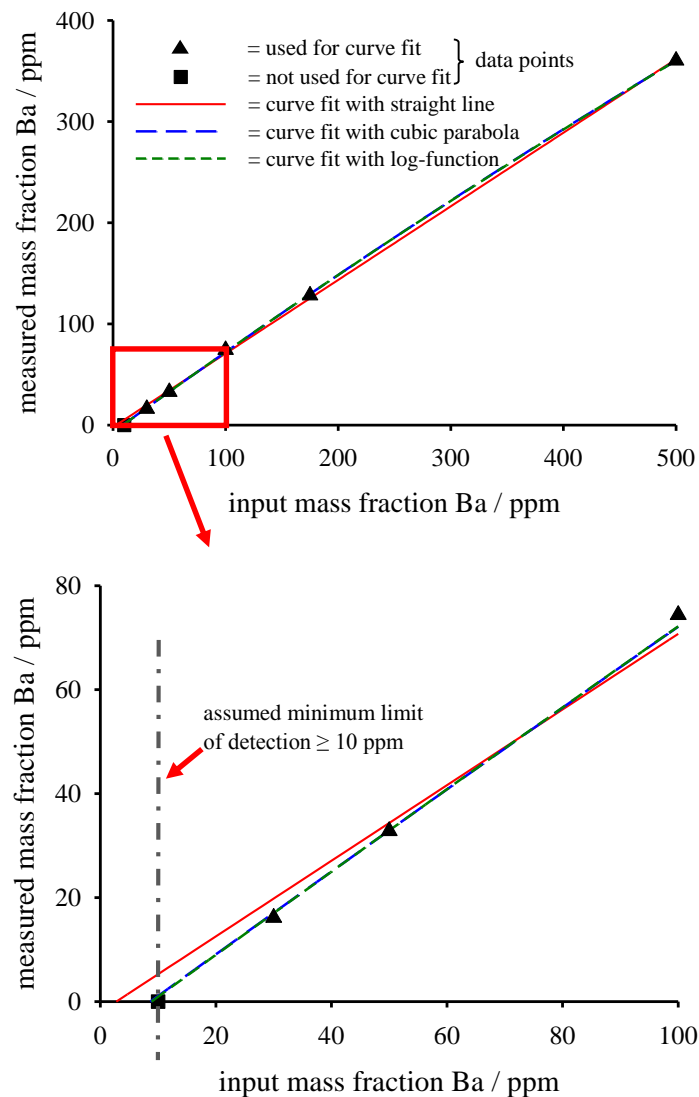


**Fig. 3.14:** Plot of the measured mass fraction Ba / ppm versus the input mass fraction Ba / ppm. XRF was used to conduct the analyses.

In order to verify the elemental concentrations obtained by the EMP and the thereby derived age determinations, an Erzgebirge sample (E97) with a known age, which contains monazite grains (see Massonne et al. 2007a), was treated as a rock with an unknown age. After conducting 30 EMP analyses on 5 monazite grains of this saidenbachite (see sections 4.3 and 4.6), we got a mean age of  $329.7 \pm 11.3$  Ma (two-sigma:  $2\sigma$ ). Due to clearly too low ages, judged on the basis of their  $2\sigma$  errors, 3 analyses had to be discarded. Massonne et al. (2007a) reported two monazite ages, which are within the error range of this study. Their ages are  $324.7 \pm 8.0$  Ma ( $2\sigma$ ), obtained by 113 EMP analyses, and  $332.4 \pm 2.1$  Ma, received by 6 SHRIMP measurements. More details are shown in Fig. 3.15. Additionally, SHRIMP ages of zircon are in corroboration of this study (Massonne et al. 2007a).

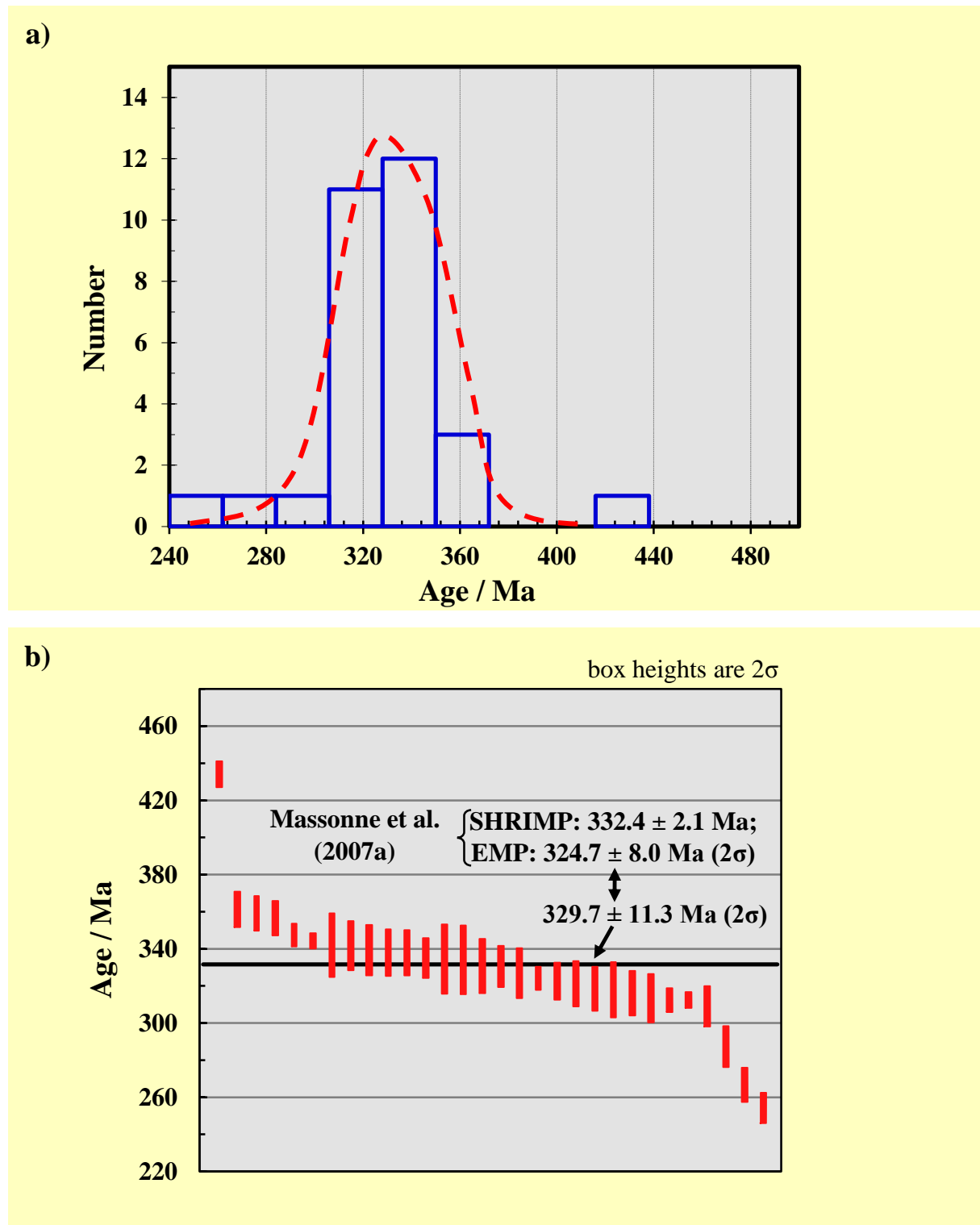


**Fig. 3.15:** Probability density plot (a) and weighted averages (b) of monazites ages, obtained with a CAMECA SX100 EMP. Parallel to Massonne et al. (2007a), one age population of  $329.7 \pm 11.3$  Ma ( $2\sigma$ ) was found in this study. All 30 monazite analyses on 5 grains with the EMP (including 3 outliers) are shown.

## 4. Monazite in a Variscan Mylonitic Paragneiss from the Münchberg Metamorphic Complex (NE Bavaria) records Cadomian Protolith Ages

Florian Waizenhöfer, Hans-Joachim Massonne

Institut für Mineralogie und Kristallchemie, Universität Stuttgart, Azenbergstraße 18, 70174 Stuttgart, Germany

### ABSTRACT

An exceptionally interesting garnet-muscovite-bearing mylonitic paragneiss from the Liegendserie unit of the Münchberg Metamorphic Complex (MMC) in north-eastern (NE) Bavaria, central Europe, was studied. The pressure ( $p$ ) - temperature ( $T$ ) evolution of this rock was derived, using contoured  $p$ - $T$  pseudosections. Mainly based on the chemical zonation of garnet porphyroblast and smaller garnet, formed later during mylonitisation, and the variable Si content in potassic white-mica, this  $p$ - $T$  evolution is characterised by an anti-clockwise path starting at 6 kbar and 600 °C. A peak temperature of c. 670 °C was reached, resulting in partial melting, followed by high-pressure (HP) metamorphism at 12.5 kbar and 650 - 670 °C accompanied by mylonitisation. The retrograde path passed through  $p$ - $T$  conditions of 9 kbar and 610 °C. Extremely small oval-shaped, unshielded monazite grains were analysed with the Electron Microprobe for age dating. These grains did not yield previously reported early Variscan metamorphic ages despite the intensive deformation of the studied rock at relatively high temperatures, but late Cadomian to early Caledonian protolith ages between ~575 Ma and ~455 Ma. Therefore, the main focus is that monazite is identified as having survived high-grade reworking, allowing a window through the metamorphic process to previous events. The obtained ages are related to magmatic events in the provenance area. Thus, the original sediments of the Liegendserie unit were probably deposited in Silurian times. The preservation of monazite is explained by specific  $p$ - $T$  conditions which have never been outside the stability field of monazite at metamorphic temperatures.

KEYWORDS: Cadomian protolith, garnet, geochronology, monazite, Münchberg Metamorphic Complex, mylonitic paragneiss, phengite,  $p$ - $T$  pseudosection, Variscan orogeny.

## 4.1 Introduction

Zircon and monazite are used for obtaining geochronological information because they commonly contain considerable amounts of Th and U. The latter mineral is widespread in Ca-poor crustal rocks and, in contrast to zircon, can be dated with an Electron Microprobe (EMP) because non-radiogenic Pb contents are virtually zero (Williams et al. 2007). Usually, in medium-grade metamorphic rocks monazite dates the late stages of metamorphism unless it is shielded by minerals such as garnet (Langone et al. 2011; Massonne 2014). However, in low-grade metamorphic rocks monazite can also occur as an inherited grain (Suzuki et al. 1994; Catlos et al. 2001; Rubatto et al. 2001; Rasmussen et al. 2002). During prograde metamorphism of metapelites with common Ca and Al contents, monazite reacts to form, for instance, other rare-earth element (REE)-bearing accessory minerals like allanite (Finger et al. 1998; Ferry 2000; Spear and Pyle 2002; Wing et al. 2003). At higher pressure ( $p$ ) - temperature ( $T$ ) conditions, allanite is commonly replaced by newly formed monazite (Wing et al. 2003; Gieré and Sorensen 2004; Janots et al. 2007, 2008; Goswami-Banerjee and Robyr 2015), which in a retrograde metamorphic evolution may be destabilised again. For instance, coronitic microstructures around relics of monazite imply that this mineral can partially be replaced by REE-bearing accessory phases (Finger et al. 1998; Broska et al. 2005; Massonne 2014; Balen et al. 2015).

The above information (see also section 5.1) suggests that monazite in medium-grade metamorphic rocks cannot be used as an indicator of the provenance of clastic sediments. Instead, the heavy-mineral zircon in such rocks is frequently analysed because it can be dated and additionally bears clues on the nature of the rock from which it was derived (e.g. Harley and Kelly 2007; Willner et al. 2013). This study demonstrates that detrital monazite grains can also survive in metapsammopelites at medium-temperature conditions even when a strong deformational event, leading to a mylonite, has overprinted such rocks.

Monazite from several paragneiss samples in the Münchberg Metamorphic Complex (MMC), a Variscan crystalline area in central Europe, was examined to establish its metamorphic evolution and to elucidate a new geodynamic model for the formation of Pangaea. For this reason, monazite from several samples was dated with the EMP. One of the samples, 13Mm3, apparently preserved detrital monazite, which is rather unusual behaviour, and therefore warranted an additional study to elucidate its metamorphic  $p$ - $T$  evolution in detail.

#### 4.2 Geological Setting

The MMC is located in north-eastern (NE) Bavaria (Fig. 4.1). It forms an oval-shaped complex (about  $25 \times 15 \text{ km}^2$ ), extending from the village of Bad Berneck in the south to the town of Hof in the north. As part of the Saxo-Thuringian Zone (STZ), the metamorphism of the MMC took place during the early Variscan orogeny in Palaeozoic times (Gebauer and Grünenfelder 1979; Kreuzer et al. 1989, 1993; Stosch and Lugmair 1990; Hammerschmidt and Franz 1992). This orogeny resulted from the movement of Gondwana to the north-west and its collision with Laurussia (Laurentia + Baltica) to form Pangaea (Franke 1989; Massonne and O'Brien 2003; Linnemann et al. 2003; Massonne 2005; Linnemann and Romer 2010; Arenas et al. 2014).

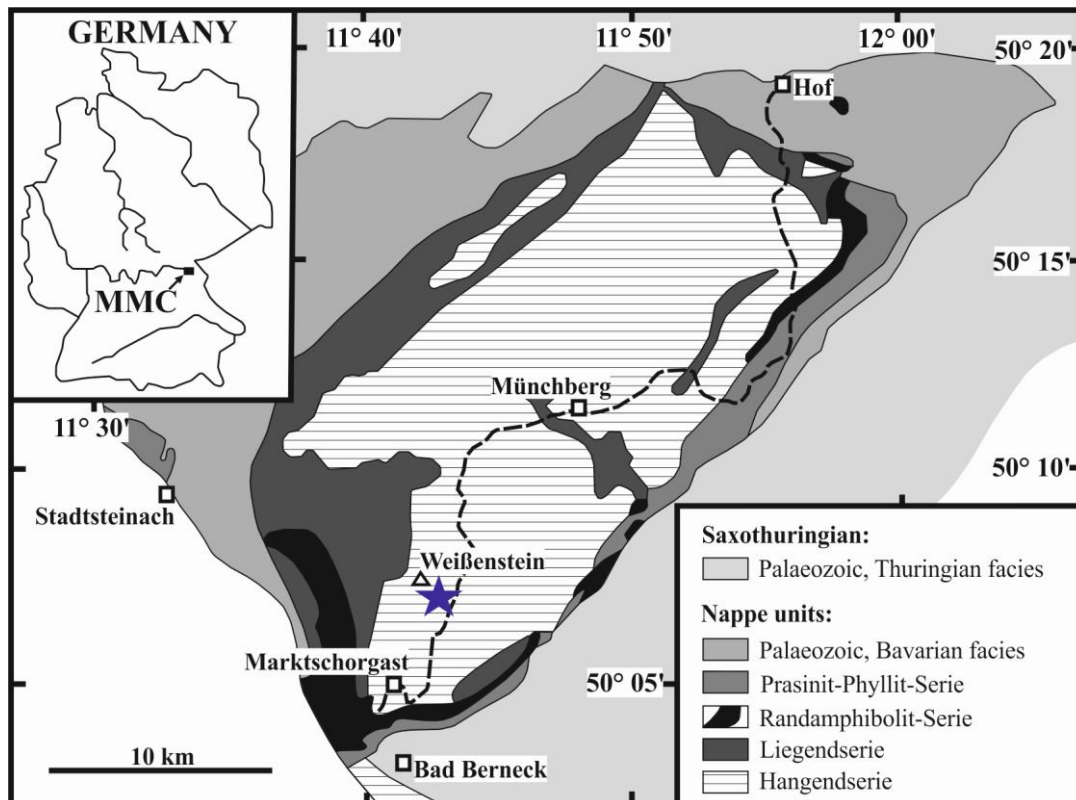


**Fig. 4.1:** Simplified geological map of the Münchberg Metamorphic Complex (MMC) in NE Bavaria (Germany), modified after Klemd et al. (1994). The location of the studied sample is highlighted.

The MMC is regarded as a nappe pile transported on top of autochthonous, anchi-metamorphic Palaeozoic sequences of the Thuringian lithofacies, as exposed in the south-eastern Frankenwald, in the Lower Carboniferous (Franke 1984; Klemd et al. 1994, Klemd 2010). This nappe pile is subdivided from the bottom to the top into the following units: Prasinit-Phyllit, Rand-Amphibolit, Liegendserie, and Hangendserie (e.g. Stettner 1960a; Kreuzer et al. 1989;

Okrusch et al. 1990). The Prasinit-Phyllit unit mainly consists of greenschist-facies metavolcanic and metasedimentary rocks. The Rand-Amphibolit unit is composed of amphibolites. Gneisses, mostly derived from clastic sediments, characterise the Liegendserie unit. The Hangendserie unit is dominated by various types of acidic to basic amphibolite-facies rocks, but also eclogite bodies like the famous one from the Weißenstein peak (e.g. Stosch and Lugmair 1990; O'Brien 1993; Klemd et al. 1994) are part of this unit.

The MMC (see also sections 5.2 and 6.2) is well known for its eclogites with omphacite records dating from the beginning of the 19th century (see Godard 2001). One of the first who had studied the eclogites from the MMC was Düll (1902). Detailed mineralogical studies followed later (e.g. Matthes et al. 1975; Matthes 1978). The peak  $p$ - $T$  conditions of the eclogites from the MMC were estimated by several studies (Franz et al. 1986; Klemd 1989; Klemd et al. 1991; O'Brien 1993; Klemd et al. 1994; Liebscher et al. 2007). According to Massonne and O'Brien (2003), these conditions cluster in the  $p$ - $T$  range of 20 - 34 kbar and 550 - 750 °C.

In contrast to the eclogites, little is known about the MMC gneisses, which can also contain garnet. A peak  $T$  range of 630 - 670 °C was assumed by Vollbrecht et al. (2006). Blümel (1986) reported a medium- $p$  event for the Hangendserie unit at about 8 kbar and c. 610 °C with a subsequent mylonitisation. Klemd (2010) estimated  $p$ - $T$  conditions of 6 - 10 kbar and  $620 \pm 30$  °C for the metasedimentary rocks of the same unit.

Various authors using different geochronological methods accomplished age dating. Gebauer and Grünenfelder (1979) determined U-Pb ages on zircon from the Weißenstein eclogite body (Fig. 4.1) and related them to the eclogitisation of the studied rocks ( $380 + 14 / - 22$  Ma (two-sigma:  $2\sigma$ )) and their protoliths ( $525 + 40 / - 31$  Ma). Kreuzer et al. (1989) got slightly different ages for the metamorphism (410 - 345 Ma), applying the K-Ar method to biotite, hornblende, and muscovite from all four units of the MMC. Sm-Nd isochrons (clinopyroxene-amphibole-garnet) and K-Ar ages (amphibole and mica) on the MMC eclogites gave a high-pressure (HP:  $> 10$  kbar) metamorphic age of 395 - 380 Ma, followed by amphibolite facies metamorphism at 380 - 365 Ma (Stosch and Lugmair 1990). A whole-rock Sm-Nd isochron, interpreted as a protolith age of  $480 \pm 23$  Ma, was obtained by Stosch and Lugmair (1990). Ar-Ar plateau and isochron ages, determined on phengites from eclogites, yielded  $365 \pm 7$  Ma (Hammerschmidt and Franz 1992). Kreuzer et al. (1993) obtained an age of  $379 \pm 1$  Ma (Ar-Ar plateau and K-Ar isochron), studying muscovite and hornblende of eclogites from the Hangendserie unit. The above ages clearly point to major Middle to Late Devonian metamorphic events during the early Variscan orogeny in the MMC (Massonne and O'Brien 2003). Such events were found to have

also occurred in other crystalline complexes of the Bohemian Massif (see, e.g. Kröner and Willner 1998; sections 3.1-3.2; 5.2; 6.2).

The studied gneiss 13Mm3 was sampled from a larger block in the forest between the top of the Weißenstein peak and a railroad track connecting the towns of Münchberg and Marktschorgast (see Fig. 4.1). This block was found close to this railroad track (N 50.1314° / E 11.7027°, WGS 84). From the 1:25000 geological map (No. 5836 Münchberg), the studied sample belongs to the uppermost part of the Liegendserie unit, which is at the sample site directly overlain by the Weißenstein eclogite body near the sample site. The sampled block and several smaller ones around showed the same characteristics, which are (1) a platy appearance, (2) a grey colour of the fresh surface, (3) a few reddish spots at this surface due to single mm-sized garnet grains and (4) sub-mm thick bands typical for a mylonite. In fact, Stettner (1960b) named this rock type a metahornfels, but its mesoscopic description, given by this author, is compatible with our observations (see also below).

#### 4.3 Analytical Procedures

For the determination of the bulk-rock composition (see also sections 3.3, 5.3 and 6.3), a representative piece of the rock sample (volume c.  $10 \times 5 \times 2 \text{ cm}^3$ ) was crushed and subsequently ground with a tungsten carbide dish-and-puck mill. The obtained rock powder was either fused with lithium borate, consisting of 66 wt%  $\text{Li}_2\text{B}_4\text{O}_7$  and 34 wt%  $\text{LiBO}_2$ , in a mass ratio of 1:10 to prepare a glass disk or mixed with the wax  $\text{C}_{38}\text{H}_{76}\text{N}_2\text{O}_2$  (mass ratio 4:1) to press a tablet, which were analysed for major and trace elements, respectively, with a Panalytical PW 2400 X-ray Fluorescence Spectrometer (XRF), considering certified geostandards. The rock powder was also used to analyse the total carbon (< 0.1 wt%) and water (< 2 wt%) contents, using a LECO<sup>®</sup> RC-412 elemental analyser, based on IR techniques.

According to the analytical procedure described by Massonne (2012), carbon-coated thin sections (area c.  $2 \times 4 \text{ cm}^2$ ) were employed to analyse the compositions of minerals, such as garnet, mica, monazite, and rutile, using a CAMECA SX100 EMP with five wavelength-dispersive (WD) spectrometers (see also sections 3.3, 5.3 and 6.3). For silicates (+ ilmenite), the concentrations of F, Na, Mg, Al, Si, K, Ca, Ti, Cr, Mn, Fe and Ba were determined, using counting times of 20 s at the peak and on the background. Synthetic and natural minerals, glasses (e.g. Ba glass for the  $\text{BaLa}1$ -peak), and pure oxides were used as standards. The applied acceleration voltage and beam current were 15 kV and 15 nA, respectively. The beam diameter

was approximately 3  $\mu\text{m}$ . The PaP correction procedure provided by CAMECA was applied. Analytical errors of the applied method were reported by Massonne (2012).

The analysis of rutile with the EMP for the Zr-in-rutile thermometry was achieved for Si, Cr, Fe, Zr, and Nb (Ti was calculated). The beam current and acceleration voltage were set to 100 nA and 15 kV, respectively. The counting time for the Zr  $L\alpha$ -radiation at the peak and the background was 100 s each. Natural zircon was used as a standard for this radiation.

In order to recognise zoning patterns of garnet, potassic white-mica, and monazite, element concentration maps for major elements were prepared by step-wise movement of a thin section under the electron beam of the EMP (step scanning) and subsequent computer-aided evaluation. For the mapping, counting times per step of 100 ms were applied. The electric current was either 150 nA (monazite), 70 nA (garnet) or 25 nA (mica).

Backscattered electron (BSE) images were prepared with the EMP, for instance, to document specific textural relations. For small inclusions in garnet, BSE images were also prepared with a CamScan CS44 Scanning Electron Microscope (SEM). For the calculation of structural formulae of minerals and the content of molar fractions of mineral components from EMP analyses, the computer programme CALCMIN (Brandelik 2009) was used.

For age dating of monazite, full analyses of this mineral with the EMP, including the elements Si, P, S, Ca, Y, La, Ce, Pr, Nd, Sm, Eu, Gd, Pb, Th, and U were achieved. The analytical procedure followed the approach of Massonne et al. (2012). This procedure gives a good match with more precise mass spectrometric methods (see Massonne et al. 2007a; Van Leeuwen et al. 2016) including a reference monazite from Brazil, the age dating of which varies, however, between 514 and 471 Ma (see Gasquet et al. 2010). This coincidence was also reasonable even for Tertiary monazite (see Liu et al. 2011; Massonne 2014, 2016a). To test the reliability of the procedure, a monazite from a saidenbachite was used as a reference during our major dating campaign. The age of this monazite had been dated with a Sensitive High Resolution Ion Microprobe (SHRIMP) to  $332.4 \pm 2.1$  Ma ( $2\sigma$ ) (Massonne et al. 2007a). The  $2\sigma$  uncertainty of our age dating results with respect to a single analysis was calculated by error propagation of the  $2\sigma$  errors of the counting rates of the peak and background intensities of the relevant elements. Since many monazite analyses yielded  $\text{ThO}_2$  contents between 4 and 5 wt%, a  $2\sigma$  error between 8 and 10 Ma often resulted for a single analysis. After determining all monazite ages with the MINCALC-V5 software programme and their corresponding  $2\sigma$  errors with MZ-Age, we used the Isoplot programme of Ludwig (1999) to illustrate the results graphically.

The amounts of different minerals in the rock sample, including specific types of garnet and potassic white-mica, were determined with the programme Adobe Photoshop CC 2015 (version 2015.0.1) which allows the counting of specific pixels in digital images. For this purpose, we used overview images of the entire thin sections produced with a slide scanner. In these images, specific phases were marked before starting the counting procedure. In addition, large areas (up to 2 cm<sup>2</sup>) of thin sections were scanned with the EMP to obtain element concentration maps (see above), applying a beam current of 50 nA and an acceleration voltage of 15 kV. For instance, from the K-map, the amount of micas could be determined.

#### 4.4 Mineral Compositions and Textures

The studied rock is a metamorphic psammopelite based on its relatively K- and Al-rich bulk-rock composition (Tabs. 4.1 and 8.10) and shows a very strong foliation due to a late mylonitisation event.

**Tab. 4.1:** Bulk-rock composition (compare Tab. 8.10) of the studied sample (oxides in wt%) from the Münchberg Metamorphic Complex (MMC), determined by XRF spectrometry and modified for PERPLE\_X calculations as explained in the text.

Sample	13Mm3		
	Oxides in wt%	XRF analysis	modified -group (I) garnet -Ti-poor mica
SiO <sub>2</sub>	71.083	72.056	69.133
TiO <sub>2</sub>	0.779	0.813	0.757
Al <sub>2</sub> O <sub>3</sub>	15.061	11.969	14.648
FeO		5.022	4.847
Fe <sub>2</sub> O <sub>3</sub>	5.539		
O <sub>2</sub>		0.056	0.053
MnO	0.071	0.048	0.069
MgO	1.556	1.391	1.513
CaO	0.256	0.197	0.178
Na <sub>2</sub> O	1.424	1.535	1.384
K <sub>2</sub> O	3.622	2.444	3.522
P <sub>2</sub> O <sub>5</sub>	0.055		
H <sub>2</sub> O		4.469	3.890
SUM	99.445	100.000	100.000

The sample has got a foliation defined by this event that wraps around elongate domains of fine grained, equigranular fabric. This makes up considerable portions of the metapsammopelite. The protolith is interpreted as a clastic sediment, probably a greywacke, that now contains a major mineral assemblage of quartz (41 vol% determined with Photoshop), mica (29 vol%),

feldspar (19 vol%), and garnet (9 vol% with inclusions). Accessory phases are apatite, chlorite, kyanite, monazite, rutile, zircon and opaque phases (ilmenite, magnetite).

Two distinct groups of garnet grains were observed (Fig. 4.2). One group (I) consists of medium-grained (0.5 - 2 mm diameter) garnet porphyroblasts with subhedral forms mainly due to a late mylonitisation event. Tiny, heavily corroded fragments of this garnet group that were separated from the original grains during the mylonitisation event are still loosely arranged around these grains, often forming tail-like structures aligned parallel to the foliation (Fig. 4.2c). Somewhat less than 5 vol% of the total garnet occurs as group I garnet. Inclusions in this garnet are mostly feldspar with K-feldspar prevailing over plagioclase, biotite (often altered to chlorite), ilmenite, potassic white-mica, and quartz.

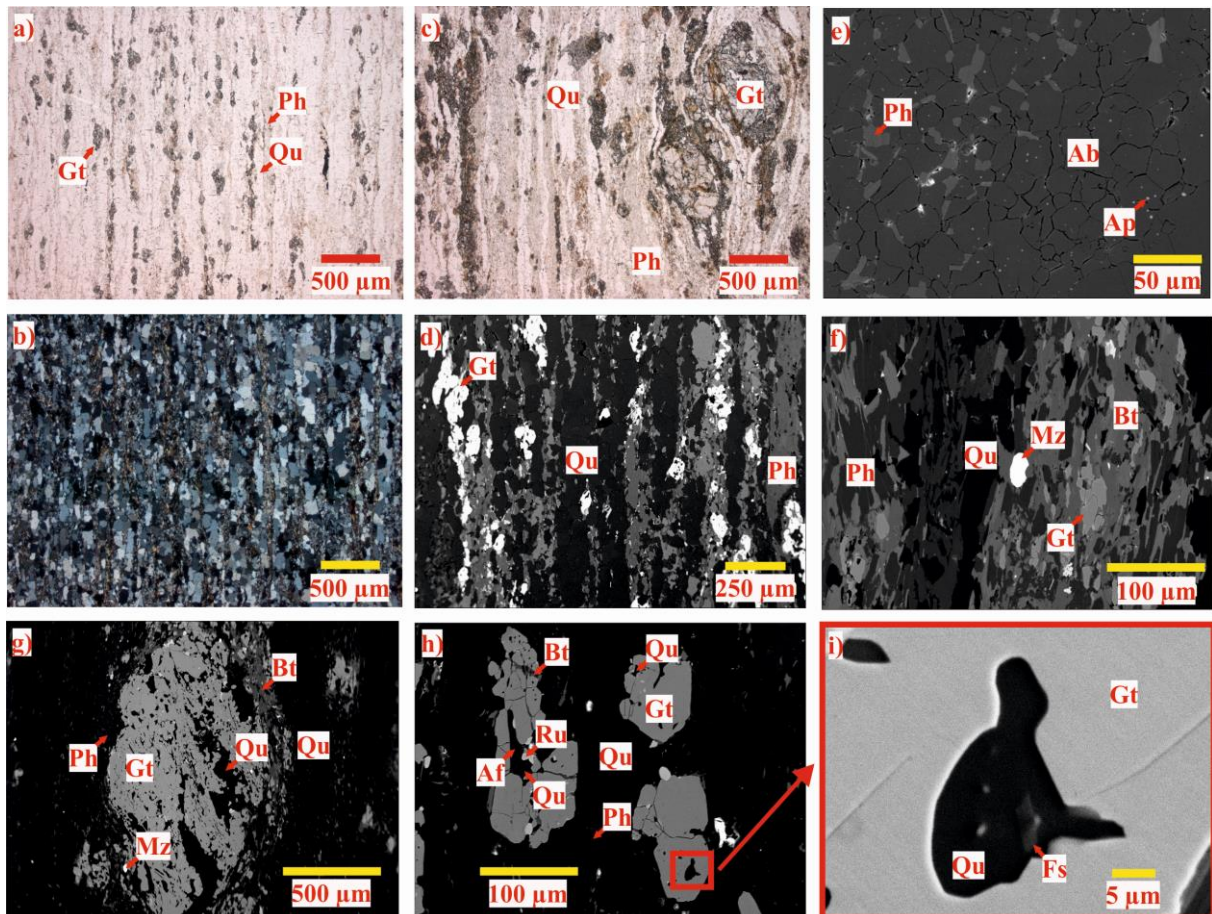


**Fig. 4.2:** Photomicrographs of objects in thin sections of sample 13Mm3 seen under plane polarised light (a,c) and crossed polarisers (b) with a ZEISS Axioplan. Backscattered electron (BSE) images (d-i) of objects in the same thin sections were obtained with a CAMECA SX100 EMP (d-h) and a CamScan CS44 SEM (i): Ab = albite-rich plagioclase, Ap = apatite, Bt = biotite, Fs = feldspar (consisting of alkali feldspar and plagioclase), Gt = garnet, Mz = monazite, Ph = potassic white-mica, Qu = quartz.

Elemental mapping with the EMP defined the following chemical zonation pattern for garnet of group I (Figs. 4.3 and 4.4): The content of the grossular (+ andradite) component increases slightly from the core to the rim from 2 to almost 4 mol%, whereas the content of the pyrope component increases considerably from 11 to almost 23 mol%. The content of the spessartine component shows a core to rim decrease from 12 to 1.3 mol%. Thus, the average composition of the core of garnet group I in sample 13Mm3 is  $\text{Alm}_{75}\text{GrAn}_2\text{Py}_{11}\text{Sp}_{12}$ . The garnet rim composition is  $\text{Alm}_{72.2}\text{GrAn}_{3.9}\text{Py}_{22.6}\text{Sp}_{1.3}$ .

**Tab. 4.2:** Representative analyses (in wt%) of garnet from the studied gneiss of the Münchberg Metamorphic Complex (MMC), obtained with a CAMECA SX100 EMP. The structural formulae were calculated as follows: 24 oxygen (double formula unit) and cation sum of Al + Ca + Cr + Fe + Mg + Mn + Na = 10. Abbreviations: calc = calculated, inter = intermediate.

Mineral	Garnet					
	Sample	13Mm3o B2-gt7-7	13Mm3o B2-gt7-4	13Mm3o B2-gt7-1	13Mm3- gt2-7	13Mm3- gt2-6
Comment	core,old	inter,old	rim,old	core,young	inter,young	rim,young
SiO <sub>2</sub>	36.64	36.86	37.63	37.77	37.75	37.61
TiO <sub>2</sub>	0.09	0.02	0.03	0.07	0.10	0.02
Al <sub>2</sub> O <sub>3</sub>	21.56	21.39	21.82	21.37	21.43	21.47
Cr <sub>2</sub> O <sub>3</sub>	0.02	0.02	0.02	0.04	0.02	0.03
Fe <sub>2</sub> O <sub>3</sub> <sub>calc</sub>	0.20	0.68	0.66	0.00	0.08	0.00
FeO	34.33	34.12	33.96	33.60	33.40	32.97
MnO	5.45	4.77	0.58	0.38	0.39	0.42
MgO	2.84	3.45	5.97	5.80	5.83	4.87
CaO	0.69	0.78	1.45	0.63	0.93	2.38
Na <sub>2</sub> O	0.03	0.03	0.00	0.03	0.03	0.01
Total	101.85	102.12	102.11	99.68	99.96	99.78
Si	5.732	5.728	5.738	5.993	5.960	5.962
Ti	0.011	0.002	0.003	0.008	0.011	0.002
Al	3.974	3.917	3.922	3.996	3.987	4.010
Cr	0.002	0.002	0.001	0.005	0.002	0.003
Fe <sup>3+</sup>	0.023	0.079	0.075	0.000	0.009	0.000
Fe <sup>2+</sup>	4.491	4.435	4.330	4.459	4.410	4.371
Mg	0.662	0.798	1.358	1.373	1.371	1.150
Ca	0.116	0.129	0.236	0.106	0.158	0.404
Mn	0.722	0.627	0.074	0.050	0.052	0.056
Na	0.008	0.009	0.000	0.008	0.007	0.002

Garnet of group II is characterised by its occurrence as clusters of several grains. Individual grains are frequently anhedral with diameters of 30 - 100 µm. This garnet, which can also be marginally corroded, shows the same type of inclusion minerals as garnet of group I. In addition, multiphase inclusions of feldspar and quartz are present (Fig. 4.2i). Such a type of

inclusions was interpreted as enclosed melt (see Cesare et al. 2011 and references therein). The garnet clusters are strongly elongated parallel to the strong foliation. Occasionally, garnet porphyroblasts occur which display almost symmetric tails of such clusters. This feature gives evidence of the formation of the garnet clusters from former group I garnet. The following chemical zonation pattern was noted (Figs. 4.3 and 4.4) for garnet group II: from the core to the rim, the content of the pyrope component decreases from 23 to 19 mol% and the grossular (+ andradite) component increases from 2 to 7 mol%. Mn is homogeneously distributed in garnet group II grains with a spessartine content that is significantly lower ( $\leq 1$  mol%) than that of group I garnet (see Tab. 4.2).

**Tab. 4.3:** Representative analyses (in wt%) of potassic white-mica from the studied gneiss of the Münchberg Metamorphic Complex (MMC), obtained with a CAMECA SX100 EMP. The structural formulae were calculated as follows: 22 oxygen (double formula unit). For all micas the total was corrected for F. Abbreviation: calc = calculated.

Mineral	Potassic white-mica					
	13Mm3oB- ms4-4	13Mm3oB- ms4-5	13Mm3oB- ms4-6	13Mm3oB -ms4-1	13Mm3oB -ms4-2	13Mm3oB -ms4-9
Sample	old, Ti-poor	old, Ti-poor	old, Ti-poor	young, Ti- rich	young, Ti- rich	young, Ti- rich
SiO <sub>2</sub>	45.72	44.96	46.82	47.24	47.39	46.75
TiO <sub>2</sub>	0.48	0.42	0.47	1.14	1.12	1.15
Al <sub>2</sub> O <sub>3</sub>	33.45	33.43	31.91	31.15	30.57	31.16
FeO	1.53	1.47	1.66	1.49	1.83	1.50
MgO	1.62	1.51	1.96	2.00	2.11	1.87
Na <sub>2</sub> O	0.54	0.59	0.35	0.34	0.32	0.29
K <sub>2</sub> O	10.53	10.76	10.94	10.91	10.56	10.71
BaO	0.12	0.18	0.22	0.25	0.17	0.13
H <sub>2</sub> O <sub>calc</sub>	4.43	4.37	4.43	4.44	4.43	4.41
Total	98.42	97.70	98.79	99.00	98.55	97.97
Si	6.194	6.165	6.339	6.379	6.413	6.359
Ti	0.048	0.042	0.048	0.115	0.114	0.118
Al	3.535	3.569	3.431	3.337	3.288	3.356
Fe <sup>2+</sup>	0.173	0.168	0.188	0.167	0.207	0.170
Mg	0.327	0.308	0.395	0.402	0.424	0.378
Na	0.140	0.155	0.091	0.088	0.083	0.077
K	1.819	1.883	1.889	1.880	1.823	1.858
Ba	0.006	0.009	0.011	0.013	0.009	0.006

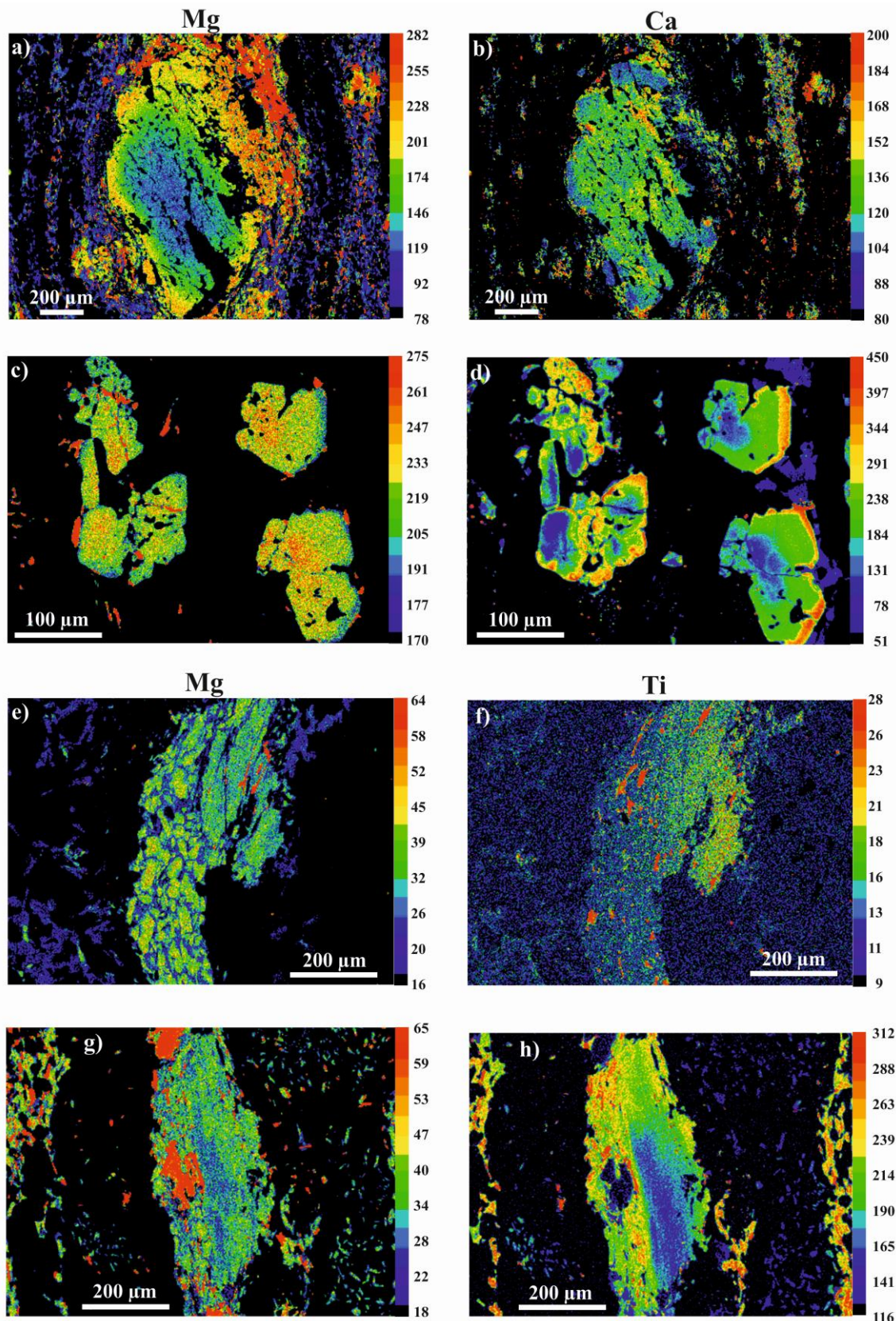


**Fig. 4.3:** Elemental maps of garnet (a-d: Mg and Ca) and clusters of potassic white-mica (e-h: Mg and Ti) in the studied sample, obtained with a CAMECA SX100 EMP. The scales for the colour code on the right hand side of each image indicate counts of specific X-ray radiation per time unit. a) and b) refer to a large pre-mylonitisation garnet (group I); c) and d) represent small garnet grains (group II) formed after mylonitisation. Ti-poor domains of potassic white-mica form cores in larger grains and are, thus, older than Ti-rich domains.

**Tab. 4.4:** Representative analyses (in wt%) of biotite, plagioclase and K-feldspar from the studied gneiss of the Münchberg Metamorphic Complex (MMC), obtained with a CAMECA SX100 EMP. The structural formulae were calculated as follows: a) biotite: 11 oxygen, b) plagioclase and K-feldspar: eight oxygen. For all micas the total was corrected for F. Abbreviation: calc = calculated.

Mineral	Biotite		Plagioclase		K-feldspar
	Sample	13Mm3-bt4	13Mm3-bt5	13Mm3-albite4	13Mm3-albite6
Comment			matrix		
SiO <sub>2</sub>	34.96	33.5	67.91	67.74	64.22
TiO <sub>2</sub>	2.55	2.17	0.00	0.00	0.10
Al <sub>2</sub> O <sub>3</sub>	17.75	18.12	19.71	20.06	19.26
Fe <sub>2</sub> O <sub>3</sub> <sub>calc</sub>			0.08	0.02	3.24
FeO	22.96	24.37			
MnO	0.07	0.06	0.00	0.00	0.01
MgO	7.42	7.91	0.01	0.01	1.38
CaO	0.03	0.04	0.30	0.53	0.00
Na <sub>2</sub> O	0.15	0.13	11.34	11.48	0.21
K <sub>2</sub> O	8.96	7.96	0.01	0.06	10.89
BaO	0.05	0.04			0.28
H <sub>2</sub> O <sub>calc</sub>	3.85	3.81			
Total	98.76	98.11	99.37	99.89	99.59
Si	2.720	2.636	2.984	2.966	2.925
Ti	0.149	0.128	0.000	0.000	0.004
Al	0.348	0.317	1.021	1.035	1.034
Fe <sup>3+</sup>			0.003	0.001	0.111
Fe <sup>2+</sup>	1.494	1.604			
Mg	0.861	0.928			
Ca	0.003	0.003	0.014	0.025	0.000
Mn	0.005	0.004	0.000	0.000	0.001
Na	0.023	0.019	0.966	0.975	0.019
K	0.889	0.800	0.001	0.004	0.633
Ba	0.002	0.001			0.005

The grain size of potassic white-mica generally ranges between 20 and 60  $\mu\text{m}$  (Fig. 4.2) but a few grains are as large and 0.1 - 0.5 mm. White mica grains are oriented parallel to and concentrated in layers where potassic white-mica clearly dominates biotite. Elongate aggregates of fine-grained mica, again with prevailing white mica but without orientation, were observed. Since such aggregates were found to occur around clusters of fine-grained kyanite, they are interpreted as late replacement products of this phase. According to the elemental mapping of some clusters of potassic white-mica in mica-rich layers (Fig. 4.3), most grains are chemically fairly homogeneous. However, some larger grains show a chemical zonation in regard to their Mg and Ti contents. As demonstrated in Fig. 4.3h, inner portions of zoned potassic white-mica are poorer in Ti (< 0.5 wt% TiO<sub>2</sub>) than the outer portions (> 1.0 wt% TiO<sub>2</sub>). The Photoshop

analyses indicate that 44 vol% of the entire potassic white-mica in layers belongs to the early Ti-poor generation. The Si contents in potassic white-mica (Tab. 4.3) of both generations and non-oriented white mica in aggregates are between 3.08 and 3.21 per formula unit (pfu). The composition of larger biotite in mica-rich layers is characterised by 2.69 Si pfu and  $X_{Mg} = Mg/(Mg+Fe) = 0.37$  (Tab. 4.4).

The size of feldspar grains, with plagioclase clearly dominating K-feldspar, varies mostly between 20 and 100  $\mu m$ . Similar to quartz, plagioclase forms aggregates of equigranular grains (Fig. 4.2). These aggregates are strongly elongated parallel to the foliation of the rock. Thus, former, significantly larger feldspar grains were strongly flattened, owing to the mylonitisation event, and recrystallised.

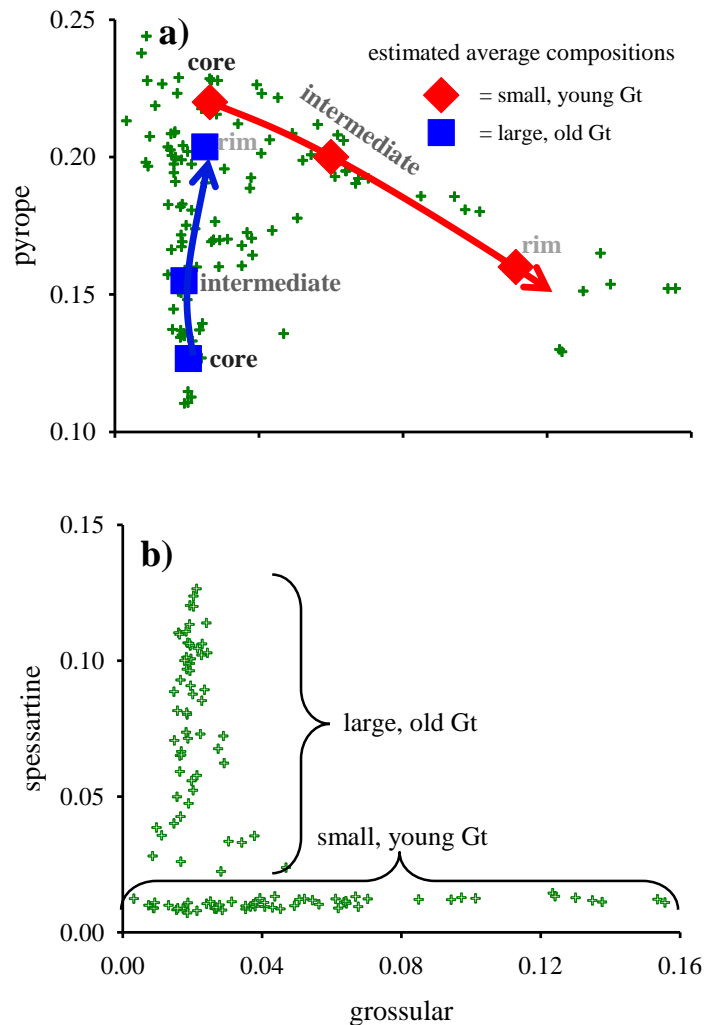


**Fig. 4.4:** Garnet (Gt) analyses, obtained with a CAMECA SX100 EMP, in terms of molar fractions of (a) pyrope and (b) spessartine versus that of grossular (+ andradite). The solid lines show chemical trends from core to rim compositions of garnet, considering both the large and small garnet grains (groups I and II).

Very few relics of mm-sized feldspar grains confirm this interpretation. Plagioclase is composed of 98 mol% albite, up to 2 mol% anorthite, and less than 0.1 mol% orthoclase components (Tab. 4.4). Rare K-feldspar contains 3 mol% albite and less than 1 mol% anorthite components (Tab. 4.4).

Kyanite has experienced the same fate as large garnet and feldspar grains due to the mylonitisation event because clusters of about 50  $\mu\text{m}$  sized, unoriented kyanite grains occur in the studied sample. These clusters are surrounded by small, non-oriented muscovite grains (see above). Kyanite contains around 0.2 wt%  $\text{Fe}_2\text{O}_3$  (Tab. 4.5).

**Tab. 4.5:** Representative analyses (in wt%) of ilmenite and kyanite from the studied gneiss of the Münchberg Metamorphic Complex (MMC), obtained with a CAMECA SX100 EMP. The structural formulae were calculated as follows: a) kyanite: three cations, and b) ilmenite: three oxygen. Abbreviation: calc = calculated.

Mineral	Ilmenite		Kyanite	
Sample	13Mm3-ilmenite1	13Mm3-ilmenite2	13Mm3-kyanite5	13Mm3-kyanite6
Comment			matrix	
SiO <sub>2</sub>			37.35	36.88
TiO <sub>2</sub>	53.43	53.32	0.00	0.01
Al <sub>2</sub> O <sub>3</sub>	0.00	0.00	63.08	62.91
Cr <sub>2</sub> O <sub>3</sub>	0.02	0.01	0.04	0.05
Fe <sub>2</sub> O <sub>3</sub> calc	0.00	0.00	0.21	0.20
FeO	41.09	41.46		
MnO	4.17	4.11	0.00	0.00
MgO	0.00	0.02		
CaO			0.00	0.02
Na <sub>2</sub> O			0.01	0.00
Total	98.71	98.92	100.69	100.06
Si			1.001	0.994
Ti	1.029	1.024	0.0000	0.0002
Al	0.000	0.000	1.993	1.999
Cr	0.0004	0.0003	0.001	0.001
Fe <sup>3+</sup>	0.000	0.000	0.004	0.004
Fe <sup>2+</sup>	0.880	0.886		
Mg	0.000	0.001		
Ca			0.000	0.001
Mn	0.091	0.089	0.000	0.000
Na			0.0003	0.0000

Rutile grains are elongated and anhedral with lengths up to 100  $\mu\text{m}$ . This mineral usually occurs in the matrix and is rarely enclosed in garnet. Rutile is often partially replaced by ilmenite. The

latter contains neither geikielite nor hematite (+ corundum) but on average 9 mol% pyrophanite components (Tab. 4.5). The composition of rutile is characterised by 0.5 wt% FeO and 0.2 wt% Nb<sub>2</sub>O<sub>5</sub> (Tab. 4.6).

**Tab. 4.6:** Representative analyses (in wt%) of rutile from the studied gneiss of the Münchberg Metamorphic Complex (MMC), obtained with a CAMECA SX100 EMP. The structural formula of rutile is based on two oxygen anions.

Mineral	Rutile					
	13Mm3-rt1- 1	13Mm3-rt2- 1	13Mm3-rt2- 6	13Mm3-rt3- 1	13Mm3-rt3- 3	13Mm3-rt3- 4
Oxides in wt%						
TiO <sub>2</sub>	99.28	99.24	99.49	99.46	99.53	99.48
SiO <sub>2</sub>	0.000	0.000	0.000	0.000	0.000	0.000
Nb <sub>2</sub> O <sub>5</sub>	0.212	0.215	0.119	0.102	0.107	0.133
FeO	0.493	0.531	0.365	0.435	0.350	0.385
ZrO <sub>2</sub>	0.020	0.016	0.023	0.019	0.018	0.012
Total	100.01	100.00	100.00	100.01	100.01	100.01
Ti	0.9931	0.9927	0.9951	0.9944	0.9954	0.9948
Si	0.0000	0.0000	0.0000	0.0000	0.0000	0.0000
Nb	0.0013	0.0013	0.0007	0.0006	0.0006	0.0008
Fe	0.0055	0.0059	0.0041	0.0048	0.0039	0.0043
Zr	0.0001	0.0001	0.0001	0.0001	0.0001	0.0001

## 4.5 Pressure-Temperature Evolution

### 4.5.1 Calculation Methods

In order to derive the  $p$ - $T$  evolution for the studied rock from the MMC,  $p$ - $T$  pseudosections were calculated with the PERPLE\_X computer programme package (see Connolly 2005; version from August 2011 downloaded from the internet site <http://www.perplex.ethz.ch/>) for the  $p$ - $T$  range of 2 - 24 kbar and 350 - 750 °C (see also sections 5.6.1 and 6.6.1). These  $p$ - $T$  pseudosections, which were calculated in the eleven-component system SiO<sub>2</sub>-TiO<sub>2</sub>-Al<sub>2</sub>O<sub>3</sub>-MgO-MnO-FeO-CaO-Na<sub>2</sub>O-K<sub>2</sub>O-H<sub>2</sub>O-O<sub>2</sub>, were contoured by isopleths for molar fractions of garnet components, Si contents in potassic white-mica and modal contents of garnet.

The thermodynamic data set of Holland and Powell (1998, updated 2002) for minerals and H<sub>2</sub>O was applied to all PERPLE\_X calculations. For these calculations, the following solid-solution models were chosen: (1) Gt(HP) for garnet (Holland and Powell 1998); (2) Opx(HP) for orthopyroxene (Powell and Holland 1999); (3) Ep(HP) for clinozoisite-epidote (see Holland and Powell 1998); (4) Mica(M) for paragonite (Massonne 2010) with maximal 50 mol% muscovite component; (5) Chl(HP) for chlorite based on the formulation by Holland et al.

(1998); (6) TiBio(HP) for biotite being identical to the previous model Bio(HP) created by Powell and Holland (1999) as the tbi component was removed (see below); (7) Omph(HP) for clinopyroxene based on the thermodynamic data given by Holland and Powell (1996) augmented by those related to the end-members aegirine (acm) and  $\text{CaAl}_2\text{SiO}_6$  (cats); (8) feldspar for ternary feldspar according to Fuhrman and Lindsley (1988) using a subdivision into two models feldspar1 and feldspar2 with different compositional limits (1: max. 8 mol% sanidine component, 2: max. 10 mol% anorthite and max. 10 mol% albite components) as proposed by Massonne (2009); (9) St(HP) for staurolite (“from THERMOCALC”, written comm. by J.A.D. Connolly); (10) Stlp(M) for stilpnomelane (Massonne 2010); (11) MtUl(A) for magnetite (see Andersen and Lindsley 1988); (12) Pheng(HP) for potassic white-mica (see Powell and Holland 1999 as well as comments in file newest\_format\_solut.dat) with maximal 50 mol% paragonite component; (13) IlHm(A) for hematite (Andersen and Lindsley 1988) with maximal 50 mol% ilmenite component; (14) GlTrTsPg for amphibole (glaucophane-tremolite-tschermakite-pargasite + corresponding  $\text{Fe}^{2+}$ -bearing components), and (15) Ctd(HP) for chloritoid (“from THERMOCALC”, written comm. by J.A.D. Connolly). For cordierite, ilmenite, carpholite, and talc, the ideal mixing models hCrd, IlGkPy (max. 30 mol% geikielite component), Carp, and T, respectively, were used, which are based on the thermodynamic data for the corresponding end-members given by Holland and Powell (1998).

To obtain the  $p$ - $T$  conditions of solidus curves in the range of 2 - 24 kbar and 560 - 750 °C, PERPLE\_X calculations were achieved with a version downloaded in August 2006. In order to consider granitic melt, only the model melt(HP), according to White et al. (2001), was added to the aforementioned solid solution models.

The abbreviated end-member phases acti (actinolite), ann1 (annite), mic (microcline), ab (low  $T$  albite), cumm (cummingtonite), grun (grunerite), and the  $\text{O}_2$  buffers qfm and mthm in the applied data file were not considered. Both Ti end-members tip and tbi in white and dark micas, respectively, were excluded as argued by Massonne et al. (2017). The  $\text{H}_2\text{O}$  component in the haplogranitic melt model (h2oL) was only neglected for calculations without melt.

The bulk-rock composition of the studied sample 13Mm3 (Tab. 4.1), determined by XRF spectrometry, was modified for PERPLE\_X calculations: (1) CaO was reduced because some Ca is bound to apatite. The content of (ideally composed) apatite was calculated on the basis of the determined content of  $\text{P}_2\text{O}_5$  in the bulk-rock. (2) The oxygen content, which is related to the amount of trivalent iron in the rock, was estimated according to a value corresponding to 10 wt% of the iron being trivalent during metamorphism as assumed for previous calculations of

$p$ - $T$  pseudosections for HP and UHP rocks (e.g. Massonne et al. 2007b). (3) A water content of 4 wt% was considered to permit the formation of a free hydrous fluid already at relatively low temperatures. (4) For a late metamorphic stage, the effective bulk-rock composition can differ from the determined bulk-rock composition because, for instance, the garnet core, formed during an early metamorphic stage, would not participate in later metamorphic reactions. Although the  $p$ - $T$  pseudosection calculation after subtraction of the garnet core from the bulk-rock composition might result only in minor changes compared to the  $p$ - $T$  pseudosection calculated for the bulk-rock (see Massonne 2014), such a procedure was undertaken to obtain the effective bulk-rock composition for PERPLE\_X calculations of a late metamorphic stage. For this purpose the average chemical composition ( $\text{Alm}_{73.6}\text{GrAn}_{2.0}\text{Py}_{16.6}\text{Sp}_{7.7}$ ) of large garnet grains (type I), amounting to 0.5 vol% of the whole rock (see above), was subtracted from the bulk-rock composition. In addition, a subtraction of early Ti-poor potassic white-mica from the bulk-rock composition was considered (see above). (5) For all rock compositions, involved in PERPLE\_X calculations, the sums of the oxide contents in wt% were normalised to 100 wt% (Tab. 4.1).

Generally speaking, four different calibrations of the Zr-in-rutile thermometer (two by Zack et al. 2004; Watson et al. 2006; Tomkins et al. 2007) were applied to all samples of this study:

- $T(^{\circ}\text{C}) = 134.7 \cdot \ln(\text{Zr}) - 25$  (after Zack et al. 2004 (a))
- $T(^{\circ}\text{C}) = 127.8 \cdot \ln(\text{Zr}) - 10$  (after Zack et al. 2004 (b))
- $T(^{\circ}\text{C}) = \frac{4470 \pm 120}{(7.36 \pm 0.10) - \log(\text{Zr})} - 273$  (after Watson et al. 2006)
- $T(^{\circ}\text{C}) = \frac{83.9 + 0.410 \cdot p}{0.1428 - R \cdot \ln(\text{Zr})} - 273$  (after Tomkins et al. 2007 for  $\alpha$ -quartz)

Abbreviations:  $p$  = pressure,  $R$  = gas constant,  $T$  = temperature,  $\text{Zr}$  = zirconium contents in rutile in ppm.

Only the calibration by Tomkins et al. (2007) for  $\alpha$ -quartz considers a pressure dependence and was, thus, favoured. The temperature values resulting from all conducted measurements of the Zr content in rutile were averaged and a  $2\sigma$  error was calculated for this average. The error propagation of the  $1\sigma$  of the counting rates of the peak and background intensities of the Zr  $L\alpha$ -radiation resulted in a temperature error of about  $\pm 40^{\circ}\text{C}$  ( $1\sigma$ ) for a single analysis.

4.5.2 Results of the Calculated  $p$ - $T$  Pseudosections

As it turned out that the  $p$ - $T$  range of at most 2 - 17 kbar and 510 - 750 °C is of relevance for this study, the calculated  $p$ - $T$  pseudosection for the modified bulk-rock composition (without subtraction of any mineral domains) is solely shown for this range in Fig. 4.5. Only quartz and water are present in the entire  $p$ - $T$  range of this graph. K-phases occur as biotite, K-feldspar, and potassic white-mica in the  $p$ - $T$  range of Fig. 4.5.

The micas are present nearly throughout the whole  $p$ - $T$  range of Fig. 4.5. Biotite does not appear close to 17 kbar and 510 °C as well as 2 kbar and 750 °C. Potassic white-mica is only missing at a pressure below 7 kbar if the temperatures are above 630 °C. The chemical composition of potassic white-mica in terms of its Si content strongly depends on the  $p$ - $T$  conditions (see Fig. 4.6): A Si content of 3.55 pfu occurs at 440 °C and 24 kbar. At 2 kbar and 550 °C, the Si content is only 3.05 pfu. K-feldspar only occurs at pressures below 8 kbar (750 °C) or at temperatures above 590 °C (2 kbar).

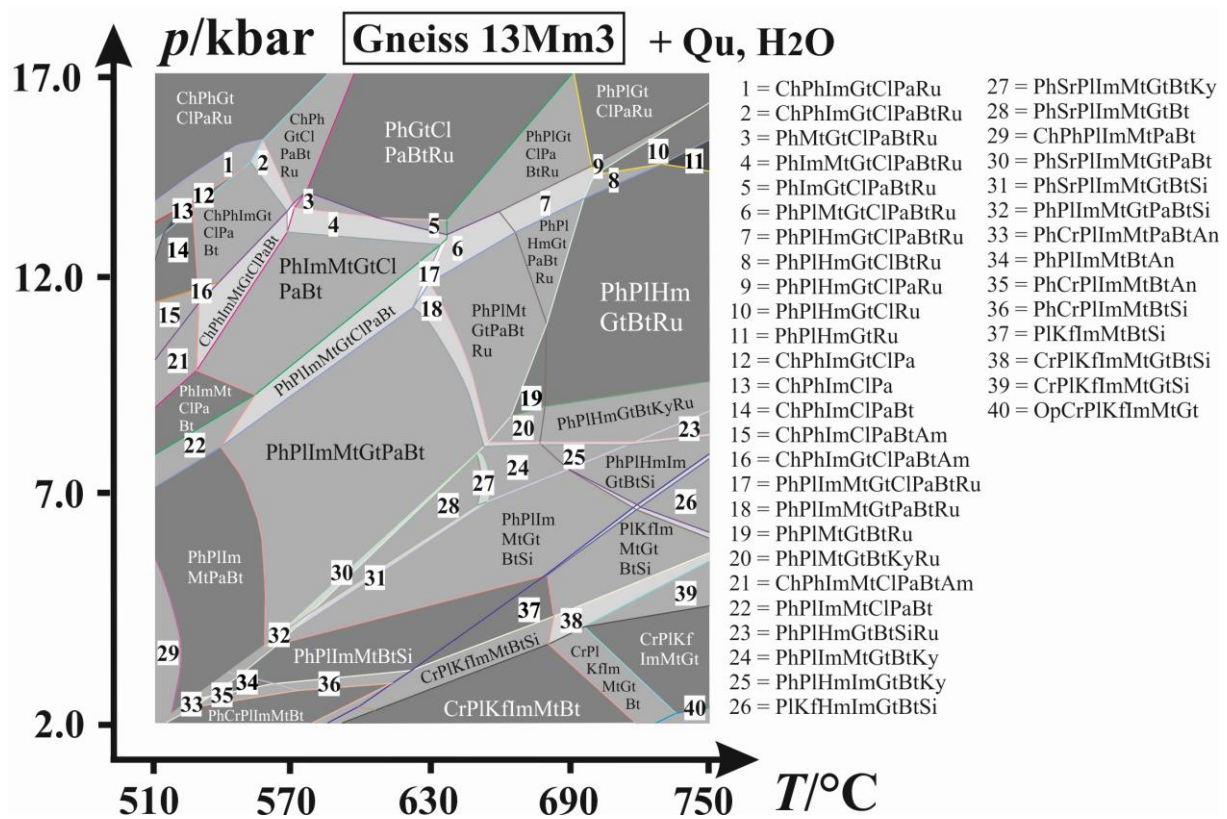


**Fig. 4.5:**  $p$ - $T$  pseudosection (without melt) calculated for the composition of sample 13Mm3 (see Tab. 4.1) with the computer software package PERPLE\_X (see text). Abbreviations: Am = Na-rich amphibole, An = andalusite, Bt = biotite, Ch = chlorite, Cl = clinopyroxene, Cr = cordierite, Gt = garnet, Hm = hematite-rich ilmenite, Im = ilmenite, Kf = K-feldspar, Ky = kyanite, Mt = magnetite, Op = orthopyroxene, Pa = paragonite, Ph = potassic white-mica, Pl = plagioclase, Qu = quartz, Ru = rutile, Si = sillimanite, Sr = staurolite.

The lower temperature limit of garnet is 430 and 710 °C at 17 and 2 kbar, respectively, in both  $p$ - $T$  pseudosections. With rising pressures and temperatures, more and more garnet is present in the various mineral assemblages. The maximum modal content of garnet is somewhat above 8 vol% in Fig. 4.7. The  $p$ - $T$  field of garnet in the  $p$ - $T$  pseudosections was contoured by isopleths for molar fractions of grossular  $X(\text{Ca})$  and pyrope  $X(\text{Mg})$  (see Fig. 4.6). The higher the temperatures, the more Mg is stored in garnet, which is a typical feature of many rock types (e.g. Săbău 2000; Massonne 2014).

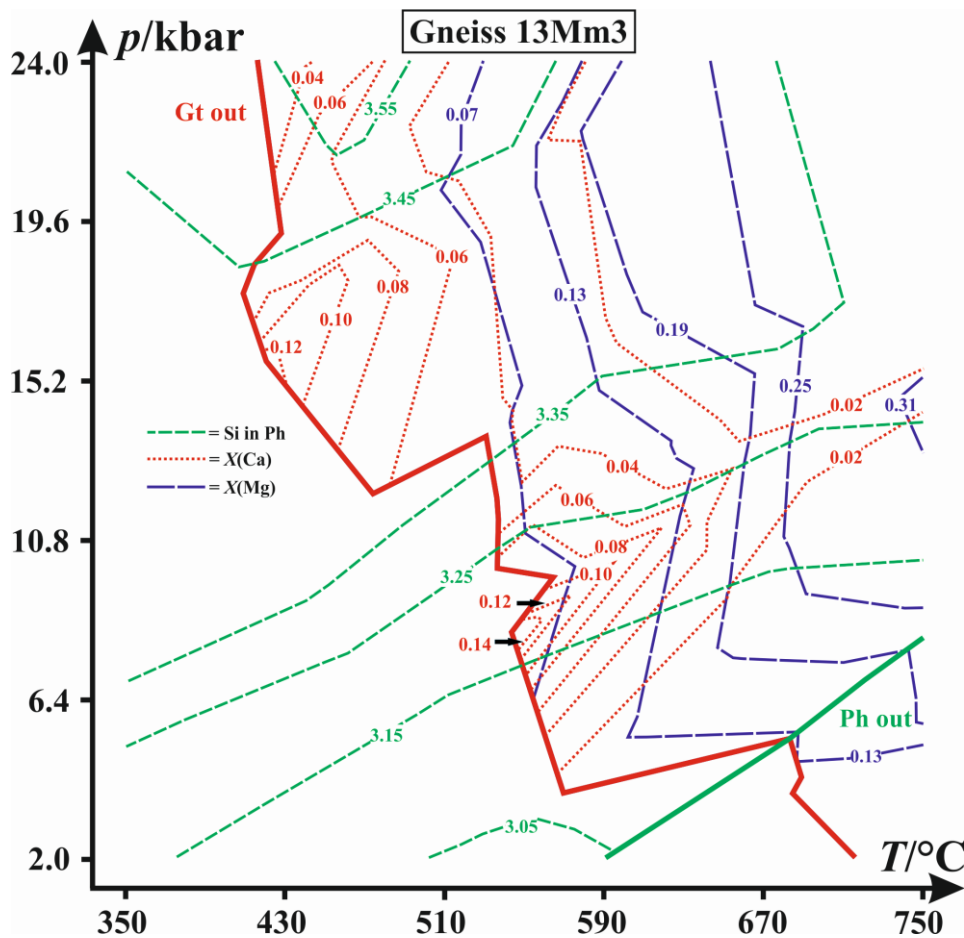


**Fig. 4.6:** Contouring of the calculated  $p$ - $T$  pseudosection of Fig. 4.5 by isopleths for the molar fractions of garnet (Gt) components and the Si contents per formula unit (pfu) in potassic white-mica (Ph). The thick curves mark the limits of the occurrence of garnet and potassic white-mica.

The minimum Mg content given as  $X(\text{Mg})$  is about 0.07 at  $p$ - $T$  conditions of > 6 kbar and 510 °C. The maximum  $X(\text{Mg}) = 0.31$  is reached at > 10 kbar and 750 °C in both  $p$ - $T$  pseudosections. In contrast, the lower the temperature, the more Ca is incorporated into garnet. The pressure plays a more important role for the Ca than for the Mg incorporation in garnet. The minimum

Ca content in garnet, expressed as  $X(\text{Ca})$ , is 0.02 at elevated temperatures. The maximum  $X(\text{Ca})$  is 0.14 at about 7 kbar and 580 °C for both  $p$ - $T$  pseudosections.

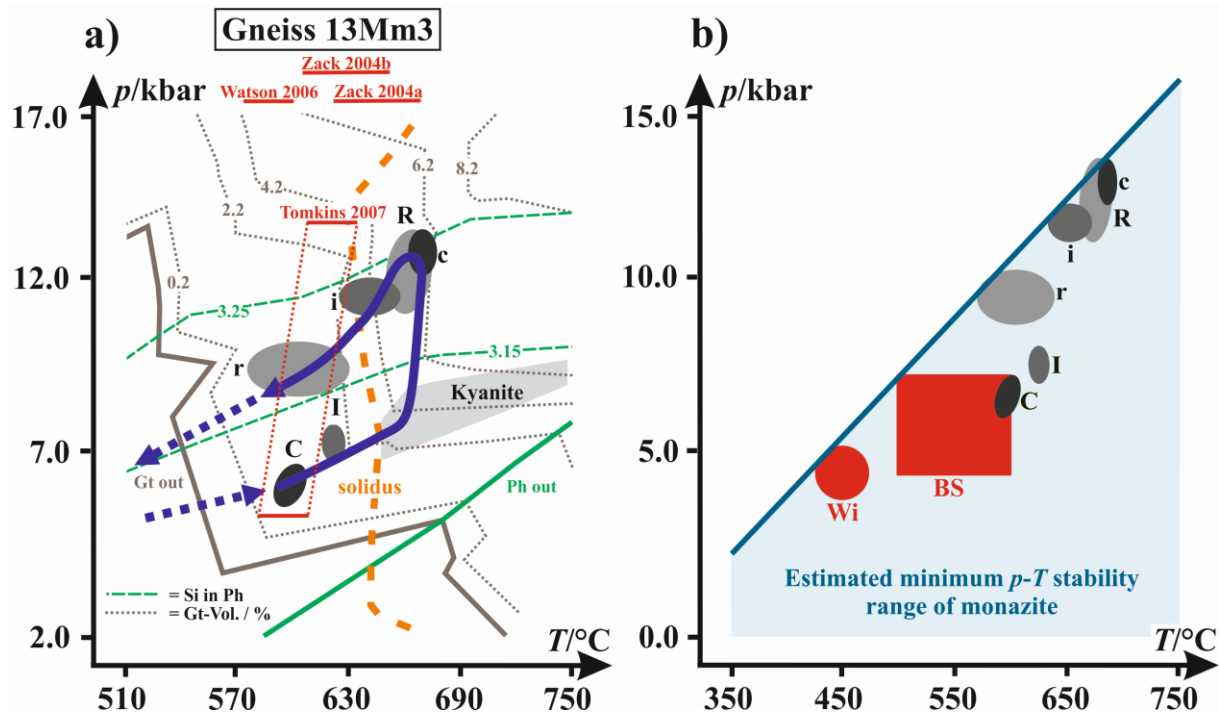


**Fig. 4.7:** a)  $p$ - $T$  estimates (error ellipses) for the studied rock, using garnet isopleths of Fig. 4.6. The constructed  $p$ - $T$  path is shown by a solid line, the direction of which is given by an arrow. The presumed  $p$ - $T$  path towards early metamorphic conditions (stage I) and along late metamorphic conditions is given by thick, dotted lines with arrows. The thick curves mark the limits of the occurrences of garnet (Gt) and potassic white-mica (Ph). The wet solidus curve is indicated by a thick, dashed line. Results of three calibrations of the Zr-in-rutile thermometer are indicated as  $2\sigma$  error bars. The fourth calibration of this thermometer, which is pressure-dependent, is shown by a parallelogram (connected  $2\sigma$  error bars). b) Estimated minimum  $p$ - $T$  stability range of monazite (see text). Estimated breakdown conditions of monazite after Broska and Siman (1998) = BS and Williams et al. (2011) = Wi. Further abbreviations: C and c = core, I and i = intermediate, R and r = rim with upper and lower case letters referring to large, early Gt and small, late Gt, respectively.

Plagioclase is stable up to 8 kbar at 510 °C and 17 kbar at 650 °C. At these conditions, pure albite is the stable plagioclase. With decreasing pressure, the anorthite component in plagioclase is rising. A content of 5 vol% of this component is reached, for instance, at 9 kbar and 750 °C and 11 kbar and 635 °C. The low pressure limit for the occurrence of Na-rich clinopyroxene is at somewhat lower pressures compared to the upper pressure limit of plagioclase. Moreover, kyanite appears only in a small elongated  $p$ - $T$  area, ranging from 7 kbar and 640 °C to 8 kbar and 750 °C. Rutile occurs from 14 kbar at 510 °C to 8 kbar at 750 °C. The phase relations at high temperatures shown in Fig. 4.5 are partially metastable, because the calculated solidus

curve at wet conditions runs, for instance, through the following  $p$ - $T$  conditions: 2 kbar, 670 °C; 8 kbar, 660 °C; 13 kbar, 650 °C; 17 kbar, 680 °C (see Fig. 4.7).

#### 4.5.3 Construction of the $p$ - $T$ Path

As outlined above, the results of the calculations of  $p$ - $T$  pseudosections for both modified bulk-rock compositions given in Tab. 4.1 (with and without subtraction of garnet and potassic white-mica cores; see section 4.5.1) are nearly identical. Therefore, only the results for the composition without subtraction of mineral portions were used to reconstruct the  $p$ - $T$  path.

A major criterion for the derivation of a specific  $p$ - $T$  condition is the intersection of isopleths for molar fractions of garnet components (e.g. Caddick and Kohn 2013; Massonne 2013). In this study, we use those of the  $X(\text{Ca})$  and  $X(\text{Mg})$  isopleths. For the core of the large, early garnet ( $\text{Alm}_{75}\text{GrAn}_2\text{Py}_{11}\text{Sp}_{12}$ ), the corresponding isopleths intersect at about 6 kbar and 600 °C (Fig. 4.7). An additional intersection at 23 kbar and 580 °C is not shown in Fig. 4.7. Only the intersection at 6 kbar (stage I) is compatible with low Si contents found in early potassic white-mica (Si = 3.15 pfu). The calculated mineral assemblage at this stage is potassic white-mica, plagioclase, ilmenite, magnetite, garnet, paragonite, biotite, and quartz (Fig. 4.5). Only paragonite (calculated content 2 - 2.5 mol%) could not be identified. The calculated garnet volume of 1 vol% signals the beginning of garnet growth at stage I (garnet core).

Using the composition of the intermediate domain ( $\text{Alm}_{73}\text{GrAn}_2\text{Py}_{15.5}\text{Sp}_{9.5}$ ) of group I garnet, an intersection of the  $X(\text{Ca})$  and  $X(\text{Mg})$  isopleths occurs at 7 kbar and 630 °C. An additional intersection at 16 kbar and 590 °C is not shown in Fig. 4.7 as it is incompatible to the analysed potassic white-mica (calculated Si pfu: 3.35, observed maximal Si pfu: 3.21). We derive further increasing pressures and temperatures to reach 12.5 kbar and 670 °C (stage II), at which the  $X(\text{Ca})$  and  $X(\text{Mg})$  isopleths for the rim composition ( $\text{Alm}_{72}\text{GrAn}_4\text{Py}_{22.5}\text{Sp}_{1.5}$ ) of group I garnet intersect. At these  $p$ - $T$  conditions, the calculated modal content of garnet and the Si content in potassic white-mica is 6 vol% and 3.25 pfu, which are, however, lower and somewhat higher, respectively, than observed (see section 4.4). Rutile, which is omnipresent in the studied rock, is the stable Ti-rich oxide at stage II according to the calculation results shown in Fig. 4.5. The high albite content of plagioclase is also compatible with the calculated content of 98 mol% albite in plagioclase at the  $p$ - $T$  conditions of 12.5 kbar and 670 °C.

On the trajectory towards pressures of 12.5 kbar, the  $p$ - $T$  fields of kyanite and melt were crossed (Fig. 4.7), which is consistent with the occurrence of kyanite in the rock and melt inclusions in garnet. Thus,  $p$ - $T$  conditions of about 9 kbar and 660 °C were attained before reaching stage II.

The small, late garnet (group II) has formed at or near the  $p$ - $T$  conditions of stage II because the compositions of the core of this garnet type and the rim of group I garnet are very similar. Thus, the mylonitisation event, concomitant with the formation of garnet II (see Fig. 4.2c), should have occurred close to 12.5 kbar and 670 °C (see also the aforementioned albite content of recrystallised plagioclase).  $X(\text{Ca})$  and  $X(\text{Mg})$  isopleths for the intermediate zone of group II garnet intersect at 11 kbar and 660 °C. These isopleths for the rim of this garnet type yield  $p$ - $T$  conditions of about 9 kbar and 610 °C (stage III; Fig. 4.7). At these conditions, the calculated modal content of garnet is close to 2 vol%. The calculated Si content in potassic white-mica is 3.20 pfu for stage III, which is compatible with the observed late white mica compositions.

The 26 analyses of rutile yielded Zr contents between 59 and 310 ppm. After subtraction of a few outliers at the highest and lowest Zr contents, the remaining range of Zr contents is limited between about 100 and 220 ppm. A single rutile population is likely because of this limited range and many data close to the average of 182 ppm Zr in rutile. The calculated temperatures range from 546 °C (59 ppm Zr in rutile) to 665 °C (310 ppm) with a mean value of 618 (182 ppm)  $\pm$  13 °C ( $2\sigma$ ) using the calibration by Tomkins et al. (2007) for  $\alpha$ -quartz at 13 kbar. The calibration by Watson et al. (2006) yielded a mean temperature of 598  $\pm$  13 °C. Temperatures of 663  $\pm$  24 and 643  $\pm$  23 °C were obtained from the calibrations by Zack et al. (2004). The Zr-in-rutile thermometers hardly yield temperatures of stage II but mainly those from this stage towards stage III. This is compatible with the calculated growth of rutile from ilmenite after peak temperatures of 670 °C were reached close to stage II (Fig. 4.7). At the late stage III, ilmenite has overgrown rutile in the rock in accordance with the calculation results.

When we connect the derived  $p$ - $T$  conditions, an anti-clockwise  $p$ - $T$  path (Fig. 4.7) results. This path has got a hairpin shape close to the peak  $p$ - $T$  conditions of 12.5 kbar and 670 °C (stage II). This HP stage was followed by a retrograde path running through 9 kbar and 610 °C (stage III).

#### 4.6 Age Dating of Monazite

Monazite appears as small, oval-shaped grains in the mylonitic gneiss 13Mm3 (Figs. 4.2 and 4.8). Their long-axes are usually in the range of 10  $\mu\text{m}$ . Approximately 25 such grains were found in a single thin section. Monazite is evenly distributed in the rock matrix without showing any indication of (considerable) corrosion although monazite grains are not shielded, for instance, as inclusions in garnet. Larger monazite grains were scanned with the EMP to produce elemental maps (Fig. 4.8), which demonstrate a moderate chemical zonation. The most conspicuous zonation is exhibited by the grain of Fig. 4.8, where the La contents decrease from

the core to the rim. To a much lesser extent, the same is true for Y and Th. At the rim, an enrichment of Th (upper right position of the grain) is correlated with a slightly brighter tone in the BSE image and a depletion of Y but seems to be uncorrelated with the La concentration. A tiny inclusion in this grain, characterised by high Y and Th contents, was considered as Th-rich xenotime. Chemical differences of monazite grains are exemplarily shown in Tab. 4.7. It is noteworthy that the ThO<sub>2</sub> contents of monazite are occasionally above 10 wt%. All monazite shows La / Gd ratios < 12 and Y<sub>2</sub>O<sub>3</sub> contents > 1.5 wt%.

Altogether 105 monazite analyses were conducted on 83 grains with the EMP. Five analyses were discarded because of low oxide sums (< 96.0 wt%) and high SiO<sub>2</sub> contents (> 0.9 wt%). The obtained ages range between ~575 and ~455 Ma. The probability density plot (Fig. 4.9a) shows an accumulation of ages between 550 and 490 Ma with 2σ errors of single measurements in the range of 5 to 20 Ma (Fig. 4.9b). In the arbitrarily fitted curve of the histogram of Fig. 4.9a, three maxima at about 545 Ma, 520 Ma, and 495 Ma for these accumulated ages occur. In addition, two side maxima at ~575 Ma and ~455 Ma are shown. Due to the small sizes of the monazite grains, it was impossible to determine ages from different chemical domains in such grains (the only exception is the grain of Fig. 4.8).

On 5 monazite grains of a saidenbachite 30 EMP analyses were performed. After discarding 3 analyses because of clearly too low ages, judged on the basis of their 2σ errors, a mean age of 329.7 ± 11.3 Ma (2σ) results (Fig. 4.9), which is close to the SHRIMP dating result (332.4 ± 2.1 Ma (2σ)).

**Tab. 4.7:** Representative analyses (in wt%) of monazite from the studied gneiss of the Münchberg Metamorphic Complex (MMC), obtained with a CAMECA SX100 EMP. The structural formula of monazite is based on four oxygen anions. The sulphur content was below the detection limit.

Mineral	Monazite					
	13Mm3oB 2-mz11	13Mm3oB 2-mz12-1	13Mm3oB 2-mz13	13Mm3oB 2-mz15	13Mm3oB 2-mz16-1	13Mm3oB 2-mz16-2
SiO <sub>2</sub>	0.21	0.16	0.14	0.15	0.25	0.22
P <sub>2</sub> O <sub>5</sub>	28.79	29.03	29.02	29.09	28.13	28.67
CaO	0.527	0.824	1.032	0.717	2.671	1.297
Y <sub>2</sub> O <sub>3</sub>	1.460	2.148	2.241	1.700	2.125	1.887
La <sub>2</sub> O <sub>3</sub>	13.72	12.68	12.02	13.99	10.71	12.00
Ce <sub>2</sub> O <sub>3</sub>	28.75	28.71	27.81	29.67	23.95	26.25
Pr <sub>2</sub> O <sub>3</sub>	3.168	3.177	3.152	3.142	2.715	3.049
Nd <sub>2</sub> O <sub>3</sub>	12.60	11.76	11.77	11.57	9.70	10.94
Sm <sub>2</sub> O <sub>3</sub>	2.449	2.149	2.155	1.970	1.748	1.970
Gd <sub>2</sub> O <sub>3</sub>	2.028	1.788	1.847	1.605	1.516	1.626
Dy <sub>2</sub> O <sub>3</sub>	0.731	0.830	0.903	0.713	0.774	0.770
PbO	0.0928	0.1360	0.1531	0.1263	0.2830	0.1982
ThO <sub>2</sub>	2.069	3.265	4.473	2.668	12.941	7.193
UO <sub>2</sub>	0.520	0.815	0.665	0.862	0.493	0.631
SUM	97.111	97.504	97.411	97.986	98.015	96.754
Si	0.0083	0.0064	0.0057	0.0058	0.0102	0.0088
P	0.9871	0.9878	0.9883	0.9874	0.9661	0.9860
Ca	0.0229	0.0355	0.0445	0.0308	0.1161	0.0565
Y	0.0315	0.0460	0.0480	0.0363	0.0459	0.0408
La	0.2050	0.1879	0.1784	0.2069	0.1602	0.1805
Ce	0.4263	0.4225	0.4095	0.4354	0.3557	0.3905
Pr	0.0468	0.0465	0.0462	0.0459	0.0401	0.0451
Nd	0.1822	0.1688	0.1690	0.1656	0.1405	0.1587
Sm	0.0342	0.0298	0.0299	0.0272	0.0244	0.0276
Gd	0.0272	0.0238	0.0246	0.0213	0.0204	0.0219
Dy	0.0095	0.0108	0.0117	0.0092	0.0101	0.0101
Pb	0.0010	0.0015	0.0017	0.0014	0.0031	0.0022
Th	0.0191	0.0299	0.0409	0.0243	0.1195	0.0665
U	0.0047	0.0073	0.0060	0.0077	0.0045	0.0057
Age/Ma	569.3	531.5	535.3	534.7	455.0	500.3
2σ error/Ma	16.2	10.6	9.6	11.5	4.9	7.2

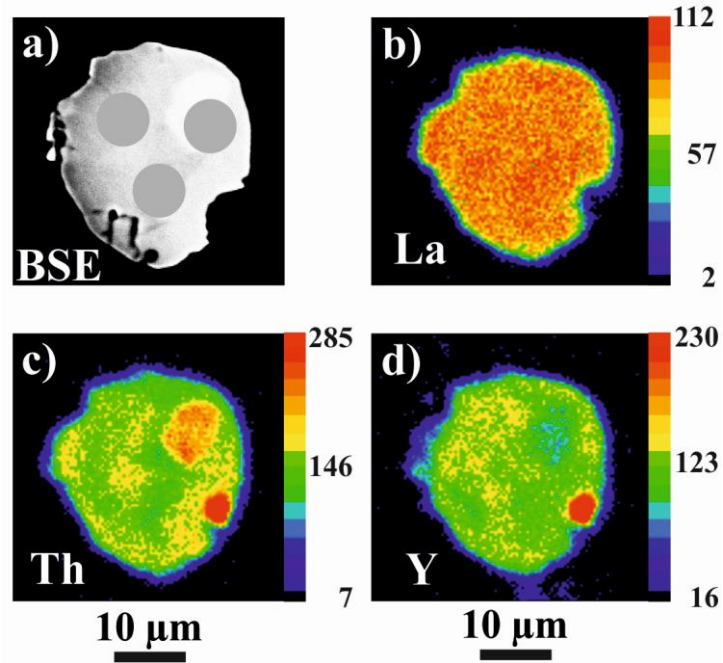


**Fig. 4.8:** Backscattered electron (BSE) image (a) and elemental maps (b-d) of a monazite grain of sample 13Mm3, obtained with a CAMECA SX100 EMP. The scales for the colour code on the right hand side of each image indicate counts of specific X-ray radiation per time unit. The grey spots mark the locations of the three analyses achieved.

## 4.7 Discussion

### 4.7.1 $p$ - $T$ Evolution, Melting and Mylonitisation

The  $p$ - $T$  path of the studied rock, shown in Fig. 4.7, is widely compatible with the observed mineral assemblages and compositions of garnet, plagioclase, and potassic white-mica as outlined in section 4.5.3. Discrepancies, such as the observed garnet volume, which is higher than calculated (9 versus 6 vol% at the peak  $p$ - $T$  conditions), can be explained by analytical errors, particularly given the method for estimating the garnet volume (see above). This determination included minerals enclosed in garnet and, additionally, might not be fully representative for the rock volume which was analysed for the bulk-rock composition, using XRF spectrometry. The modal content of garnet at stage III (c. 2 vol%) differs significantly from the observed one but the once formed garnet was hardly decomposed at this stage so that only the outermost garnet rim was in equilibrium with stage III minerals.

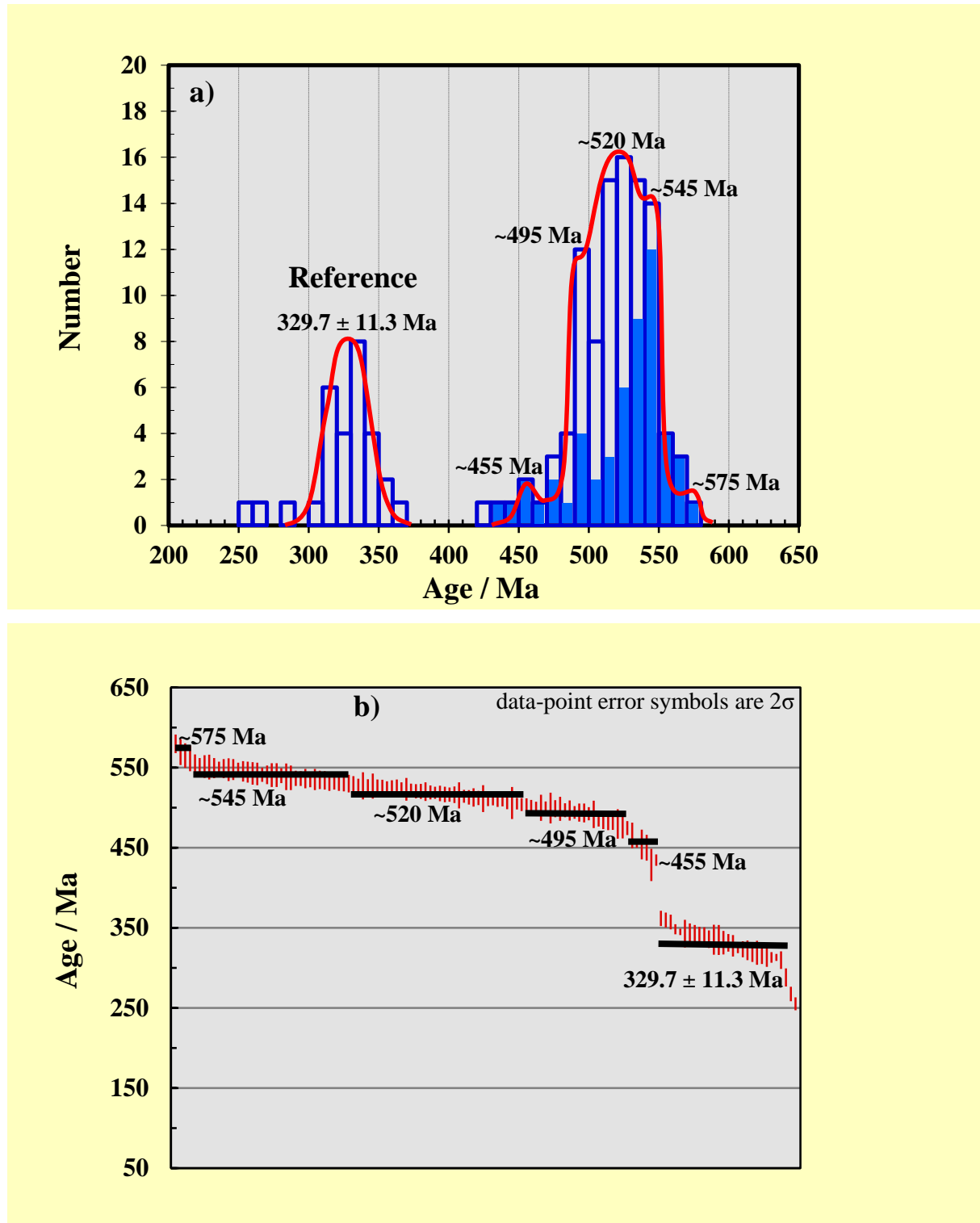


**Fig. 4.9:** Probability density plot (a) and weighted averages (b) of monazite ages (sample 13Mm3), obtained with a CAMECA SX100 EMP. Five age populations were arbitrarily defined yielding average ages of  $\sim 575$  Ma,  $\sim 545$  Ma,  $\sim 520$  Ma,  $\sim 495$  Ma, and  $\sim 455$  Ma. The age at  $329.7 \pm 11.3$  Ma ( $2\sigma$ ) was obtained for monazite from a saidenbachite, for which a SHRIMP age of  $332.4 \pm 2.1$  Ma ( $2\sigma$ ) was reported (Massonne et al. 2007a). Different dating campaigns are indicated by filled and unfilled histograms.

The obtained peak temperature at  $670 \pm 30$  °C (error estimated according to Massonne 2013) is compatible with minor partial melting (melt inclusions in garnet) of the studied rock and with the peak temperature estimate of 630 - 670 °C by Vollbrecht et al. (2006) for gneisses of the MMC. The HP event at  $12.5 \pm 1$  kbar (error estimated according to Massonne 2013) in the Liegendserie unit was not realised before. HP conditions were, however, noted for eclogites and gneisses of the Hangendserie unit by Klemd et al. (1991). The Weißenstein eclogite body is only a few hundred metres away from the current locality but the reported conditions of  $> 20$  kbar are significantly higher (see, e.g. Klemd 1989; Massonne and O'Brien 2003).

At metamorphic stage I, the studied rock consisted of mm-sized minerals based on the presence of rare, relatively large relics of garnet, feldspar, and potassic white-mica. Paragonite could have been part of this assemblage, as calculated (see above), but, if so, it was decomposed during further prograde metamorphism of the rock. It is conceivable that the rock once had the appearance of a common micaschist before mylonitisation. The last named event could be related to  $p$ - $T$  conditions at or close to the metamorphic peak (stage II) based mainly on the composition of small garnet that formed elongated clusters during mylonitisation.

Reports of anti-clockwise  $p$ - $T$  paths are rare in literature (e.g. for the Bohemian Massif: Pitra and Guiraud 1996). Sometimes, anti-clockwise  $p$ - $T$  paths are suggested by the determined  $p$ - $T$  conditions for different metamorphic stages of a polymetamorphic rock. However, two clockwise  $p$ - $T$  paths instead of a single anti-clockwise path can be a viable alternative (see, e.g. Massonne 2014; Lo Pò et al. 2016). In case of the studied rock, a more or less continuous  $p$ - $T$  record for the critical  $p$ - $T$  range close to the metamorphic peak based on garnet compositions excludes the alternative of two clockwise paths. However, because of the hairpin shape of the path in this critical range, the change of the effective bulk-rock composition could result in the underestimation of the temperature of the early decompression path. This was checked by calculating a  $p$ - $T$  pseudosection after subtraction of relic phases (garnet group I, cores of large potassic white-mica flakes) from the bulk-rock. We noted virtually no change compared to the  $p$ - $T$  pseudosection for the bulk-rock as was observed for a rock of similar bulk-rock composition at comparable  $p$ - $T$  conditions by Massonne (2014). Moreover, the results obtained from the Zr-in-rutile thermometry support our view that the temperatures at stage III were lower than those at the pressure peak (stage II).

The  $p$ - $T$  path derived here certainly contributes to a better understanding of the geodynamic process leading to the nappe pile of the MMC. However, we use the derived  $p$ - $T$  conditions here (see Fig. 4.7) to discuss the preservation of monazite in the studied rock. With regard to

the addressed geodynamic process, we are currently studying further garnet-bearing metasediments of the MMC and will report about the results in the near future.

#### 4.7.2 Monazite Ages and Their Interpretation

The age range between ~575 and ~455 Ma, obtained from monazite grains of the studied rock, is incompatible with metamorphic ages reported for diverse rocks of the MMC, using different dating techniques (see section 4.2). The metamorphism of MMC rocks resulted from an early Variscan event which happened in the time span 410 - 370 Ma (see also O'Brien 2000; Massonne and O'Brien 2003). The age range defined here, comprising c. 150 Ma, also excludes a single (metamorphic or) protolith age (see the results for the siadenbachite monazite; Fig. 4.9) as was, for instance, determined for the precursor rock of a MMC eclogite ( $480 \pm 23$  Ma; Stosch and Lugmair 1990).

As the studied rock is a metamorphosed clastic sediment according to its bulk-rock composition (Tab. 4.1), the most likely explanation is that monazite was part of this sediment as a heavy mineral. In this case, the ages of the monazite grains reflect the ages of rocks where the monazite originally was formed. Usually, zircon is considered as a heavy mineral which can (partially) survive the metamorphism of sediments, even at relatively high temperatures. Thus, the application of zircon as a monitor for the provenance of sediments, even after severe metamorphism, was successful also for metasediments of the Variscan orogen. Thus, we can check our hypothesis that monazite yielded provenance ages by a comparison with corresponding zircon data from metasediments of the STZ of which the MMC is part of. Tichomirowa (2002) dated zircon of ortho- and paragneisses from the Erzgebirge and received age clusters at c. 575 Ma, 540 - 530 Ma, and 500 - 470 Ma. These ages were confirmed by Tichomirowa et al. (2012). Linnemann et al. (2007) investigated zircon particularly from metasediments of the Elbe zone, Torgau-Doberlug syncline, Lausitz antiform, Rothstein Formation, Schwarzburg antiform, and the Vesser complex. These authors obtained age clusters at 650 - 600 Ma, c. 540 Ma, and 490 - 480 Ma. Zeh et al. (2003) studied monazite and zircon of paragneisses from the Ruhla Crystalline Complex and found detrital zircon cores, which are older than 460 Ma. Moreover, Gerdes and Zeh (2006) analysed zircon of high-grade metasediments from the Mid-German Crystalline Rise (north-western STZ), obtaining magmatic ages of 2.9 - 2.7 Ga, 2.1 - 1.8 Ga, 595 - 575 Ma, and 515 - 500 Ma.

The aforementioned authors referred the detrital zircon to igneous rocks because of the oscillatory zonation discernible in BSE and particularly cathodoluminescence images. We also

hypothesise that the here obtained age cluster is related to different magmatic activities in the provenance area, which was assigned to Cadomian magmatic arcs at the northern Gondwana margin (e.g. Linnemann et al. 2007; Linnemann and Romer 2010) before the collision with Laurussia. This hypothesis is supported by the similarity of age clusters given by Tichomirowa (2002), Gerdes and Zeh (2006), Linnemann et al. (2007), and Tichomirowa et al. (2012) with our ages shown in Fig. 4.9. A cluster at c. 575 Ma, as reported by Tichomirowa (2002) and Tichomirowa et al. (2012), can also exist in our monazite population but too few age data around 575 Ma were obtained. A cluster of younger zircon ages, as found here for monazite (~455 Ma), were not reported by the aforementioned authors. Thus, it could be that our youngest ages were influenced by the early Variscan metamorphism.

The magmatic character of monazite cannot be deduced as easily as for zircon. However, the determined chemical character of the analysed monazite (Tab. 4.4), La / Gd ratios between 6.5 and 10.9, Y<sub>2</sub>O<sub>3</sub> contents between 1.5 and 2.5 wt%, and Th / U ratios between 3.1 and 12.0 (without outliers), is compatible with magmatic monazite (compare Martins et al. 2009).

The relative young ages of detrital monazite (around 455 Ma) in the studied rock give an upper age limit for the sedimentation of clastic grains, which the magmatic monazite became part of after erosion of the source rock and transportation to the area of deposition. The sizes of these monazite grains (frequently 10 µm only), which remained nearly unchanged during metamorphism, could have been determined by the transportation process or by their magmatic nature because monazite is frequently characterised by very small sizes in igneous rocks (Williams et al. 2007). The sediment with the small monazite grains was likely deposited in front of the northern continental margin of Gondwana (or a Peri-Gondwanan terrane). This occurred probably in Silurian times although both a Late Ordovician and an Early Devonian sedimentation cannot be completely ruled out. Already in the latter period of time, the sediment was buried, accompanied by increasing pressure and temperature.

The question arises why the monazite grains were not decomposed during burial or grew further in the metamorphic environment. The latter process was suggested, for instance, by Franz et al. (1996), Rubatto et al. (2001), and Spear and Pyle (2002). Partial decomposition of monazite during prograde metamorphism (and later re-growth) was, for instance, reported by Massonne (2014). The absence of a hydrous fluid cannot be the reason for lacking growth or decomposition of monazite during prograde metamorphism. The invoked clastic sediment was certainly capable of releasing considerable amounts of such a fluid with rising temperature as was demonstrated, for instance, by results of thermodynamic calculations for metapelites

(Massonne 2016b). Thus, we conclude that a fluid-mediated (partial) breakdown of monazite during prograde metamorphism towards medium-grade conditions, as reported in literature (Broska and Siman 1998; Williams et al. 2011; Massonne 2014; Lo Pò et al. 2016), did not occur in our rock, although the monazite grains were not shielded (see Langone et al. 2011), due to specific  $p$ - $T$  conditions. These conditions were probably those along a geotherm from surface conditions to stage I, which is characterised by c. 30 °C/km (Fig. 4.7b). Broska and Siman (1998) reported amphibolite facies conditions (4 - 7 kbar and 500 - 600 °C) for the breakdown of monazite. Williams et al. (2011) obtained similar  $p$ - $T$  conditions, namely 4.5 kbar and 450 °C, for the alteration of monazite. Eventually, the monazite alteration studied by Broska and Siman (1998) as well as Williams et al. (2011) took place at slightly higher pressures than experienced by the monazite of sample 13Mm3. In the rocks studied by Langone et al. (2011), Massonne (2014), and Lo Pò et al. (2016) the prograde geotherm was significantly lower than 30 °C/km. If this is the case, monazite is decomposed, e.g. to allanite, and can re-grow at higher temperatures at the expense of La, Ce-bearing phases (allanite) as observed by Wing et al. (2003), Gieré and Sorensen (2004), Janots et al. (2007, 2008), and Goswami-Banerjee and Robyr (2015). A growth of monazite at medium-grade conditions implies that a source exists which can deliver La, Ce, and P. In case that detrital monazite survives a prograde metamorphism (see Suzuki et al. 1994; Catlos et al. 2001; Rubatto et al. 2001; Rasmussen et al. 2002), no such source might be available. Thus, we assume that both, failing decomposition and re-growth of monazite, point to metamorphic conditions at relatively low pressures (prograde geotherms > 30 °C/km).

Even the limited partial melting of the studied rock has not resulted in the decomposition of the detrital monazite. According to the bulk composition of this rock given in Tab. 4.1, the character of the partial melt should have been peraluminous. As the solubility of monazite is very limited in such kind of silicate melt (Spear and Pyle 2002; Kelsey et al. 2008), the partial melting had no effect on the preservation of detrital monazite.

Monazite is frequently (partially) decomposed during retrogression (Finger et al. 1998; Broska et al. 2005; Massonne 2014; Balen et al. 2015). This is not the case in our studied rock. Again, specific  $p$ - $T$  conditions could have prevented the decomposition process. However, the absence of a hydrous fluid at temperatures lower than c. 600 °C could also have been responsible for the preservation of monazite. As we noted that garnet and feldspar are still relatively fresh and hardly replaced by phyllosilicates, as it is not often the case for metamorphic rocks, the absence of a hydrous fluid is likely at the late  $p$ - $T$  conditions in our rock. Mylonitisation at relatively

high temperatures ( $\geq 600$  °C according to Blümel 1986;  $\geq 650$  °C as suggested here), which has not affected monazite grains in the studied sample but all silicates, seems to be a minor parameter for decomposition / preservation of monazite. The reason might be the high temperature strength of this phase. In this respect, it must be considered that monazite grains in the studied rock are small and surrounded by silicates of lower strength.

#### 4.8 Conclusions

A paragneiss from the MMC has reached peak  $p$ - $T$  conditions of 12.5 kbar and 670 °C after initial growth of garnet at 6 kbar and 600 °C. During corresponding burial from c. 20 to 40 km Earth's depths, partial melting occurred in the studied rock resulting in the formation of kyanite and additional growth of (peritectic) garnet. Mylonitisation close to peak  $p$ - $T$  conditions possibly initiated the exhumation of the paragneiss. A late metamorphic stage is characterised by  $p$ - $T$  conditions of 9 kbar and 610 °C. Thus, the obtained  $p$ - $T$  path must be anti-clockwise.

Small oval-shaped, detrital monazite grains, although unshielded, survived prograde metamorphism, partial melting, mylonitisation at high temperatures, and retrogression of the studied paragneiss. As the reason for the survival, we determine: (1) a prograde metamorphism along a relatively high geotherm ( $\geq 30$  °C/km) despite a proven release of H<sub>2</sub>O during this metamorphic stage, (2) the ineffectiveness of partial melting (at  $T \geq 640$  °C) and mylonitisation to chemically and physically destabilise monazite, and (3) either favourable  $p$ - $T$  conditions during retrogression, as prevailed during prograde metamorphism, or the lack of a hydrous fluid after temperatures have fallen below 600 °C.

The detrital monazite grains yielded an age range between ~575 and ~455 Ma, which characterises the provenance area of the monazite. In analogy to conclusions drawn from studied zircon of metamorphic sediments from the central European STZ (e.g. Erzgebirge in Saxony, Ruhla Crystalline Complex), we relate this area to Cadomian (and early Caledonian) arcs at the northern margin of Gondwana (or Peri-Gondwanan terranes). From there, monazite was transported to the front of this margin to be deposited in sediments of probably Silurian age according to the younger ages around 455 Ma determined on monazite.

More geochronological data and  $p$ - $T$  evolutions of metamorphic rocks from the MMC are planned to be released soon.

## **Acknowledgements**

The authors thank Thomas Theye (Stuttgart) for his support of the work with the EMP and Gisela Kwiatkowski, Matthias Leiss, Moritz Schmelz and Alexander Schopf for technical assistance. The manuscript benefited from comments made by Antonio Langone (Pavia) and William McClelland (Iowa City). F.W. is deeply grateful to Maria-Anna Waizenhöfer (Ellwangen) for her generous subsistence support.

*Note:* A shortened version of this chapter was published in the *Journal of Metamorphic Geology*, 2017, **35**, 453-469 (DOI: 10.1111/jmg.12240).

## 5. Contribution to the Metamorphic Evolution of Gneisses from the Münchberg Metamorphic Complex (NE Bavaria)

Florian Waizenhöfer, Hans-Joachim Massonne, Joachim Opitz

Institut für Mineralogie und Kristallchemie, Universität Stuttgart, Azenbergstraße 18, 70174 Stuttgart, Germany

### ABSTRACT

This section deals with gneisses from the Münchberg Metamorphic Complex (MMC) in north-eastern (NE) Bavaria (Germany). All studied rock samples belong to the Liegendserie unit, except for the one from the Poppenreuther Berg, which is part of the Hangendserie unit. The most abundant minerals in these rocks are feldspar, garnet, potassic white-mica, and quartz as well as biotite, chlorite, clino- / orthopyroxene, monazite, rutile, xenotime, and zircon as accessories. Monazite ages of the gneisses, which were obtained by an Electron Microprobe (EMP), show a bimodal distribution of two main populations, ranging from c. 575 to c. 455 Ma and from c. 430 to c. 340 Ma. The younger group probably refers to the Variscan orogeny and the older one is likely to represent magmatic events in Late Proterozoic and Cambrian times. In this case, the older group refers to late Cadomian events of the protoliths. These precursor rocks are immature sediments which were located on an active continental margin (ACM) with a strong relief. Pressure ( $p$ ) - temperature ( $T$ ) evolutions of these rocks were derived, using contoured  $p$ - $T$  pseudosections produced with the computer programme package PERPLE\_X. Mainly based on different chemical zonation patterns of garnet grains and variable Si contents in potassic white-mica, the  $p$ - $T$  paths are usually characterised by clockwise shapes, reaching peak metamorphic conditions at about 12 kbar and 660 °C.

KEYWORDS: EMP, garnet, geochronology, gneiss, LA ICP-MS, monazite, Münchberg Metamorphic Complex, PERPLE\_X, protolith,  $p$ - $T$  pseudosection, Variscan orogeny.

## 5.1 Introduction

It is the aim of this study to obtain detailed information about Cadomian and / or Variscan events. Our investigations are focused on gneiss samples from the Münchberg Metamorphic Complex (MMC), a crystalline area in central Europe. In section 4, we got important results by dating monazite grains from the MMC with an Electron Microprobe (EMP) for the first time (analogue to Williams et al. 2007). In the present section, we extend our research to the protoliths of further gneiss samples via spider diagrams (e.g. Toulkeridis et al. 1999), based on bulk-rock elemental concentrations. Geological events, which the rocks were exposed to, are determined by further monazite age dating.

Monazite, acting as a rare-earth element (REE)-bearing accessory mineral (see also section 4.1), is widespread in lots of crustal rocks (Williams et al. 2007). Age dating of monazite in medium-grade metamorphic rocks normally refers to late stages of metamorphism unless monazite is shielded by minerals such as garnet (Langone et al. 2011; Massonne 2014). However, monazite of section 4 acts as an exception because it survived Variscan metamorphic / deformational events. Moreover, in low-grade metamorphic rocks monazite can also occur as an inherited grain (Suzuki et al. 1994; Catlos et al. 2001; Rubatto et al. 2001; Rasmussen et al. 2002). During prograde metamorphism of metapelites with common Ca and Al contents, monazite usually reacts to form other REE-bearing accessory minerals like allanite (Finger et al. 1998; Ferry 2000; Spear and Pyle 2002; Wing et al. 2003). At higher pressure ( $p$ ) - temperature ( $T$ ) conditions, allanite is commonly replaced by newly formed monazite (Wing et al. 2003; Gieré and Sorensen 2004; Janots et al. 2007, 2008; Goswami-Banerjee and Robyr 2015). The retrograde metamorphic evolution may destabilise monazite again. For instance, coronitic microstructures around relics of monazite imply that this mineral can partially be replaced by REE-bearing accessory phases (Finger et al. 1998; Broska et al. 2005; Massonne 2014; Balen et al. 2015).

## 5.2 Geological Setting

The MMC is located in north-eastern (NE) Bavaria (see Fig. 5.1). It forms an oval-shaped complex (about  $25 \times 15 \text{ km}^2$ ), extending from the village of Bad Berneck in the south to the town of Hof in the north. As part of the north-western edge of the Bohemian Massif and, thereby, the Saxo-Thuringian Zone (STZ), the metamorphism of the MMC took place during the early Variscan orogeny in Palaeozoic times (Gebauer and Grünenfelder 1979; Kreuzer et al. 1989, 1993; Stosch and Lugmair 1990; Hammerschmidt and Franz 1992). This orogeny

resulted from the movement of Gondwana to the north-west and its collision with Laurussia (Laurentia + Baltica) to form Pangaea (Franke 1989; Massonne and O'Brien 2003; Linnemann 2004; Massonne 2005; Linnemann and Romer 2010; Arenas et al. 2014).

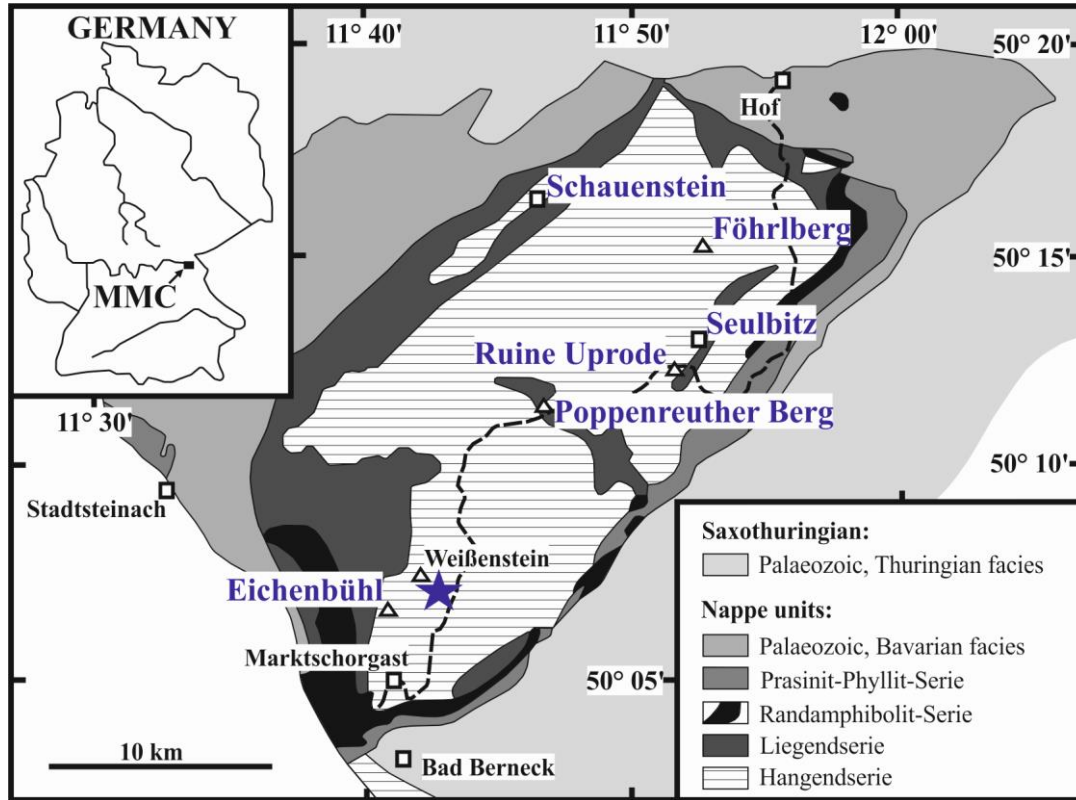


**Fig. 5.1:** Simplified geological map of the Münchberg Metamorphic Complex (MMC) in NE Bavaria (Germany), modified after Klemd et al. (1994). The locations of the studied gneiss samples are highlighted.

The MMC (see also sections 4.2 and 6.2) is regarded as a nappe pile transported on top of autochthonous, anchi-metamorphic Palaeozoic sequences of the Thuringian lithofacies, as exposed in the south-eastern Frankenwald, in the Lower Carboniferous (Franke 1984; Klemd et al. 1994). This nappe pile is subdivided from the bottom to the top into the following units: Prasinit-Phyllit, Rand-Amphibolit, Liegendserie, and Hangendserie (e.g. Stettner 1960a; Kreuzer et al. 1989; Okrusch et al. 1990). The Prasinit-Phyllit unit mainly consists of greenschist-facies metavolcanic and metasedimentary rocks. The Rand-Amphibolit unit is composed of amphibolites. Amphibolite facies ortho- and paragneisses dominate the Liegendserie unit. The Hangendserie unit contains similar gneisses, but also eclogite bodies like the famous one from the Weißenstein peak (e.g. Stosch and Lugmair 1990; O'Brien 1993; Klemd et al. 1994).

The MMC is well known for its eclogites with omphacite records dating from the beginning of the 19th century (see Godard 2001). One of the first who had studied the eclogites from the MMC was Düll (1902). Detailed mineralogical studies followed later (e.g. Matthes et al. 1975; Matthes 1978). The peak  $p$ - $T$  conditions of the eclogites from the MMC were estimated by several studies (Franz et al. 1986; Klemd 1989; Klemd et al. 1991; O'Brien 1993; Klemd et al. 1994; Liebscher et al. 2007). According to Massonne and O'Brien (2003), these conditions cluster in the  $p$ - $T$  range of 20 - 34 kbar and 550 - 750 °C.

In contrast to the eclogites, little is known about the MMC gneisses, which can also contain garnet, but a peak  $T$  range of 630 - 670 °C was assumed by Vollbrecht et al. (2006). Blümel (1986) reported a medium- $p$  event for the Hangendserie unit at about 8 kbar and c. 610 °C with a subsequent mylonitisation. Klemd (2010) estimated  $p$ - $T$  conditions of 6 - 10 kbar and  $620 \pm 30$  °C for the metasedimentary rocks of the same unit. In section 4, a paragneiss from the Liegendserie unit was studied. This rock was exposed to an anti-clockwise  $p$ - $T$  path, reaching peak metamorphic conditions at 12.5 kbar and 670 °C.

Various authors using different geochronological methods accomplished age dating. Gebauer and Grünenfelder (1979) determined U-Pb ages on zircon from the Weißenstein eclogite body (Fig. 5.1) and related them to the eclogitisation of the studied rocks ( $380 + 14 / - 22$  Ma (two-sigma:  $2\sigma$ )) and their protoliths ( $525 + 40 / - 31$  Ma). Kreuzer et al. (1989) reported a wider age range for the metamorphism (410 - 345 Ma), applying the K-Ar method to biotite, hornblende, and muscovite from all four units of the MMC. Sm-Nd isochrons (clinopyroxene-amphibole-garnet) and K-Ar ages (amphibole and mica) on the MMC eclogites gave a high-pressure (HP:  $> 10$  kbar) metamorphic age of 395 - 380 Ma, followed by amphibolite facies metamorphism at 380 - 365 Ma (Stosch and Lugmair 1990). A whole-rock Sm-Nd isochron, interpreted as a protolith age of  $480 \pm 23$  Ma, was obtained by Stosch and Lugmair (1990). Ar-Ar plateau and isochron ages, determined on phengites from Weißenstein and Oberkotzau eclogites, yielded  $365 \pm 7$  Ma (Hammerschmidt and Franz 1992). Kreuzer et al. (1993) obtained an age of  $379 \pm 1$  Ma (Ar-Ar plateau and K-Ar isochron), studying muscovite and hornblende of eclogites from the Hangendserie unit. The above ages clearly point to major Middle to Late Devonian metamorphic events during the early Variscan orogeny in the MMC (Massonne and O'Brien 2003). As explained in sections 3.1-3.2, such events were found to have also occurred in other crystalline complexes of the Bohemian Massif (see, e.g. Kröner and Willner 1998), such as the Zone of Erbendorf-Vohenstrauß, the Frankenberg and Wildenfels Nappes, the Góry Sowie Block (GSB; Owl Mountains) and the Mariánské Lázně Complex (MLC). Besides, this study

(section 4) got monazite ages of ~575 Ma, ~545 Ma, ~520 Ma, ~495 Ma, and ~455 Ma, dating Cadomian and / or Caledonian protoliths of the studied mylonitic gneiss from the MMC.

The studied gneisses (see Fig. 5.1) were sampled at the following locations (corresponding 1:25000 geological maps are also provided): 13Mm3 (see section 4) south of the Weißenstein peak (N 50.1314° / E 11.7027°, WGS 84, No. 5836 Münchberg); 13Mm6 near the village of Seulbitz (N 50.2142° / E 11.8681°, No. 5737 Schwarzenbach a.d.sächs.Saale); 13Mm8 and 13Mm10 close to the top of the Föhlberg (N 50.2493° / E 11.8781°, No. 5737 Schwarzenbach a.d.sächs.Saale); 13Mm11 and 13Mm12 at the Ruine Uprode (N 50.2063° / E 11.8587°, No. 5737 Schwarzenbach a.d.sächs.Saale); 13Mm13 close to Schloss Schauenstein (N 50.2801° / E 11.7401°, No. 5736 Helmbrechts); 13Mm14 as a field stone around the town of Schauenstein (N 50.2768° / E 11.7470°, No. 5736 Helmbrechts); 13Mm16\_1 on top of the Poppenreuther Berg (N 50.1922° / E 11.7410°, No. 5836 Münchberg); and 13Mm18\_1 in an outcrop at the Eichenbühl peak (N 50.1094° / E 11.6801°, No. 5836 Münchberg). All samples belong to the Liegendserie unit, except for sample 13Mm16\_1, which is part of the Hangendserie unit. A simplification of the real geological setting is shown in Fig. 5.1.

### 5.3 Analytical Procedures

For the determination of the bulk-rock composition (see also sections 3.3, 4.3 and 6.3), a representative piece of the rock sample (volume c.  $10 \times 5 \times 2 \text{ cm}^3$ ) was crushed and subsequently ground with a tungsten carbide dish-and-puck mill. The obtained rock powder was either fused with lithium borate, consisting of 66 wt%  $\text{Li}_2\text{B}_4\text{O}_7$  and 34 wt%  $\text{LiBO}_2$ , in an optimised mass ratio of 1:6 to prepare a glass disk or mixed with the wax  $\text{C}_{38}\text{H}_{76}\text{N}_2\text{O}_2$  (mass ratio 4:1) to press a tablet. Disk and tablet were analysed for major and trace elements, respectively, with a Panalytical PW 2400 X-ray fluorescence spectrometer (XRF), considering certified geostandards. Moreover, the rock powder was also used to determine the total carbon and water contents, using a LECO<sup>®</sup> RC-412 elemental analyser, based on IR techniques.

After XRF analyses, the prepared glass disks were further ablated by a Cetac LSX-213 laser connected to an AGILENT SERIE 7700 inductively coupled plasma - mass spectrometer (LA ICP-MS) to additionally determine trace element contents. The laser energy was regulated to 20 %, the beam size was set to 150  $\mu\text{m}$  and 450 shots per spot were fired with a frequency of 20 Hz. With a gas mixture consisting of 300 ml/min of helium and 800 ml/min of argon transporting the ablated material, the plasma torch of the mass spectrometer was operated at an

argon flow of 15 l/min. DLH 7 and DLH 8 from P&H Developments Ltd. as well as NIST 612 reference glasses were used for the calibration of the instrument under the same experimental conditions as applied to the samples under investigation. As internal standard elements Si and Ba, whose concentrations had been determined by XRF, were employed. The obtained results were verified by analysing lithium borate glass disks prepared from the geostandards Diorite (DR-N) and Zinnwaldite (ZW-C), obtained from the Service d'Analyse des Roches et des Minéraux (SARM), part of the Centre National de Recherche Scientifique (CNRS). In addition, the MLS-ETHOS plus microwave lab system was employed to dissolve rock powder in a mixture of HF, HCl and HNO<sub>3</sub> at elevated pressures and temperatures. The resulting liquids were analysed with the AGILENT SERIE 7700 ICP-MS (liquid ICP-MS).

According to the analytical procedure described by Massonne (2012), carbon-coated thin sections (area c.  $2 \times 4 \text{ cm}^2$ ) were employed to analyse the compositions of minerals, such as garnet, mica, monazite, and rutile, using a CAMECA SX100 EMP with five wavelength-dispersive (WD) spectrometers (see also sections 3.3, 4.3 and 6.3). For silicates (+ ilmenite), the concentrations of F, Na, Mg, Al, Si, K, Ca, Ti, Cr, Mn, Fe and Ba were determined, using counting times of 20 s at the peak and on the background. Synthetic and natural minerals, glasses (e.g. Ba glass for the BaL $\alpha$ 1-peak), and pure oxides were used as standards. The applied acceleration voltage and beam current were 15 kV and 15 nA, respectively. The beam diameter was approximately 3  $\mu\text{m}$ . The PaP correction procedure provided by CAMECA was applied. Analytical errors of the applied method were reported by Massonne (2012).

The analysis of rutile with the EMP for the Zr-in-rutile thermometry was achieved for Si, Cr, Fe, Zr, and Nb (Ti was calculated). The beam current and acceleration voltage were set to 100 nA and 15 kV, respectively. The counting time for the Zr L $\alpha$ -radiation at the peak and the background was 100 s each. Natural zircon was used as a standard for this radiation.

In order to recognise zoning patterns of garnet, potassic white-mica, and monazite, element concentration maps for major elements were prepared by step-wise movement of a thin section under the electron beam of the EMP (step scanning) and subsequent computer-aided evaluation. For the mapping, counting times per step of 100 ms were applied. The electric current was either 150 nA (monazite), 70 nA (garnet) or 25 nA (mica).

Backscattered electron (BSE) images were prepared with the EMP, for instance, to document specific textural relations. For the calculation of structural formulae of minerals and the content of molar fractions of mineral components from EMP analyses, the computer programme CALCMIN (Brandelik 2009) was used.

For age dating of monazite, full analyses of this mineral with the EMP, including the elements Si, P, S, Ca, Y, La, Ce, Pr, Nd, Sm, Eu, Gd, Pb, Th, and U were achieved. The analytical procedure followed the approach of Massonne et al. (2012). This procedure gives a good match with more precise mass spectrometric methods (as reported by Massonne et al. 2007a; Van Leeuwen et al. 2016) including a reference monazite from Brazil, the age dating of which varies, however, between 514 and 471 Ma (see Gasquet et al. 2010). This coincidence was also reasonable even for Tertiary monazite (see Liu et al. 2011; Massonne 2014, 2016a). To test the reliability of the procedure, a monazite from a saidenbachite was used as a reference during a previous dating campaign (see section 4). The age of this monazite had been dated with a Sensitive High Resolution Ion Microprobe (SHRIMP) to  $332.4 \pm 2.1$  Ma ( $2\sigma$ ) (Massonne et al. 2007a). The  $2\sigma$  uncertainty of our age dating results with respect to a single analysis was calculated by error propagation of the  $2\sigma$  errors of the counting rates of the peak and background intensities of the relevant elements. Since many monazite analyses yielded ThO<sub>2</sub> contents between 4 and 5 wt%, a  $2\sigma$  error between 8 and 10 Ma often resulted for a single analysis. After determining all monazite ages with the MINCALC-V5 software programme and their corresponding  $2\sigma$  errors with MZ-Age, we used the Isoplot programme of Ludwig (1999) to illustrate the results graphically.

#### 5.4 Mineral Compositions and Textures

All studied samples are gneisses and most of them show a foliation pattern. The most abundant minerals in all rocks are feldspar, garnet (not found in sample 13Mm13), potassic white-mica, and quartz (see Fig. 5.2). Sometimes, there is also biotite, chlorite, and clino- / orthopyroxene. Monazite, which is the most important accessory mineral (see above) because it acts as a geological clock (e.g. Williams et al. 2007), may be found in every rock except for samples 13Mm8, 13Mm13 and 13Mm16\_1. In case of these rocks, xenotime seems to substitute monazite. Generally speaking, quartz, rutile and zircon are in contact (not valid for samples 13Mm6, 13Mm8 and 13Mm14). Consequently, four calibrations of the Zr-in-rutile thermometer (two by Zack et al. 2004; Watson et al. 2006; Tomkins et al. 2007 for  $\alpha$ -quartz) can be applied to these samples.

In the following, the mineralogical properties of a representative sample, 13Mm6, are shortly described. It is a metamorphic psammopelite, according to its relatively K- and Al-rich bulk-rock composition (Tab. 5.1), and shows a distinct foliation pattern probably due to the metamorphism of the Variscan orogeny (Fig. 5.2). According to the original character of a

clastic sediment, probably a greywacke, major minerals in descending order are quartz (45 vol% as determined with a polarisation microscope ZEISS Axioplan), mica (35 vol%), garnet (10 vol%), and feldspar (5 vol%). Accessory phases are chlorite, monazite, rutile, zircon, and opaque phases like ilmenite.

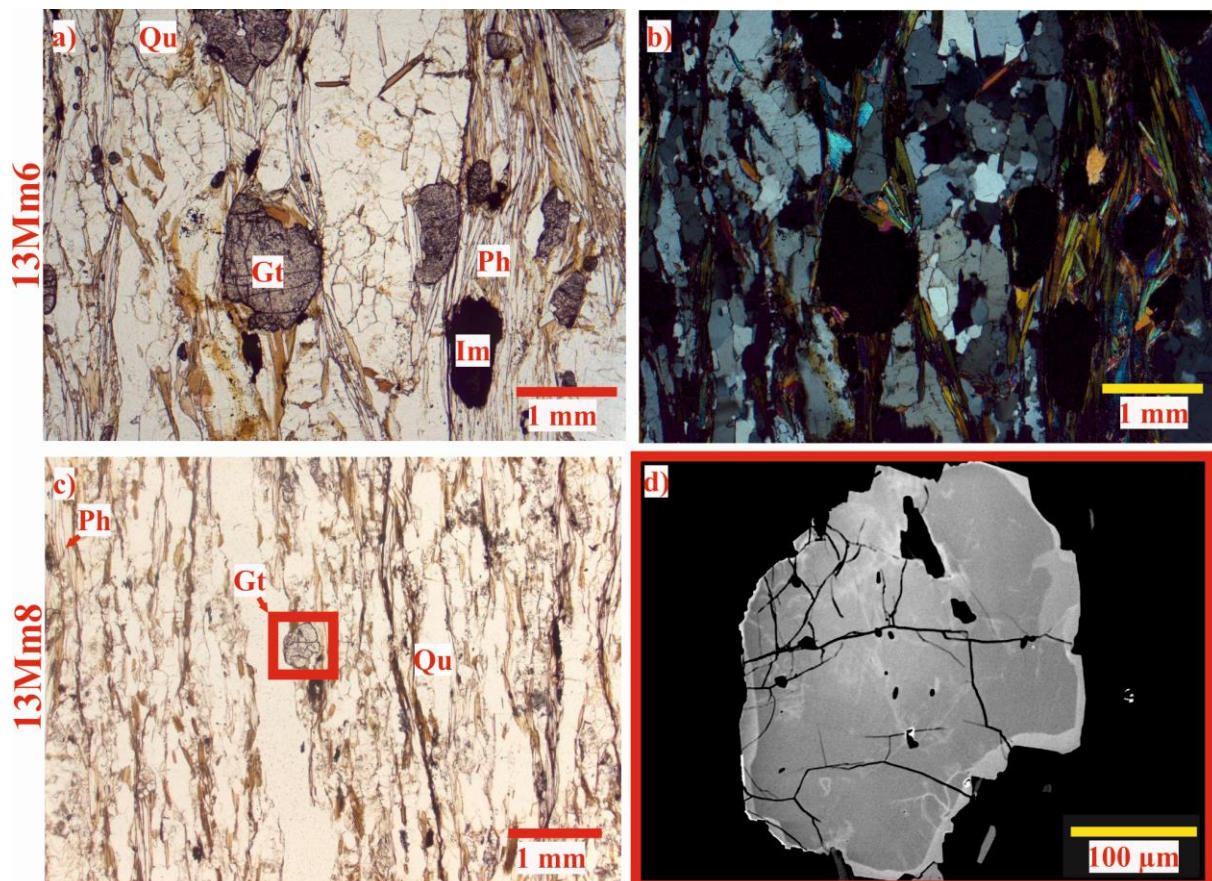


**Fig. 5.2:** Photomicrographs of objects in thin sections of samples 13Mm6 (a,b) and 13Mm8 (c) seen under plane polarised light (a,c) and crossed polarisers (b) with a ZEISS Axioplan. Backscattered electron (BSE) image (d) of a garnet grain in sample 13Mm8, obtained with a CAMECA SX100 EMP. These images are aimed at showing the fabric of the rocks and the chemical zonation of garnet: Gt = garnet, Im = ilmenite, Ph = potassic white-mica, Qu = quartz.

Considering sample 13Mm6, the garnet grains seem to be subhedral and fine-grained (500 - 900  $\mu\text{m}$ ). They usually lack any inclusions. From the core to the rim, the Ca content decreases, whereas the Mg concentration goes up (Figs. 5.3 and 5.4, Tab. 5.2), which is an indication for increasing temperatures (compare Săbău 2000 and Massonne 2014). The distribution of Mn in garnet is similar to Ca but, in the outer rim, the Mn content slightly goes up, representing a small overgrowth zone. On average, the garnet core of sample 13Mm6 is made up of about 69.0 mol% almandine component, 19.1 mol% grossular (+ andradite) components, 9.6 mol% pyrope

component, and 2.3 mol% spessartine component ( $\text{Alm}_{69.0}\text{GrAn}_{19.1}\text{Py}_{9.6}\text{Sp}_{2.3}$ ). In contrast to that, the average garnet rim consists of  $\text{Alm}_{73.8}\text{GrAn}_{10.6}\text{Py}_{13.0}\text{Sp}_{2.4}$ .

**Tab. 5.1:** Bulk-rock composition of gneiss sample 13Mm6 from the Münchberg Metamorphic Complex (MMC), obtained with XRF, liquid ICP-MS, and LA ICP-MS. XRF results were modified for PERPLE\_X calculations as explained in the text.

Constituent	XRF	modified	liquid ICP-MS	LA ICP-MS
Na <sub>2</sub> O / wt%	3.041	2.951		2.177
MgO / wt%	1.813	1.760		2.068
Al <sub>2</sub> O <sub>3</sub> / wt%	16.330	15.849		15.650
SiO <sub>2</sub> / wt%	67.886	65.886		66.949
P <sub>2</sub> O <sub>5</sub> / wt%	0.130			
K <sub>2</sub> O / wt%	2.715	2.635		3.061
CaO / wt%	0.884	0.692		0.923
TiO <sub>2</sub> / wt%	0.728	0.707		1.004
MnO / wt%	0.099	0.096		
Fe <sub>2</sub> O <sub>3</sub> / wt%	5.727			6.188
FeO / wt%		5.002		
O <sub>2</sub> / wt%		0.056		
H <sub>2</sub> O / wt%		4.367		
SUM / wt%	99.353	100.000		
Sc / ppm	7.9		12.3	18.5
V / ppm	113		111.3	130.4
Cr / ppm	68		59.2	100.6
Ni / ppm	14		26.4	39.5
Rb / ppm	80		77.8	101.4
Sr / ppm	122		131.4	157.9
Y / ppm	28		21.9	30.5
Zr / ppm	192		202.7	280.1
Nb / ppm	12		11.3	14.1
Cs / ppm	3.8			4.5
Ba / ppm	594		512.6	591.3
La / ppm	27		13.2	24.8
Ce / ppm	28		22.9	38.6
Pr / ppm	5.7		3.7	6.5
Nd / ppm	24		15.7	29.7
Sm / ppm	5.3		3.5	6.5
Eu / ppm			1.0	1.3
Gd / ppm			4.1	5.8
Tb / ppm			0.7	1.1
Dy / ppm			4.4	6.3
Ho / ppm			0.9	1.3
Er / ppm			2.8	4.0
Tm / ppm			0.4	0.6
Yb / ppm			3.0	4.0
Lu / ppm			0.5	0.6
Hf / ppm			4.8	8.1
Ta / ppm			0.9	1.0
Th / ppm	7.4		6.5	10.7
U / ppm	1.2		3.0	3.4

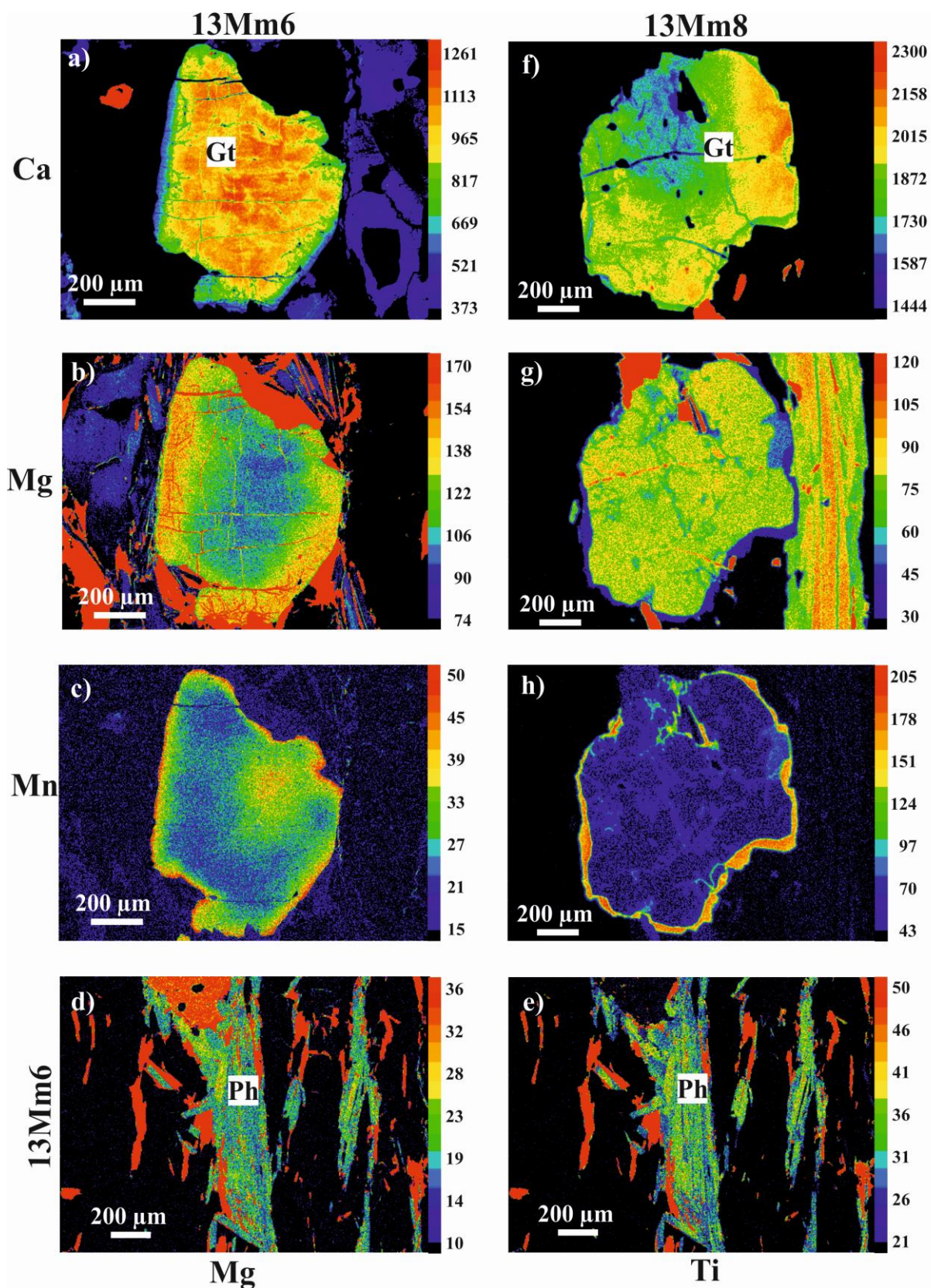


**Fig. 5.3:** Elemental maps of garnet (Gt) (a-c for 13Mm6; f-h for 13Mm8: Ca, Mg, and Mn) as well as potassic white-mica (Ph) grains (d-e for 13Mm6: Mg and Ti) in the studied samples, obtained with a CAMECA SX100 EMP. The scales for the colour code on the right hand side of each image indicate to counts X-ray radiation per time unit.

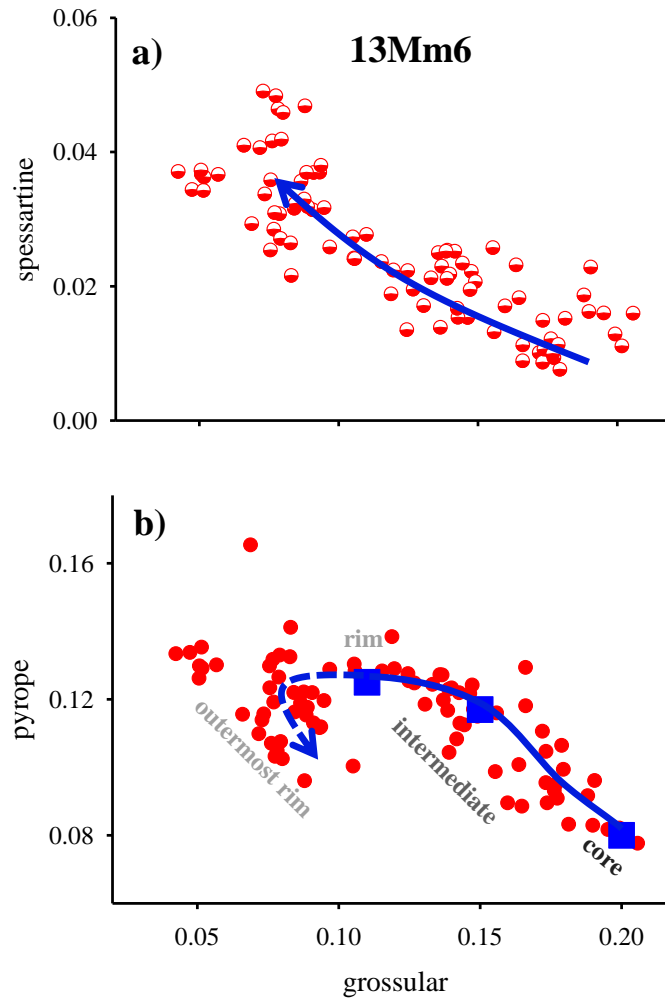


**Fig. 5.4:** Garnet analyses, obtained with a CAMECA SX100 EMP, in terms of molar fractions of spessartine (a) and pyrope (b) versus that of grossular (+ andradite). The solid lines show chemical trends from core to rim compositions of garnet for sample 13Mm6. The dashed line represents a speculative assumption of the composition in the outermost rim of garnet (13Mm6).

A unique mineralogical feature was observed in garnet grains of sample 13Mm8. Although they are similar in form and size to their counterparts of sample 13Mm6, garnets of sample 13Mm8 have got more inclusions like (altered) biotite, chlorite, feldspar, muscovite, quartz, and titanite. They show a different chemical zonation pattern (Figs. 5.3f-h), which is less distinct: The Ca content increases from the core to the rim. Mg is nearly evenly distributed within the grain with the exception of a sudden drop in the outer rim. Moreover, a Mn enrichment in the outer rim is clearly visible, referring to a resorption process. This is probably the reason for remarkably bright colours in the outer rim of the BSE image (Fig. 5.2). Such a connection between the Mn content and the BSE image is unique among all studied gneisses. To sum it up, the average garnet core consists of  $\text{Alm}_{48.2}\text{GrAn}_{41.0}\text{Py}_{6.0}\text{Sp}_{4.8}$  and the average rim (not outer rim!) is made up of  $\text{Alm}_{62.1}\text{GrAn}_{32.9}\text{Py}_{2.0}\text{Sp}_{3.0}$ . Representative analyses of garnet grains are shown in Tab. 5.2.

**Tab. 5.2:** Representative analyses (in wt%) of garnet from the studied gneisses of the Münchberg Metamorphic Complex (MMC), obtained with a CAMECA SX100 EMP. The structural formulae were calculated as follows: 24 oxygen (double formula unit) and cation sum of Al + Ca + Cr + Fe + Mg + Mn + Na = 10. Abbreviations: calc = calculated, inter = intermediate.

Mineral	Garnet				
	Sample	13Mm6-gt2-72	13Mm6-gt2-75	13Mm6-gt2-87	13Mm8-gt4-4
Comment	core	inter	rim	core	rim
SiO <sub>2</sub>	37.12	37.09	37.22	37.68	36.36
TiO <sub>2</sub>	0.09	0.14	0.02	0.06	0.16
Al <sub>2</sub> O <sub>3</sub>	21.23	21.14	21.32	20.86	20.14
Cr <sub>2</sub> O <sub>3</sub>	0.00	0.01	0.03	0.01	0.00
Fe <sub>2</sub> O <sub>3</sub> calc	0.78	0.66	0.72	0.76	1.68
FeO	31.70	32.44	34.45	23.12	27.20
MnO	1.03	1.04	1.17	1.77	0.90
MgO	2.47	2.57	3.32	0.78	1.11
CaO	6.84	5.83	3.49	14.67	11.44
Na <sub>2</sub> O	0.01	0.02	0.02	0.03	0.04
Total	101.27	100.93	101.78	99.73	99.02
Si	5.798	5.837	5.795	5.987	5.817
Ti	0.010	0.016	0.003	0.007	0.019
Al	3.908	3.920	3.911	3.907	3.797
Cr	0.000	0.001	0.004	0.002	0.000
Fe <sup>3+</sup>	0.092	0.078	0.084	0.091	0.202
Fe <sup>2+</sup>	4.140	4.270	4.486	3.072	3.639
Mg	0.575	0.603	0.772	0.184	0.265
Ca	1.144	0.984	0.582	2.498	1.961
Mn	0.136	0.138	0.154	0.238	0.122
Na	0.004	0.004	0.006	0.008	0.013

Regarding sample 13Mm6 (Figs. 5.3d-e), potassic white-mica seems to be fine-grained (200 - 800  $\mu\text{m}$ ) and subhedral (mostly elongated). Moreover, it can be considered as inclusion free. Some distinct zones are slightly Mg-enriched, which is probably unrelated to a core-rim relationship. The Si content per formula unit (pfu) in potassic white-mica varies between 3.03 and 3.15. Higher Si contents pfu correlate with a Mg enrichment. In the large core domain, higher Ti concentrations may be found than in the small rim area. Representative analyses of potassic white-mica grains are shown in Tab. 5.3.

All rutiles of the studied gneisses (see Tab. 5.4) are elongated (subhedral) and very fine-grained (< 100  $\mu\text{m}$ ). Most of them are located in the rock matrix and cannot be found as inclusions in other minerals, such as garnet. Sometimes, rutile is altered to ilmenite. For example, the average composition of rutile of sample 13Mm10 is characterised by 0.23 wt% FeO, 0.28 wt% Nb<sub>2</sub>O<sub>5</sub> and 0.03 wt% ZrO<sub>2</sub> (Tab. 5.4).

**Tab. 5.3:** Representative analyses (in wt%) of potassic white-mica from the studied gneisses of the Münchberg Metamorphic Complex (MMC), obtained with a CAMECA SX100 EMP. The structural formulae were calculated as follows: 22 oxygen (double formula unit). For all micas the total was corrected for F. Abbreviation: calc = calculated.

Mineral	Potassic white-mica						
	Sample	13Mm6- ms1-2	13Mm6- ms1-3	13Mm6- ms1-4	13Mm8- ms1-4	13Mm8- ms1-5	13Mm8- ms1-6
SiO <sub>2</sub>		47.03	47.01	45.77	47.52	47.55	48.05
TiO <sub>2</sub>		0.70	0.73	0.60	0.76	0.78	0.80
Al <sub>2</sub> O <sub>3</sub>		33.02	32.75	35.52	27.57	28.39	28.08
FeO		1.45	1.51	1.13	4.39	3.99	3.87
MgO		1.41	1.63	0.84	2.10	1.8	1.86
Na <sub>2</sub> O		1.48	1.55	1.92	0.33	0.34	0.28
K <sub>2</sub> O		8.93	9.11	8.57	10.92	11.08	10.89
BaO		0.23	0.27	0.30	0.16	0.17	0.22
H <sub>2</sub> O <sub>calc</sub>		4.48	4.48	4.50	4.33	4.35	4.37
Total		98.79	99.04	99.13	98.11	98.48	98.42
Si		6.297	6.299	6.106	6.576	6.547	6.598
Ti		0.070	0.074	0.060	0.079	0.080	0.082
Al		3.508	3.471	3.690	3.074	3.155	3.141
Fe <sup>2+</sup>		0.163	0.170	0.126	0.509	0.459	0.445
Mg		0.282	0.326	0.167	0.434	0.370	0.381
Na		0.385	0.402	0.495	0.088	0.090	0.076
K		1.526	1.557	1.458	1.928	1.947	1.908
Ba		0.012	0.014	0.015	0.009	0.009	0.012

**Tab. 5.4:** Representative analyses (in wt%) of rutile from the studied gneisses of the Münchberg Metamorphic Complex (MMC), obtained with a CAMECA SX100 EMP. The structural formula of rutile is based on two oxygen anions.

Mineral	Rutile						
	Oxides in wt%	13Mm10- rt5-1	13Mm10- rt5-2	13Mm10- rt1-5	13Mm11- rt1-7	13Mm11- rt1-8	13Mm11- rt1-9
TiO <sub>2</sub>		99.42	99.39	99.41	98.97	98.79	99.23
SiO <sub>2</sub>		0.000	0.000	0.000	0.000	0.000	0.000
Nb <sub>2</sub> O <sub>5</sub>		0.290	0.280	0.260	0.500	0.240	0.250
FeO		0.200	0.230	0.220	0.490	0.890	0.460
ZrO <sub>2</sub>		0.030	0.030	0.050	0.030	0.040	0.030
Total		99.94	99.93	99.94	99.99	99.96	99.96
Ti		0.9959	0.9956	0.9956	0.9913	0.9884	0.9932
Si		0.0000	0.0000	0.0000	0.0000	0.0000	0.0000
Nb		0.0017	0.0017	0.0016	0.0030	0.0015	0.0015
Fe		0.0022	0.0026	0.0025	0.0055	0.0099	0.0051
Zr		0.0002	0.0002	0.0003	0.0002	0.0003	0.0002

## 5.5 Results of the Bulk-Rock Analyses

Important bulk-rock data of sample 13Mm3 are provided in Tab. 4.1 and more details in Tab. 8.10. Results of bulk-rock analyses of gneiss samples 13Mm6, 13Mm8, 13Mm10, 13Mm11, 13Mm12, 13Mm13, 13Mm14, 13Mm16\_1, and 13Mm18\_1 obtained by different methods (XRF, liquid ICP-MS, and LA ICP-MS) are shown in Tabs. 5.1, 8.8, 8.9, and 8.10. Only samples 13Mm3, 13Mm6, 13Mm8, and 13Mm10 were analysed by liquid ICP-MS but in all cases optically observable residua were detected in the liquids, which might lead to reduced concentrations for some elements (similar to section 3.3.5). The elemental contents of the aforementioned residua were not determined.

Nevertheless, the results for the concentrations of most elements are similar within experimental error ranges of 25 % (of the corresponding calculated average values). We verified the reliability of the individual analytical results by comparing all available elemental concentrations for every gneiss sample. In general, for the presentation of selected major (in wt% of the oxides; see, e.g. Tab. 5.1) and trace (in ppm; see, e.g. Tab. 5.1) elements, for instance in discrimination diagrams, we used the averaged values of the elemental contents of XRF (if applicable), liquid ICP-MS (if applicable), and LA ICP-MS. Therefore, the reliable LA ICP-MS results are the basis for drawing spider diagrams in this section. However, to conduct all the PERPLE\_X calculations, merely modified XRF results were employed. Moreover, it turned out that the carbon and water contents are always below 0.4 and 2 wt%, respectively.

To characterise the protoliths of the studied gneiss samples, the following element concentration plots were applied (see Fig. 5.5): a) chondrite-normalised REE pattern after Taylor and McLennan (1985); b) upper-continental crust-normalised multi-element pattern after Floyd et al. (1991) (normalisation values are from Taylor and McLennan 1985); c)  $\text{TiO}_2$  / wt% versus Ni / ppm after Floyd et al. (1991); d) ratio of  $\text{Al}_2\text{O}_3$  /  $\text{SiO}_2$  versus the sum of  $\text{Fe}_2\text{O}_3^{\text{T}}$  +  $\text{MgO}$  / % after Bhatia (1983); e) ternary diagram of molecular  $\text{Al}_2\text{O}_3 - (\text{CaO} + \text{Na}_2\text{O} + \text{K}_2\text{O}) - (\text{FeO}^{\text{T}} + \text{MgO})$  after McLennan (1993) and Toulkeridis et al. (1999); and f) ternary plot of molecular  $\text{CaO} - \text{Na}_2\text{O} - \text{K}_2\text{O}$  after Bhatia (1983).

In Fig. 5.5a, the corresponding values range between 4 and 91 rock / chondrite. The normalised values in the multi-element pattern of Fig. 5.5b vary between 0.07 and 2.9. All experimentally determined points of Fig. 5.5c are distributed close to the acidic field. Besides, fields A (13Mm6, 13Mm11, 13Mm12, 13Mm14, 13Mm16\_1, 13Mm18\_1) and B (13Mm3, 13Mm8, 13Mm13) of Fig. 5.5d contain all points except for the one representing sample 13Mm10, which is outside any field. In Fig. 5.5e, the experimentally determined values form a homogenous

group close to the igneous rock line. Last but not least, in Fig. 5.5f, all points are inside the ACM field with the exception of 13Mm3 (PM field), 13Mm11 (CIA), and 13Mm16\_1 (OIA).

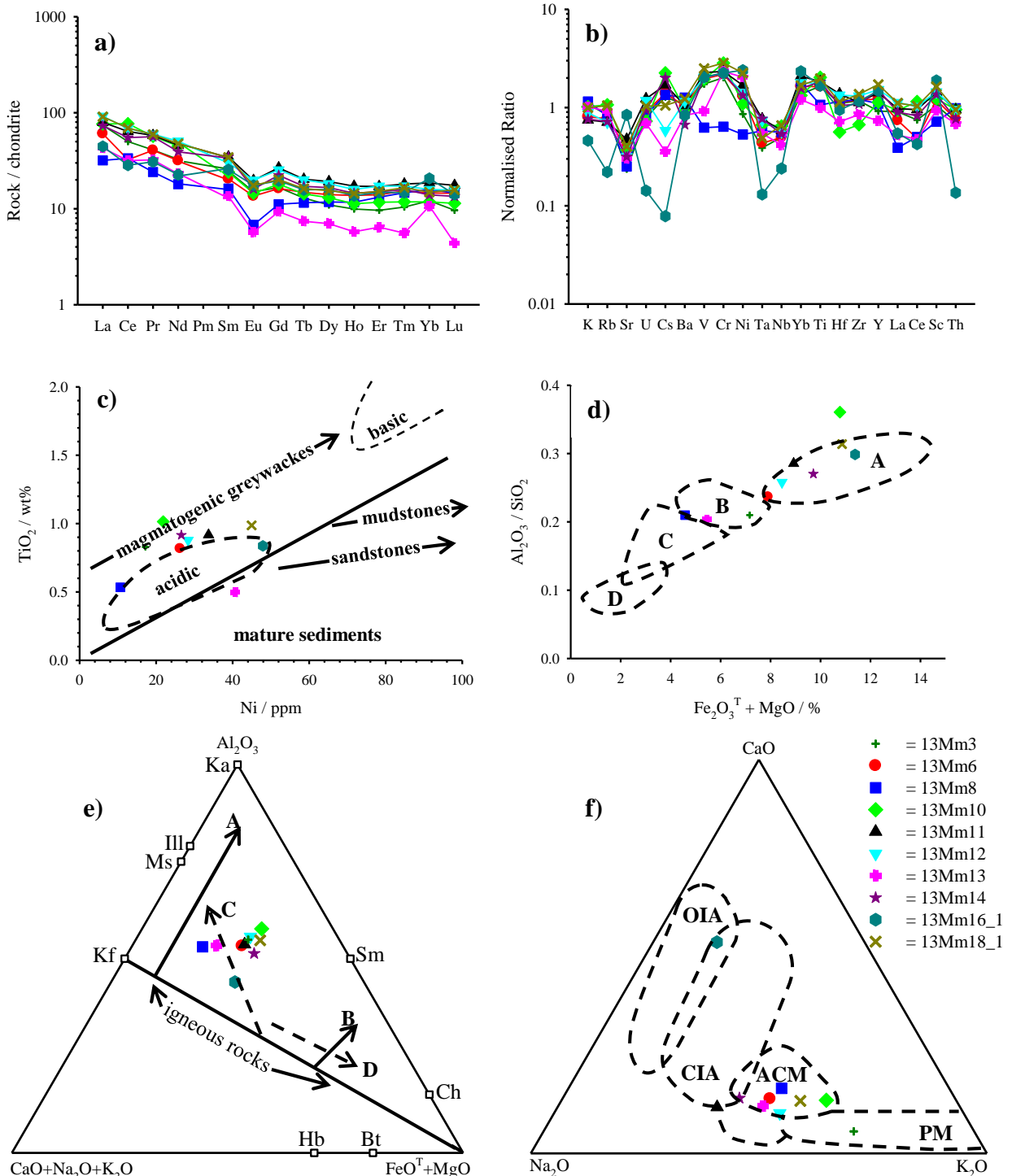


**Fig. 5.5:** It is the aim of these graphs to determine the protoliths of the studied gneisses: a) is a chondrite-normalised rare-earth element (REE) pattern after Taylor and McLennan (1985); b) is an upper-continental crust-normalised multi-element pattern after Floyd et al. (1991) (normalisation values are from Taylor and McLennan 1985); c) plots TiO<sub>2</sub> / wt% versus Ni / ppm after Floyd et al. (1991); d) plots the ratio of Al<sub>2</sub>O<sub>3</sub> / SiO<sub>2</sub> versus the sum of Fe<sub>2</sub>O<sub>3</sub><sup>T</sup> + MgO / % after Bhatia (1983) (A = oceanic island arc; B = continental island arc; C = active continental

margin; D = passive margin); e) is a ternary diagram of molecular  $\text{Al}_2\text{O}_3 - (\text{CaO} + \text{Na}_2\text{O} + \text{K}_2\text{O}) - (\text{FeO}^{\text{T}} + \text{MgO})$  after McLennan (1993) and Toulkeridis et al. (1999) (A = granitic source; B = basaltic source; C = diagenetic and / or metasomatic transformation of kaolinite (Ka) into illite (Ill) with fluids characterised by high  $\text{K}^+ / \text{H}^+$  ratios; D = diagenetic and / or metasomatic transformation of kaolinite into chlorite (Ch) with fluids characterised by high  $\text{Mg}^{2+} / \text{H}^+$  ratios; Bt = biotite; Kf = K-feldspar; Hb = hornblende; Ms = muscovite; Sm = smectite); and f) is a ternary plot of molecular  $\text{CaO} - \text{Na}_2\text{O} - \text{K}_2\text{O}$  after Bhatia (1983) (OIA = ocean island arc; CIA = continental island arc; ACM = active continental margin; PM = passive margin).

## 5.6 Pressure-Temperature Evolution

### 5.6.1 Calculation Methods

In order to derive the  $p$ - $T$  evolution for the studied rocks from the MMC,  $p$ - $T$  pseudosections were calculated with the PERPLE\_X computer programme package (see Connolly 2005; version from August 2011 downloaded from the internet site <http://www.perplex.ethz.ch/>) for the  $p$ - $T$  range of 2 - 24 kbar and 350 - 750 °C (see also sections 4.5.1 and 6.6.1). These  $p$ - $T$  pseudosections, which were calculated in the eleven-component system  $\text{SiO}_2$ - $\text{TiO}_2$ - $\text{Al}_2\text{O}_3$ - $\text{MgO}$ - $\text{MnO}$ - $\text{FeO}$ - $\text{CaO}$ - $\text{Na}_2\text{O}$ - $\text{K}_2\text{O}$ - $\text{H}_2\text{O}$ - $\text{O}_2$ , were contoured by isopleths for molar fractions of garnet components, Si contents in potassic white-mica and modal contents of garnet. In case of sample 13Mm8, the  $p$ - $T$  pseudosection was calculated in a ten-component system (without  $\text{O}_2$  compared to the aforementioned system) and the  $p$ - $T$  range was extended to 2 - 30 kbar and 350 - 950 °C because it was more difficult to establish a proper  $p$ - $T$  path due to a partial lacking of intersections of isopleths.

The thermodynamic data set of Holland and Powell (1998, updated 2002) for minerals and  $\text{H}_2\text{O}$  was applied to all PERPLE\_X calculations. For these calculations, the following solid-solution models were chosen: (1) Gt(HP) for garnet (Holland and Powell 1998); (2) Opx(HP) for orthopyroxene (Powell and Holland 1999); (3) Ep(HP) for clinozoisite-epidote (see Holland and Powell 1998); (4) Mica(M) for paragonite (Massonne 2010) with maximal 50 mol% muscovite component; (5) Chl(HP) for chlorite based on the formulation by Holland et al. (1998); (6) TiBio(HP) for biotite being identical to the previous model Bio(HP) created by Powell and Holland (1999) as the tbi component was removed (see below); (7) Omph(HP) for clinopyroxene based on the thermodynamic data given by Holland and Powell (1996) augmented by those related to the end-members aegirine (acm) and  $\text{CaAl}_2\text{SiO}_6$  (cats); (8) feldspar for ternary feldspar according to Fuhrman and Lindsley (1988) using a subdivision into two models feldspar1 and feldspar2 with different compositional limits (1: max. 8 mol% sanidine component, 2: max. 10 mol% anorthite and max. 10 mol% albite components) as

proposed by Massonne (2009); (9) St(HP) for staurolite (“from THERMOCALC”, written comm. by J.A.D. Connolly); (10) Stlp(M) for stilpnomelane (Massonne 2010); (11) MtUl(A) for magnetite (see Andersen and Lindsley 1988); (12) Pheng(HP) for potassic white-mica (see Powell and Holland 1999 as well as comments in file newest\_format\_solut.dat) with maximal 50 mol% paragonite component; (13) IHm(A) for hematite (Andersen and Lindsley 1988) with maximal 50 mol% ilmenite component; (14) GlTrTsPg for amphibole (glaucophane-tremolite-tschermakite-pargasite + corresponding Fe<sup>2+</sup>-bearing components); and (15) Ctd(HP) for chloritoid (“from THERMOCALC”, written comm. by J.A.D. Connolly). For cordierite, ilmenite, carpholite, and talc, the ideal mixing models hCrd, IGkPy (max. 30 mol% geikielite component), Carp and T, respectively, were used, which are based on the thermodynamic data for the corresponding end-members given by Holland and Powell (1998).

To obtain the *p-T* conditions of solidus curves in the range of 2 - 24 kbar and 560 - 750 °C, PERPLE\_X calculations were achieved with a version downloaded in August 2006. Considering sample 13Mm8, the *p-T* range was set to 2 - 30 kbar and 560 - 950 °C. In order to consider granitic melt, only the model melt(HP), according to White et al. (2001), was added to the aforementioned solid solution models.

The abbreviated end-member phases acti (actinolite), ann1 (annite), mic (microcline), ab (low *T* albite), cumm (cummingtonite), grun (grunerite), and the O<sub>2</sub> buffers qfm and mthm in the applied data file were not considered. Both Ti end-members tip and tbi in white and dark micas, respectively, were excluded as argued by Massonne et al. (2017). The H<sub>2</sub>O component in the haplogranitic melt model (h2oL) was only neglected for calculations without melt.

The bulk-rock compositions of the studied samples, such as 13Mm6 (Tab. 5.1) and 13Mm8 (Tab. 8.8), determined by XRF spectrometry, were modified for the PERPLE\_X calculations: (1) CaO was reduced since some Ca is bound to apatite. The content of (ideally composed) apatite was calculated on the basis of the determined content of P<sub>2</sub>O<sub>5</sub> in the bulk-rock. (2) The oxygen content, which is related to the amount of trivalent iron in the rock, was estimated according to a value corresponding to 10 wt% of the iron being trivalent during metamorphism as assumed for previous calculations of *p-T* pseudosections for HP-UHP rocks (e.g. Massonne et al. 2007b). However, this content could be lower because Fe<sup>3+</sup> contents in the analysed minerals are very low (see above). Regarding sample 13Mm8, the O<sub>2</sub> content was set to zero (see also above). (3) Water contents of 4.5 and 3.0 wt% for samples 13Mm6 and 13Mm8, respectively, were considered to permit the formation of free hydrous fluids already at relatively

low temperatures. (4) For all rock compositions, involved in PERPLE\_X calculations, the sums of the oxide contents in wt% were normalised to 100 wt% (e.g. Tab. 5.1).

Four different calibrations of the Zr-in-rutile thermometer (two by Zack et al. 2004; Watson et al. 2006; Tomkins et al. 2007 for  $\alpha$ -quartz) were applied to the studied samples. Only the calibration by Tomkins et al. (2007) for  $\alpha$ -quartz considers a pressure dependence and was, thus, favoured. The temperature values resulting from all conducted measurements of the Zr contents in rutile were averaged and a  $2\sigma$  error was calculated for this average. The error propagation of the  $1\sigma$  of the counting rates of the peak and background intensities of the Zr  $L\alpha$ -radiation resulted in a temperature error of about  $\pm 40$  °C ( $1\sigma$ ) for a single analysis.

### 5.6.2 Results of the Calculated $p$ - $T$ Pseudosection of Sample 13Mm6

The results of gneiss sample 13Mm6 are exemplarily discussed in this section. Only the  $p$ - $T$  range of 6 - 24 kbar and 430 - 670 °C is of relevance for the aforementioned sample. Therefore, the calculated  $p$ - $T$  pseudosection for the modified bulk-rock composition is merely shown for this range in Fig. 5.6. Only quartz, potassic white-mica, and water are excess phases in the  $p$ - $T$  pseudosection. Rutile occurs throughout the whole  $p$ - $T$  pseudosection (Fig. 5.6), except for pressures below 10 kbar and temperatures below 600 °C. At elevated pressures and temperatures, the phases get larger and have got less mineral components (darker colours in Fig. 5.6). Furthermore, biotite, potassic white-mica, and stilpnomelane are the only K-bearing minerals. Biotite may be found beyond 15 kbar and 670 °C, 14.5 kbar and 570 °C as well as 8 kbar and 440 °C. On the other hand, stilpnomelane is only stable at pressures above 18 kbar and temperatures below 500 °C. Feldspar only exists as plagioclase, which can be found below 8 kbar (430 °C) and 16 kbar (670 °C).

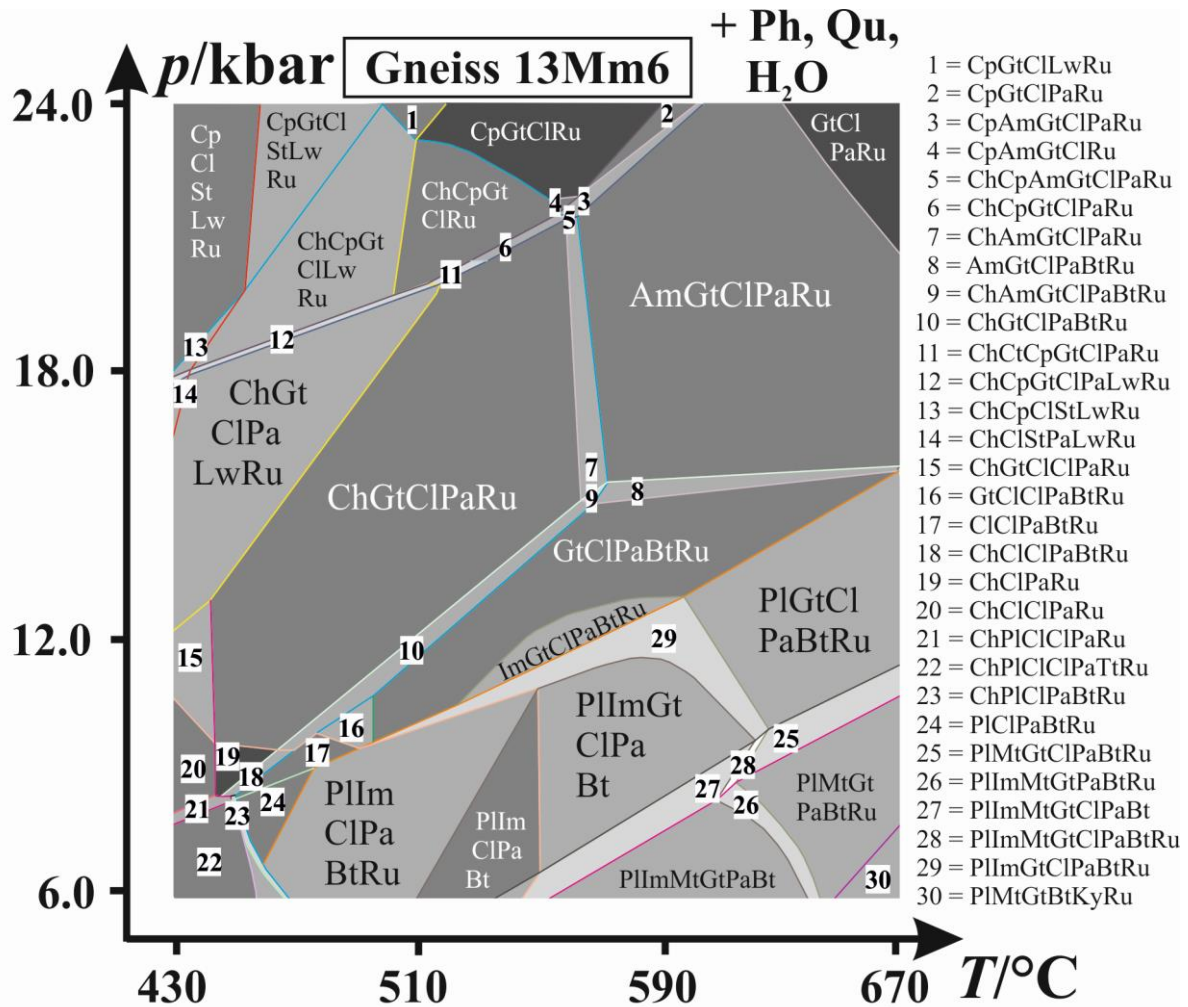


**Fig. 5.6:**  $p$ - $T$  pseudosection (without melt) calculated for the composition of sample 13Mm6 (see Tab. 5.1) with the computer software package PERPLE\_X (see text). Abbreviations: Am = amphibole, Bt = biotite, Ch = chlorite, Cl = clinopyroxene, Cp = carpholite, Ct = chloritoid, Gt = garnet, Im = ilmenite, Ky = kyanite, Lw = lawsonite, Mt = magnetite, Pa = paragonite, Ph = potassic white-mica, Pl = plagioclase, Qu = quartz, Ru = rutile, St = stilpnomelane, Tt = titanite.

The calculated Si content pfu in potassic white-mica (sample 13Mm6) can be found in the range of 3.20 (6 kbar, 540 °C as well as 9 kbar, 670 °C) and 3.50 (20 kbar, 430 °C as well as 24 kbar, 550 °C) (Figs. 5.7-5.8): Higher pressures and / or temperatures favour higher Si contents pfu. In the studied  $p$ - $T$  range (Figs. 5.6-5.8), the garnet volume varies between 0 vol% (24 kbar (450 °C), 18 kbar (430 °C), 9 kbar (430 °C), 9 kbar (540 °C) as well as 6 kbar (540 °C)) and above 10 vol%, reaching its peak at about 15 kbar and 750 °C. Consequently, with rising pressures and temperatures more garnet (in vol%) occurs in the various mineral assemblages of the rock. Besides, the  $p$ - $T$  field of garnet (sample 13Mm6) in the  $p$ - $T$  pseudosection was contoured by isopleths for molar fractions of grossular  $X(\text{Ca})$  and pyrope  $X(\text{Mg})$  (see Fig. 5.7).

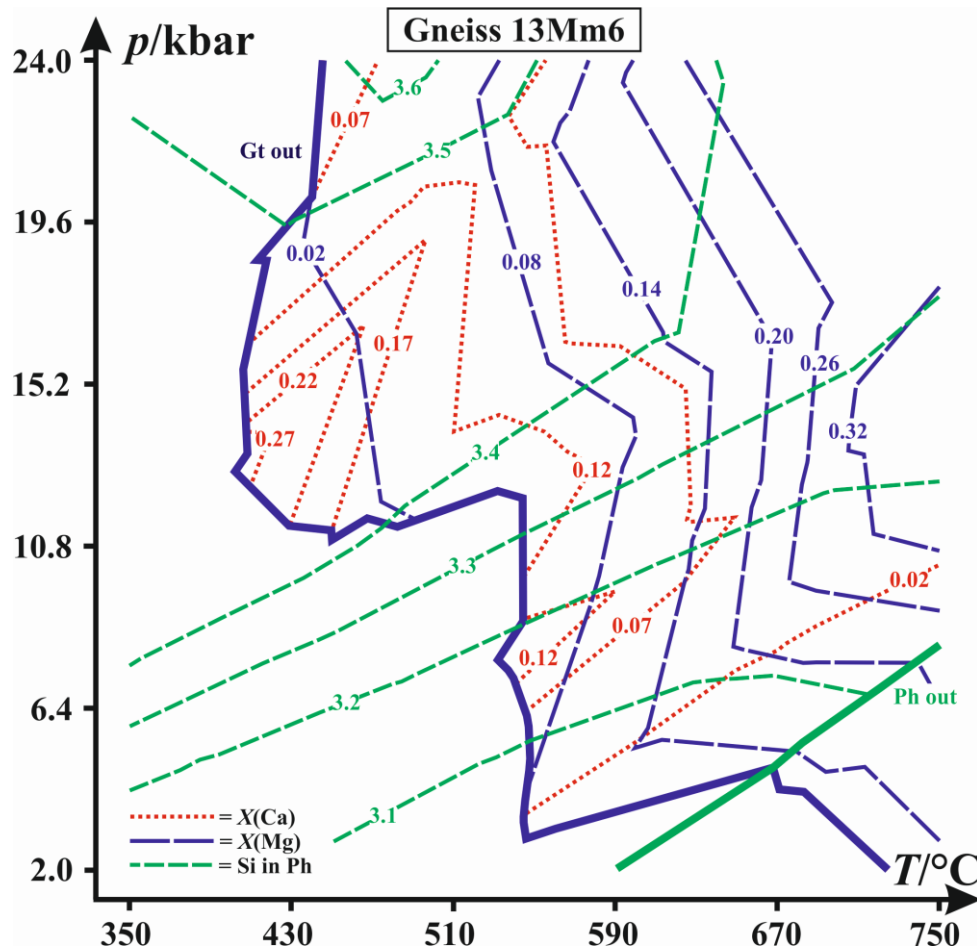


**Fig. 5.7:** Contouring of the calculated  $p$ - $T$  pseudosection of Fig. 5.6 by isopleths for the molar fractions of garnet (Gt) components and the Si contents per formula unit (pfu) in potassic white-mica (Ph). The thick curves mark the limits of the occurrence of garnet and potassic white-mica.

Therefore, two opposed trends become visible: While the amount of Ca in garnet goes down with increasing temperatures, Mg is more and more likely to be stored in garnet. This is in agreement with Săbău (2000) and Massonne (2014). In general, the grossular and pyrope components are within the following limits:  $0.02$  (10 kbar and  $750\text{ }^{\circ}\text{C}$ )  $\leq X(\text{Ca}) \leq 0.27$  (13 kbar and  $420\text{ }^{\circ}\text{C}$ ) as well as  $0.02$  (15 kbar and  $460\text{ }^{\circ}\text{C}$ )  $\leq X(\text{Mg}) \leq 0.32$  (13 kbar and  $710\text{ }^{\circ}\text{C}$ ).

The phase relations at high temperatures shown in Fig. 5.6 (sample 13Mm6) are partially metastable because the calculated solidus curve at wet conditions runs, for instance, through the following  $p$ - $T$  conditions: 6 kbar,  $660\text{ }^{\circ}\text{C}$ ; 15 kbar,  $650\text{ }^{\circ}\text{C}$ ; and 17 kbar,  $670\text{ }^{\circ}\text{C}$  (see Fig. 5.8).

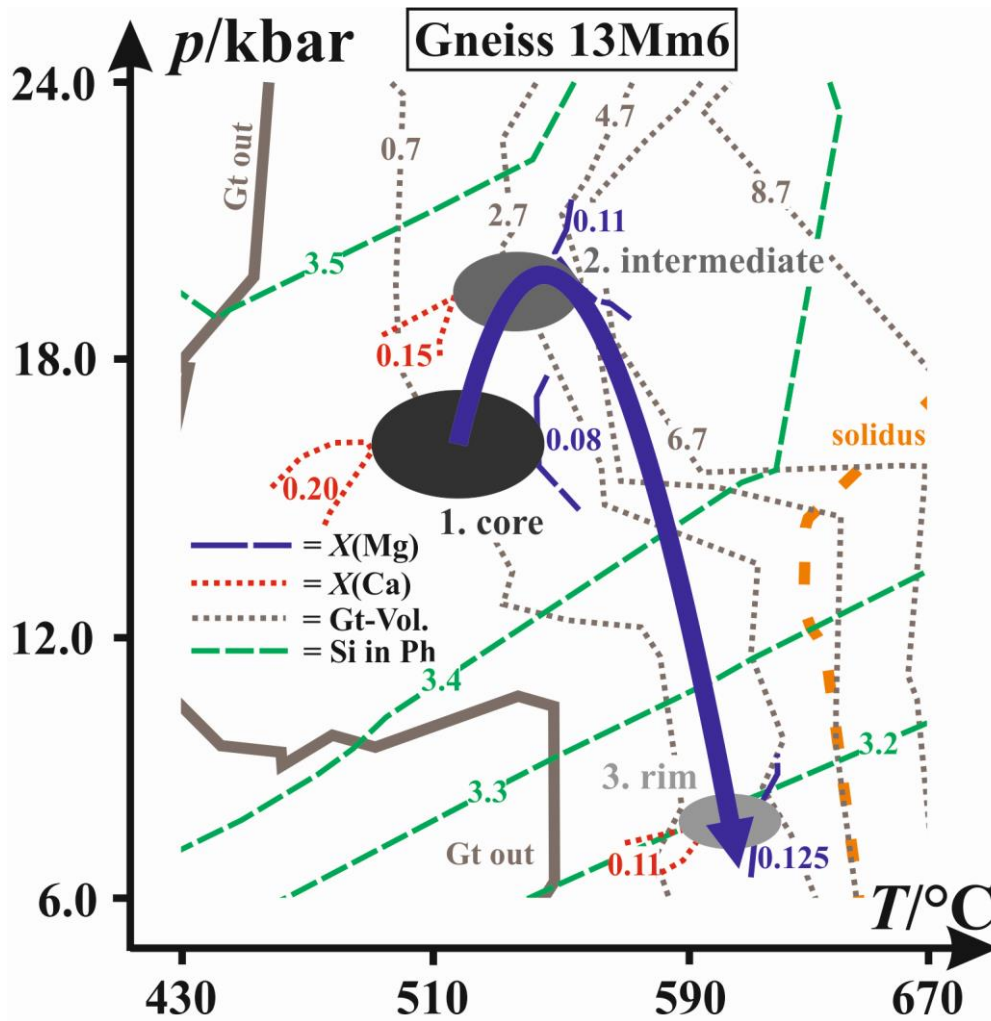


**Fig. 5.8:**  $p$ - $T$  estimates (error ellipses) of sample 13Mm6, using isopleths of Fig. 5.7 for garnet. The constructed  $p$ - $T$  path is shown by a solid line with an arrow. The thick curves mark the limits of the occurrence of garnet (Gt). The wet solidus curve is indicated by a thick, dashed line. Abbreviation: Ph = potassic white-mica.

### 5.6.3 Construction of $p$ - $T$ Paths

A major criterion for the derivation of a specific  $p$ - $T$  condition is the intersection of isopleths for molar fractions of garnet components (e.g. Caddick and Kohn 2013; Massonne 2013). In this study, we use those of  $X(\text{Ca})$  and  $X(\text{Mg})$ . Therefore, the isopleths relevant for the (inner / outer) core, intermediate domain and (outermost) rim of garnet were intersected (see Figs. 5.8-5.9). When these intersections were connected,  $p$ - $T$  paths of the corresponding rocks occurred.

In case of sample 13Mm6 (Fig. 5.8), a common clockwise  $p$ - $T$  path gets visible, which starts at 17 kbar / 510 °C, reaches its peak at 20 kbar / 540 °C and comes to an end at about 10 kbar / 600 °C. The aforementioned  $p$ - $T$  data represent isopleth intersections of the garnet core ( $\text{Alm}_{69.0}\text{GrAn}_{19.1}\text{Py}_{9.6}\text{Sp}_{2.3}$ ), intermediate domain ( $\text{Alm}_{71.6}\text{GrAn}_{15.0}\text{Py}_{11.7}\text{Sp}_{1.7}$ ) and rim

(Alm<sub>73.8</sub>GrAn<sub>10.6</sub>Py<sub>13.0</sub>Sp<sub>2.4</sub>), respectively. The composition of the outermost garnet rim of sample 13Mm6 (Fig. 5.4) could not be taken into account for the derivation of a valid  $p$ - $T$  path due to its unclear and therefore highly speculative nature. Despite the fact that a wet solidus line (thick, dashed line in Fig. 5.8) is evident, this line is not crossed by the  $p$ - $T$  path. Consequently, forming of melt during metamorphism seems to be rather unlikely. Moreover, the calculated garnet volume in sample 13Mm6 starts at 0.7 vol% and ends at about 1.7 vol%. The calculated Si content in potassic white-mica pfu is between 3.20 (intersection of isopleths relevant for the rim of garnet) and 3.50 (intermediate), which is confirmed by EMP measurements of potassic white-mica in such a way that the orders of magnitude are similar (see above). However, analogue to section 6, the calculated values are higher than the experimentally determined ones.

In Fig. 5.9, there is a collection of  $p$ - $T$  paths: Considering sample 13Mm8 (Fig. 5.9a), no intersection of isopleths relevant for the core may be detected. Nevertheless, a reduced  $p$ - $T$  path could be constructed. It starts at 12 kbar / 600 °C and ends at a slightly lower pressure and temperature (from intermediate via rim to outermost rim). Remarkably, it is nearly completely beyond the wet solidus line. While the calculated garnet volume reaches its maximum at 1.5 vol% (intermediate), finally, there is only c. 0.5 vol% garnet. The calculated Si content in potassic white-mica pfu merely varies between 3.25 and 3.40.

Furthermore, the  $p$ - $T$  path of sample 13Mm10 (Fig. 5.9b) shows an unusual anti-clockwise movement with peak conditions at 12 kbar / 650 °C. Only a small part of the  $p$ - $T$  path (at higher temperatures) intersects the wet solidus line. The calculated garnet volume decreases from 13 vol% (1. inner core) to 9 vol% (5. rim). The calculated Si content in potassic white-mica pfu varies between 3.10 and 3.23, but ends at 3.14.

The direction of the  $p$ - $T$  path of sample 13Mm12 in Fig. 5.9c is similar to the one in Fig. 5.9a because there is only a slight decrease in pressure and temperature. In both cases the  $p$ - $T$  conditions are similar but the wet solidus line of sample 13Mm12 hardly intersects the corresponding  $p$ - $T$  path. The calculated garnet volume goes down again, from 4.1 vol% (1. inner core) to 2.1 vol% (5. rim). The calculated Si content in potassic white-mica pfu varies between 3.20 and 3.30.

In Fig. 5.9d, the  $p$ - $T$  path of sample 13Mm14 is shown. It steadily increases in pressure and temperature from 6 kbar / 610 °C until it finally intersects the wet solidus line at some 12 kbar / 660 °C. The calculated garnet volume goes up as well, from 0.5 vol% (1. core) to 6.5 vol% (3.

rim). Besides, the calculated Si content in potassic white-mica pfu also increases from 3.10 (1. core) to 3.25 (3. rim).

Similar to Fig. 5.8, the  $p$ - $T$  path of sample 13Mm16\_1 in Fig. 5.9e shows a clockwise movement with peak metamorphic conditions at 10 kbar / 590 °C. There is quite a distance between the  $p$ - $T$  path and the wet solidus line. In this case, the calculated garnet volume varies in the range of 0.5 vol% (1. core) and 6.5 vol% (2. intermediate), but ends at 3.5 vol% (3. rim). At least, the maximum value of the garnet volume is higher than the one of its counterpart of 13Mm6. Unlike 13Mm6, most of the  $p$ - $T$  path of sample 13Mm16\_1 is located beyond the occurrence of potassic white-mica in Fig. 5.9e. Close to the maximum pressure and temperature, the calculated Si content in potassic white-mica pfu may be determined to be around 3.20.

Furthermore, the  $p$ - $T$  path of 13Mm18\_1 (Fig. 5.9f) is very similar to its counterparts of samples 13Mm8 (Fig. 5.9a) and 13Mm12 (Fig. 5.9c). At peak metamorphic conditions (about 12 kbar / 660 °C), the  $p$ - $T$  path hardly intersects the wet solidus line (see Fig. 5.9f). The rest is a mere decrease in pressure and temperature until 9 kbar and 620 °C are reached. Moreover, the calculated garnet volume is in the range of 3 and 9 vol% (higher than in Fig. 5.9a or 5.9c) but decreases only while following the  $p$ - $T$  evolution. The same is true for the calculated Si content in potassic white-mica pfu, which varies between 3.15 and 3.30 (lower than in Fig. 5.9a and nearly identical to Fig. 5.9c).

Generally speaking, all calculated Si contents in potassic white-mica pfu are reasonably similar their counterparts obtained by EMP measurements of potassic white-mica and subsequent data evaluation by CALCMIN (applicable to results in Figs. 5.8 and 5.9).

Regarding sample 13Mm10, 31 analyses of rutile yielded Zr contents between 162 and 319 ppm. After subtraction of a few outliers at the highest and lowest Zr contents, the remaining range of Zr contents is limited between about 200 and 300 ppm. A single rutile population is likely because of this limited range and many data close to the average of 249 ppm Zr in rutile. The calculated temperatures range from 611 °C (162 ppm Zr in rutile) to 663 °C (319 ppm) with a mean value of 643 (249 ppm)  $\pm$  5 °C ( $2\sigma$ ) using the calibration by Tomkins et al. (2007) for  $\alpha$ -quartz at 12 kbar. The calibration by Watson et al. (2006) yielded a mean temperature of 627  $\pm$  5 °C. Temperatures of 716  $\pm$  8 and 693  $\pm$  7 °C were obtained from the calibrations by Zack et al. (2004). The Zr-in-rutile thermometers of sample 13Mm10 yield temperatures of the anti-clockwise  $p$ - $T$  path during peak metamorphic conditions (shown in Fig. 5.9b), which are 12 kbar and 650 °C according to PERPLE\_X calculations. The same procedure was applied to samples 13Mm12, 13Mm16\_1, and 13Mm18\_1.

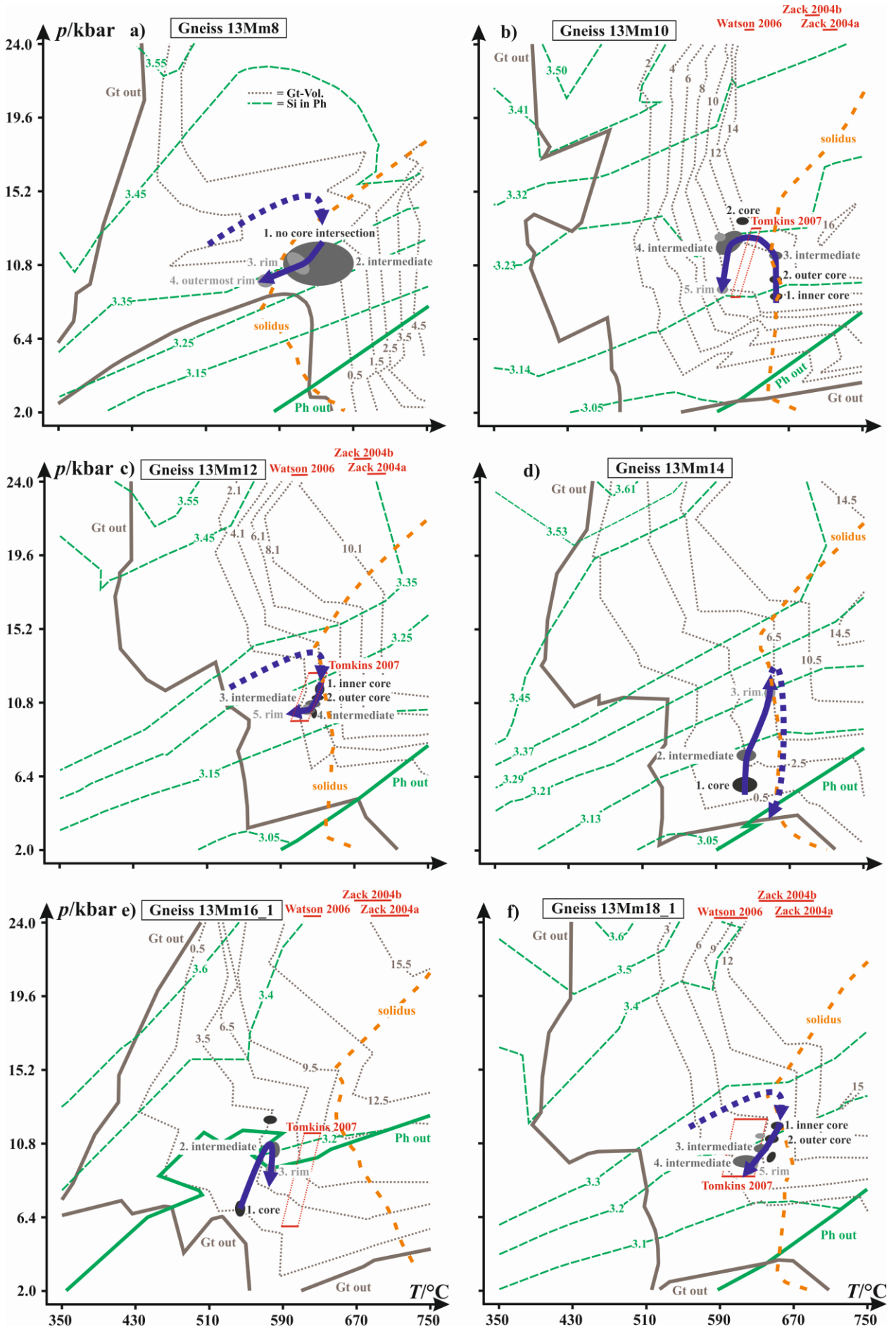


**Fig. 5.9:** *p-T* paths of samples 13Mm8 (a), 13Mm10 (b), 13Mm12 (c), 13Mm14 (d), 13Mm16\_1 (e) and 13Mm18\_1 (f). Additionally, the calculated modal garnet (Gt) contents and Si contents per formula unit (pfu) in potassic white-mica (Ph) are plotted for every sample. The thick curves mark the limits of the occurrence of garnet and potassic white-mica. The wet solidus curves are indicated by thick, dashed lines. In some cases, the *p-T* paths are expanded by thick, dotted lines with arrows.

In summary, an anti-clockwise (Fig. 5.9b) and six clockwise (Figs. 5.8; 5.9a,c,d,e,f) *p-T* paths were reconstructed from the observed mineral assemblages and the chemical compositions of minerals. In general, peak metamorphic conditions during these evolutions were at about 12 kbar and 660 °C.

### 5.7 Age Dating of Monazite

Monazite appears as small oval-shaped grains in the studied gneisses. The average diameter lies in the range of 10 - 20 µm. Monazite is evenly distributed in the rock matrix, sometimes showing indications of (considerable) corrosion. Monazite grains are not shielded, for example, as inclusions in garnet. Approximately 20 - 30 such grains were found in a single thin section. For instance, an unusually large monazite grain of sample 13Mm18\_1 is shown in Fig. 5.10. Its BSE image (Fig. 5.10a) shows no chemical heterogeneities but the elemental maps of La, Gd and Th prove otherwise. Consequently, in the core area of the grain, these elements have got higher concentrations than in the rim. Zones that are enriched with La and Gd are depleted by Th and vice versa (see Williams et al. 2007).

Altogether 345 monazite analyses (including data of section 4) were conducted on 201 grains with the EMP to discriminate between different groups of monazites. 43 analyses were discarded because of low oxide sums (< 96.0 wt%) and high SiO<sub>2</sub> contents (> 0.9 wt%). The obtained ages range between ~575 and ~340 Ma. The probability density plot (Fig. 5.11a) suggests a bimodal distribution of two main populations, ranging from ~575 to ~455 Ma and from ~430 to ~340 Ma. These two main groups can be subdivided into smaller populations, which provides more details. Apart from detrital ages (identical to section 4), the following metamorphic ages are important:  $403.5 \pm 2.1$  Ma ( $2\sigma$ ), MSWD = 5.1 Ma;  $384.4 \pm 1.2$  Ma ( $2\sigma$ ), MSWD = 1.1 Ma;  $368.5 \pm 1.9$  Ma ( $2\sigma$ ), MSWD = 2.5 Ma; including the side maxima of ~430 Ma and ~340 Ma. Due to overlapping of the single ages and their corresponding errors, it is not possible to determine how many single values belong to one of these sub-groups. Weighted averages show  $2\sigma$  errors of single measurements, which are in the range of 5 to 20 Ma (Fig.

5.11b). Single analyses of one age population can differ by up to 70 Ma. Due to the small sizes of the monazite grains, it was impossible to determine ages from different chemical domains in such grains (one of the very rare exceptions is the corroded grain of Fig. 5.10).

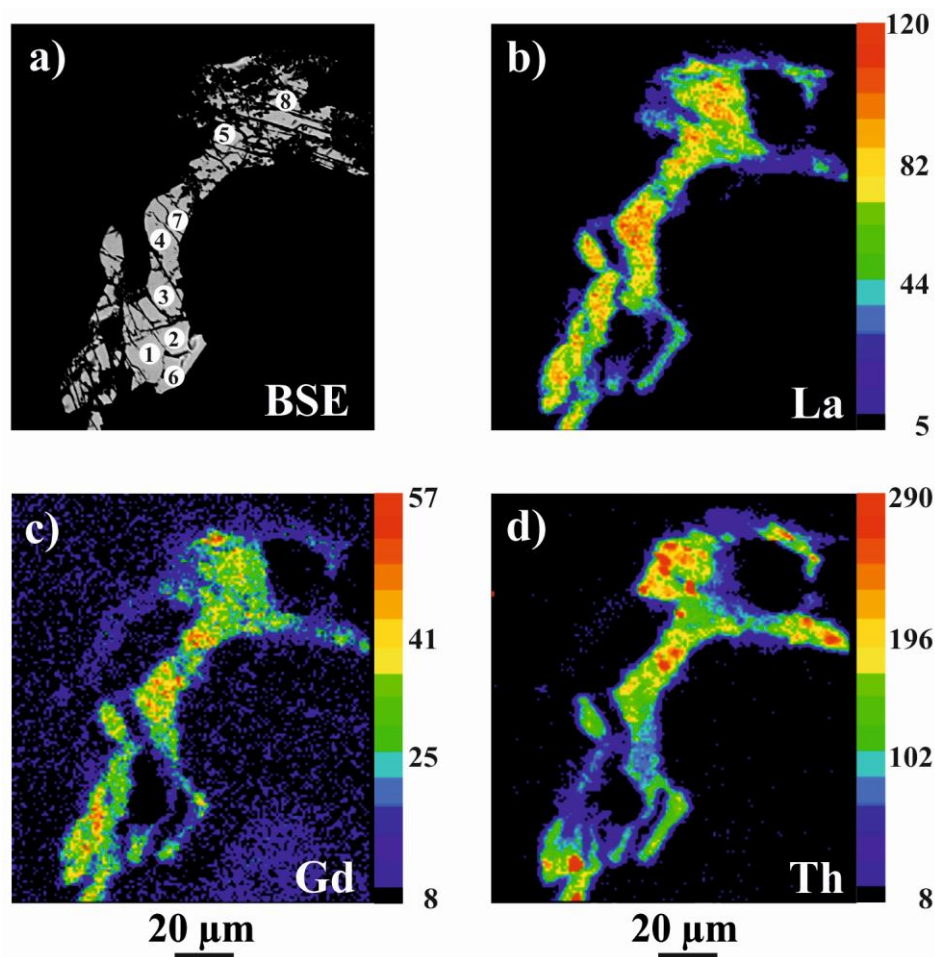


**Fig. 5.10:** Backscattered electron (BSE) image (a) and elemental maps (b-d) of a monazite grain of sample 13Mm18\_1, obtained with a CAMECA SX100 EMP. The scales for the colour code on the right hand side of each image indicate to counts X-ray radiation per time unit. The numbers on the studied monazite grain refer to specific EMP measurements: 1 =  $404.1 \pm 8.8$  Ma ( $2\sigma$ ); 2 =  $367.1 \pm 14.4$  Ma; 3 =  $409.5 \pm 14.8$  Ma; 4 =  $332.6 \pm 14.1$  Ma; 5 =  $373.3 \pm 14.1$  Ma; 6 =  $360.4 \pm 8.7$  Ma; 7 = failed measurement; 8 =  $406.6 \pm 15.9$  Ma.

It is also remarkable that monazites show different chemical compositions depending on their ages (Fig. 5.12). The following trends become evident: The older the monazites, the smaller the La / Gd ratio and the more  $Y_2O_3$  / wt% is incorporated. This La / Gd ratio (Fig. 5.12a) can be considered as a slope in an imaginary REE pattern, providing information about the distribution of light and heavy REEs. As Y has got a similar radius to heavy REEs, it behaves likewise (e.g. Housecroft and Sharpe 2006). Due to the  $Y_2O_3$  pattern in Fig. 5.12b, it is evident that the

incorporation of heavy REEs was the decisive factor, causing the trend of the La / Gd ratio in Fig. 5.12a. Chemical differences of monazite grains are also exemplarily shown in Tab. 5.5.

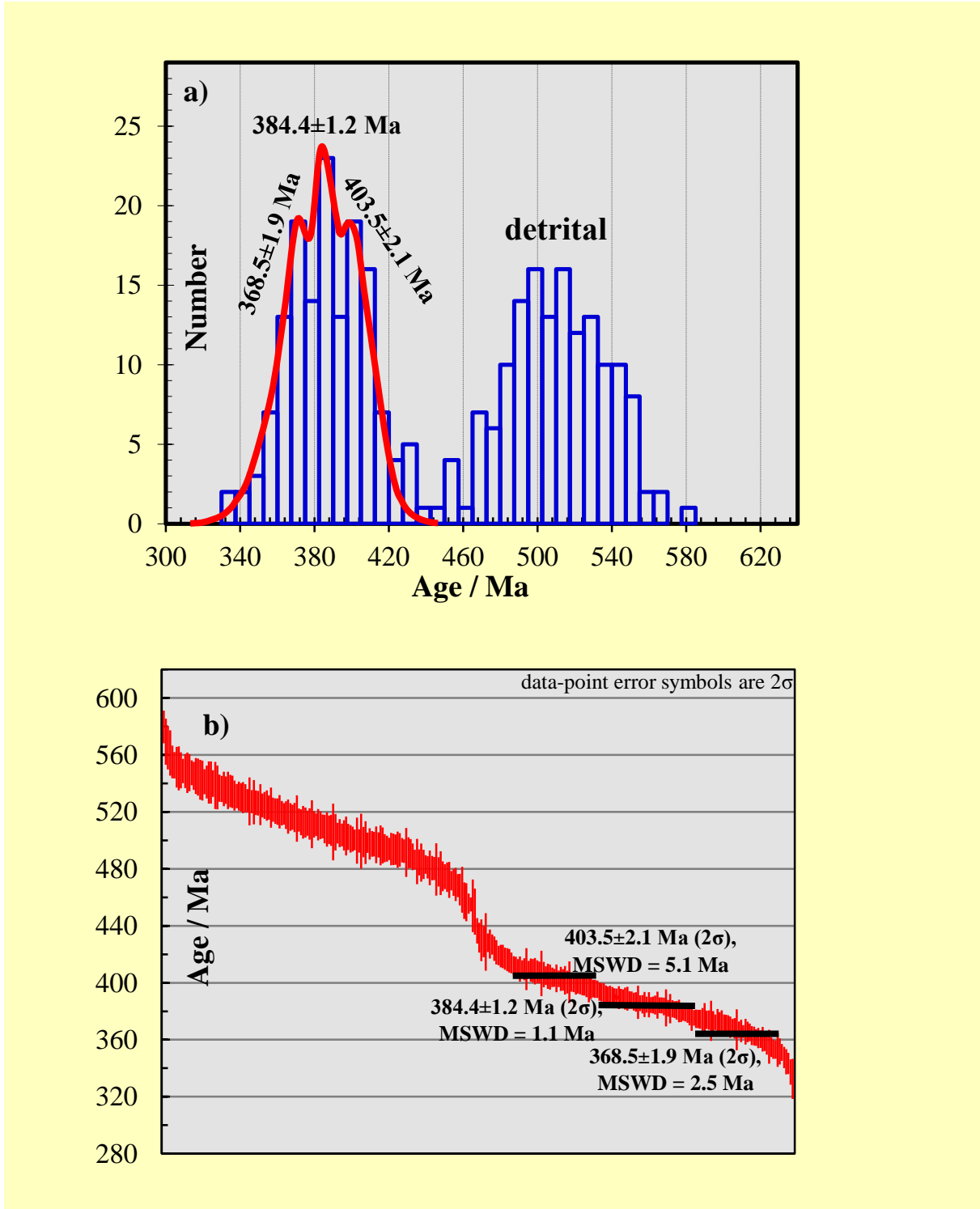


**Fig. 5.11:** Probability density plot (a) and weighted averages (b) of monazite ages, obtained with a CAMECA SX100 EMP (including data of section 4). There are basically two groups of age populations, which can further be subdivided.

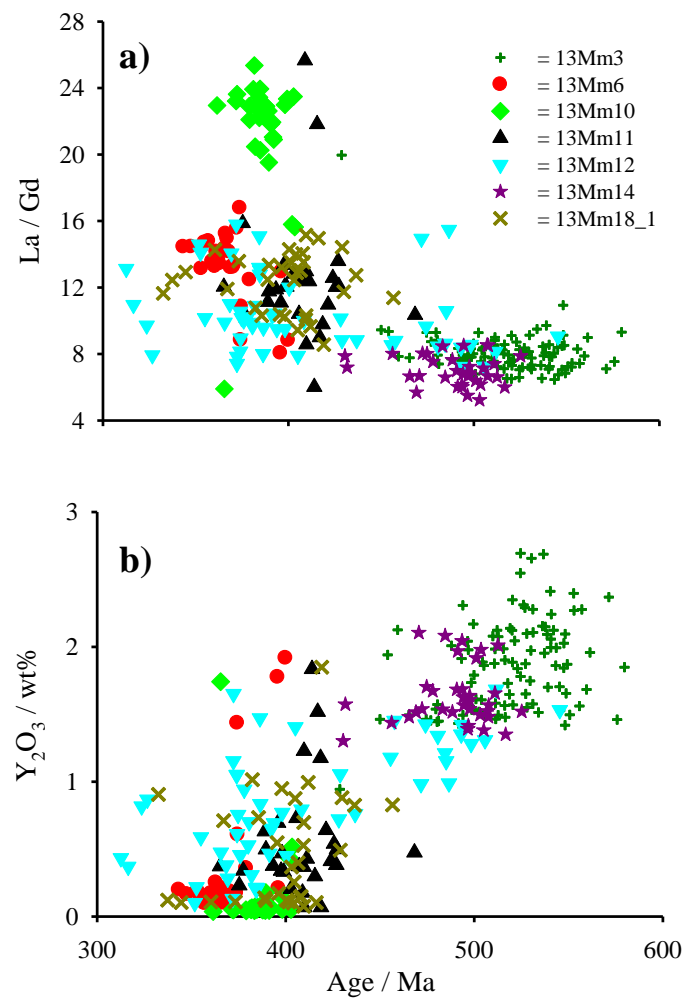


**Fig. 5.12:** Monazite analyses, obtained with a CAMECA SX100 EMP, in terms of the La / Gd ratios (a) and the Y<sub>2</sub>O<sub>3</sub> / wt% contents (b) versus the corresponding ages.

**Tab. 5.5:** Representative analyses (in wt%) of monazite from the studied gneisses of the Münchberg Metamorphic Complex (MMC), obtained with a CAMECA SX100 EMP. The structural formula of monazite is based on four oxygen anions. The sulphur content was below the detection limit.

Mineral	Monazite					
	Oxides in wt%	13Mm6oB -M1-1	13Mm6oB -M2-1	13Mm6oB -M4-2	13Mm10o B-M1-3	13Mm10o B-M2-1
SiO <sub>2</sub>	0.29	0.34	0.25	0.22	0.16	0.20
P <sub>2</sub> O <sub>5</sub>	29.87	30.37	29.79	30.40	30.73	30.53
CaO	0.754	0.802	0.649	0.964	0.932	0.993
Y <sub>2</sub> O <sub>3</sub>	0.151	0.170	0.069	0.042	0.058	0.052
La <sub>2</sub> O <sub>3</sub>	14.65	13.95	14.54	14.58	14.99	14.92
Ce <sub>2</sub> O <sub>3</sub>	29.60	28.96	29.96	29.43	30.11	29.99
Pr <sub>2</sub> O <sub>3</sub>	3.429	3.426	3.454	3.146	3.298	3.189
Nd <sub>2</sub> O <sub>3</sub>	12.21	12.24	11.93	10.80	10.90	10.60
Sm <sub>2</sub> O <sub>3</sub>	2.188	2.159	2.046	1.556	1.584	1.545
Gd <sub>2</sub> O <sub>3</sub>	1.176	1.169	1.036	0.731	0.754	0.689
Dy <sub>2</sub> O <sub>3</sub>	0.193	0.185	0.154	0.116	0.148	0.126
PbO	0.0976	0.1046	0.0850	0.1218	0.1220	0.1281
ThO <sub>2</sub>	4.033	4.313	3.406	4.800	4.605	4.861
UO <sub>2</sub>	0.718	0.785	0.612	0.858	0.889	0.924
SUM	99.360	98.976	97.979	97.772	99.269	98.742
Si	0.0113	0.0133	0.0100	0.0086	0.0061	0.0079
P	0.9967	1.007	1.0030	1.0153	1.0138	1.0123
Ca	0.0318	0.0336	0.0277	0.0407	0.0389	0.0417
Y	0.0032	0.0035	0.0015	0.0009	0.0012	0.0011
La	0.2130	0.2016	0.2133	0.2121	0.2154	0.2155
Ce	0.4272	0.4152	0.4363	0.4250	0.4295	0.4301
Pr	0.0492	0.0489	0.0500	0.0452	0.0468	0.0455
Nd	0.1718	0.1713	0.1695	0.1522	0.1516	0.1483
Sm	0.0297	0.0291	0.0280	0.0212	0.0213	0.0208
Gd	0.0154	0.0152	0.1370	0.0096	0.0097	0.0090
Dy	0.0024	0.0023	0.0020	0.0015	0.0019	0.0016
Pb	0.0010	0.0011	0.0009	0.0013	0.0013	0.0014
Th	0.0362	0.0384	0.0308	0.0431	0.0408	0.0433
U	0.0063	0.0068	0.0054	0.0075	0.0077	0.0081
Age/Ma	362.6	360.4	372.4	379.1	384.4	384.7
2σ error/Ma	6.6	6.2	7.7	5.7	5.8	5.6

## 5.8 Discussion

### 5.8.1 *p-T* Evolution of the Studied Samples

The *p-T* path of sample 13Mm6 (Fig. 5.8) shows a HP metamorphism. Compared to the *p-T* conditions in Fig. 5.9, the peak pressure seems to be quite high. In Fig. 5.9, all peak values of the *p-T* conditions are pretty similar. Except for samples 13Mm6 (Fig. 5.8) and 13Mm16\_1 (Fig. 5.9e), every *p-T* path is partly beyond the wet solidus line. The formation of melt is also

confirmed by the occurrence of feldspar-quartz inclusions in garnet grains of samples 13Mm3, 13Mm10, 13Mm12 and 13Mm14 (see section 4; Cesare et al. 2011; Massonne 2014 and references therein).

Regarding the calculated courses of the  $p$ - $T$  paths in Fig. 5.9 (solid lines with arrows), it is evident that, at least in case of samples 13Mm8, 13Mm12, 13Mm14 and 13Mm18\_1, the whole  $p$ - $T$  paths could not be deduced by PERPLE\_X calculations (especially via intersections of garnet isopleths alone) but parts of them (compare section 6.7.2). Sometimes, it is only the part of increasing pressures and temperatures (13Mm14) and, sometimes, of decreasing pressures and temperatures (13Mm8, 13Mm12, 13Mm18\_1). The calculated  $p$ - $T$  paths of samples 13Mm6 (Fig. 5.8), 13Mm10 (Fig. 5.9b) and 13Mm16\_1 (Fig. 5.9e) seem to show the “entire” metamorphism at peak conditions during an orogeny that led to the formation of the studied metapelites. Therefore, it is probably a good approximation to “artificially” add the missing pieces to the other  $p$ - $T$  paths (thick, dotted lines with arrows in Figs. 5.9a,c,d,f). Obviously, the results in Fig. 5.8 and Figs. 5.9b,e serve as suitable templates. What becomes evident is that most garnet grains (with very few exceptions like 13Mm6, 13Mm10 and 13Mm16\_1) do not store information about the whole metamorphism at peak conditions but merely fragments of it. It is still unclear why in one sample it is the first (prograde) part of the  $p$ - $T$  path that is “remembered” by garnet grains and in another sample it is the second (retrograde) part.

In general, there are two different kinds of  $p$ - $T$  paths, which may be attributed to gneisses from the MMC, namely a clockwise (see Figs. 5.8; 5.9a,c,d,e,f) and an anti-clockwise (see Figs. 4.7; 5.9b) movement in a  $p$ - $T$  diagram. It is clear that a subduction and the following exhumation event is described here. Reports of anti-clockwise  $p$ - $T$  paths are rare in literature (e.g. for the MMC: section 4; for the Bohemian Massif: Pitra and Guiraud 1996). Sometimes, anti-clockwise  $p$ - $T$  paths are suggested by the determined  $p$ - $T$  conditions for different metamorphic stages of a polymetamorphic rock. However, two clockwise paths instead of a single anti-clockwise path can be a viable alternative (see, e.g. Massonne 2014; Lo Pò et al. 2016). It is quite possible that a “forced flow” mechanism (see Gerya et al. 2002) may explain the occurrence of both clockwise and anti-clockwise  $p$ - $T$  paths in the MMC.

Nevertheless, compared to literature (e.g. Matthes 1978; Franz et al. 1986; Vollbrecht et al. 2006), nearly all peak values for the temperature are in good agreement but our results for the peak pressure are substantially higher. Moreover, the results obtained from the Zr-in-rutile thermometry support our temperature values. The here derived  $p$ - $T$  paths certainly contribute to a better understanding of the geodynamic processes leading to the nappe pile of the MMC.

### 5.8.2 Monazite Ages and Their Interpretation

The bimodal age range between ~575 and ~340 Ma, obtained from monazite grains of the studied rocks, is partly compatible with metamorphic ages reported for diverse rocks of the MMC, using different age dating techniques (see, e.g. section 5.2). The metamorphism of MMC rocks are Variscan events which mostly happened in the time span of 430 - 370 Ma (see, e.g. O'Brien 2000; Massonne and O'Brien 2003).

Considering Fig. 5.11, the youngest age group (c. 430 - 340 Ma) probably refers to the Variscan orogeny in Devonian times. The huge time span of this age population can be explained by the occurrence of a series of metamorphic events. Consequently, one huge (Gaussian) curve would be an oversimplification. Despite the fact that monazites of the MMC have not been dated so far, the presented metamorphic ages are in good agreement with values obtained for other minerals in literature (see Gebauer and Grünenfelder 1979; Kreuzer et al. 1989; Stosch and Lugmair 1990; Hammerschmidt and Franz 1992; Kreuzer et al. 1993). It is assumed that the monazite age of ~430 Ma represents an important pre-Variscan event, such as the subduction of oceanic crust. At  $403.5 \pm 2.1$  Ma ( $2\sigma$ ), there was probably the first collision of Gondwana and Laurussia, leading to the formation of metamorphic monazites. At  $384.4 \pm 1.2$  Ma ( $2\sigma$ ), the precursor rocks of the studied gneisses were likely to be exposed to peak metamorphic conditions (see section 7.1). The age of  $368.5 \pm 1.9$  Ma ( $2\sigma$ ) stands for a step during the exhumation history of the rocks. For the age of ~340 Ma, a delamination process due to the aforementioned continent-continent collision is suggested (e.g. Massonne 2005).

Furthermore, the older age group (c. 575 - 455 Ma) is likely to represent magmatic events in Late Proterozoic and Cambrian times. This older group can also be subdivided into smaller age populations, dating the protoliths of the studied gneisses in the provenance areas. These precursor rocks may be related to Cadomian magmatic arcs at the northern Gondwana margin (e.g. Linnemann et al. 2007; Linnemann and Romer 2010) prior the collision with Laurussia. It is our interpretation that the studied, detrital monazite grains of magmatic origin remained (nearly) unaltered due to specific *p-T* conditions. These conditions were probably those along a geotherm from surface conditions to metamorphic conditions, which is characterised by c. 30 °C/km. For a detailed discussion see section 4.7. Unfortunately, it is still unclear why one rock sample, namely 13Mm12, can contain both young and old monazite grains.

These two monazite groups do not show different shapes or forms. There is no sign of young grains using their old counterparts as initial nuclei, either. It is only their chemical heterogeneity that may be linked to their ages (Fig. 5.12). As mentioned before, the old (detrital) grains have

got lower La / Gd ratios and more  $Y_2O_3$  / wt% than the younger (metamorphic) ones. This points to an influence of the presence of garnet (a metamorphic mineral), which incorporates heavy REEs and Y quite easily. In case of the old monazites, there was no garnet present, so it could not store any of these elements. In contrast to that, the younger monazites were in contact with garnet. Therefore, especially heavy REEs including Y were preferentially incorporated into garnet (see Massonne 2014; Williams et al. 2007). We set the following limits (despite some outliers):  $4 < La / Gd < 9$  as well as  $1.1 < Y_2O_3 / wt\% < 3.0$  refer to detrital monazite grains of magmatic origin and  $9 < La / Gd < 28$  as well as  $0 < Y_2O_3 / wt\% < 3.0$  refer to metamorphic grains (compare Martins et al. 2009). In general, it can be ruled out that monazite of this study is of diagenetic origin due to its elevated concentrations of  $ThO_2$  ( $> 4.0$  wt%),  $UO_2$  ( $> 0.6$  wt%), and  $PbO$  ( $> 0.08$  wt%) (compare Kryza et al. 2004).

Thanks to the elemental maps of Fig. 5.10, it may be concluded that Th-poor parts of the monazite grain are older than Th-rich ones. As explained in section 5.7, high Th contents are associated with low La and Gd concentrations and vice versa (see Williams et al. 2007).

### 5.8.3 Protoliths of the Studied Samples

All graphs in Fig. 5.5 deal with the determination of protoliths of the studied gneisses. For instance, Fig. 5.5a shows chondrite-normalised REE patterns after Taylor and McLennan (1985). There are three important aspects: Firstly, an enrichment of light REEs, secondly, a negative Eu anomaly and, thirdly, relatively flat heavy REE patterns. These features, which can be observed for all gneisses, are typical for upper-continental crust rocks. The aforementioned negative Eu anomalies (bulk-rock data) indicate that feldspar, such as plagioclase, was probably absent during (re-)crystallisation (compare Hoskin and Schaltegger 2003; Rubatto and Hermann 2007).

Furthermore, Fig. 5.5b shows upper-continental crust-normalised multi-element patterns after Floyd et al. (1991) (normalisation values are from Taylor and McLennan 1985), meaning that the deviation of the studied rocks from the upper-continental crust can be assessed. This deviation is not distinctive at all with the experimental values only fluctuating slightly around the ideal literature value of one. Sample 13Mm16\_1 should be regarded as an exception because it is probably a restite. Nevertheless, this graph clearly confirms that the protoliths came from the upper-continental crust and not the lower crust or the mantle.

Moreover, the next graph (Fig. 5.5c), which plots  $\text{TiO}_2$  / wt% versus Ni / ppm (see Floyd et al. 1991), provides the following information: The protoliths are rather acidic and immature. XRF measurements (also bulk-rock data) confirm the acidity of the rocks with  $\text{SiO}_2$  contents of at least 57 wt%.

Besides, Fig. 5.5e represents a ternary diagram of molecular  $\text{Al}_2\text{O}_3 - (\text{CaO} + \text{Na}_2\text{O} + \text{K}_2\text{O}) - (\text{FeO}^{\text{T}} + \text{MgO})$  after McLennan (1993) and Toulkeridis et al. (1999). It is supposed to provide information about weathering trends: The studied gneisses form a homogeneous group (see above) plotting close to the igneous trend between the weathering trends of basaltic and granitic rocks, indicating that the source material has not been significantly affected by chemical weathering. This is suitable for a strong relief found on active continental rims or island arcs.

Fig. 5.5f is a ternary plot of molecular  $\text{CaO} - \text{Na}_2\text{O} - \text{K}_2\text{O}$  after Bhatia (1983). All experimental values (except for three points) are located in the ACM field. The interpretation that the protoliths came from an ACM is further supported by Figs. 5.5c,e since immature rocks cannot be weathered to a significant extent. They were positioned on a high relief which caused a fast removal from their original location followed by burying.

Fig. 5.5d is a plot of the ratio of  $\text{Al}_2\text{O}_3 / \text{SiO}_2$  versus the sum of  $\text{Fe}_2\text{O}_3^{\text{T}} + \text{MgO} / \%$  after Bhatia 1983. Based on the previous discrimination diagrams, it should be expected that the experimental values are located in field C (active continental margin). However, the experimental data are mostly found in fields A (oceanic island arc) and B (continental island arc). Moreover, the point representing sample 13Mm10 is not even located inside any of the prepared fields. Although this is an inherent contradiction, our interpretation of the protoliths is strongly supported by all other plots.

From a geochemical point of view, it is evident that the studied gneisses represent one type of metapelites with only minor differences. Their protoliths are immature (not much weathered or otherwise altered) sediments, which were located on an ACM with a strong relief. Generally speaking, the precursor rocks came from the upper-continental crust of the STZ.

## 5.9 Conclusions

This study has provided important contributions to the evolution of rocks from the MMC. Firstly, the age of the main metamorphic event, probably the Variscan orogeny, which the rocks were exposed to, was determined to be Devonian. In addition, magmatic events could be dated to be in Late Proterozoic and Cambrian times. These are probably the ages of Cadomian and

Caledonian protoliths. Secondly, these precursor rocks have been identified as immature sediments, which were located on an ACM with a strong relief. In general, the protoliths came from the upper-continental crust of the STZ. Thirdly, the  $p$ - $T$  paths of the rocks were calculated with the PERPLE\_X computer programme package. They normally show a clockwise movement, reaching peak metamorphic conditions at about 12 kbar and 660 °C. Anti-clockwise  $p$ - $T$  paths are rather rare for MMC rocks.

It has been shown that monazite age dating in combination with spider diagrams, established from bulk-rock elemental concentrations, provides results comparable to zircon analyses. Therefore, this method competes with studies of the far less abundant mineral zircon, which indeed also acts as a geochronometer and bears clues on the nature of the precursor rocks (e.g. Harley and Kelly 2007; Willner et al. 2013).

### **Acknowledgements**

The authors thank Thomas Theye (Stuttgart) for his support of the work with the EMP and Gisela Kwiatkowski, Matthias Leiss, and Moritz Schmelz (Stuttgart) for their technical assistance. F.W. is deeply grateful to Maria-Anna Waizenhöfer (Ellwangen) for her generous subsistence support.

*Note:* A shortened version of this chapter is planned to be submitted to *Chemie der Erde – Geochemistry* for publication.

## 6. Revision of the Pressure - Temperature Evolution of Eclogites from the Münchberg Metamorphic Complex, NE Bavaria (Germany)

Florian Waizenhöfer, Hans-Joachim Massonne, Joachim Opitz

Institut für Mineralogie und Kristallchemie, Universität Stuttgart, Azenbergstraße 18, 70174 Stuttgart, Germany

### ABSTRACT

We investigated rocks from three larger eclogite bodies (Weißenstein hill, village of Fattigau, town of Oberkotzau) of the Variscan Münchberg Metamorphic Complex (MMC) in north-eastern (NE) Bavaria, central Europe. Typical features of the studied fresh eclogites are (1) garnet with abundant inclusions mainly in the core, (2) a garnet core composition that is relatively poor in Mn ( $\leq 3$  mol% spessartine) and rich in Mg ( $> 15$  mol% pyrope), and (3) small amounts of amphibole and phengite that, for textural reasons, might have coexisted with garnet and omphacite. The pressure ( $p$ ) - temperature ( $T$ ) evolution of the rocks were derived, using contoured  $p$ - $T$  pseudosections constructed with PERPLE\_X. Mainly based on the chemical zonation of garnet, Si contents in amphibole and potassic white-mica, modal contents of diverse minerals, and mineral inclusions in garnet, clockwise  $p$ - $T$  paths resulted which show similar shapes for all three eclogite bodies. These paths start at 5 - 7 kbar and 475 - 580 °C and reach peak  $p$ - $T$  conditions of 26 - 30 kbar and 670 - 740 °C. The range of peak temperatures was corroborated by Zr-in-rutile thermometry. Minor and trace elements in the eclogites confirm previous views that the protoliths of the eclogites were mid-ocean ridge basalts / gabbros. We assume that subducted oceanic crust was first stored at deeper crustal levels, to explain early  $p$ - $T$  conditions around 10 kbar and 600 °C, and then further transported to greater depths with the subducting plate initiated by tectonic erosion. The exhumation of the eclogites could have taken place in a subduction channel.

**KEYWORDS:** eclogite, garnet, high-pressure metamorphism, MORB, Münchberg Metamorphic Complex, potassic white-mica,  $p$ - $T$  pseudosection.

## 6.1 Introduction

Almost two centuries after Haüy had coined the term eclogite (Godard 2001) and defined it as being mainly composed of garnet and clinopyroxene (which must be omphacite; Carswell 1990), numerous petrological studies on this rare rock type have been undertaken, especially in the last three decades. According to these studies, most eclogite has formed at great Earth's depth ( $> 50$  km) during subduction of oceanic crust. Hence, this rock type is, nowadays, taken as a witness of this process when detected in the field where it commonly occurs as (sometimes only small) bodies embedded in country rocks. If this were true, the common eclogite would show a mid-ocean ridge basalt (MORB) - signature and an early pressure ( $p$ ) - temperature ( $T$ ) evolution characterised by a more or less steady increase of both  $p$  and  $T$  starting from very-low metamorphic grade. However, many exceptions exist which do not fulfil these characteristics (see, e.g. Rowley et al. 1997; Jahn 1998; Jahn et al. 2001 for the MORB signature and Moore and Blake 1989; Oh and Liou 1990; Li and Massonne 2016; Petrie et al. 2016; Li et al. 2017 for the early  $p$ - $T$  evolution). Consequently, an eclogite must carefully be investigated before conclusions, such as “subducted oceanic crust”, can be drawn.

In this study, we demonstrate such detailed investigations on three eclogite bodies from the Münchberg Metamorphic Complex (MMC), which had intensively petrologically and geochemically been studied in the past (e.g. Matthes 1978; Gebauer and Grünenfelder 1979; Klemm 1989; Stosch and Lugmair 1990; Hammerschmidt and Franz 1992; O'Brien 1993). However, the methods of geochemical analytics and their evaluation have been improved during the last decades. Thus, it is justified to revisit these eclogites as they play an important role in understanding the early evolution of the Variscan orogeny in central Europe (see Massonne and O'Brien 2003; Klemm 2010). For this revision, fresh eclogite samples of the MMC were analysed with inductively coupled plasma - mass spectrometry + X-ray fluorescence (ICP-MS + XRF) spectrometry. In addition, the minerals in these rocks were petrologically investigated with an Electron Microprobe (EMP). The metamorphic evolution was modelled with the computer programme package PERPLE\_X. The resulting prograde segments of the  $p$ - $T$  paths are characterised by a nearly isothermal pressure increase. Thus, a simple subduction of oceanic crust can be excluded. However, the geochemical character of the studied eclogites is that of MORBs as already suggested for the eclogite from the Weißenstein hill (Stosch and Lugmair 1990). We present geodynamic reasons to explain the above findings.

## 6.2 Geological Setting

The MMC forms an oval-shaped complex (about  $25 \times 15 \text{ km}^2$ ), which is located in north-eastern (NE) Bavaria (Fig. 6.1) and, thus, at the north-western edge of the Bohemian Massif (in the Saxo-Thuringian Zone (STZ)). The metamorphism of the MMC took place during the early Variscan orogeny in Palaeozoic times (Gebauer and Grünenfelder 1979; Kreuzer et al. 1989, 1993; Stosch and Lugmair 1990; Hammerschmidt and Franz 1992). This orogeny resulted from the north-westward movement of Gondwana (or Peri-Gondwanan terranes) and its collision with Laurussia (Laurentia + Baltica) to form Pangaea (Franke 1989; Massonne and O'Brien 2003; Linnemann 2004; Massonne 2005; Linnemann and Romer 2010; Arenas et al. 2014).

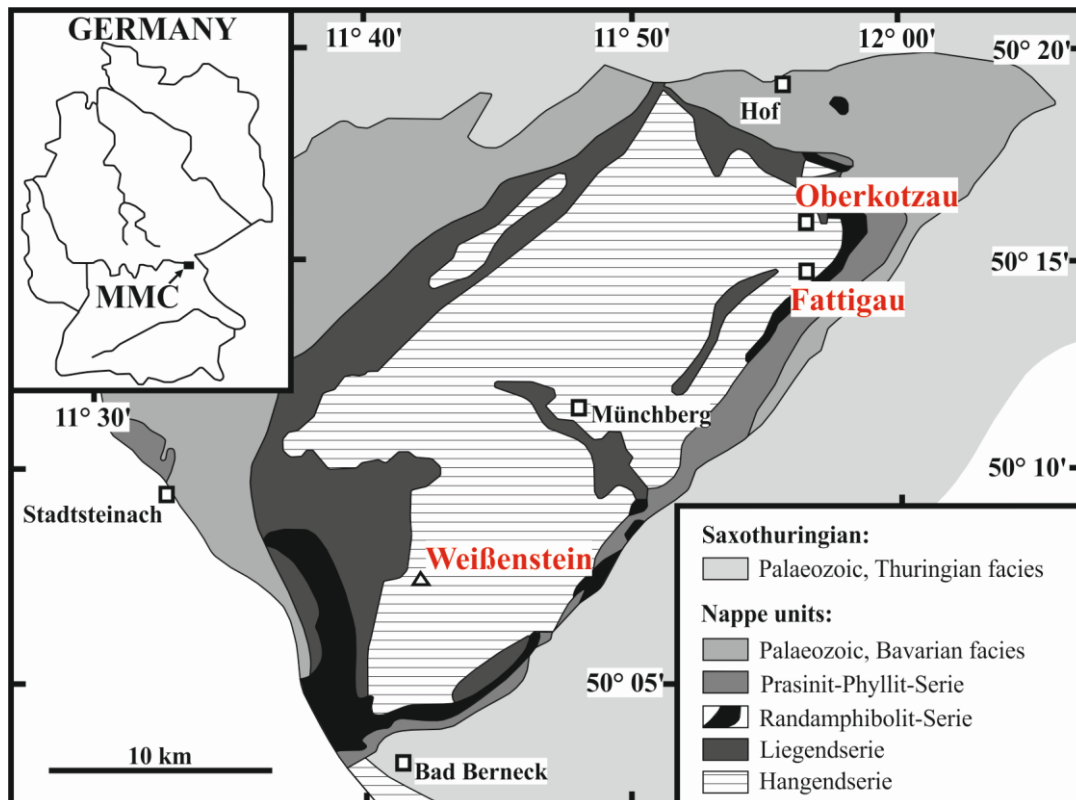


**Fig. 6.1:** Simplified geological map of the Münchberg Metamorphic Complex (MMC) in NE Bavaria (Germany), modified after Klemd et al. (1994). The locations of the studied samples are highlighted.

The MMC (see also sections 4.2 and 5.2) is regarded as a nappe pile transported on top of autochthonous, anchi-metamorphic Palaeozoic sequences of the Thuringian lithofacies, as exposed in the south-eastern Frankenwald, in the Lower Carboniferous (Franke 1984; Klemd et al. 1994). This nappe pile is subdivided from the bottom to the top into the following units: Prasinit-Phyllit (greenschist-facies metavolcanic and metasedimentary rocks), Rand-

Amphibolit (amphibolites), Liegendserie, and Hangendserie (e.g. Stettner 1960a; Kreuzer et al. 1989; Okrusch et al. 1990). Amphibolite-facies ortho- and paragneisses dominate the Liegendserie unit. The Hangendserie unit contains similar gneisses, but also eclogite bodies (e.g. Stosch and Lugmair 1990; O'Brien 1993; Klemd et al. 1994) including the studied ones.

The MMC is well known for its eclogites with omphacite records dating from the beginning of the 19th century (see Godard 2001). One of the first who had studied the eclogites from the MMC was Düll (1902). Detailed mineralogical studies followed later (e.g. Matthes et al. 1975; Matthes 1978). The peak  $p$ - $T$  conditions of the eclogites from the MMC were estimated by several studies. For example, Matthes (1978) assumed minimum values of 5 - 6 kbar and  $550 \pm 50$  °C for the eclogitisation. Franz et al. (1986) published minimum values of 13 - 17 kbar and  $620 \pm 50$  °C, solely studying the Weißenstein eclogite body. Klemd (1989) estimated that the eclogite formation occurred under water-saturated conditions at pressures between 20 and 26 kbar and temperatures ranging between 590 and 660 °C. Okrusch et al. (1990) calculated minimum values of 14.5 kbar (600 °C) to 17 kbar (700 °C). Similar minimum values of 15 kbar and  $600 \pm 30$  °C were obtained by Klemd et al. (1991) for the eclogitisation. O'Brien (1993) received minimum values of  $14.3 \pm 1$  kbar and  $650 \pm 60$  °C for the same event. Klemd et al. (1994) reported pressures above 31 kbar and temperatures in the range of 630 °C for the metamorphism of MMC eclogites. In summary, Massonne and O'Brien (2003) reported that the peak  $p$ - $T$  conditions for the eclogites cluster in the  $p$ - $T$  range of 20 - 34 kbar and 550 - 750 °C. Peak  $p$ - $T$  conditions ranging from 23 kbar and  $\geq 680$  °C to 31 kbar and 750 °C were published by Liebscher et al. (2007), who assumed that the Weißenstein eclogite body from the MMC has partially been melted at these conditions.

In contrast to the eclogites, little is known about the gneisses of the MMC. A peak  $T$  range of 630 - 670 °C was assumed by Vollbrecht et al. (2006). Blümel (1986) reported a medium- $p$  event for the Hangendserie unit at about 8 kbar and c. 610 °C with a subsequent mylonitisation. Klemd (2010) estimated  $p$ - $T$  conditions of 6 - 10 kbar and  $620 \pm 30$  °C for the metasedimentary rocks of the same unit. In section 4, a paragneiss from the Liegendserie unit was studied. This rock was exposed to an anti-clockwise  $p$ - $T$  path, reaching peak metamorphic conditions at 12.5 kbar and 670 °C.

Various authors using different geochronological methods accomplished age dating. Gebauer and Grünenfelder (1979) determined U-Pb ages on zircon from the Weißenstein eclogite body (Fig. 6.1) and related them to the eclogitisation of the studied rocks ( $380 + 14 / - 22$  Ma (two-sigma:  $2\sigma$ )) and their protoliths ( $525 + 40 / - 31$  Ma). Kreuzer et al. (1989) reported a wider age

range for the metamorphism (410 - 345 Ma), applying the K-Ar method to biotite, hornblende, and muscovite from all four units of the MMC, including the Hangendserie unit. Sm-Nd isochrons (clinopyroxene-amphibole-garnet) and K-Ar ages (amphibole and mica) on the MMC eclogites gave a high-pressure (HP: > 10 kbar) metamorphic age of 395 - 380 Ma, followed by amphibolite facies metamorphism at 380 - 365 Ma (Stosch and Lugmair 1990). A whole-rock Sm-Nd isochron ( $480 \pm 23$  Ma) was obtained by Stosch and Lugmair (1990) and interpreted as a protolith age. Ar-Ar plateau and isochron ages, determined on phengites from the Weißenstein and Oberkotzau eclogites, yielded  $365 \pm 7$  Ma (Hammerschmidt and Franz 1992). Kreuzer et al. (1993) obtained an age of  $379 \pm 1$  Ma (Ar-Ar plateau and K-Ar isochron), studying muscovite and hornblende of eclogites from the Hangendserie unit. The above ages clearly point to major Middle to Late Devonian metamorphic events during the early Variscan orogeny in the MMC (Massonne and O'Brien 2003). Such events were found to have also occurred in other crystalline complexes of the Bohemian Massif (see, e.g. Beard et al. 1995; O'Brien et al. 1997; Bröcker et al. 1998; Kröner and Willner 1998; Kryza and Pin 2002; Timmermann et al. 2004), such as the Zone of Erbendorf-Vohenstrauß, the Frankenberg and Wildenfels Nappes, the Góry Sowie Block (GSB; Owl Mountains) and the Mariánské Lázně Complex (MLC; see sections 3.1-3.2; 4.2; 5.2).

Our eclogite samples from the MMC, which had already been mapped in detail a long time ago (see Geological Map of Bavaria 1:25000 such as sheets No. 5737 Schwarzenbach a.d.sächs.Saale and No. 5836 Münchberg), were taken from loose blocks at the Weißenstein hill (sample 13Mm1; N  $50.1301^\circ$  / E  $11.6969^\circ$ , WGS 84), an abandoned quarry at the western periphery of the village of Fattigau (13Mm7\_2; N  $50.2461^\circ$  / E  $11.9363^\circ$ ), and a former quarry wall at the northern outskirts of the town of Oberkotzau (MüMa03\_3c; N  $50.2722^\circ$  / E  $11.9169^\circ$ , now completely covered). Details of these sampling sites were reported by Okrusch et al. (1990).

### 6.3 Analytical Procedures

For the determination of the bulk-rock composition (see also sections 3.3, 4.3 and 5.3), a representative portion (volume c.  $10 \times 5 \times 2$  cm<sup>3</sup>) of the rock was crushed and subsequently ground with a tungsten carbide dish-and-puck mill. The obtained rock powder was either fused with lithium borate (66 wt% Li<sub>2</sub>B<sub>4</sub>O<sub>7</sub> and 34 wt% LiBO<sub>2</sub>) in an optimised mass ratio of 1:6 to prepare a glass disk or mixed with the wax C<sub>38</sub>H<sub>76</sub>N<sub>2</sub>O<sub>2</sub> (mass ratio 4:1) to press a tablet. Disk and tablet were analysed for major and trace elements, respectively, with a Panalytical PW 2400

XRF spectrometer, considering certified geostandards. Moreover, the rock powder was also used to determine the total carbon (as CO<sub>2</sub>) and water contents, using a LECO<sup>®</sup> RC-412 elemental analyser, based on IR techniques.

After XRF analyses, the prepared glass disks were further ablated by a Cetac LSX-213 laser connected to an AGILENT SERIE 7700 ICP-MS (LA ICP-MS) to additionally determine trace element contents. The following conditions were applied: the laser energy was regulated to 20 %, the beam size was set to 150 µm and 450 shots per spot were fired with a frequency of 20 Hz. With a gas mixture consisting of 300 ml/min of helium and 800 ml/min of argon transporting the ablated material, the plasma torch of the mass spectrometer was operated at an argon flow of 15 l/min. DLH 7 and DLH 8 from P&H Developments Ltd. as well as NIST 612 reference glasses were used for the calibration of the instrument under the same experimental conditions as applied to the eclogite samples under investigation. Silicon, the concentration of which had been determined by XRF spectrometry, was employed as an internal standard element. The obtained results were verified by analysing lithium borate glass disks prepared from the geostandards Diorite (DR-N) and Zinnwaldite (ZW-C), provided by the Service d'Analyse des Roches et des Minéraux (SARM), part of the Centre National de Recherche Scientifique (CNRS). In addition, the MLS-ETHOS plus microwave lab system was employed to dissolve rock powder in a mixture of HF, HCl and HNO<sub>3</sub> at elevated pressures and temperatures. The resulting liquids (1.5 vol% HNO<sub>3</sub> / HCl, approximate dilution of the rock = 1:1000) were analysed with the AGILENT SERIE 7700 ICP-MS (liquid ICP-MS).

According to the analytical procedure described by Massonne (2012), carbon-coated thin sections (area c. 2 × 4 cm<sup>2</sup>) were employed to analyse the compositions of minerals, such as garnet, mica, and rutile, using a CAMECA SX100 EMP with five wavelength-dispersive (WD) spectrometers (see also sections 3.3, 4.3 and 5.3). For silicates (+ ilmenite), the concentrations of F, Na, Mg, Al, Si, K, Ca, Ti, Cr, Mn, Fe and Ba (ignored for ilmenite) were determined, using counting times of 20 s at the peak and on the background. Synthetic and natural minerals, glasses (e.g. Ba glass for the BaL $\alpha$ 1-peak), and pure oxides were used as standards. The applied acceleration voltage and beam current were 15 kV and 15 nA, respectively. The beam diameter was approximately 3 µm. The PaP correction procedure provided by CAMECA was applied. Analytical errors of the applied method were reported by Massonne (2012).

The analysis of rutile with the EMP for the Zr-in-rutile thermometry was achieved for Si, Cr, Fe, Zr, and Nb (Ti was calculated). The beam current and acceleration voltage were set to 100

nA and 15 kV, respectively. The counting time for the Zr  $L\alpha$ -radiation at the peak and the background was 100 s each. Natural zircon was used as a standard for this radiation.

In order to recognise zoning patterns of garnet and potassic white-mica, element concentration maps for major elements were prepared by step-wise movement of a thin section under the electron beam of the EMP (step scanning) and subsequent computer-aided evaluation. For the mapping, counting times per step of 100 ms were applied. The electric current was either 70 nA (garnet) or 25 nA (mica).

Backscattered electron (BSE) images were prepared with the EMP, for instance, to document specific textural relations. For the calculation of structural formulae of minerals and the content of molar fractions of mineral components (e.g.  $X(\text{Ca})$  and  $X(\text{Mg})$  = molar fractions of the garnet components grossular (+ andradite) and pyrope, respectively) from EMP analyses, the computer programme CALCMIN (Brandelik 2009) was used.

#### 6.4 Mineral Compositions and Textures

The studied eclogites (for their bulk-rock compositions see Tabs. 6.1 and 8.5) are hardly foliated. They are fine- to medium-grained and fairly equigranular (see Fig. 6.2).

**Tab. 6.1:** Bulk-rock composition of eclogite sample 13Mm1 from the Münchberg Metamorphic Complex (MMC), obtained with XRF, liquid ICP-MS, and LA ICP-MS. XRF results were modified for PERPLE\_X calculations as explained in the text. Abbreviation: \* = same content as determined with XRF.

Constituent	XRF	modified	liquid ICP-MS	LA ICP-MS
Na <sub>2</sub> O / wt%	2.747	2.600		
MgO / wt%	7.902	7.481		
Al <sub>2</sub> O <sub>3</sub> / wt%	14.084	13.335		
SiO <sub>2</sub> / wt%	49.121	46.509		*
P <sub>2</sub> O <sub>5</sub> / wt%	0.138			0.147
K <sub>2</sub> O / wt%	0.099	0.093		0.096
CaO / wt%	11.711	10.916		
TiO <sub>2</sub> / wt%	1.583	1.498		1.645
MnO / wt%	0.205	0.194		
Fe <sub>2</sub> O <sub>3</sub> / wt%	13.018			
FeO / wt%		11.091		
O <sub>2</sub> / wt%		0.123		
H <sub>2</sub> O / wt%		6.154		
SUM / wt%	98.181	100.000		
Cr / ppm	123		125.2	
Ni / ppm	25		29.4	
Rb / ppm	0.8		1.4	1.4
Sr / ppm	99		114.6	116.5
Y / ppm	32		27.0	32.8
Zr / ppm	71		26.9	110.8
Nb / ppm	12		5.3	5.6
Ba / ppm	30		15.9	15.2
La / ppm			5.4	6.4
Ce / ppm	25		15.7	17.3
Pr / ppm			2.4	3.0
Nd / ppm	11		12.5	14.9
Sm / ppm	3.9		3.6	4.4
Eu / ppm			1.3	1.3
Gd / ppm			4.6	5.3
Tb / ppm			0.8	0.9
Dy / ppm			5.4	5.7
Ho / ppm			1.1	1.3
Er / ppm			3.2	4.0
Tm / ppm			0.5	0.6
Yb / ppm			3.2	3.9
Lu / ppm			0.5	0.6
Hf / ppm			1.0	3.4
Ta / ppm	1.4		1.8	0.5
Th / ppm			0.4	0.5

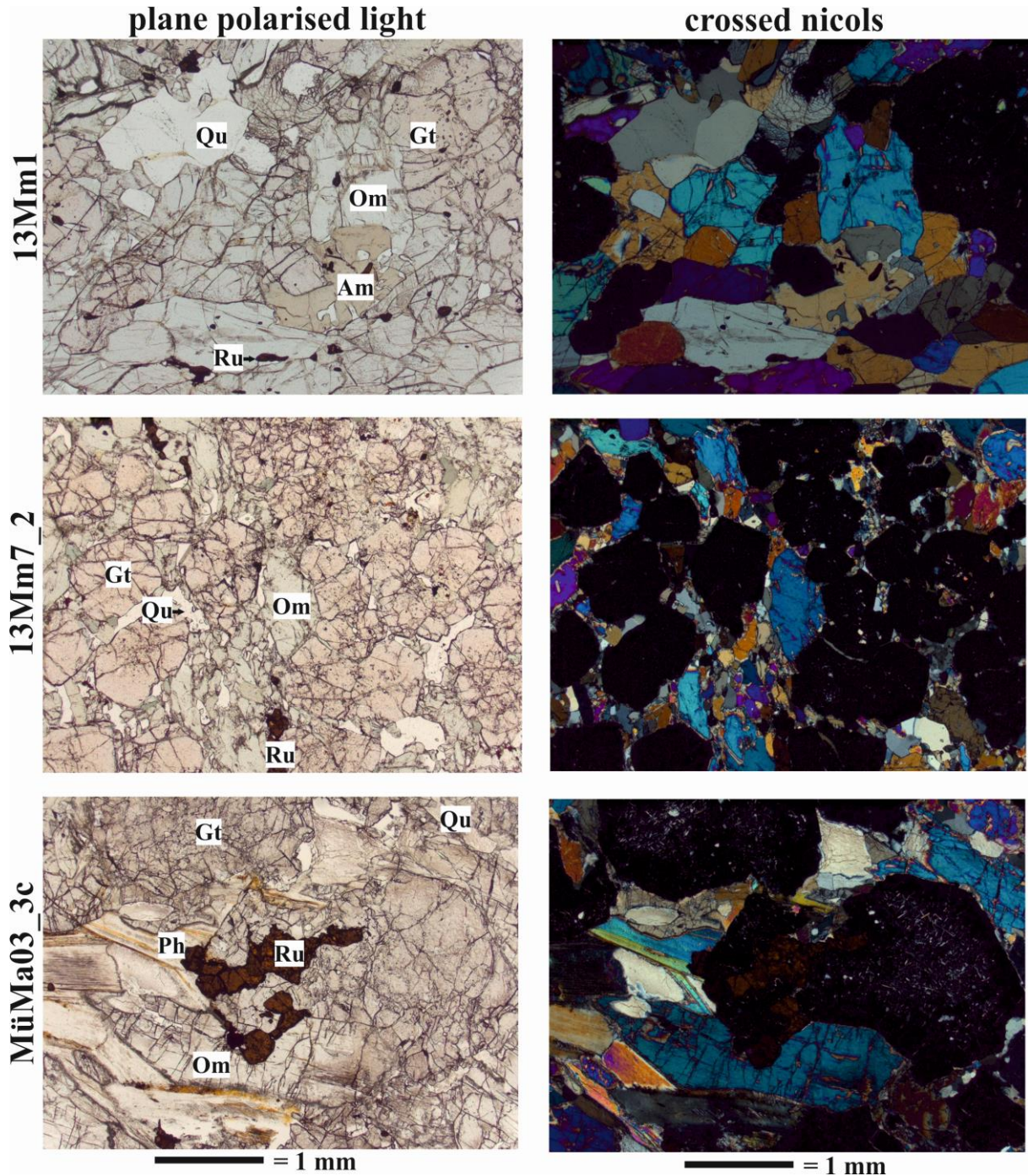


**Fig. 6.2:** Photomicrographs of objects in thin sections of the studied eclogites seen under plane polarised light and crossed nicols with a ZEISS Axioplan: Am = amphibole, Gt = garnet, Om = omphacite, Ph = potassic white-mica, Qu = quartz, Ru = rutile.

#### 6.4.1 Eclogite 13Mm1

Sample 13Mm1 contains omphacite (45 vol% as determined with Adobe Photoshop CC; version 2017.0.0; for the procedure see section 4), garnet (39 vol% after subtraction of inclusions), quartz (12 vol%), amphibole (3 vol%), and rutile (1 vol%). Allanite-clinozoisite-

epidote, ilmenite, plagioclase, potassic white-mica, titanite, zircon and diverse sulphides are accessory minerals, which partially resulted from retrograde metamorphic processes.

Garnet grains, exhibiting subhedral shapes, are as large as 3 mm and show a continuous chemical change from the core to the rim: Ca decreases, Mg increases, whereas Mn and Fe remain constant (Figs. 6.3 and 6.4, Tab. 6.2) (see also O'Brien 1993). The composition of the average garnet core of sample 13Mm1 is characterised by about 49 mol% almandine (Alm), 29 mol% grossular (+ andradite: GrAn), 21 mol% pyrope (Py), and 1 mol% spessartine (Sp) components ( $\text{Alm}_{49}\text{GrAn}_{29}\text{Py}_{21}\text{Sp}_1$ ). The average composition of the garnet rim is  $\text{Alm}_{51}\text{GrAn}_{22}\text{Py}_{26}\text{Sp}_1$ .

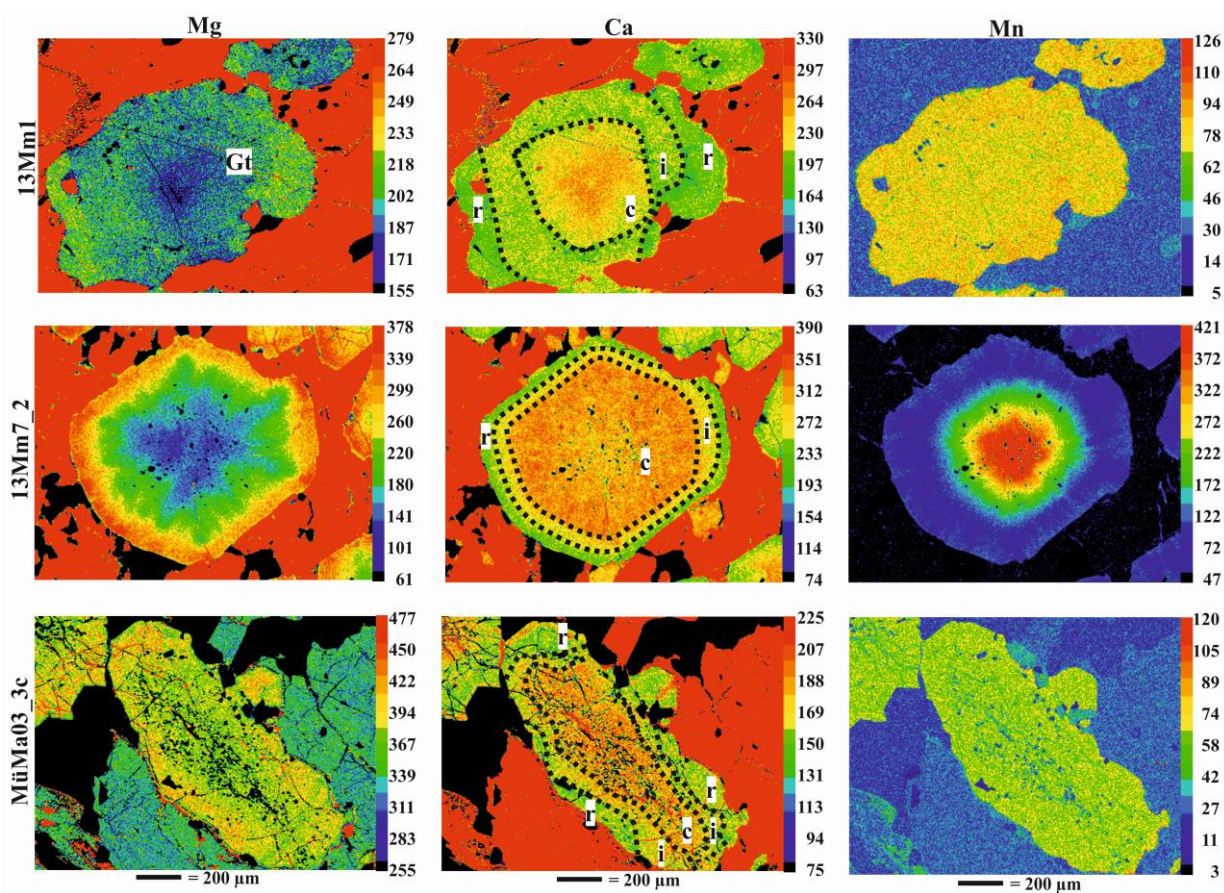


**Fig. 6.3:** Elemental maps (Mg, Ca and Mn) of garnet (Gt) grains in the studied eclogites, obtained with a CAMECA SX100 EMP. The scales for the colour code on the right hand side of each image refer to counts of X-ray radiation per time unit: c = core, i = intermediate, r = rim.

The size of rare potassic white-mica grains varies between 20 and 400 μm. They usually occur in the rock matrix with anhedral shapes. Elemental mapping of several mica grains resulted in

the following zonation pattern (Fig. 6.5): Compared to a thin rim domain, the extended core region is slightly enriched in Mg. The Mg concentrations are directly correlated to the Si contents due to Tschermak's substitution ( $\text{Mg} + \text{Si} = 2 \text{Al}$ ). The depletion of Mg at the rim is accompanied by a slight increase in Na. The Si contents in potassic white-mica range between 3.41 and 3.47 per formula unit (pfu) in the core and between 3.24 and 3.37 pfu in the rim (Tab. 6.3). Similar values have been reported by Franz et al. (1986) for phengite in an eclogite sample from the Weißenstein hill.

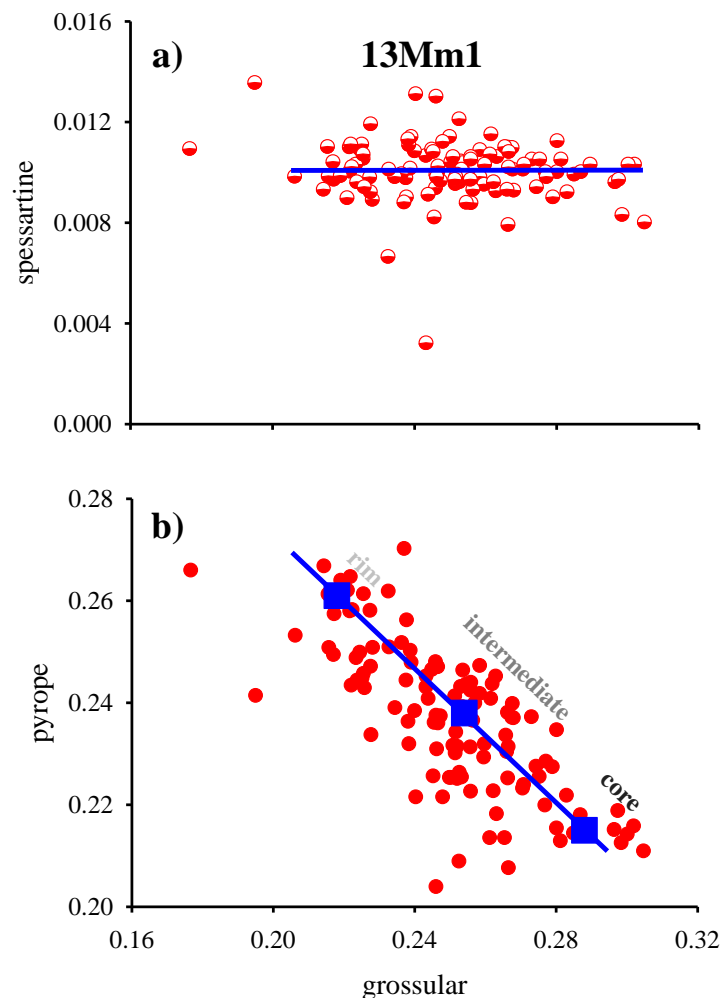


**Fig. 6.4:** Garnet analyses of sample 13Mm1, obtained with a CAMECA SX100 EMP, in terms of molar fractions of spessartine (a) and pyrope (b) versus that of grossular (+ andradite). The solid lines show chemical trends from core to rim compositions of garnet.

Rutile of sample 13Mm1 is enclosed in the core area of garnet and occurs in the matrix with variable size (10  $\mu\text{m}$  - 1 mm). Forty-one analyses of rutile yielded Zr contents between 66 and

265 ppm with no compositional difference between enclosed and matrix rutile. The average rutile composition (189 ppm Zr: Tab. 6.4) contains 0.34 wt% FeO and 0.05 wt% Nb<sub>2</sub>O<sub>5</sub>. Locally, ilmenite occurs in rutile as an inclusion and contains on average 4 mol% geikielite and 1 mol% pyrophanite components (Tab. 8.6).

Most omphacite is anhedral and its size varies between 0.2 and 1 mm. Locally, a fine-grained symplectite of plagioclase and amphibole occurs around omphacite. A clear zoning pattern could not be recognised. On average, omphacite contains 48 mol% diopside, 11 mol% hedenbergite, 40 mol% jadeite and < 1 mol% aegirine. The Na contents pfu vary between 0.34 and 0.43 (Tab. 6.5).

**Tab. 6.2:** Representative analyses (in wt%) of garnet from sample 13Mm1 of the Münchberg Metamorphic Complex (MMC), obtained with a CAMECA SX100 EMP. The structural formulae were calculated as follows: 24 oxygen (double formula unit) and cation sum of Al + Ca + Cr + Fe + Mg + Mn + Na = 10. Abbreviations: calc = calculated, inter = intermediate.

Mineral	Garnet					
	Sample	13Mm1-gt6-18	13Mm1-gt6-19	13Mm1-gt6-8	13Mm1-gt6-9	13Mm1-gt6-6
Comment	rim	rim	inter	inter	core	core
SiO <sub>2</sub>	38.09	38.15	37.96	37.88	37.92	37.92
TiO <sub>2</sub>	0.05	0.05	0.06	0.07	0.07	0.15
Al <sub>2</sub> O <sub>3</sub>	22.46	22.03	22.28	22.42	22.44	21.89
Cr <sub>2</sub> O <sub>3</sub>	0.03	0.04	0.05	0.04	0.04	0.02
Fe <sub>2</sub> O <sub>3</sub> calc	0.00	0.39	0.32	0.33	0.00	0.35
FeO	24.25	23.69	23.48	23.75	22.75	22.55
MnO	0.44	0.31	0.68	0.50	0.78	0.83
MgO	6.63	6.61	6.10	6.47	5.10	5.09
CaO	8.25	8.81	9.75	9.41	11.52	11.12
Na <sub>2</sub> O	0.00	0.04	0.02	0.02	0.04	0.03
Total	100.21	100.12	100.69	100.88	100.64	99.93
Si	5.782	5.803	5.723	5.676	5.730	5.819
Ti	0.006	0.006	0.006	0.008	0.008	0.018
Al	4.019	3.951	3.958	3.959	3.996	3.958
Cr	0.004	0.005	0.006	0.004	0.005	0.002
Fe <sup>3+</sup>	0.000	0.044	0.036	0.037	0.000	0.040
Fe <sup>2+</sup>	3.079	3.014	2.960	2.976	2.876	2.893
Mg	1.501	1.500	1.371	1.445	1.149	1.163
Ca	1.341	1.435	1.575	1.511	1.865	1.828
Mn	0.056	0.040	0.087	0.063	0.100	0.107
Na	0.000	0.011	0.007	0.006	0.010	0.008

Amphibole in the rock matrix shows subhedral shapes with sizes of 0.5 - 1 mm. The following zonation pattern was noted: Contents of Mg (1.94 - 2.92 pfu) and K (0.07 - 0.11 pfu) decrease and contents of (calculated)  $\text{Fe}^{2+}$  (0.99 - 1.51 pfu) increase from the core to the rim. Concentrations of Ca (c. 1.52 pfu) and Na (c. 1.07 pfu) remain constant throughout the grains. The Si contents range between 6.13 (rim) and 7.06 (core) pfu (Fig. 8.4, Tab. 6.6).

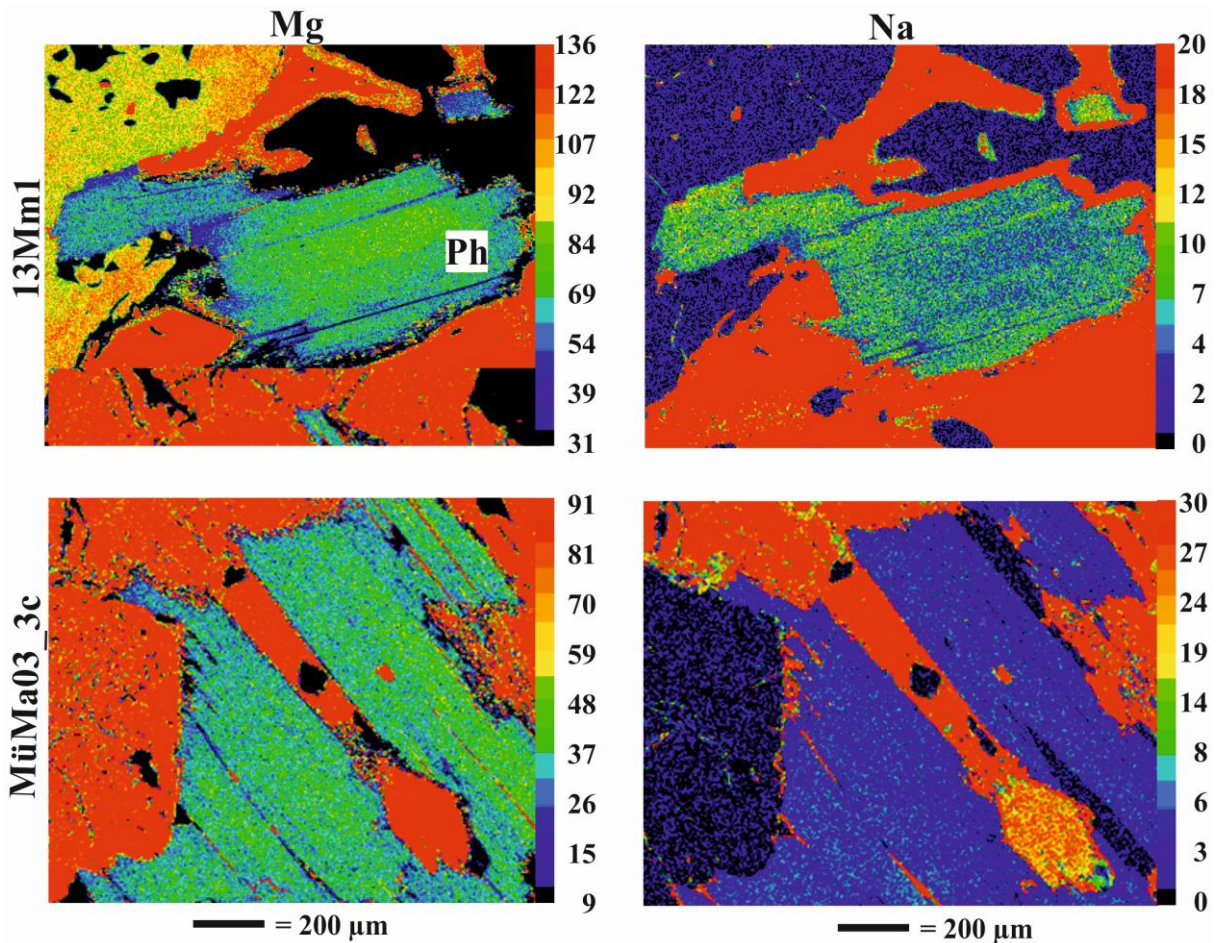


**Fig. 6.5:** Elemental maps (Mg and Na) of potassic white-mica (Ph) grains in the studied eclogites, obtained with a CAMECA SX100 EMP. The scales for the colour code on the right hand side of each image refer to counts of X-ray radiation per time unit.

Inclusions in garnet are preferentially located in its core and intermediate domains. The minerals enclosed in these domains are amphibole, apatite, clinozoisite-epidote, omphacite, plagioclase, quartz, rutile, titanite, zircon, zoisite and various copper-iron sulphides (Tabs. 6.5, 6.6 and 8.6). The chemical compositions of enclosed rutile (< 10 μm), occurring as elongated columns to needles that form clusters as large as 1 mm in garnet, are similar to those of matrix rutile (see above). Several multiphase inclusions with sizes between 250 and 500 μm, which

are of importance to understand the early metamorphic evolution, were noted to occur in garnet of a single thin section (see Fig. 8.5). These large inclusions are frequently surrounded by cracks. However, many different combinations of coexisting minerals were also observed in small bimineralic inclusions without cracks in the host garnet. According to the inclusions in the garnet core, early amphibole occurred together with quartz, plagioclase, omphacite, titanite, ilmenite, rutile, and apatite. Furthermore, omphacite was observed to have coexisted with clinozoisite-epidote, but not with plagioclase, titanite and ilmenite. In addition, an inclusion with omphacite + quartz + idiomorphic garnet of 20  $\mu\text{m}$  diameter, showing the composition  $\text{Alm}_{48.5}\text{GrAn}_{30}\text{Py}_{20}\text{Sp}_{1.5}$  (Tab. 8.7), was found. This garnet could be pristine early garnet. On average, enclosed omphacite, which shows sizes between 20 and 350  $\mu\text{m}$ , contains 47 mol% diopside, 10 mol% hedenbergite, 38 mol% jadeite, and < 1 mol% aegirine comparable to matrix omphacite. The Na contents pfu lie between 0.36 and 0.40.

**Tab. 6.3:** Representative analyses (in wt%) of potassic white-mica from eclogite samples 13Mm1, 13Mm7\_2 and MüMa03\_3c of the Münchberg Metamorphic Complex (MMC), obtained with a CAMECA SX100 EMP. The structural formulae were calculated as follows: 22 oxygen (double formula unit). For all micas the total was corrected for F. Abbreviations: calc = calculated, Gt = garnet.

Mineral	Potassic white-mica					
	Sample	13Mm1- ms1-2	13Mm1- ms1-8	13Mm1- ms1-16	13Mm7_ 2-ms1-1	MüMa03_3c -ms1-4
Comment	rim	intermediate	core			enclosed in Gt
SiO <sub>2</sub>	50.77	51.91	53.76	51.55	48.88	54.60
TiO <sub>2</sub>	0.90	0.81	0.76	0.50	0.56	0.04
Al <sub>2</sub> O <sub>3</sub>	30.67	28.22	26.08	28.68	27.05	26.72
FeO	1.54	1.75	1.55	2.00	1.02	2.28
MgO	2.50	3.37	4.33	3.38	3.94	3.40
Na <sub>2</sub> O	0.75	0.64	0.35	0.76	0.46	0.17
K <sub>2</sub> O	9.79	9.45	9.67	9.77	10.73	10.04
BaO	0.21	0.16	0.19	0.18	0.27	0.20
H <sub>2</sub> O <sub>calc</sub>	4.63	4.61	4.64	4.60	4.37	4.67
Total	101.76	100.99	101.35	101.44	97.28	102.33
Si	6.576	6.751	6.947	6.713	6.703	7.014
Ti	0.088	0.080	0.074	0.049	0.058	0.004
Al	3.259	3.078	2.918	3.114	3.074	3.060
Fe <sup>2+</sup>	0.167	0.190	0.168	0.218	0.117	0.245
Mg	0.483	0.653	0.834	0.656	0.805	0.651
Na	0.188	0.162	0.087	0.193	0.122	0.042
K	1.618	1.568	1.595	1.623	1.877	1.645
Ba	0.011	0.008	0.010	0.009	0.015	0.010

**Tab. 6.4:** Representative analyses (in wt%) of rutile from eclogite samples 13Mm1, 13Mm7\_2 and MüMa03\_3c of the Münchberg Metamorphic Complex (MMC), obtained with a CAMECA SX100 EMP. The structural formula of rutile is based on two oxygen anions.

Oxides in wt%	13Mm1-ru1-2	13Mm1-ru2-3	13Mm1-ru4-1	13Mm1-ru7-4	13Mm1-ru9-4	13Mm7_2-rt3-2	MüMa03_3c-rt4-1
TiO <sub>2</sub>	99.53	99.49	99.49	99.57	99.55	99.34	99.71
SiO <sub>2</sub>	0.00	0.00	0.00	0.00	0.00	0.00	0.00
Nb <sub>2</sub> O <sub>5</sub>	0.07	0.05	0.06	0.06	0.05	0.08	0.12
FeO	0.32	0.39	0.37	0.32	0.30	0.57	0.17
ZrO <sub>2</sub>	0.04	0.03	0.03	0.02	0.03	0.04	0.04
Total	99.95	99.96	99.94	99.96	99.93	100.02	100.03
Ti	0.9958	0.9952	0.9954	0.9960	0.9962	0.9930	0.9972
Si	0.0000	0.0000	0.0000	0.0000	0.0000	0.0000	0.0000
Nb	0.0004	0.0003	0.0003	0.0003	0.0003	0.0005	0.0070
Fe	0.0036	0.0043	0.0041	0.0035	0.0034	0.0063	0.0019
Zr	0.0002	0.0002	0.0002	0.0001	0.0002	0.0002	0.0002

**Tab. 6.5:** Representative analyses (in wt%) of omphacite from eclogite samples 13Mm1, 13Mm7\_2 and MüMa03\_3c of the Münchberg Metamorphic Complex (MMC), obtained with a CAMECA SX100 EMP. The structural formula of omphacite is based on four cations and six oxygen. Abbreviations: calc = calculated, Gt = garnet.

Mineral	Omphacite				
Sample	13Mm1-gt1-e3-6	MüMa03_3c-gte32	13Mm1-om1-1	13Mm7_2-om1-1	MüMa03_3c-om1-1
Comment	enclosed in Gt				
SiO <sub>2</sub>	56.16	54.73	55.63	54.47	54.84
TiO <sub>2</sub>	0.13	0.10	0.13	0.08	0.09
Al <sub>2</sub> O <sub>3</sub>	10.08	9.86	10.07	9.15	9.59
Cr <sub>2</sub> O <sub>3</sub>	0.00	0.00	0.00	0.00	0.00
Fe <sub>2</sub> O <sub>3calc</sub>	0.00	1.61	0.00	4.40	0.11
FeO	3.49	0.84	3.55	1.64	2.07
MnO	0.00	0.02	0.03	0.00	0.06
MgO	9.98	11.21	8.94	9.29	10.81
CaO	15.51	16.73	15.23	14.86	16.93
Na <sub>2</sub> O	5.63	4.93	5.95	6.03	4.87
K <sub>2</sub> O	0.00	0.12	0.00	0.00	0.01
Total	100.99	100.15	99.54	99.92	99.34
Si	1.980	1.942	1.991	1.955	1.963
Ti	0.003	0.003	0.003	0.002	0.003
Al	0.398	0.355	0.416	0.342	0.368
Cr	0.000	0.000	0.000	0.000	0.000
Fe <sup>3+</sup>	0.000	0.043	0.000	0.119	0.003
Fe <sup>2+</sup>	0.103	0.025	0.106	0.049	0.062
Mg	0.525	0.593	0.477	0.497	0.577
Ca	0.586	0.636	0.584	0.571	0.649
Mn	0.000	0.001	0.001	0.000	0.001
Na	0.385	0.340	0.413	0.420	0.338
K	0.000	0.006	0.000	0.000	0.000

**Tab. 6.6:** Representative analyses (in wt%) of amphibole from eclogite samples 13Mm1, 13Mm7\_2 and MüMa03\_3c of the Münchberg Metamorphic Complex (MMC), obtained with a CAMECA SX100 EMP. The structural formula of amphibole is based on 13 cations and 23 oxygen. Abbreviations: calc = calculated, Gt = garnet.

Mineral	Amphibole				
	Sample	13Mm1- gte-30-8	MüMa03_ 3c-gte-23	13Mm1- am1-1	13Mm7_2 -am1-2
Comment	enclosed in Gt				
SiO <sub>2</sub>	44.73	45.70	46.20	45.15	50.14
TiO <sub>2</sub>	0.68	0.14	0.53	0.32	0.29
Al <sub>2</sub> O <sub>3</sub>	15.52	17.64	14.36	11.20	10.9
Cr <sub>2</sub> O <sub>3</sub>	0.00	0.00	0.00	0.00	0.00
Fe <sub>2</sub> O <sub>3</sub> <sub>calc</sub>	1.77	0.00	0.00	7.19	2.82
FeO	8.70	7.13	8.93	3.85	2.03
MnO	0.09	0.06	0.03	0.00	0.02
MgO	12.07	10.45	12.42	14.06	17.62
CaO	9.60	7.69	9.65	8.82	10.35
Na <sub>2</sub> O	3.81	3.48	3.90	3.45	2.59
K <sub>2</sub> O	0.56	2.48	0.57	0.54	0.51
BaO	0.00	0.07	0.00	0.00	0.00
H <sub>2</sub> O <sub>calc</sub>	2.08	2.03	2.07	2.03	2.15
Total	99.60	96.86	98.67	96.62	99.42
Si	6.446	6.737	6.708	6.656	6.986
Ti	0.073	0.016	0.058	0.035	0.030
Al	1.554	1.263	1.292	1.344	1.014
Cr	0.000	0.000	0.000	0.000	0.000
Fe <sup>3+</sup>	0.192	0.000	0.000	0.798	0.295
Fe <sup>2+</sup>	1.048	0.879	1.084	0.475	0.236
Mg	2.593	2.296	2.688	3.091	3.660
Ca	1.483	1.214	1.502	1.393	1.545
Mn	0.010	0.008	0.004	0.000	0.002
Na	1.063	0.993	1.099	0.986	0.701
K	0.103	0.466	0.106	0.102	0.091
Ba	0.000	0.004	0.000	0.000	0.000

The size of amphibole grains in the inclusions is usually between 20 and 250  $\mu\text{m}$ . Similar to amphibole in the matrix, the Ca and Na contents are fairly constant around average values of 1.52 and 1.11 pfu, respectively. However, the Si contents are generally lower than in matrix amphibole and range between 5.60 and 6.45 pfu (Fig. 8.4). Clinzoisite-epidote inclusions (< 25  $\mu\text{m}$ ) consist of about 23 mol% pistacite ( $\text{Ca}_2\text{Al}_2\text{Fe}^{3+}\text{Si}_3\text{O}_{12}\text{OH}$ ) component. Titanite (< 10  $\mu\text{m}$ ) shows low Al (0.07 pfu) and Fe (0.03 pfu) contents. Enclosed plagioclase (c. 15  $\mu\text{m}$ ) is oligoclase with c. 13 mol% anorthite.

#### 6.4.2 Eclogite 13Mm7\_2

Sample 13Mm7\_2 is composed of omphacite (46 vol%), garnet (38 vol% after subtraction of inclusions), quartz (12 vol%), amphibole (2 vol%), and rutile (1 vol%). Accessory minerals are clinzoisite-epidote, ilmenite, plagioclase, potassic white-mica, zircon and diverse sulphides.

Both samples 13Mm1 and 13Mm7\_2 belong to the dark eclogite type as defined by Matthes et al. (1975) due to the absence of kyanite (see also Stosch and Lugmair 1990).

Garnet of sample 13Mm7\_2 has got a maximum size of about 0.5 mm. It contains only few and small inclusion minerals ( $< 5 \mu\text{m}$ ) in the core domain, which are usually quartz and rarely clinzoisite-epidote with c. 54 mol% pistacite (Tab. 8.6). The chemical zonation of garnet is similarly continuous from the core to the rim as in garnet of sample 13Mm1 (Fig. 6.3, Tab. 8.7). The average composition of the garnet core and rim is  $\text{Alm}_{54.5}\text{GrAn}_{26}\text{Py}_{16.5}\text{Sp}_3$  and  $\text{Alm}_{51}\text{GrAn}_{21}\text{Py}_{27}\text{Sp}_1$ , respectively.

Potassic white-mica grains in the rock matrix are subhedral with sizes between 50 and 200  $\mu\text{m}$ . No clear zonation pattern was recognised. The Si contents in white mica (Tab. 6.3) vary only between 3.31 and 3.39 pfu.

Rutile shows elongated, subhedral shapes with sizes between 0.1 and 0.5 mm. (Bladed) ilmenite occasionally penetrates rutile probably due to exsolution (Fig. 6.6). The average composition of rutile contains 0.83 wt% FeO and 0.08 wt%  $\text{Nb}_2\text{O}_5$  (Tab. 6.4). Analysed Zr contents scatter between 119 and 300 ppm (42 analyses, mean 224 ppm).

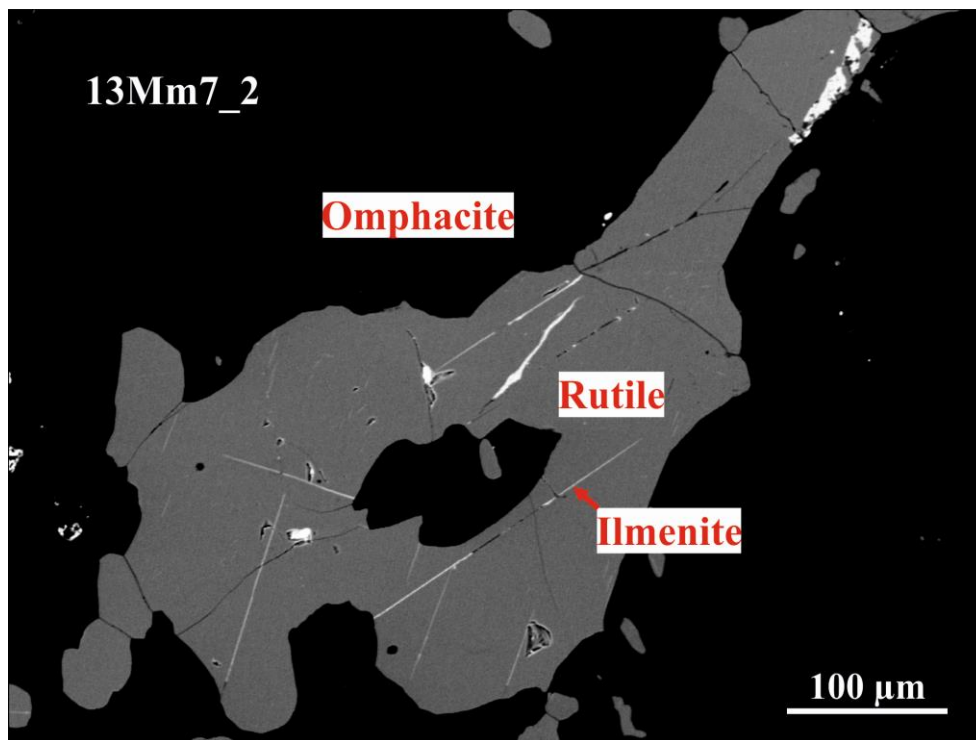


**Fig. 6.6:** Backscattered electron (BSE) image of a rutile grain of sample 13Mm7\_2, which contains small amounts of ilmenite as white lines, obtained with a CAMECA SX100 EMP.

Omphacite only occurs in the rock matrix as subhedral grains with sizes of 0.2 to 0.7 mm. It shows a slight, continuous compositional change from the core to the rim: Mg decreases, Fe and Ti increase, whereas Na and Ca remain constant. On average, omphacite contains 48 mol% diopside, 7 mol% hedenbergite, 31 mol% jadeite and 9 mol% aegirine. The Na content pfu ranges between 0.37 and 0.41 (Tab. 6.5).

Amphibole grains in the rock matrix are subhedral with sizes between 0.1 and 0.3 mm. Contents of Mg (2.85 - 3.09 pfu) and K (0.10 - 0.14 pfu) decrease and those of (calculated) Fe<sup>2+</sup> (0.46 - 0.74 pfu) and Ca (1.39 - 1.49 pfu) increase from the core to the rim. The Na contents are fairly constant around 1.00 pfu. The Si contents range between 6.44 and 6.66 pfu, which seem to be unrelated to the aforementioned core-rim relationship (Tab. 6.6).

#### 6.4.3 Eclogite MüMa03\_3c

Sample MüMa03\_3c contains omphacite (43 vol%), garnet (43 vol% after subtraction of inclusions), quartz (12 vol%), and rutile (1 vol%). Accessory minerals are amphibole, phengite, kyanite (therefore light eclogite type after Matthes et al. 1975), zoisite-clinozoisite-epidote, plagioclase, pumpellyite, and zircon, which partially resulted from retrograde metamorphic processes. However, thin sections prepared from various portions of the sample (a few kg heavy) show variable contents of phengite and kyanite (up to 3 vol% each) in the rock, which seem to be enriched in layers.

Garnet of sample MüMa03\_3c can be as large as 2.5 mm and is slightly corroded. It usually shows subhedral shapes and a moderate zonation with average compositions of the core, intermediate domain, and rim of Alm<sub>33.4</sub>GrAn<sub>20.9</sub>Py<sub>45</sub>Sp<sub>0.7</sub>, Alm<sub>33.7</sub>GrAn<sub>19.2</sub>Py<sub>46.2</sub>Sp<sub>0.9</sub> and Alm<sub>33.6</sub>GrAn<sub>17.5</sub>Py<sub>48</sub>Sp<sub>0.9</sub>, respectively (Fig. 6.3, Tab. 8.7). The core and intermediate domains are optically discernible because of abundant mineral inclusions (see below) whereas the rim domain is almost free of inclusions.

Potassic white-mica grains in the matrix are subhedral with sizes as large as 1 mm (Fig. 6.5). Locally, they are slightly curved. The Si content is fairly constant (3.32 - 3.36 pfu, Tab. 6.3). However, up to 25 µm sized phengite inclusions in garnet can show variable Si contents between 3.26 and 3.51 pfu (Tab. 6.3).

The size of anhedral rutile grains in the rock matrix is frequently in the range of 0.1 - 1 mm. The average composition of rutile is characterised by 0.15 wt% FeO and 0.11 wt% Nb<sub>2</sub>O<sub>5</sub> (Tab. 6.4). Contents of Zr scatter between 148 and 321 ppm (48 analyses, mean 241 ppm).

Omphacite in the matrix is characterised by anhedral shapes and sizes between 0.5 and 2 mm. Locally, there are fine-grained symplectites of plagioclase and amphibole around omphacite grains. No chemical core-rim zonation pattern could be detected. On average, omphacite contains 56 mol% diopside, 5 mol% hedenbergite, 32 mol% jadeite and 2 mol% aegirine. The Na content pfu is 0.32 - 0.35 (Tab. 6.5).

Subhedral amphibole in the rock matrix is as large as 1.5 mm. Even large grains do not show any clear chemical core-rim relation. Nevertheless, the Si contents were found to vary between 5.98 and 6.99 pfu (Tab. 6.6). Elemental contents pfu range within the following limits: Mg = 3.19 - 3.66, K = 0.06 - 0.09, (calculated)  $Fe^{2+}$  = 0.08 - 0.24, Ca = 1.55 - 1.66, Na = 0.70 - 0.86.

Single inclusion minerals in garnet are amphibole, apatite, clinozoisite-epidote, omphacite, potassic white-mica, rutile, kyanite, and quartz (Tabs. 6.3, 6.5, 6.6 and 8.6). The chemical compositions of enclosed rutile grains (< 10  $\mu$ m), locally forming clusters as large as 1 mm in garnet, are similar to those of matrix rutile (see above). Clusters of unoriented, needle-like kyanite (with c. 0.7 wt%  $Fe_2O_3$  and a length of < 100  $\mu$ m, average length c. 40  $\mu$ m) as well as roundish quartz crystals (30 - 60  $\mu$ m) are common in garnet (Fig. 8.5). The size of these clusters is 0.5 - 1 mm. In addition to clusters of single phases, multiphase inclusions with sizes between 50 and 100  $\mu$ m occur. These clusters can be surrounded by local cracks in garnet (Fig. 8.5) and show coexisting quartz + omphacite, quartz + potassic white-mica as well as omphacite + quartz + potassic white-mica + intergrown silicate phases, which were too small to be unequivocally identified with the EMP. Omphacite in the multiphase inclusions can be as large as 35  $\mu$ m and contains 54 mol% diopside, 4 mol% hedenbergite, 33 mol% jadeite and 4 mol% aegirine on average. The Na content (0.33 - 0.37 pfu) is higher than in matrix omphacite. The size of amphibole is in the range of 10 - 15  $\mu$ m. Its Si contents vary between 5.98 and 6.74 pfu. On average, Ca (1.44 pfu) and Na (0.93 pfu) contents are lower and higher, respectively, compared to matrix amphibole. Clinozoisite-epidote inclusions (50 - 70  $\mu$ m) consist of about 26 mol% pistacite.

## 6.5 Results of the Bulk-Rock Analyses

The results of the bulk-rock analyses of eclogite samples 13Mm1, 13Mm7\_2, and MüMa03\_3c using different methods (XRF, liquid ICP-MS, and LA ICP-MS) are given in Tabs. 6.1 and 8.5.

The concentrations of most elements for a specific eclogite, resulting from the application of these methods, are identical within error ranges of 10 % (of the corresponding calculated

average values). For the presentation of selected major (in wt% of the oxides; see Tabs. 6.1 and 8.5) and trace (in ppm; see Tabs. 6.1 and 8.5) elements in discrimination diagrams, we used the concentrations obtained by XRF and mainly liquid ICP-MS, respectively. For the trace elements Rb, Sr, Y, and Sm, we employed the average of XRF and liquid ICP-MS data due to deviations of more than 10 % between them. As contents of Zr obtained by liquid ICP-MS were significantly lower than the corresponding XRF and LA ICP-MS data, we assumed incomplete dissolution of zircon, the main Zr-containing phase, despite our acid dissolution procedure at elevated pressures and temperatures (analogue to section 3.3.5). Therefore, Zr contents determined with XRF were used. As Hf is also mainly concentrated in zircon, we preferred the Hf / Zr ratio of liquid ICP-MS (see Massonne and Czambor 2007) in order to estimate the (true) Hf contents by the relation  $(\text{Hf} / \text{Zr})_{\text{liquid ICP-MS}} \cdot \text{Zr}_{\text{XRF}}$ . Because of difficulties with the determination of Nb and Ta contents with both XRF (Nb contents were apparently too high, see Tabs. 6.1 and 8.5) and liquid ICP-MS (calibrations were unreliable even after addition of diluted HCl to the ICP-MS liquids), we used the values for these elements obtained by LA ICP-MS. Low Ba contents (< 100 ppm) were taken from liquid ICP-MS measurements because XRF spectrometry resulted in significantly higher values probably due to a partial overlap of Ba and Ti signals (see section 3.3.5). Moreover, it turned out that the carbon and water contents are below 0.1 and 0.3 wt%, respectively.

To characterise the protoliths of the studied eclogites, the following elemental concentration plots were applied (see Fig. 6.7): a) Nb / Ta versus Nb discrimination diagram (Rudnick et al. 2000); b) ternary discrimination diagram using Ti, Zr and Y (Pearce and Cann 1973); c) ternary discrimination diagram using Nb, Zr and Y (Meschede 1986); d) rare-earth element (REE) pattern normalised against the chondrite values given by Boynton (1984); and e) MORB-normalised trace element variation diagram (Pearce 1983).

In the applied discrimination diagrams (Figs. 6.7a-c), our analyses plot inside the corresponding MORB-fields. The REE patterns (Fig. 6.7d) are rather flat ranging between values of 8 and 21 rock / chondrite. No clear enrichment of light or heavy REEs is discernible. The values for the various elements in the MORB-normalised diagram (Fig. 6.7e) vary between 0.35 and 6.

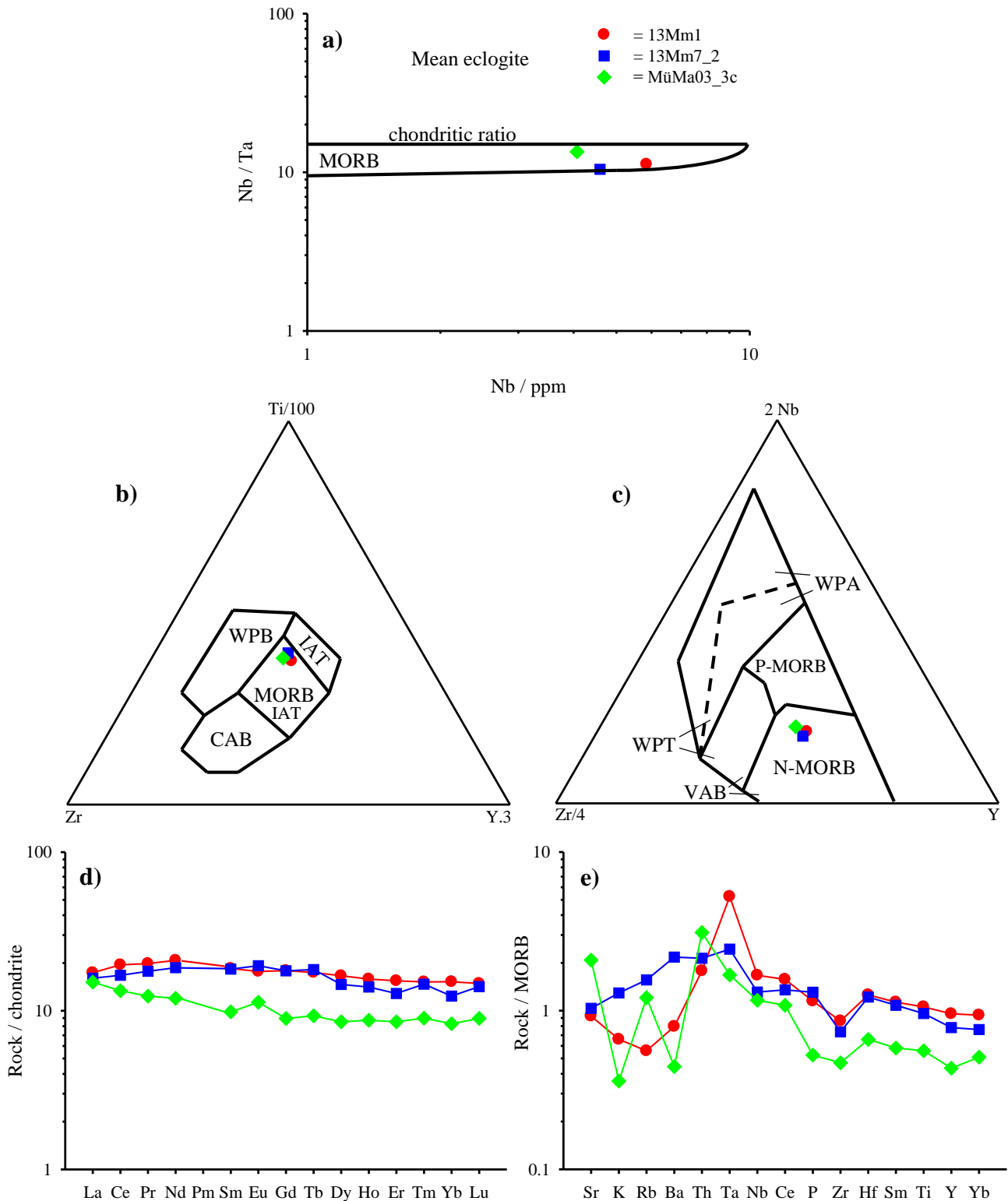


**Fig. 6.7:** It is the aim of these graphs to determine the protoliths of the studied eclogites: a) plots the ratio of Nb / Ta versus Nb / ppm (Rudnick et al. 2000); b) is a ternary discrimination diagram using Ti, Zr and Y: CAB = calc-alkali basalts; IAT = island arc tholeiites; MORB = mid-ocean ridge basalt; WPB = “within plate” basalts (Pearce and Cann 1973); c) is a ternary discrimination diagram using Nb, Zr and Y: N-MORB = normal mid-ocean ridge basalt; P-MORB = plume-influenced regions of MORB; VAB = volcanic arc basalts; WPA = within-

plate alkali basalts; WPT = within-plate tholeiites (Meschede 1986); d) shows a chondrite-normalised rare-earth element (REE) pattern (Boynnton 1984); and e) is a MORB-normalised trace element variation diagram (Pearce 1983).

## 6.6 Pressure-Temperature Evolution

### 6.6.1 Calculation Methods

In order to reconstruct  $p$ - $T$  paths for the three eclogites from the MMC,  $p$ - $T$  pseudosections were calculated with the PERPLE\_X computer programme package (see Connolly 2005; version from August 2011 downloaded from the internet site <http://www.perplex.ethz.ch/>) for the  $p$ - $T$  range of 5 - 30 kbar and 400 - 800 °C (see also sections 4.5.1 and 5.6.1). These  $p$ - $T$  pseudosections, which were calculated in the eleven-component system  $\text{SiO}_2$ - $\text{TiO}_2$ - $\text{Al}_2\text{O}_3$ - $\text{MgO}$ - $\text{MnO}$ - $\text{FeO}$ - $\text{CaO}$ - $\text{Na}_2\text{O}$ - $\text{K}_2\text{O}$ - $\text{H}_2\text{O}$ - $\text{O}_2$ , were contoured by isopleths for molar fractions of garnet components, Si contents in amphibole as well as potassic white-mica, Na contents in omphacite, and modal contents of various minerals especially garnet.

The thermodynamic data set of Holland and Powell (1998, updated 2002) for minerals and  $\text{H}_2\text{O}$  was considered for all PERPLE\_X calculations, for which the following solid-solution models were chosen: (1) Gt(HP) for garnet (Holland and Powell 1998); (2) Opx(HP) for orthopyroxene (Powell and Holland 1999); (3) Ep(HP) for clinozoisite-epidote (see Holland and Powell 1998); (4) Mica(M) for paragonite (Massonne 2010) with maximal 50 mol% muscovite component; (5) Chl(HP) for chlorite based on the formulation by Holland et al. (1998); (6) TiBio(HP) for biotite being identical to the previous model Bio(HP) created by Powell and Holland (1999) as the tbi component was excluded (see below); (7) Omph(HP) for clinopyroxene based on the thermodynamic data given by Holland and Powell (1996) augmented by data for the end-members aegirine (acm) and  $\text{CaAl}_2\text{SiO}_6$  (cats); (8) feldspar for ternary feldspar according to Fuhrman and Lindsley (1988) using a subdivision into two models feldspar1 and feldspar2 with different compositional limits (1: max. 8 mol% sanidine component, 2: max. 10 mol% anorthite and max. 10 mol% albite components) as proposed by Massonne (2009); (9) St(HP) for staurolite (“from THERMOCALC”, written comm. by J.A.D. Connolly); (10) Stlp(M) for stilpnomelane (Massonne 2010); (11) MtUl(A) for magnetite (see Andersen and Lindsley 1988); (12) Pheng(HP) for potassic white-mica (see Powell and Holland 1999 as well as comments in file newest\_format\_solut.dat) with maximal 50 mol% paragonite component; (13) IlHm(A) for hematite (Andersen and Lindsley 1988) with maximal 50 mol% ilmenite component; and (14) GlTrTsPg for amphibole (glaucophane-tremolite-tschemmakite-pargasite + corresponding  $\text{Fe}^{2+}$ -bearing components). The preference for this amphibole model in

combination with Omph(HP) resulted from a comparison of various amphibole and clinopyroxene models undertaken by Li et al. (2017). For cordierite, ilmenite, and talc, the ideal mixing models hCrđ, IlGkPy (max. 30 mol% geikielite component), and T, respectively, were used, which are based on the thermodynamic data for the corresponding end-members given by Holland and Powell (1998).

To obtain the  $p$ - $T$  conditions of solidus curves in the range of 5 - 30 kbar and 550 - 800 °C, PERPLE\_X calculations were achieved with a version downloaded in August 2006 and the melt(HP) model (White et al. 2001), which was added to the aforementioned solid solution models.

The abbreviated end-member phases acti (actinolite), ann1 (annite), mic (microcline), ab (low  $T$  albite), cumm (cummingtonite), grun (grunerite), and the O<sub>2</sub> buffers qfm and mthm in the applied data file were not considered. Both Ti end-members tip and tbi in white and dark micas, respectively, were excluded as argued by Massonne et al. (2017). The H<sub>2</sub>O component in the haplogranitic melt model (h2oL) was neglected for calculations without melt. As we also calculated  $p$ - $T$  pseudosections without garnet to unravel the  $p$ - $T$  conditions before garnet growth, we also excluded the garnet end-members spss, alm, py, and gr.

The bulk-rock compositions of the studied samples (see Tabs. 6.1 and 8.5), determined by XRF spectrometry, were modified for the PERPLE\_X calculations: (1) CaO was reduced considering that some Ca is bound to apatite, the content of which was calculated on the basis of the analysed P<sub>2</sub>O<sub>5</sub> content in the bulk-rock. (2) The oxygen content, which is related to the amount of trivalent iron in the rock, was estimated assuming that 10 % of the iron was trivalent during metamorphism (see previous calculations of  $p$ - $T$  pseudosections for HP-UHP rocks: e.g. Massonne et al. 2007b). This content could also be lower because Fe<sup>3+</sup> contents in the major Fe-bearing minerals are very low (except for omphacite in eclogite sample 13Mm7\_2 with a calculated aegirine component as high as 12 mol%). Consequently, other percentage values than 10 % of iron being trivalent (0, 15, 20 %) were used in our PERPLE\_X calculations as well (except for garnet-absent conditions). (3) Water contents were enhanced (6.5 wt% for samples 13Mm1 and MüMa03\_3c as well as 6.0 wt% for 13Mm7\_2) to permit the formation of free hydrous fluids already at relatively low temperatures. (4) For all rock compositions, involved in PERPLE\_X calculations, the sums of the oxide components were normalised to 100 wt% (Tabs. 6.1 and 8.5).

Four different calibrations of the Zr-in-rutile thermometer (two by Zack et al. 2004; Watson et al. 2006; Tomkins et al. 2007 for  $\alpha$ -quartz) were applied to the studied samples. Only in case of

eclogite sample 13Mm7\_2, the following calibration by Tomkins et al. (2007) was additionally employed due to the extreme  $p$ - $T$  conditions involved (see below):

$$\triangleright T(^{\circ}\text{C}) = \frac{88.1 + 0.206 \cdot p}{0.1412 - R \cdot \ln(\text{Zr})} - 273 \text{ (after Tomkins et al. 2007 for the coesite field)}$$

Abbreviations:  $p$  = pressure,  $R$  = gas constant,  $T$  = temperature,  $\text{Zr}$  = zirconium contents in rutile in ppm.

Merely the calibrations by Tomkins et al. (2007) consider a  $p$ -dependence and were, thus, favoured. The temperature values resulting from all conducted measurements of the Zr contents in rutile, which were rather similar in every eclogite sample (see above), were averaged. A  $2\sigma$  error was calculated for this average. The error propagation of the  $1\sigma$  of the counting rates of the peak and background intensities of the Zr  $L\alpha$ -radiation resulted in a temperature error of about  $\pm 40^{\circ}\text{C}$  ( $1\sigma$ ) for a single analysis.

### 6.6.2 Results of the Calculated $p$ - $T$ Pseudosections

In general, calculations without  $\text{O}_2$  have not always led to intersecting garnet isopleths ( $X(\text{Mg})$ ,  $X(\text{Ca})$ ); those with  $\text{O}_2$  contents equivalent to 15 or 20 % of Fe being trivalent yielded maximum garnet volumes which were too low compared to the estimated garnet modal contents (see above). Such inconsistencies did not arise when we used the results from pseudosections for 10 %  $\text{Fe}^{3+}$  of total Fe. Thus, we present subsequently only calculation results for these pseudosections ignoring the results of pseudosections calculated with other percentages of  $\text{Fe}^{3+}$ .

Garnet, omphacite, rutile, and  $\text{H}_2\text{O}$  are excess phases in such  $p$ - $T$  pseudosections for all studied eclogite samples (excluding those calculated without garnet and melt) as far as the  $p$ - $T$  range limited to 15 - 30 kbar and 500 - 800  $^{\circ}\text{C}$  is concerned (see the representative examples of 13Mm1 and MüMa03\_3c in Fig. 6.8), which is of relevance for the here derived eclogitic  $p$ - $T$  conditions. Biotite, potassic white-mica, and stilpnomelane are the only K-bearing minerals in this limited  $p$ - $T$  range for all three samples. Biotite usually occurs at  $p < 21$  kbar and  $T > 620^{\circ}\text{C}$ . Stilpnomelane merely appears at  $p > 22$  kbar and  $T < 550^{\circ}\text{C}$ . Thus, potassic white-mica is the only K-bearing mineral over a wide  $p$ - $T$  range (concerning 15 - 30 kbar and 500 - 800  $^{\circ}\text{C}$ ). The only feldspar phase is plagioclase, which occurs in the  $p$ - $T$  pseudosections below 15 kbar. Amphibole, which is exclusively calcic, appears at pressures below 20 kbar. For all eclogites, lawsonite occurs below the following conditions: 30 kbar (740  $^{\circ}\text{C}$ ), 20 kbar (590  $^{\circ}\text{C}$ ) and 16 kbar (500  $^{\circ}\text{C}$ ). Pure zoisite appears in a field below 23 kbar and 670  $^{\circ}\text{C}$ , whereas clinsoisite-

epidote occurs at  $p < 12$  kbar and  $T < 640$  °C. In the limited  $p$ - $T$  range shown in Fig. 6.8a for sample 13Mm1, neither ilmenite nor paragonite appears. Titanite (in sample 13Mm1) occurs in this figure only in a tiny field close to 15 kbar and 500 °C. Kyanite occurs exclusively in the pseudosection of MüMa03\_3c (e.g. Fig. 6.8b) in a  $p$ - $T$  triangle with vertices at 10 kbar (640 °C), 25 kbar (700 °C) and 12 kbar (740 °C).

The contouring of the  $p$ - $T$  pseudosections is exemplarily shown in Fig. 6.9 for sample 13Mm1. For the chemical compositions of garnet, two opposed trends are discernible:  $X(\text{Ca})$  of garnet decreases with increasing temperatures, whereas  $X(\text{Mg})$  increases (see, e.g. Săbău 2000; Massonne 2014). However,  $X(\text{Ca})$  also depends on the pressure (the higher the pressure, the lower  $X(\text{Ca})$ ; see Fig. 6.9) in the  $p$ - $T$  range of 15 - 30 kbar and 500 - 800 °C. In this range,  $X(\text{Ca})$  and  $X(\text{Mg})$  vary in the following limits for sample 13Mm1:  $0.15 \leq X(\text{Ca}) \leq 0.40$  and  $0.05 \leq X(\text{Mg}) \leq 0.30$ . Similar limits were calculated for the other two eclogite samples.

Clinopyroxene and H<sub>2</sub>O are excess phases in the garnet-free  $p$ - $T$  pseudosections for all studied eclogite samples for the  $p$ - $T$  range of 5 - 20 kbar and 400 - 600 °C (see the representative example for 13Mm1 in Fig. 6.10a). In these pseudosections, the  $p$ - $T$  boundaries limiting biotite, potassic white-mica, stilpnomelane, plagioclase, amphibole, lawsonite, zoisite, clinozoisite-epidote, and paragonite are surprisingly similar to those in the pseudosections with garnet (see Fig. 6.8). Only the  $p$ - $T$  fields for ilmenite and kyanite (exclusively in MüMa03\_3c) differ significantly from their counterparts in the garnet-bearing pseudosections (e.g. Fig. 6.11). In the garnet-free pseudosections ( $p$ - $T$  range: 5 - 30 kbar, 400 - 800 °C), ilmenite occurs up to 30 kbar and above 460 °C, whereas this phase in the garnet-containing pseudosections is limited to 15 kbar and  $T > 480$  °C. The  $p$ - $T$  field for kyanite is shifted to higher pressures ( $> 30$  kbar) and temperatures ( $> 740$  °C) in the garnet-free pseudosection for MüMa03\_3c.

In Fig. 6.10b, the contouring of the garnet-free  $p$ - $T$  pseudosection (Fig. 6.10a) is exemplarily shown for sample 13Mm1 and isopleths for the Si content in amphibole (6.10 - 6.90 pfu) and Na content in omphacite (0.31 - 0.43 pfu). At temperatures above 500 °C, with increasing amounts of garnet in the regular  $p$ - $T$  pseudosections, such isopleths deviate in the two types of pseudosections without clear systematics. For instance, the Na contents in omphacite are 0.40 (with garnet) and 0.43 (without garnet) pfu at 30 kbar and 610 °C or 0.37 (with garnet) and 0.34 (without garnet) pfu at 20 kbar and 620 °C. The Si contents in amphibole are 6.90 (with garnet) and 6.50 (without garnet) pfu at 15 kbar and 640 °C as well as 9 kbar and 730 °C.



**Fig. 6.8:**  $p$ - $T$  pseudosections (without melt) calculated for the compositions of samples 13Mm1 (a) and MüMa03\_3c (b) (see Tabs. 6.1 and 8.5) with the computer software package PERPLE\_X (see text). Abbreviations: Am = amphibole, Bt = biotite, Ch = chlorite, Cl = clinopyroxene (second such phase), Co = coesite, Gt = garnet, Ky = kyanite, Lw = lawsonite, Om = omphacite, Pa = paragonite, Ph = potassic white-mica, Pl = plagioclase, Qu = quartz, Ru = rutile, St = stilpnomelane, Ta = talc, Tt = titanite, Zo = zoisite.

The modal content of garnet, calculated for the regular pseudosections, varies between 0 and 36 vol% for sample 13Mm1 (see Fig. 6.11a), reaching its maximum at about 29 kbar and 680 °C. For samples 13Mm7\_2 (Fig. 6.11b) and MüMa03\_3c (Fig. 6.11c), these maximum values are 35 vol% at 30 kbar (740 °C) and 40 vol% at 29 kbar (720 °C), respectively. In general, higher pressures and / or lower temperatures favour higher Si contents in potassic white-mica. Calculated values are between 3.35 (17 kbar, 600 °C) and 3.55 pfu (27 kbar, 670 °C) for sample 13Mm1 (Fig. 6.11a). For samples 13Mm7\_2 (Fig. 6.11b) and MüMa03\_3c (Fig. 6.11c), the variation is characterised by 3.45 - 3.55 Si pfu between 21 (610 °C) and 30 kbar (740 °C) and 3.38 - 3.50 Si pfu between 23 (720 °C) and 29 kbar (720 °C), respectively. The calculated Na contents in omphacite are 0.35 - 0.39 (13Mm1), 0.36 - 0.40 (13Mm7\_2) and 0.30 - 0.36 (MüMa03\_3c) pfu for the  $p$ - $T$  range of 15 - 30 kbar and 500 - 800 °C. In this range, the calculated Si contents and modal contents of amphibole are as follows: 6.90 - 7.10 pfu and up to 20 vol% (13Mm1), 6.90 - 7.40 pfu and up to 15 vol% (13Mm7\_2), as well as 6.60 - 7.40 pfu and up to 60 vol% (MüMa03\_3c).

The calculated phase relations at high temperatures (e.g. Fig. 6.8) are partially metastable because of melting. The calculated solidus curve at wet conditions runs, for instance, through the following  $p$ - $T$  conditions (Fig. 6.11a; sample 13Mm1): 15 kbar (660 °C), 18 kbar (720 °C), 21 kbar (750 °C) and 23 kbar (800°C).

### 6.6.3 Construction of $p$ - $T$ Paths on the Basis of the Chemical Zonation of Garnet

A major criterion for the derivation of a specific  $p$ - $T$  condition is the intersection of isopleths for molar fractions of garnet components (e.g. Caddick and Kohn 2013; Massonne 2013). In this study, we constructed prograde  $p$ - $T$  paths on the basis of those for  $X(\text{Ca})$  and  $X(\text{Mg})$  and compared, whenever possible, the results with the  $p$ - $T$  position of isopleths for other chemical and modal parameters as given above. In addition, we applied Zr-in-rutile thermometry.

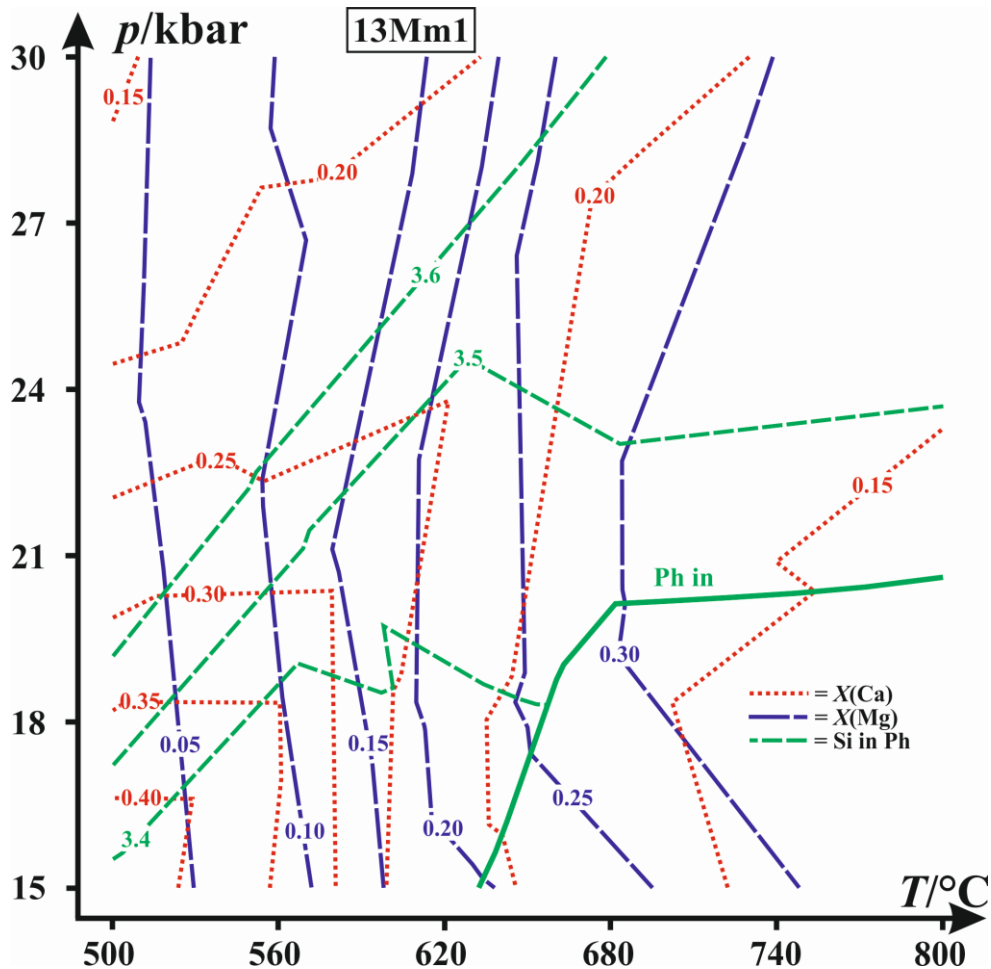


**Fig. 6.9:** Contouring of the calculated  $p$ - $T$  pseudosection of Fig. 6.8 by isopleths for the molar fractions of garnet (Gt) components and the Si contents per formula unit (pfu) in potassic white-mica (Ph). The thick curve marks the limit of the occurrence of potassic white-mica.

For sample 13Mm1 (Fig. 6.11a), intersections of the garnet isopleths for core ( $\text{Alm}_{49}\text{GrAn}_{29}\text{Py}_{21}\text{Sp}_1$ ) and rim ( $\text{Alm}_{51}\text{GrAn}_{22}\text{Py}_{26}\text{Sp}_1$ ) compositions occur at about 17 kbar / 600 °C and 27 kbar / 670 °C, respectively. The corresponding intersections of intermediate garnet compositions are located between these  $p$ - $T$  data (e.g.:  $\text{Alm}_{50}\text{GrAn}_{25.5}\text{Py}_{23.5}\text{Sp}_1$ : 23 kbar and 630 °C). The resulting  $p$ - $T$  path does not cross the calculated wet solidus line. Along this path (Fig. 6.11a), the calculated change of the rock is related to (1) the growth of garnet (modal content from 26 to 36 vol%), (2) an increase of the Si content in potassic white-mica from 3.35 to 3.55 pfu, (3) a slight increase of the Na contents in omphacite from 0.36 to 0.37 pfu and (4) the disappearance of amphibole at 18 kbar (610 °C) and chlorite at a slightly higher pressure in the assemblage garnet, omphacite, rutile, potassic white-mica, talc, chlorite, amphibole and quartz.

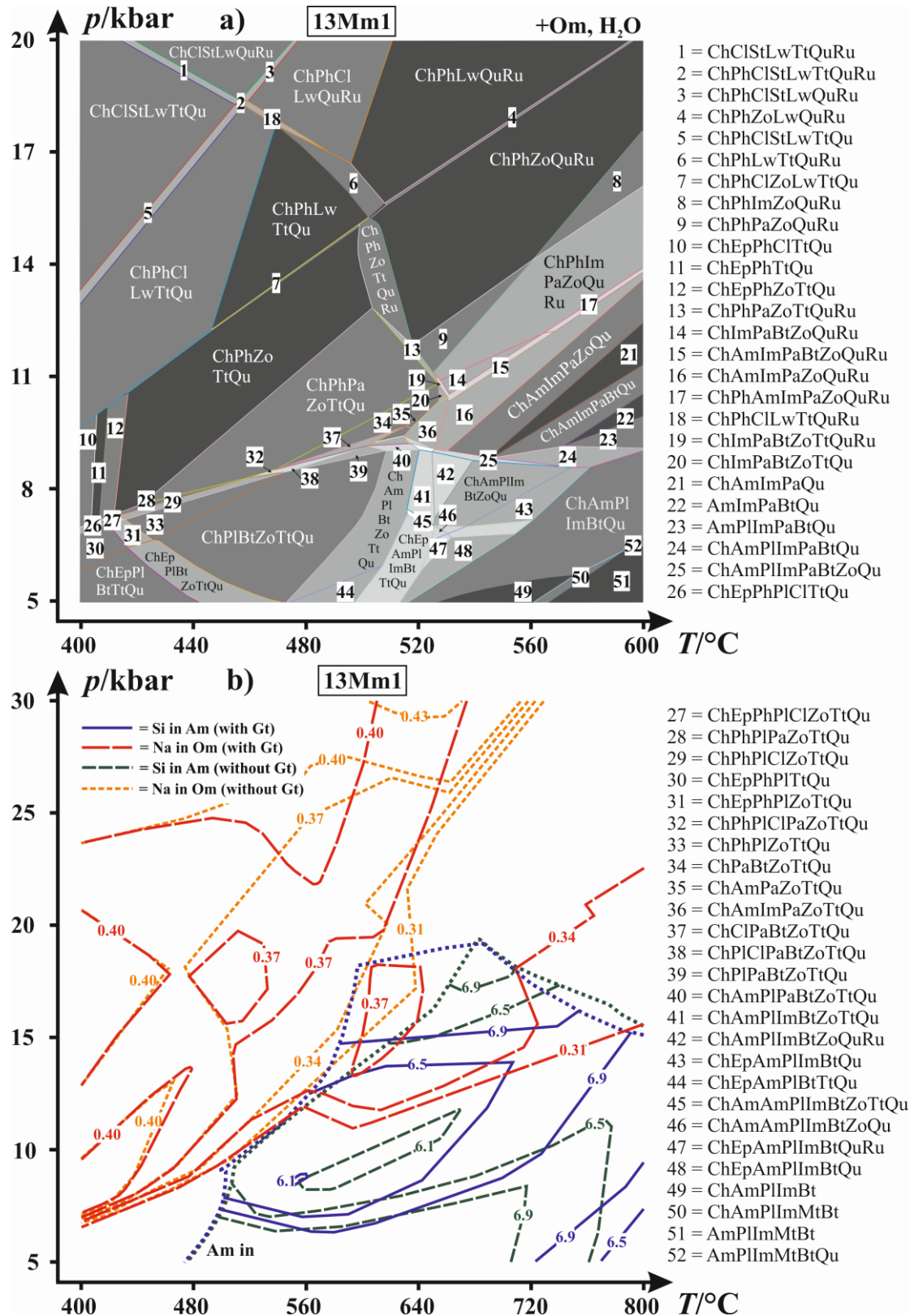


**Fig. 6.10:** (a)  $p$ - $T$  pseudosection (without melt and garnet) calculated for the composition of sample 13Mm1 (see Tab. 6.1) with the computer software package PERPLE\_X (see text). Abbreviations as in Fig. 6.8 and Ep = clinozoisite-epidote, Im = ilmenite, Mt = magnetite. (b) Contouring of the calculated  $p$ - $T$  pseudosections of Figs. 6.8a (with garnet (Gt)) and 6.10a (without garnet) by isopleths for the Si contents per formula unit (pfu) in amphibole (Am) and Na contents pfu in omphacite (Om), respectively. The dotted lines mark the limits of the occurrence of amphibole (b).

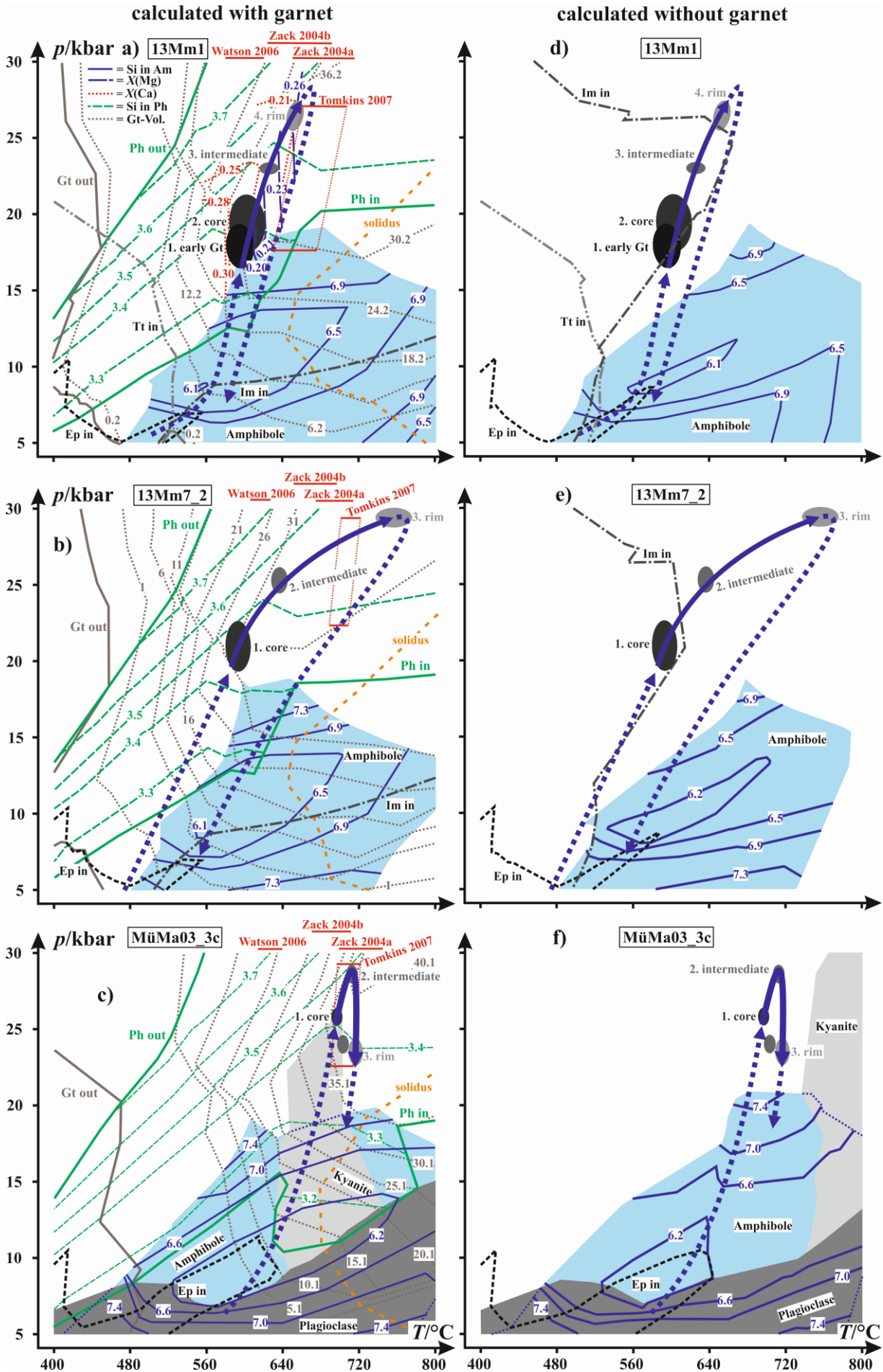


**Fig. 6.11:**  $p$ - $T$  estimates (error ellipses) for sample 13Mm1 (a), using isopleths of Fig. 6.9 for garnet. The  $p$ - $T$  paths of samples 13Mm7\_2 (b) and MüMa03\_3c (c) using garnet compositions are indicated by solid lines with arrows. Thick, dotted lines with arrows represent less certain extensions of the aforementioned  $p$ - $T$  paths. Different types of curves mark the limits of the occurrence of garnet (Gt), potassic white-mica (Ph), clinozoisite-epidote (Ep), ilmenite (Im), and titanite (Tt). The fields for amphibole, kyanite and plagioclase are coloured. The wet solidus curves are shown by thick, dashed lines. The results of four applied calibrations of the Zr-in-rutile thermometer are indicated by  $2\sigma$  error bars. The above  $p$ - $T$  paths are also exhibited in pseudosections calculated without garnet (d-f).

For sample 13Mm7\_2 (Fig. 6.11b), intersections of the garnet isopleths for core ( $\text{Alm}_{54.5}\text{GrAn}_{26}\text{Py}_{16.5}\text{Sp}_3$ ) and rim ( $\text{Alm}_{51}\text{GrAn}_{21}\text{Py}_{27}\text{Sp}_1$ ) occur at about 21 kbar (610 °C) and 30 kbar (740 °C), respectively. Again, the corresponding intersections of intermediate garnet compositions are located between the above  $p$ - $T$  data (e.g.:  $\text{Alm}_{52}\text{GrAn}_{23.5}\text{Py}_{23.5}\text{Sp}_1$ : 25 kbar and 635 °C) and the resulting  $p$ - $T$  path (Fig. 6.11b) does not cross the wet solidus line. Calculated changes along this path are related to (1) an increase of the garnet modal content from 27 to 35 vol%, (2) an increase of the Si content in potassic white-mica from 3.45 to 3.55 pfu, (3) a decrease of the Na content in omphacite from 0.39 to 0.37 pfu and (4) a change of the mineral assemblage garnet, omphacite, rutile, potassic white-mica, talc, and quartz (a tiny chlorite field occurs only at 21 kbar and 610 °C) by disappearance of talc at 25.5 kbar (660 °C) and the replacement of quartz by coesite at 28 kbar (730 °C).

The intersections of the garnet isopleths for core ( $\text{Alm}_{33.4}\text{GrAn}_{20.9}\text{Py}_{45}\text{Sp}_{0.7}$ ), intermediate region ( $\text{Alm}_{33.7}\text{GrAn}_{19.2}\text{Py}_{46.2}\text{Sp}_{0.9}$ ) and rim ( $\text{Alm}_{33.6}\text{GrAn}_{17.5}\text{Py}_{48}\text{Sp}_{0.9}$ ) compositions occur at about 26 kbar (700 °C), 29 kbar (720 °C) and 23 kbar (720 °C), respectively, for sample MüMa03\_3c (Fig. 6.11c). Along the corresponding  $p$ - $T$  path (Fig. 6.11c), the wet solidus line is not crossed and the following, calculated changes occur: (1) an increase of the garnet modal content from 35 to 40 vol% at peak pressure conditions followed by a decrease to 37 vol%, (2) an increase of the Si content in potassic white-mica from 3.40 to 3.50 pfu at peak pressure conditions and a subsequent decrease to 3.38 pfu, (3) a decrease of the Na content in omphacite from 0.33 to 0.30 pfu and (4) a change of the mineral assemblage potassic white-mica, talc, garnet, omphacite, kyanite, quartz and rutile by disappearance of both kyanite at 26 kbar (700 °C) and talc at a slightly higher pressure.

The Zr-in-rutile thermometry using the calibrations by Watson et al. (2006) yielded temperatures of  $604 \pm 6$  °C ( $2\sigma$ ) for the mean Zr content of 189 ppm in rutile from sample 13Mm1 which are lower compared to those resulting from the PERPLE\_X calculations and the other Zr-in-rutile thermometers. The calibrations by Zack et al. (2004) gave temperatures of

$677 \pm 11$  and  $656 \pm 10$  °C ( $2\sigma$ ). The resulting temperatures employing the calibration by Tomkins et al. (2007) for  $\alpha$ -quartz and 189 ppm Zr at 17 and 27 kbar are  $641 \pm 6$  and  $682 \pm 6$  °C ( $2\sigma$ ), respectively. Within errors, these temperatures are compatible with the above derived  $p$ - $T$  path. For sample 13Mm7\_2 (mean: 224 ppm), temperatures of  $691 \pm 5$  ( $2\sigma$ ) and  $710 \pm 5$  °C (at 21 for  $\alpha$ -quartz and 30 kbar for coesite) result from the Tomkins et al. (2007) calibrations. For sample MüMa03\_3c (mean: 241 ppm), the calibration for  $\alpha$ -quartz yielded  $718 \pm 8$  ( $2\sigma$ ) and  $720 \pm 7$  °C (at 23 and 29 kbar). These temperatures for sample MüMa03\_3c are also compatible with the above derived  $p$ - $T$  paths. However, the temperatures obtained for sample 13Mm7\_2 are about 30 °C lower than those resulting from the PERPLE\_X calculations.

#### 6.6.4 Hints at $p$ - $T$ Conditions Before and After Garnet Growth

The early prograde parts (Fig. 6.11) of the above  $p$ - $T$  paths cannot be determined as precisely as the late prograde branches using the chemical composition of zoned garnet, but there are multiple indications to reconstruct them approximately: Minerals enclosed in garnet core domains, such as clinozoisite-epidote, ilmenite, and titanite (see section 6.4), are incompatible with the above derived late prograde  $p$ - $T$  paths. These phases grew before garnet. The same is probably true for enclosed amphibole and omphacite although they can coexist with garnet at the above derived prograde  $p$ - $T$  conditions. The early prograde  $p$ - $T$  conditions were reconstructed using enclosed minerals in garnet including their compositions as well as contoured garnet-free and garnet-bearing pseudosections.

According to the pseudosections for 13Mm1, (1) clinozoisite-epidote occurs at  $p < 12$  kbar and  $T < 640$  °C (with and without garnet; see section 6.6.2), (2) ilmenite is limited to  $p < 15$  kbar and  $T > 480$  °C in the regular pseudosection with garnet, and (3) titanite (with and without garnet) appears only at temperatures below 560 °C. Thus, a rough  $p$ - $T$  range ( $< 12$  kbar,  $> 480$  °C) can be defined for the early metamorphism. Enclosed amphibole with observed Si contents between 5.60 and 6.45 pfu should have grown at pressures between 8.5 and 12 kbar (pseudosection with garnet) or 7.5 and 12 kbar (pseudosection without garnet). The compositions of enclosed omphacite considering pseudosections with and without garnet do not contribute to the estimation of early metamorphic conditions because their Na isopleths are hardly pressure-sensitive (e.g. Fig. 6.10b). According to the above information, an early  $p$ - $T$  path (Figs. 6.11a,d) is approximated running from 6 kbar (510 °C) to 15 kbar (580 °C) for sample 13Mm1.

Based on the pseudosections for 13Mm7\_2, clinozoisite-epidote and ilmenite are limited to  $p < 12$  kbar and  $T < 640$  °C (with and without garnet) and  $p < 15$  kbar and  $T > 480$  °C (with garnet), respectively. Thus, a rough  $p$ - $T$  range ( $< 12$  kbar,  $> 480$  °C) can be defined for the early metamorphism. Due to the absence of enclosed amphibole, we assume that the calculated amphibole field was not passed during early prograde metamorphism. According to the above information, an early  $p$ - $T$  path (Figs. 6.11b,e) is approximated running from 5 kbar (475 °C) to 19 kbar (590 °C) for sample 13Mm7\_2.

In the pseudosections for MüMa03\_3c with and without garnet, clinozoisite-epidote occurs at  $p < 12$  kbar and  $T < 650$  °C. Thus, we constructed on the basis of clinozoisite-epidote inclusions in garnet and the assumption of a similar early metamorphic evolution as in the other studied rocks an early  $p$ - $T$  path (Figs. 6.11c,f) running from 7 kbar (580 °C) to 25 kbar (690 °C) for this sample. This path is in agreement with the following observations: Enclosed amphibole with observed Si contents between 5.98 and 6.74 pfu should have grown at pressures between 9 and 16 kbar (with and without garnet). Enclosed phengite with observed Si contents between 3.26 and 3.51 pfu should have formed between 17 and 29 kbar (with garnet) and, thus, at higher pressures together with garnet (see above).

For the estimation of the  $p$ - $T$  paths at retrograde conditions (Fig. 6.11), the following information was applied: In sample 13Mm1, observed Si contents in phengite decrease from 3.41 - 3.47 in the core (around 21 kbar, 650 °C) to 3.24 - 3.37 pfu in the rim (12.5 kbar, around 620 °C). At  $p < 20$  kbar, amphibole formed again in the matrix. Observed Si contents in this mineral decrease from 7.06 to 6.13 pfu from core to rim pointing to a  $p$ - $T$  evolution from 15 to 8 kbar (see the Si isopleths in Fig. 6.11a). At  $p < 15$  kbar and  $T > 480$  °C, ilmenite newly formed. Thus, a late  $p$ - $T$  path (Fig. 6.11a) was constructed running from 27 kbar (670 °C) to 8 kbar (580 °C) for sample 13Mm1. In sample 13Mm7\_2, observed Si contents in phengite drop from 3.39 (17.5 kbar, 640 °C) to 3.31 pfu (14 kbar, around 620 °C). These contents in amphibole, which newly formed at  $p < 20$  kbar, decrease from 6.66 to 6.44 (possible  $p$ - $T$  range: from 14 kbar, 610 °C to 11 kbar, 580 °C) pfu. Thus, a late  $p$ - $T$  path (Fig. 6.11b) was estimated running from 30 kbar (740 °C) to 7.5 kbar (560 °C) for sample 13Mm7\_2 compatible with the late appearance of ilmenite in its matrix. In sample MüMa03\_3c, decreasing Si contents in the phengite rim domain from 3.36 to 3.32 pfu point to a pressure decrease (Fig. 6.11c) from 23 to 19 kbar at temperatures around 700°C. The Si contents in amphibole of the matrix (formed at  $p < 20$  kbar), decreasing from 6.99 to 5.98 pfu, suggest a further pressure lowering to  $p < 15$  kbar at slightly falling temperatures ( $< 700$  °C). As amphibole-plagioclase symplectites around omphacite

might represent local equilibria not encompassed by the calculated  $p$ - $T$  pseudosections, they were not considered but are compatible with the above estimated retrograde paths.

## 6.7 Discussion

### 6.7.1 Protoliths of the Studied Samples

According to the discrimination diagrams of Fig. 6.7, the protoliths of the studied eclogites were MORBs as previously suggested by Gebauer and Grünenfelder (1979) as well as Stosch and Lugmair (1990). However, we noted in the immobile (+ semimobile) trace elements minor deviations from typical MORBs. In the plot of Nb / Ta versus Nb (Rudnick et al. 2000; Fig. 6.7a), the determined Nb / Ta ratio for sample 13Mm7\_2 is relatively low for MORBs. The determined relatively high Ta content (Fig. 6.7a) could be related to partitioning effects between different phases already in the mantle (Jackson et al. 2008). For eclogite sample MüMa03\_3c, a positive Eu anomaly (Fig. 6.7d) was noted. This anomaly might indicate an enrichment of feldspar, such as plagioclase, during crystallisation of a basaltic magma (Hoskin and Schaltegger 2003; Rubatto and Hermann 2007).

In the MORB-normalised trace element variation diagram (Fig. 6.7e) after Pearce (1983), the trend parallel to the  $x$ -axis (close to  $y = 1$ ) for the immobile (+ semimobile) trace elements ((Th,) Ta to Yb + Sr), especially of samples 13Mm1 and 13Mm7\_2, is expected for MORB-derived eclogites. The mobile (+ semimobile) elements (K to Ta particularly of sample 13Mm7\_2) show a slight enrichment with respect to MORB probably due to interaction of hydrous fluids during prograde and retrograde metamorphism. However, the Ba and K contents (0.35 in Fig. 6.7e for sample MüMa03\_3c) can also be low and might, thus, be indicative of an extraction of such elements by infiltrating fluids in a subduction environment (see also Straub and Layne 2003).

### 6.7.2 Eclogite-facies Metamorphism of the Studied Samples

On the basis of the chemical zonation patterns of garnet grains (see section 6.6.3), we derived three similar prograde metamorphic paths starting at 17 - 26 kbar and 600 - 700 °C and reaching peak conditions in the range of 26 - 30 kbar and 670 - 740 °C (Fig. 6.11). The derived metamorphic temperatures are compatible with those applying Zr-in-rutile thermometry (Fig. 6.11). As this thermometry yielded lower temperatures for sample 13Mm7\_2 than the garnet isopleths intersection method, somewhat lower peak temperatures than 740 °C could be possible as well. In this case, a good coincidence of the here derived peak temperatures with

previous estimates (600 - 700 °C and somewhat more, Massonne and O'Brien 2003) exists. Calculated Si contents in phengite for peak pressure conditions can be similar to the observed ones as an increase of the Si content from 3.35 to 3.55 pfu (see Fig. 6.11a) was found in phengite from sample 13Mm1. However, the calculated Si contents in potassic white-mica pfu for the peak pressure conditions (3.55 pfu) of the other samples are higher than the observed ones (3.24 - 3.47 pfu). The apparent discrepancy is explained by the formation of potassic white-mica (core domain) already during garnet core formation. However, phengite inclusions in garnet of sample MüMa03\_3c exist that contain Si contents up to 3.51 pfu.

Coesite (transition from quartz at 700°C: ~28 kbar, e.g. Massonne 1999) has never been found in eclogites from the MMC. Thus, previously suggested peak pressures above 28 kbar (see Massonne and O'Brien 2003) are dubious. However, the observed modal contents of garnet (see section 6.4) point to higher peak pressures than 28 kbar. At this pressure, only 36 vol% was calculated for sample 13Mm1, but 39 vol% was observed. For sample 13Mm7\_2, it is 34 vol% (calculated) versus 38 vol% (observed) and for sample MüMa03\_3c, 40 vol% (calculated) versus 43 vol% (observed). Both a complete replacement of (possible) coesite by quartz and a slight overestimation of the garnet volume (due to the many inclusions) could be possible.

Observed and calculated mineral assemblages in the studied rocks at (and close to) peak pressure conditions are consistent. Only talc (< 3 mol%) calculated for all three samples (see section 6.6.3) could not be found. It is possible that this phase was overlooked due to its optical similarity with phengite or it was decomposed during retrogression. No signs of melt, like feldspar-quartz inclusions in garnet (Cesare et al. 2011 and references therein), have been found compatible with the calculated wet solidus lines in Fig. 6.11, which are located at higher temperatures than the derived *p-T* paths. The (crystallised) melt inclusions, reported by Massonne and O'Brien (2003) to occur in garnet cores, and the small melt pockets, suggested by Liebscher et al. (2007) in MMC eclogites, could be misinterpretations or local phenomena.

According to the constructed intersections for garnet core isopleths in Fig. 6.11, the initial garnet growth occurred at 16 kbar (590 °C for sample 13Mm1, Fig. 6.11a) or somewhat higher pressures (21 kbar for 13Mm7\_2, 26 kbar for MüMa03\_3c). However, at such conditions, already > 20 vol% of garnet should have been present. We think that kinetic factors (energetic barriers) as proposed by Spear (2017) are responsible for this late appearance of garnet. Once garnet seeds were formed, as the small idiomorphic garnet inclusion shown in Fig. 8.5, garnet grew to relatively few large crystals with extended constant core compositions. With rising pressure above 16 kbar, less extended intermediate and rim domains formed (Fig. 6.3).

Furthermore, the large inclusions in garnet are indicative of the invoked process of a significant overstepping of the garnet stability limit. These inclusions contain a variety of chemically different amphibole (e.g. 6.10 - 6.90 Si pfu) and omphacite (0.31 - 0.43 Na pfu) that had formed before garnet in an extended  $p$  range of < 10 to 16 kbar (see section 6.6.2, garnet-free pseudosections).

For eclogite sample MüMa03\_3c, an early retrograde path could be reconstructed by garnet isopleth intersections (Fig. 6.11c). This path (from 29 to 23 kbar) requires slight corrosion of garnet, as observed (see section 6.4.3), because the calculated garnet volume decreases from a maximum of 40 to 37 vol%.

### 6.7.3 Early Prograde and Late Retrograde $p$ - $T$ Evolution of the Studied Samples

The pre-eclogite facies metamorphism of the studied rocks could be deduced from the mineral inclusions in the core of garnet. It was shown above that the observed inclusion minerals and their compositions are compatible with early prograde  $p$ - $T$  paths exhibited in Fig. 6.11. In addition, the observed clusters of kyanite and rutile in garnet of sample MüMa03\_3c reflect precursor minerals of a garnet-free assemblage of the amphibolite-facies such as chlorite - amphibole - plagioclase - clinopyroxene - zoisite-epidote - biotite - quartz - ilmenite (e.g. at 8 kbar, 560 °C, see Fig. 6.10a). Minerals of this assemblage, such as amphibole, quartz and ilmenite, are still preserved in the inclusions in garnet, whereas plagioclase reacted to kyanite (eventually via clinozoisite-epidote, see, e.g. sample MüMa03\_3c in Figs. 6.11c) and the enclosing garnet core. Biotite could have been the precursor mineral of the rutile clusters as this mineral of the above amphibolite-facies assemblage usually contains TiO<sub>2</sub> contents of a few wt% (Deer et al. 1992). The corresponding reaction could have been: Ti-bearing biotite ± other phases = phengite + garnet + rutile.

Retrograde  $p$ - $T$  paths of eclogites, which have experienced similar peak  $p$ - $T$  conditions as deduced here, frequently pass the  $p$ - $T$  field of the amphibolite facies. This is, for instance, discernible by the (partial) breakdown of omphacite to amphibole + plagioclase. Although the studied eclogites are very fresh, omphacite locally shows rinds of symplectites of amphibole + plagioclase. Thus, a retrograde path through the amphibolite facies is very likely. Further indications for this assumption are Si contents, for instance, of 6.60 pfu in late amphibole (the observed range is: 6.13 - 7.06 Si pfu for 13Mm1, 6.44 - 6.66 for 13Mm7\_2, 5.98 - 6.99 for MüMa03\_3c) that are compatible with calculated  $p$ - $T$  conditions around 12 kbar (620 °C) for 13Mm1 and 13Mm7\_2 (18 kbar, 710 °C for MüMa03\_3c) using  $p$ - $T$  pseudosections. In

addition, the formation of late ilmenite, replacing rutile in samples 13Mm1 and 13Mm7\_2, points to pressures < 13 kbar and, thus, to amphibolite-facies conditions. The lowest Si contents (see section 6.6.4) in phengite grains pfu are compatible with pressures < 17 kbar.

#### 6.7.4 Geodynamic Consequences

In section 6.1, we have pointed to two provisions that subducted oceanic crust should fulfil. One provision, the MORB character, is realised in our studied eclogites (see section 6.7.1). The other provision, a continuous increase of  $p$  and  $T$  starting from very-low metamorphic grade and, thus, along an approximately constant geothermal gradient, is not realised. On the contrary, we deduced  $p$ - $T$  paths (at least for samples 13Mm1 and MüMa03\_3c) that start in the amphibolite facies (~8 kbar, 550 °C) and continuously cross geotherms from c. 20 to 8 °C/km (~700 °C at 90 km depth). Such a crossing of geotherms has already been noted in previous studies of eclogites from other areas and explained by tectonic (or subduction) erosion (Variscan NW Spain: Li and Massonne 2016; Li et al. 2017; late Palaeozoic W Canada: Petrie et al. 2016; Triassic Dabie Shan, east-central China: Massonne 2012). We suggest that this was also the case for the eclogites of the MMC. It could be that these rocks, as part of the oceanic crust, were first subducted beneath an accretionary wedge but implemented in this wedge by basal accretion (see, e.g. Willner et al. 2004; Massonne and Willner 2008; Cawood et al. 2009) to be heated at a pressure around 8 kbar (~30 km depth) reaching amphibolite-facies conditions. The tectonic erosion of accretionary wedges is probably a common phenomenon (see Meschede 2003). Thus, the amphibolite-facies rocks from the base of this wedge were then transported to greater depths with the subducting plate resulting in a (nearly isothermal) increase of the pressure (Fig. 6.11). Unusual (or not?) might be the late eclogitisation process by garnet formation at depths greater than 60 km (~16 - 20 kbar).

The return of the eclogites from depths of about 90 km could have been accomplished by the forced mass-flow in a subduction channel (Gerya and Stöckhert 2002; Gerya et al. 2002; Krebs et al. 2011; Massonne 2012). The merging of the eclogites from the MMC with the surrounding gneisses, which had experienced pressures not in excess of 13 kbar (Blümel 1986; Vollbrecht et al. 2006; Klemd 2010; section 4), might have occurred at the deepest part of an exhumation channel (Massonne 2012, 2016b) where a subhorizontal transport of the MMC rocks towards higher crustal levels took place. These geodynamic processes occurred in Devonian times according to existing geochronological data summarised in section 6.2. At that time, the Rheic Ocean was subducted beneath Gondwana-derived terranes (see scheme in Li et al. 2017). Thus,

the protolith of the studied eclogites were part of the Rheic Ocean. More details are provided in sections 3.1 - 3.2 and 7.1.

## 6.8 Conclusions

On the basis of PERPLE\_X calculations, the working out of chemical zonation patterns of garnet, the determination of variable Si contents in amphibole and potassic white-mica, and the intensive study of mineral inclusions in garnet for three eclogite samples, the understanding of the evolution of eclogite from the MMC in north-eastern Bavaria (Germany) could be significantly improved. It could be demonstrated that the deducible prograde metamorphism started in the amphibolite facies and is characterised by a continuous crossing of geotherms from c. 20 to 8 °C/km reaching peak pressure conditions between 26 and 30 kbar (around 90 km depth) at c. 700 °C. Another surprising find was that metastable garnet-free assemblages persisted even at HP conditions during this prograde evolution until (suddenly?) large quantities of garnet formed at pressures in the range of 16 - 20 kbar with unknown geodynamic consequences. According to these findings, existing geochemical and geochronological data, and our confirmation of the MORB character of the protoliths of the studied rocks there can hardly be any doubts that the eclogites of the MMC represent subducted crust of the Rheic Ocean.

## Acknowledgements

The authors thank Thomas Theye (Stuttgart) for his support of the work with the EMP and Gisela Kwiatkowski, Matthias Leiss, and Moritz Schmelz for technical assistance. F.W. is deeply grateful to Maria-Anna Waizenhöfer (Ellwangen) for her generous subsistence support.

*Note:* This chapter is planned to be submitted to *Lithos* for publication.

## 7. Argumentation

### 7.1 Geodynamic Considerations

This dissertation supports the view that the MMC, as part of the STZ, was probably connected to the West African Craton, being part of Gondwana, in Late Proterozoic times (Fig. 3.2). For the subsequent interpretation, it is assumed that an ACM acted as the provenance area of the metasediments of the MMC. The present work confirms that this ACM consisted of the Cadomian Basement about 575 Ma ago (Fig. 3.3). This ACM was accompanied by subduction of oceanic crust directed from the north to the south (Linnemann et al. 2007). This interpretation is supported by the occurrence of detrital monazite of magmatic origin, which can be deduced by the  $Y_2O_3$  content and the La / Gd ratio of the studied monazite (Fig. 5.12). The presented data for the studied eclogites show that they were derived from MORBs (section 6.7.1). Gebauer and Grünenfelder (1979) referred Late Proterozoic or Early Cambrian ages obtained from eclogites to their protoliths. This corroborates ideas of crustal thinning of the Cadomian Basement and subsequent formation of oceanic crust as postulated by Linnemann et al. (2000, 2007). Furthermore, the presented ages of magmatic events at c. 545 Ma, represented by detrital monazites of magmatic origin, are in line with Linnemann et al. (2007, 2010b). However, Linnemann et al. (2007, 2010b) explained this magmatism as temporarily restricted due to slab break-off (Fig. 3.4), whereas it is probably more likely that continued subduction of oceanic crust including an associated ACM is responsible for these events. Moreover, postulated thrusting and folding due to a collision of continental crust within Cadomia, as proposed by Linnemann et al. (2007, 2010b) (see Fig. 3.4), are contradicted by this study because such processes would have caused metamorphism and resetting of the studied magmatic monazites. No evidence for metamorphic processes at that time has been found. This work also establishes that sedimentation continued, causing the formation of detrital monazites at c. 520 Ma (see also e.g. Geyer et al. 2008). According to Linnemann et al. (2003, 2007), this was the time of initial asymmetric rifting within the Cadomian Basement (Fig. 3.5).

The presented age of c. 495 Ma for detrital monazite of magmatic origin probably represents the incision of an oceanic ridge (Fig. 3.7), which was also postulated by Linnemann et al. (2007, 2010c). According to the present work, a small continent (name?), similar to Avalonia, was separated from Gondwana (interpretation I in Fig. 7.1) or two continents within the Bohemian Massif, for example the STZ and the TBU, separated (interpretation II in Fig. 7.1). A magmatic monazite age of c. 455 Ma is probably somehow related to seafloor spreading either of the

Rheic Ocean, which is illustrated in Fig. 3.6 (interpretation I), or the Saxothuringian Ocean, which is explained in section 3.2 (interpretation II).

In literature, it is generally accepted that the Rheic Ocean was being subducted (Fig. 3.9), while Gondwana was moving towards Laurussia (e.g. Arenas et al. 2014). In this study, it is established that the metamorphic monazite age of c. 430 Ma (Fig. 5.12) represents this subduction of oceanic crust (interpretation I). Consequently, it is possible that an ACM was formed in the northern part of Gondwana, meaning that the Rheic Ocean was subducted beneath the STZ. Reasonable evidence for this suggestion is that (altered) MORBs, which can be related to the Rheic Ocean, were found as eclogite bodies in the STZ, particularly in the MMC (sections 6.7.1 and 6.7.4). Stosch and Lugmair (1990) reported Ordovician ages of some eclogite protoliths, which further strengthens this assumption. This explanation is also partly in line with that of Zeh and Will (2010) but no proof of their postulated back-arc on former Avalonia has been found in this study (Fig. 3.9). Besides, the present work specifies that Gondwana, including the MMC, collided with Laurussia, probably the former Avalonian part, at  $403.5 \pm 2.1$  Ma ( $2\sigma$ ), which is marked by the occurrence of metamorphic monazite (Fig. 5.12). About 20 Ma later ( $384.4 \pm 1.2$  Ma ( $2\sigma$ )), peak metamorphic conditions were reached in the studied gneiss samples during the Variscan orogeny. Despite the fact that eclogites were formed in greater depths than gneisses due to the more extreme  $p$ - $T$  conditions they were exposed to (see sections 4.7.1, 5.8.1 and 6.7.2), both rock types could possibly have been exposed to some kind of (local?) melt formation (see sections 4.7.2, 5.8.1, 6.7.2 and 8.1). The present study proposes that the continental crust of Gondwana was at least partially subducted during the collision with Laurussia. Evidence for that is the occurrence of gneisses from the MMC, which had experienced HP conditions (see above). This also includes a change of direction of the subduction (analogue to Zeh and Will 2010). The presented metamorphic age of  $368.5 \pm 1.9$  Ma ( $2\sigma$ ) can reasonably be related to an exhumation of both the eclogites and the gneisses of the MMC. The differences in the  $p$ - $T$  conditions are compatible with an exhumation in the collision zone due to “forced flow” (compare e.g. Krebs et al. 2011), during which material from various depths was juxtaposed. Analogue to O’Brien (2000), it is assumed in this study that the eclogites were exposed to a (partial) amphibolisation overprint during the initial steps of their rapid exhumation. Corresponding mineral reactions are provided by Franz et al. (1986). Besides, there is no denial of the fact that the “foreign” model is applicable to the MMC (see section 3.1). According to the present work, a late Variscan metamorphic event at c. 340 Ma (parallel to Förster and Romer 2010) is evidenced by some metamorphic monazite, which may be related to widespread HP metamorphism and plutonism in the Bohemian Massif concomitant with a

delamination process of thickened lithospheric mantle under the thickened continental crust due to the aforementioned continent-continent collision (e.g. Willner et al. 2000, 2002; Massonne 2005).

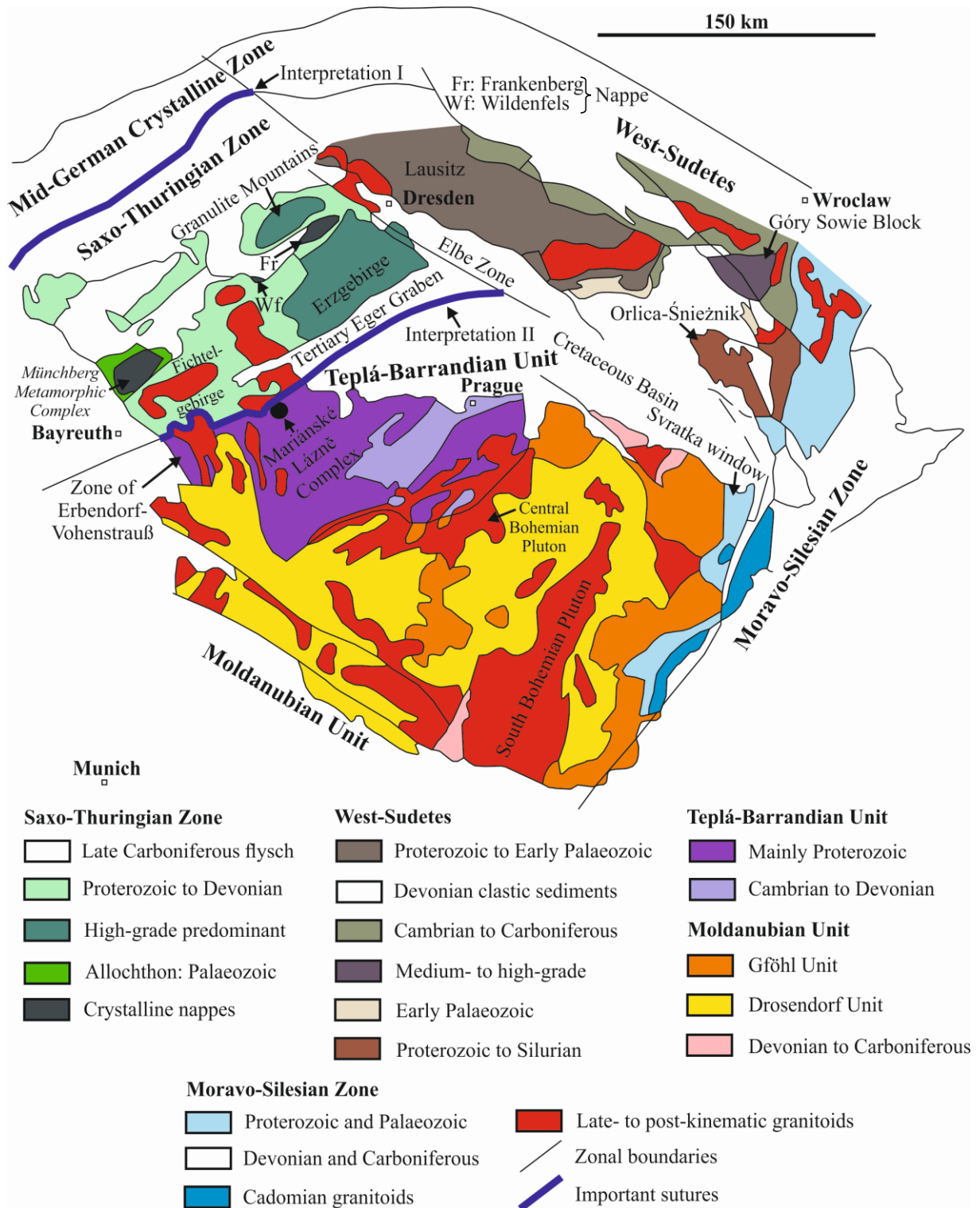


**Fig. 7.1:** Simplified geological map of the Bohemian Massif in central Europe, modified after Dallmeyer et al. (1995).

Despite the relative proximity of the MMC to the former Rheic Ocean (Fig. 7.1), there is also the possibility of interpreting the occurrence of metamorphic monazite grains, which are  $\leq 430$  Ma (Fig. 5.12), differently (interpretation II). Consequently, (altered) oceanic crust of the Saxothuringian Ocean was subducted beneath the TBU at c. 430 Ma (analogue to Schulmann et al. 2009). This means that MORBs, which can also be related to this Saxothuringian Ocean, were found as eclogite bodies in the MMC (compare sections 6.7.1 and 6.7.4). During the subsequent continent-continent collision between the STZ, including the MMC, and the TBU at  $403.5 \pm 2.1$  Ma ( $2\sigma$ ), metamorphic monazite evolved. At least parts of the STZ were subducted beneath the TBU, which explains the high pressures and temperatures that all studied rocks of the MMC had experienced (see sections 4.7.1, 5.8.1 and 6.7.2). About 20 Ma later ( $384.4 \pm 1.2$  Ma ( $2\sigma$ )), peak metamorphic conditions were reached during this orogeny. According to the current interpretation, this orogeny is especially preserved in the MLC, MMC and GSB (see sections 3.1 and 3.2). It is accepted that the MLC acts as a boundary between the STZ and the TBU (e.g. Faryad 2012). A remarkable feature of the different developments of the STZ and the TBU, probably due to the former Saxothuringian Ocean, is the scarcity of plutonic rocks in the latter, whereas plutons are rather abundant in the STZ (Dudek 1995). The age of  $368.5 \pm 1.9$  Ma ( $2\sigma$ ) marks an early step during the rather fast exhumation of the rocks, especially the eclogites of the MMC. As explained above, a “forced flow” mechanism (compare e.g. Krebs et al. 2011) is assumed for this exhumation. The eclogites were exposed to a (partial) amphibolisation overprint during the initial steps of their exhumation (analogue to O’Brien 2000). The event at c. 340 Ma probably marks a delamination process (e.g. Willner et al. 2000, 2002; Massonne 2005) caused by thickened continental lithosphere (see also above) within the Bohemian Massif on both sides of the suture between the STZ and the TBU. In general, this study tends to favour interpretation I due to its more compelling evidence.

Typical post Variscan events are related to hydrothermal mineralisations (see Romer et al. 2010). As no information about geological events that are younger than 320 Ma is available, such processes could not be detected in the MMC.

## 7.2 Further Outlook

In order to continue the research on the Variscan orogeny in Palaeozoic times, some suggestions are provided below. First of all, additional measurements on already studied rocks should be conducted. Therefore, analyses of zircon grains of both eclogites and gneisses from the MMC (e.g. by means of a LA ICP-MS or a Sensitive High Resolution Ion Microprobe (SHRIMP)) are

suggested to establish not only monazite (see sections 4 and 5) but also zircon ages. Concerning available zircon ages of the MMC, only Gebauer and Grünenfelder (1979) have dated the Weißenstein eclogite body, so far. More insights might also be provided by age dating of another mineral, like garnet (e.g. Getty et al. 1993; Hanwen et al. 1999). Lu / Hf and Ar / Ar age dating could be added, too. Besides, whole-rock Sr-Nd isotopic signatures should give us further insights into the protoliths of the studied rocks (see Romer and Hahne 2010).

Secondly, it is proposed to sample more rocks for analyses from the MMC. As this dissertation focused on the Liegendserie (9 gneiss samples studied) and the Hangendserie units (1 gneiss and 4 eclogite samples studied), the Prasinit-Phyllit and the Rand-Amphibolit units may be selected to work on.

Thirdly, for researching the Variscides, not only the STZ is of interest but also areas outside of it, such as the Moldanubian, TBU, and the Sudetes (Massonne and O'Brien 2003).



## 8. Appendix

### 8.1 Eclogite MüMa12

In addition to the already discussed eclogite samples (section 6), another eclogite (MüMa12), which had already been mentioned by Massonne (1993), was studied (see Fig. 8.1). Like MüMa03\_3c (see sheet No. 5737 Schwarzenbach a.d.sächs.Saale of the Geological Map of Bavaria 1:25000), it was sampled at a former quarry wall at the northern outskirts of the town of Oberkotzau (N 50.2722° / E 11.9169°, WGS 84). However, the latter outcrop does not exist anymore due to the construction of new buildings.

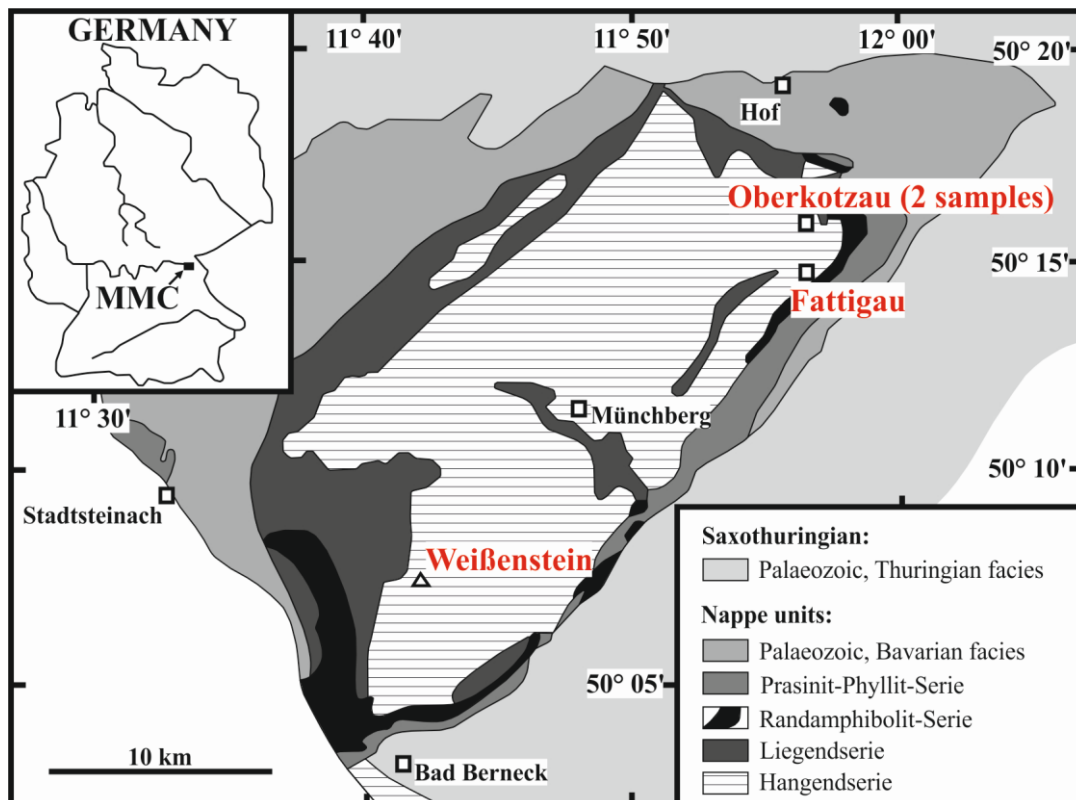


**Fig. 8.1:** Simplified geological map of the Münchberg Metamorphic Complex (MMC) in NE Bavaria (Germany), modified after Klemd et al. (1994). The locations of the studied eclogite samples are highlighted.

Sample MüMa12 (see Fig. 8.2) contains garnet (40 vol% as determined with a polarisation microscope ZEISS Axioplan), omphacite (35 vol%), quartz (15 vol%), potassic white-mica (3 vol%), amphibole (1 vol%) and rutile (1 vol%). Accessory minerals are the same as for garnet of sample 13Mm1 (section 6.4.1), except for kyanite, which does occur in sample MüMa12. The bulk-rock composition of MüMa12 is shown in Tab. 8.1.

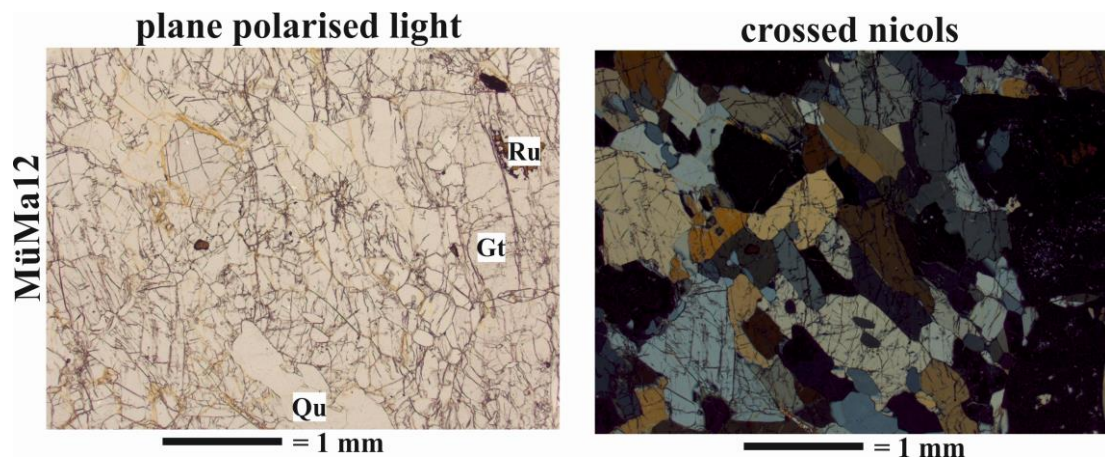


**Fig. 8.2:** Photomicrographs of objects in a thin section of the studied eclogite sample MüMa12 seen under plane polarised light and crossed nicols with a ZEISS Axioplan: Gt = garnet, Qu = quartz, Ru = rutile.

What is most interesting about this sample is that it contains a huge feldspar-quartz inclusion in a garnet grain (Fig. 8.3), which acts as a clear indication of former melt (see Massonne and O'Brien 2003; Cesare et al. 2011; Massonne 2014 and references therein).

Like eclogite sample MüMa03\_3c (section 6), sample MüMa12 can also be considered as a light eclogite (see Matthes et al. 1975; Stosch and Lugmair 1990) due to the presence of kyanite (Fig. 8.3).

Besides, representative analyses of garnet (Tab. 8.2), potassic white-mica (Tab. 8.3), and rutile (Tab. 8.4) are provided in this section.

**Tab. 8.1:** Bulk-rock composition of the studied eclogite sample MüMa12 from the Münchberg Metamorphic Complex (MMC), obtained with XRF, liquid ICP-MS, and LA ICP-MS. Abbreviation: \* = same content as determined with XRF.

Constituent	XRF	liquid ICP-MS	LA ICP-MS
Na <sub>2</sub> O / wt%	2.28		
MgO / wt%	10.31		
Al <sub>2</sub> O <sub>3</sub> / wt%	19.92		
SiO <sub>2</sub> / wt%	48.62		*
P <sub>2</sub> O <sub>5</sub> / wt%	0.034		
K <sub>2</sub> O / wt%	0.072		0.081
CaO / wt%	11.44		
TiO <sub>2</sub> / wt%	0.490		0.545
MnO / wt%	0.133		
Fe <sub>2</sub> O <sub>3</sub> / wt%	8.09		
SUM / wt%	101.39		
Cr / ppm	384	391.1	
Ni / ppm	68	77.6	
Rb / ppm	2.3	3.2	6.4
Sr / ppm	86	88.8	103.2
Y / ppm	12	8.3	11.1
Zr / ppm	30	8.1	42.3
Nb / ppm	6.8	1.7	2.1
Ba / ppm	27.5	15.8	15.6
La / ppm		3.4	3.6
Ce / ppm		7.7	7.6
Pr / ppm	1.1	1.1	1.2
Nd / ppm		5.2	5.6
Sm / ppm		1.4	1.5
Eu / ppm		0.7	0.7
Gd / ppm		1.7	1.7
Tb / ppm		0.3	0.3
Dy / ppm		1.9	2.0
Ho / ppm		0.4	0.4
Er / ppm		1.1	1.2
Tm / ppm		0.2	0.2
Yb / ppm		1.0	1.2
Lu / ppm		0.2	0.2
Hf / ppm		0.4	1.2
Ta / ppm		0.3	0.3
Th / ppm		0.3	0.3

Four different calibrations of the Zr-in-rutile thermometer (two by Zack et al. 2004; Watson et al. 2006; Tomkins et al. 2007 for  $\alpha$ -quartz) were applied to the studied sample. The 28 analyses of rutile yielded Zr contents between 204 and 349 ppm. After subtraction of a few outliers at the highest and lowest Zr contents, the remaining range of Zr contents is limited between about 230 and 310 ppm. A single rutile population is likely because of this limited range and many data close to the average of 267 ppm Zr in rutile. The calculated temperatures range from 682 °C (204 ppm Zr in rutile) to 727 °C (349 ppm) with a mean value of 703 (267 ppm)  $\pm$  5 °C ( $2\sigma$ ) using the calibration by Tomkins et al. (2007) for  $\alpha$ -quartz at 25 kbar (estimated). The calibration by Watson et al. (2006) yielded a mean temperature of 632  $\pm$  5 °C. Temperatures of 726  $\pm$  8 and 703  $\pm$  7 °C were obtained from the calibrations by Zack et al. (2004).

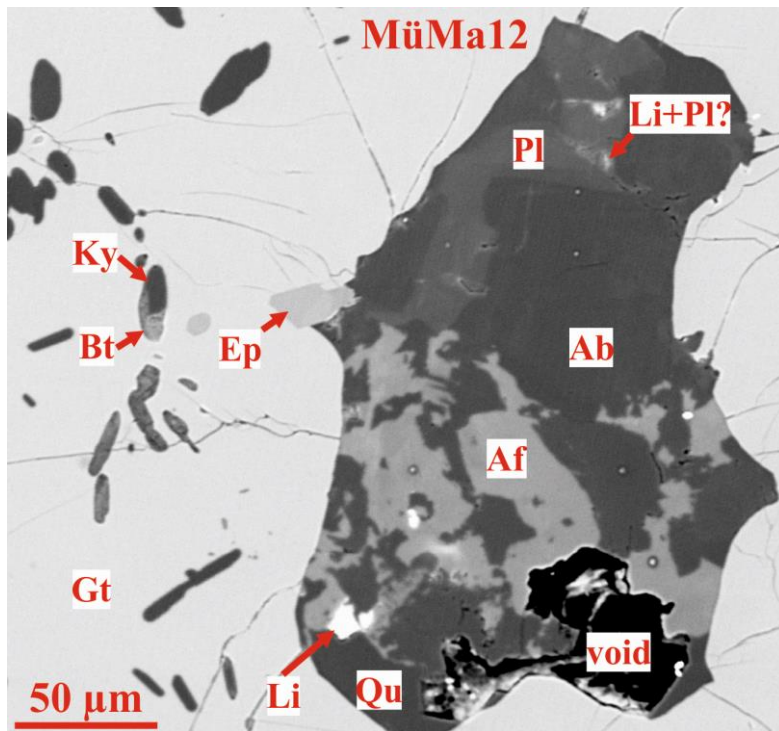


**Fig. 8.3:** Backscattered electron (BSE) image of a former melt inclusion in a garnet grain of eclogite sample MüMa12, obtained with a CAMECA SX100 EMP: Ab = albite, Af = alkali feldspar, Bt = biotite, Ep = clinozoisite-epidote, Gt = garnet, Ky = kyanite, Li = limonite, Pl = plagioclase, Qu = quartz.

**Tab. 8.2:** Representative analyses (in wt%) of garnet from the studied eclogite sample MüMa12 of the Münchberg Metamorphic Complex (MMC), obtained with a CAMECA SX100 EMP. The structural formulae were calculated as follows: 24 oxygen (double formula unit) and cation sum of Al + Ca + Cr + Fe + Mg + Mn + Na = 10. Abbreviation: calc = calculated.

Mineral	Garnet				
	Sample	MüMa12-gt2-2	MüMa12-gt2-8	MüMa12-gt3-1	MüMa12-gt3-12
SiO <sub>2</sub>	37.61	40.07	40.00	38.50	39.38
TiO <sub>2</sub>	0.04	0.02	0.00	0.02	0.06
Al <sub>2</sub> O <sub>3</sub>	22.89	23.37	23.36	22.40	22.91
Cr <sub>2</sub> O <sub>3</sub>	0.00	0.00	0.17	0.05	0.02
Fe <sub>2</sub> O <sub>3</sub> calc	0.01	0.00	0.00	0.31	0.01
FeO	17.21	16.77	18.24	16.67	16.88
MnO	0.31	0.26	0.30	0.33	0.30
MgO	11.28	11.72	11.54	12.23	11.73
CaO	8.41	8.22	7.30	7.01	8.09
Na <sub>2</sub> O	0.00	0.05	0.00	0.02	0.00
Total	97.76	100.49	100.91	97.53	99.39
Si	5.574	5.877	5.865	5.775	5.828
Ti	0.005	0.002	0.000	0.003	0.007
Al	3.999	4.041	4.036	3.960	3.996
Cr	0.000	0.000	0.020	0.006	0.002
Fe <sup>3+</sup>	0.001	0.000	0.000	0.035	0.001
Fe <sup>2+</sup>	2.133	2.057	2.237	2.091	2.089
Mg	2.492	2.563	2.524	2.735	2.589
Ca	1.335	1.292	1.147	1.127	1.283
Mn	0.039	0.033	0.037	0.042	0.038
Na	0.000	0.013	0.000	0.005	0.001

**Tab. 8.3:** Representative analyses (in wt%) of potassic white-mica from eclogite sample MüMa12 of the Münchberg Metamorphic Complex (MMC), obtained with a CAMECA SX100 EMP. The structural formulae were calculated as follows: 22 oxygen (double formula unit). For all micas the total was corrected for F. Abbreviation: calc = calculated.

Mineral	Potassic white-mica		
	Sample	MüMa12-ms1-1	MüMa12-ms1-5
SiO <sub>2</sub>	50.12	50.06	50.34
TiO <sub>2</sub>	0.59	0.53	0.55
Al <sub>2</sub> O <sub>3</sub>	29.23	29.46	29.74
FeO	0.82	0.70	0.71
MgO	3.79	3.48	3.49
Na <sub>2</sub> O	0.79	0.79	0.86
K <sub>2</sub> O	9.60	9.71	9.71
BaO	0.27	0.27	0.26
H <sub>2</sub> O <sub>calc</sub>	4.54	4.53	4.57
Total	99.75	99.55	100.26
Si	6.614	6.621	6.612
Ti	0.059	0.053	0.054
Al	3.160	3.213	3.215
Fe <sup>2+</sup>	0.090	0.077	0.078
Mg	0.746	0.687	0.684
Na	0.203	0.203	0.220
K	1.616	1.638	1.626
Ba	0.014	0.014	0.013

**Tab. 8.4:** Representative analyses (in wt%) of rutile from the studied eclogite sample MüMa12 of the Münchberg Metamorphic Complex (MMC), obtained with a CAMECA SX100 EMP. The structural formula of rutile is based on two oxygen anions.

Mineral	Rutile					
	Oxides in wt%	MüMa12-rt1-1	MüMa12-rt1-2	MüMa12-rt2-1	MüMa12-rt2-4	MüMa12-rt3-1
TiO <sub>2</sub>	99.47	99.50	99.47	99.53	99.52	99.29
SiO <sub>2</sub>	0.000	0.000	0.000	0.000	0.000	0.000
Nb <sub>2</sub> O <sub>5</sub>	0.070	0.060	0.060	0.050	0.070	0.070
FeO	0.150	0.150	0.200	0.100	0.140	0.190
ZrO <sub>2</sub>	0.040	0.030	0.030	0.040	0.040	0.040
Total	99.75	99.74	99.75	99.72	99.76	99.58
Ti	0.9976	0.9978	0.9973	0.9983	0.9978	0.9972
Si	0.0000	0.0000	0.0000	0.0000	0.0000	0.0000
Nb	0.0004	0.0004	0.0004	0.0003	0.0004	0.004
Fe	0.0017	0.0017	0.0022	0.0011	0.0015	0.0021
Zr	0.0003	0.0002	0.0002	0.0002	0.0002	0.0003

## 8.2 Additional Analyses of Eclogite Samples

In this section, additional analyses of eclogite samples 13Mm1, 13Mm7\_2 and MüMa03\_3c are provided (Tabs. 8.5 and 8.6, Figs. 8.4 and 8.5, as well as Tab. 8.7).

**Tab. 8.5:** Bulk-rock compositions of eclogite samples 13Mm7\_2 and MüMa03\_3c from the Münchberg Metamorphic Complex (MMC), obtained with XRF, liquid ICP-MS, and LA ICP-MS. XRF results were modified for PERPLE\_X calculations as explained in the text (see above). Abbreviation: \* = same content as determined with XRF.

Sample	13Mm7_2				MüMa03_3c				
	Constituent	XRF	modified	liquid ICP-MS	LA ICP-MS	XRF	modified	liquid ICP-MS	LA ICP-MS
Na <sub>2</sub> O / wt%	2.694	2.536			1.972	1.863			
MgO / wt%	7.078	6.663			10.249	9.682			
Al <sub>2</sub> O <sub>3</sub> / wt%	13.864	13.051			15.153	14.315			
SiO <sub>2</sub> / wt%	51.617	48.590			51.405	48.563			*
P <sub>2</sub> O <sub>5</sub> / wt%	0.157			0.176	0.063				0.071
K <sub>2</sub> O / wt%	0.194	0.183		0.211	0.054	0.051			0.055
CaO / wt%	11.360	10.499			11.151	10.456			
TiO <sub>2</sub> / wt%	1.439	1.355		1.627	0.838	0.792			0.884
MnO / wt%	0.201	0.189			0.172	0.162			
Fe <sub>2</sub> O <sub>3</sub> / wt%	13.177				9.277				
FeO / wt%		11.162				7.886			
O <sub>2</sub> / wt%		0.124				0.088			
H <sub>2</sub> O / wt%		5.648				6.141			
SUM / wt%	101.781	100.000			100.334	100.000			
Cr / ppm	164		168.0		420		372.2		
Ni / ppm	72		84.1		58		64.0		
Rb / ppm	2.6		3.1	3.4	2.4		2.5	2.5	
Sr / ppm	119		128.9	148.0	247		252.8	271.4	
Y / ppm	25		21.9	30.2	17		13.0	17.4	
Zr / ppm	66		21.3	99.8	42		17.7	70.7	
Nb / ppm	10		4.1	4.9	8.8		2.9	3.6	
Ba / ppm	68		43.5	44.7	22		8.9	10.0	
La / ppm			5.0	5.9	11		4.7	5.2	
Ce / ppm			13.5	14.1			10.8	11.6	
Pr / ppm			2.2	2.4			1.5	1.7	
Nd / ppm	18		11.2	12.5	4.8		7.2	8.4	
Sm / ppm	4.0		3.6	4.3			1.9	2.3	
Eu / ppm			1.4	1.4			0.8	0.9	
Gd / ppm			4.6	5.2			2.3	2.7	
Tb / ppm			0.9	0.9			0.4	0.5	
Dy / ppm			4.7	5.3			2.7	3.4	
Ho / ppm			1.0	1.1			0.6	0.8	
Er / ppm			2.7	3.1			1.8	2.3	
Tm / ppm			0.5	0.5			0.3	0.3	
Yb / ppm	3.7		2.6	3.2	3.9		1.7	2.2	
Lu / ppm			0.5	0.5			0.3	0.4	
Hf / ppm			0.9	3.2			0.7	2.1	
Ta / ppm	0.8		0.4	0.5			0.6	0.3	
Th / ppm			0.4	0.5	0.7		0.6	0.7	

**Tab. 8.6:** Representative analyses (in wt%) of clinozoisite-epidote, titanite, plagioclase, kyanite and ilmenite from eclogite samples 13Mm1, 13Mm7\_2 as well as MüMa03\_3c of the Münchberg Metamorphic Complex (MMC), obtained with a CAMECA SX100 EMP. The structural formulae were calculated as follows: a) clinozoisite-epidote: 12.5 oxygen, b) titanite: one silicon, c) plagioclase: eight oxygen, d) kyanite: three cations, e) ilmenite: three oxygen. Abbreviations: calc = calculated, Gt = garnet.

Mineral	Clinozoisite-Epidote			Titanite	Plagioclase	Kyanite	Ilmenite
	13Mm1- gt1e-11	13Mm7_2- gt3-e2-1	MüMa03_3 c-gt3e-4	13Mm1- gt-e-24	13Mm1- gt1-e6-10	MüMa03_ 3c-gt3e-1	13Mm1- gtm-15
Comment	enclosed in Gt						matrix
SiO <sub>2</sub>	37.91	38.53	38.10	30.48	67.69	36.86	
TiO <sub>2</sub>	0.24	0.15	0.02	38.46	0.02	0.01	54.74
Al <sub>2</sub> O <sub>3</sub>	29.80	27.16	32.14	1.27	18.58	63.01	0.00
Cr <sub>2</sub> O <sub>3</sub>	0.00	0.00	0.00	0.00		0.00	0.02
Fe <sub>2</sub> O <sub>3</sub> calc	3.51	9.23	3.86	0.69	3.75	0.66	0.00
FeO							44.50
MnO				0.00	0.02		0.51
MgO	0.29	0.13	0.08				0.99
CaO	22.58	23.20	22.90	28.08	2.52	0.06	
Na <sub>2</sub> O	0.00	0.01	0.15	0.05	9.68	0.00	
K <sub>2</sub> O					0.02		
H <sub>2</sub> O <sub>calc</sub>	1.89	1.93	1.95				
Total	96.22	100.42	99.31	99.13	102.29	100.66	100.75
Si	3.010	2.994	2.933	1.000	2.896	0.990	
Ti	0.014	0.009	0.001	0.949	0.001	0.000	1.026
Al	2.788	2.487	2.917	0.049	0.937	1.994	0.000
Cr	0.000	0.000	0.000	0.000		0.000	0.000
Fe <sup>3+</sup>	0.210	0.540	0.224	0.017	0.121	0.013	0.000
Fe <sup>2+</sup>							0.927
Mg	0.034	0.015	0.009				0.037
Ca	1.921	1.932	1.889	0.987	0.116	0.002	0.011
Mn				0.000	0.001		
Na	0.000	0.002	0.022	0.003	0.803	0.000	
K					0.001		

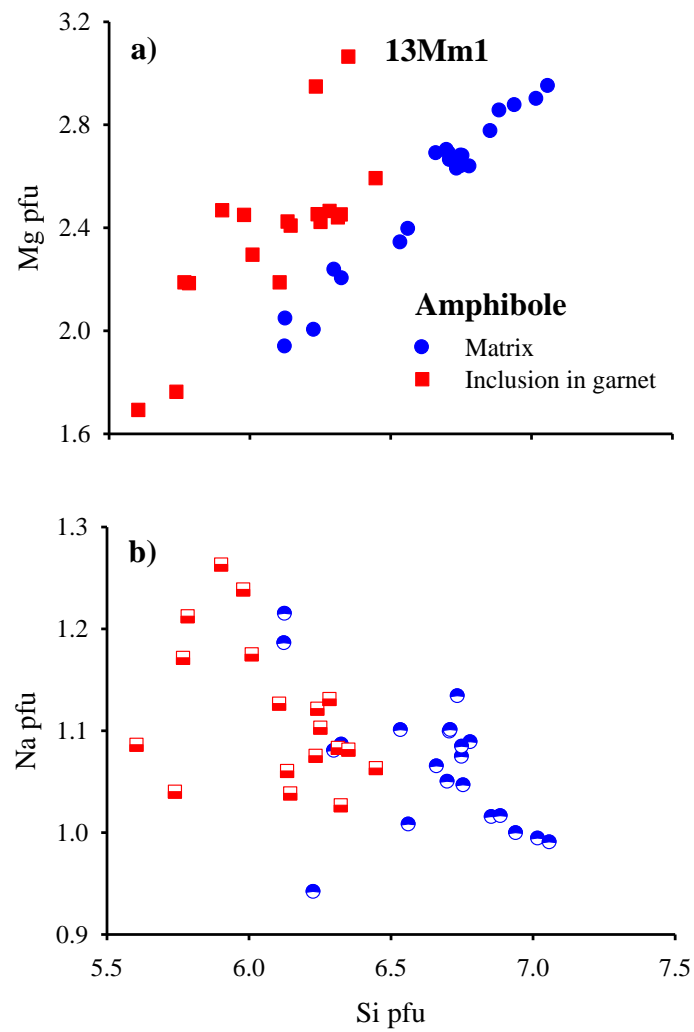


**Fig. 8.4:** Amphibole analyses of sample 13Mm1, obtained with a CAMECA SX100 EMP, in terms of contents of Mg per formula unit (pfu) (a) and Na pfu (b) versus that of Si pfu.

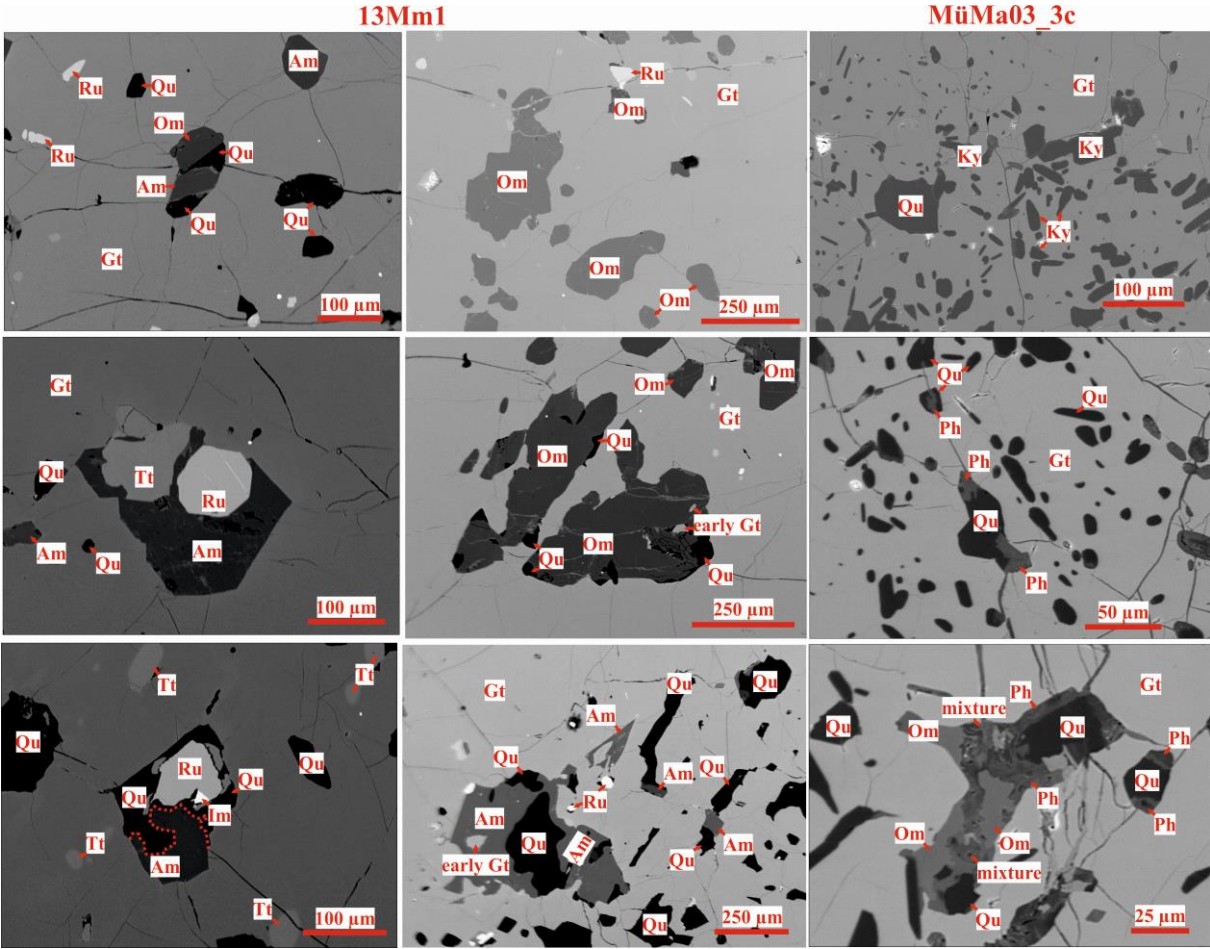


**Fig. 8.5:** Backscattered electron (BSE) images of (multiphase) garnet inclusions in eclogite samples 13Mm1 and MüMa03\_3c, obtained with a CAMECA SX100 EMP: Am = amphibole, Gt = garnet, Im = ilmenite, Ky = kyanite, Om = omphacite, Ph = potassic white-mica, Qu = quartz, Ru = rutile, Tt = titanite.

**Tab. 8.7:** Representative analyses (in wt%) of garnet (Gt) from sample 13Mm1, 13Mm7\_2 and MüMa03\_3c of the Münchberg Metamorphic Complex (MMC), obtained with a CAMECA SX100 EMP. The structural formulae were calculated as follows: 24 oxygen (double formula unit) and cation sum of Al + Ca + Cr + Fe + Mg + Mn + Na = 10. Abbreviations: calc = calculated, inter = intermediate.

Mineral	Garnet					Early Garnet
	Sample	13Mm7_ 2-gt3-1	13Mm7_ 2-gt3-5	MüMa03_ 3c-gt2-1	MüMa03_ 3c-gt2-2	MüMa03_ 3c-gt2-8
Comment	rim	core	rim	inter	core	enclosed in Gt
SiO <sub>2</sub>	36.22	35.83	40.23	40.31	40.25	38.24
TiO <sub>2</sub>	0.03	0.12	0.03	0.01	0.05	0.17
Al <sub>2</sub> O <sub>3</sub>	21.63	21.04	23.44	23.33	23.46	21.48
Cr <sub>2</sub> O <sub>3</sub>	0.04	0.04	0.02	0.05	0.02	0.05
Fe <sub>2</sub> O <sub>3</sub> <sub>calc</sub>	0.82	1.19	0.23	0.06	0.14	0.81
FeO	23.57	25.53	16.60	17.07	16.46	22.59
MnO	0.35	0.50	0.40	0.38	0.43	0.70
MgO	6.99	4.49	13.57	12.08	12.75	5.21
CaO	8.15	9.36	6.76	7.11	7.88	10.84
Na <sub>2</sub> O	0.02	0.04	0.01	0.04	0.05	0.04
Total	97.83	98.14	101.58	101.15	101.48	100.12
Si	5.543	5.573	5.831	5.846	5.796	5.891
Ti	0.004	0.014	0.003	0.002	0.006	0.019
Al	3.901	3.856	3.973	3.988	3.982	3.900
Cr	0.005	0.005	0.002	0.006	0.002	0.007
Fe <sup>3+</sup>	0.094	0.139	0.024	0.006	0.016	0.094
Fe <sup>2+</sup>	3.016	3.321	1.997	2.070	1.982	2.910
Mg	1.594	1.042	2.910	2.768	2.737	1.197
Ca	1.337	1.560	1.042	1.104	1.216	1.790
Mn	0.046	0.066	0.049	0.047	0.052	0.091
Na	0.007	0.011	0.003	0.011	0.013	0.012

## 8.3 Additional Analyses of Gneiss Samples

In this section, additional analyses of gneiss samples 13Mm8, 13Mm10, 13Mm11, 13Mm12, 13Mm13, 13Mm14, 13Mm16\_1, 13Mm18\_1, and 13Mm3 (compare Tab. 4.1) are provided (Tabs. 8.8, 8.9, and 8.10).

**Tab. 8.8:** Bulk-rock compositions of gneiss samples 13Mm8, 13Mm10, and 13Mm11 from the Münchberg Metamorphic Complex (MMC), obtained with XRF, liquid ICP-MS, and LA ICP-MS.

Sample Constituent	13Mm8			13Mm10			13Mm11	
	XRF	liquid ICP-MS	LA ICP- MS	XRF	liquid ICP-MS	LA ICP- MS	XRF	LA ICP- MS
Na <sub>2</sub> O / wt%	3.064		2.121	1.673		1.458	3.824	2.806
MgO / wt%	0.675		0.794	2.011		2.573	2.052	2.417
Al <sub>2</sub> O <sub>3</sub> / wt%	15.088		13.135	21.370		21.690	18.155	12.110
SiO <sub>2</sub> / wt%	70.006		65.403	59.482		60.102	63.654	62.152
P <sub>2</sub> O <sub>5</sub> / wt%	0.217			0.125			0.199	
K <sub>2</sub> O / wt%	3.921		3.859	3.517		3.392	2.497	2.555
CaO / wt%	1.421		1.196	0.807		0.787	0.866	1.052
TiO <sub>2</sub> / wt%	0.506		0.594	0.991		0.939	0.806	1.014
MnO / wt%	0.058			0.241			0.098	
Fe <sub>2</sub> O <sub>3</sub> / wt%	3.960		3.857	8.459		8.215	6.787	6.933
SUM / wt%	98.916			98.675			98.938	
Sc / ppm	8.0	7.1	10.5	9.6	8.9	22.1	13	20.3
V / ppm	37	35.0	40.4	112	118.1	116.7	132	140.3
Cr / ppm	21	13.2	33.1	82	90.1	127.5	65	94.6
Ni / ppm		6.1	15.2	11	23.1	33.0	21	45.4
Rb / ppm	104	56.8	115.9	151	56.8	152.6	75	83.7
Sr / ppm	99	54.3	111.5	145	78.3	167.9	151	181.8
Y / ppm	30	18.7	24.0	28	17.6	28.9	31	31.9
Zr / ppm	238	168.8	288.0	129	83.5	178.8	189	238.1
Nb / ppm	14	12.6	15.2	17	16.4	15.9	14	15.0
Cs / ppm	7.6		3.9			7.9		3.6
Ba / ppm	694	630.3	766.8	651	277.0	673.3	566	575.5
La / ppm	17	7.2	14.1	30	19.3	35.1	27	36.2
Ce / ppm	44	15.6	37.3	81	52.8	91.7	56	70.1
Pr / ppm	5.1	2.4	3.0	11	4.9	10.1	9.6	8.3
Nd / ppm	15	10.7	14.5	36	19.6	43.7	28	37.5
Sm / ppm	6.8	2.8	3.5		3.8	8.7		8.0
Eu / ppm		0.6	0.6		0.9	1.7		1.7
Gd / ppm		3.1	3.7		4.1	7.0		8.2
Tb / ppm		0.6	0.7		0.6	1.0		1.2
Dy / ppm		4.2	4.8		3.9	6.1		7.3
Ho / ppm		0.9	1.1		0.8	1.2		1.5
Er / ppm		2.8	3.7		2.2	3.6		4.2
Tm / ppm		0.5	0.6		0.4	0.5		0.6
Yb / ppm	4.2	3.2	4.4		2.4	3.3		4.6
Lu / ppm		0.5	0.6		0.4	0.5		0.7
Hf / ppm		4.1	9.3		1.5	5.1		8.0
Ta / ppm	1.4	1.1	1.3	1.8	1.3	1.3	1.9	1.1
Th / ppm	9.7	7.8	13.5	10	5.6	15.1	7.1	12.2
U / ppm		1.9	2.8		2.2	2.8		3.4

**Tab. 8.9:** Bulk-rock compositions of gneiss samples 13Mm12, 13Mm13, and 13Mm14 from the Münchberg Metamorphic Complex (MMC), obtained with XRF, liquid ICP-MS, and LA ICP-MS.

Sample	13Mm12		13Mm13		13Mm14	
	XRF	LA ICP-MS	XRF	LA ICP-MS	XRF	LA ICP-MS
Na <sub>2</sub> O / wt%	2.420	2.098	3.289	2.904	3.137	2.332
MgO / wt%	1.802	2.311	1.581	2.061	2.462	2.742
Al <sub>2</sub> O <sub>3</sub> / wt%	17.141	17.568	14.665	14.462	17.201	15.835
SiO <sub>2</sub> / wt%	66.353	69.122	70.648	72.017	63.640	59.218
P <sub>2</sub> O <sub>5</sub> / wt%	0.083		0.217		0.113	
K <sub>2</sub> O / wt%	3.000	2.991	3.423	3.463	2.676	2.482
CaO / wt%	0.600	0.628	0.894	0.938	0.947	0.917
TiO <sub>2</sub> / wt%	0.809	0.825	0.458	0.478	0.884	0.836
MnO / wt%	0.092		0.054		0.156	
Fe <sub>2</sub> O <sub>3</sub> / wt%	6.155	6.339	3.534	3.564	7.184	7.431
SUM / wt%	98.454		98.761		98.400	
Sc / ppm	13	20.6		10.3	11	19.3
V / ppm	117	126.7	51	59.3	118	124.8
Cr / ppm	58	98.6	60	103.2	59	97.2
Ni / ppm	15	41.4	24	56.6	13	39.0
Rb / ppm	74	84.5	97	108.3	76	85.4
Sr / ppm	99	121.7	99	111.8	99	122.4
Y / ppm	33	34.0	19	13.7	33	33.7
Zr / ppm	222	276.6	146	175.8	181	228.9
Nb / ppm	14	13.5	11	10.0	14	12.6
Cs / ppm		2.2		1.3	9.7	5.1
Ba / ppm	630	641.4	426	486.3	348	386.7
La / ppm	29	41.6	17	14.3	18	35.4
Ce / ppm	58	73.7	29	31.9	41	64.3
Pr / ppm	7.1	8.8	5.6	3.2		7.7
Nd / ppm	28	40.4	19	14.0	20	35.8
Sm / ppm	5.4	9.5		3.1		8.0
Eu / ppm		1.7		0.5		1.4
Gd / ppm		7.8		2.9		6.8
Tb / ppm		1.2		0.4		1.0
Dy / ppm		6.9		2.7		6.3
Ho / ppm		1.4		0.5		1.2
Er / ppm		4.3		1.6		3.7
Tm / ppm		0.6		0.2		0.6
Yb / ppm	3.7	4.3		1.2	3.2	3.7
Lu / ppm		0.6		0.2		0.5
Hf / ppm		7.7		4.2		6.1
Ta / ppm	1.5	1.1	1.6	0.8	2.5	0.8
Th / ppm	9.2	11.8	7.1	7.5	6.8	9.6
U / ppm		3.3		1.9		2.7

**Tab. 8.10:** Bulk-rock compositions of gneiss samples 13Mm16\_1, 13Mm18\_1, and 13Mm3 (compare Tab. 4.1) from the Münchberg Metamorphic Complex (MMC), obtained with XRF, liquid ICP-MS, and LA ICP-MS.

Sample	13Mm16_1		13Mm18_1		13Mm3		
	XRF	LA ICP-MS	XRF	LA ICP-MS	XRF	liquid ICP-MS	LA ICP-MS
Na <sub>2</sub> O / wt%	3.929	3.269	2.245	2.129	1.424		0.989
MgO / wt%	3.654	4.491	2.418	3.284	1.556		1.741
Al <sub>2</sub> O <sub>3</sub> / wt%	17.111	17.124	18.824	20.947	15.061		13.779
SiO <sub>2</sub> / wt%	58.049	54.902	62.358	62.163	71.083		66.328
P <sub>2</sub> O <sub>5</sub> / wt%	0.189		0.101		0.055		
K <sub>2</sub> O / wt%	1.533	1.588	3.239	3.490	3.622		3.674
CaO / wt%	6.105	5.785	0.809	0.898	0.256		0.344
TiO <sub>2</sub> / wt%	0.769	0.795	0.889	0.951	0.779		0.773
MnO / wt%	0.120		0.177		0.071		
Fe <sub>2</sub> O <sub>3</sub> / wt%	7.105	7.173	7.174	8.643	5.539		5.311
SUM / wt%	98.565		98.233		99.445		
Sc / ppm		20.7	13	22.6	8.6	8.7	16.4
V / ppm	111	133.9	140	160.1	99	102.5	114.2
Cr / ppm	55	102.9	69	130.3	54	61.2	93.3
Ni / ppm	32	63.6	23	63.4	4.2	18.5	28.8
Rb / ppm	23	25.9	91	143.0	98	75.2	111.6
Sr / ppm	270	319.1	105	176.1	78	75.8	95.2
Y / ppm	33	32.1	32	43.9	24	11.5	24.6
Zr / ppm	178	262.1	187	329.3	207	182.0	284.1
Nb / ppm	7.8	4.2	15	18.1	13	11.5	13.5
Cs / ppm		0.3		3.9	6.0		3.4
Ba / ppm	438	480.8	659	682.9	646	415.7	691.8
La / ppm	18	14.7	31	35.8		22.1	31.4
Ce / ppm	23	31.6	64	68.7	32	48.1	62.8
Pr / ppm		4.2		8.1	3.5	5.7	7.3
Nd / ppm	10	21.8	31	36.8	14	22.6	32.1
Sm / ppm		5.9		7.9		4.3	6.5
Eu / ppm		1.5		1.5		1.1	1.4
Gd / ppm		6.0		6.2		4.1	5.8
Tb / ppm		0.9		0.9		0.5	0.9
Dy / ppm		6.0		5.9		2.8	5.4
Ho / ppm		1.2		1.2		0.5	1.1
Er / ppm		3.7		3.8		1.5	3.2
Tm / ppm		0.5		0.6		0.2	0.5
Yb / ppm	6.5	3.8		3.7	4.1	1.5	3.3
Lu / ppm		0.5		0.6		0.2	0.5
Hf / ppm		5.5		6.6		4.4	7.8
Ta / ppm		0.3		1.1		0.8	0.8
Th / ppm	2.2	0.7	8.1	12.3	6.2	6.6	9.6
U / ppm		0.4		2.9		2.0	2.3

## 8.4 Analytical Work

In Tab. 8.11, there is a general overview of the analytical work of this study (XRF, liquid ICP-MS, LA ICP-MS and EMP). Additionally, all 13MmX (X = 1, 3, 6, 7\_2, 8, 10, 11, 12, 13, 14, 16\_1, 18\_1) and MüMaY (Y = 03\_3c, 12) samples were analysed by a polarisation microscope ZEISS Axioplan as well as a Carbon and Water Analyser (LECO® RC-412).

**Tab. 8.11:** Analytical overview of this study (XRF, liquid ICP-MS, LA ICP-MS and EMP). Only successful measurements are mentioned. Analyses of original (geo)standards of our equipment are left out. Abbreviations: Ala = allanite, Am = amphibole, Bt = biotite, Ch = chlorite, Ep = clinozoisite-epidote, Gt = garnet, Im = ilmenite, Kf = K-feldspar, Ky = kyanite, Mz = monazite, Om = omphacite, Pa = paragonite, Ph = potassic white-mica, Pl = plagioclase, Pu = pumpellyite, Ru = rutile, Tt = titanite.

Sample	XRF		liquid ICP-MS	LA ICP-MS	EMP
	major elements	trace elements			
13Mm1	2	2	1	2	264 Gt, 68 Om, 50 Ru, 42 Am, 26 Ph, 7 Tt, 6 Gt map, 3 Ep, 2 Ala, 2 Im, 1 Am map, 1 Om map, 1 Ph map, 1 Pl
13Mm3	2	2	1	6	116 Gt, 100 Mz, 46 Ph, 26 Ru, 18 Bt, 13 Kf, 11 Pl, 8 Gt map, 7 Ph map, 6 Ky, 2 Im, 1 Mz map
13Mm6	3	2	1	4	114 Gt, 26 Mz, 9 Ph, 4 Gt map, 1 Ph map
13Mm7_2	2	1	1	2	61 Gt, 42 Ru, 10 Am, 10 Om, 10 Ph, 3 Gt map, 1 Am map, 1 Ep, 1 Om map, 1 Ph map
13Mm8	3	2	1	4	59 Gt, 16 Bt, 12 Ph, 4 Gt map, 4 Kf, 2 Tt, 1 Ch, 1 Ph map
13Mm10	4	3	1	5	101 Gt, 31 Ru, 29 Mz, 16 Ph, 7 Ch, 5 Pl, 4 Gt map, 2 Pa, 1 Ph map
13Mm11	3	2		4	95 Gt, 34 Ru, 29 Mz, 12 Ph, 9 Bt, 6 Gt map, 1 Ch, 1 Ph map
13Mm12	4	3		5	55 Gt, 52 Mz, 29 Ph, 22 Ch, 21 Ru, 15 Pl, 13 Bt, 6 Gt map, 2 Ph map
13Mm13	2	1		3	28 Kf, 27 Ru, 26 Pl, 25 Ph, 15 Ch, 2 Ph map
13Mm14	2	1		3	53 Gt, 34 Mz, 22 Ch, 12 Ph, 4 Gt map, 2 Ph map, 2 Pl
13Mm16_1	2	1		3	61 Gt, 17 Ru, 13 Ep, 9 Ch, 8 Ph, 4 Gt map, 4 Pl, 1 Ph map, 1 Tt
13Mm18_1	2	1		3	66 Gt, 32 Mz, 18 Ru, 12 Ph, 10 Ch, 4 Gt map, 2 Mz map, 2 Pa, 1 Bt, 1 Ph map
MüMa03_3c	3	1	1	3	111 Gt, 61 Ph, 53 Ru, 25 Ky, 22 Om, 11 Am, 7 Gt map, 6 Ep, 5 Pu, 2 Kf, 2 Ph map, 1 Am map, 1 Om map
MüMa12	2	2	1	2	70 Gt, 28 Ru, 8 Ph, 7 Am, 7 Om, 4 Gt map, 1 Am map, 1 Om map, 1 Ph map
DR-N	7	3	2	4	
ZW-C	6	3	2	2	
7 pressed tablets		3 + 6			
E97					30 Mz



## 9. Bibliography

- Andersen DJ, Lindsley DH (1988) Internally consistent solution models for Fe-Mg-Mn-Ti oxides - Fe-Ti oxides. *Am Mineral* 73:714-726.
- Arenas R, Fernández RD, Martínez SS, Gerdes A, Fernández-Suárez J (2014) Two-stage collision: Exploring the birth of Pangea in the Variscan terranes. *Gondwana Res* 25:756-763.
- Balen D, Massonne H-J, Petrinc Z (2015) Collision-related Early Paleozoic evolution of a crustal fragment from the northern Gondwana margin (Slavonian Mts, Tisia Mega-Unit, Croatia): reconstruction of the P-T path, timing and paleotectonic implications. *Lithos* 232:211-228.
- Beard BL, Medaris LG, Johnson CM, Jelínek E, Tonika J, Riciputi LR (1995) Geochronology and geochemistry of eclogites from the Mariánské Lázně Complex, Czech Republic: Implications for Variscan orogenesis. *Geol Rundsch* 84:552-567.
- Bhatia MR (1983) Plate Tectonics and Geochemical Composition of Sandstones. *J Geol* 91:611-627.
- Blümel P (1986) Metamorphic processes in the Variscan crust of the central segment. In: Freeman R, Muelter S, Giese P (eds) Proceedings of the third workshop on the European geotraverse (EGT) project: the central segment. European Science Foundations, Strasbourg, pp 149-155.
- Boynton WV (1984) Geochemistry of the rare earth elements: meteorite studies. In: Henderson P (ed) Rare Earth Element Geochemistry, Elsevier, Amsterdam, pp 63-114.
- Brandelik A (2009) CALCMIN – an EXCEL™ Visual Basic application for calculating mineral structural formulae from electron microprobe analyses. *Comp Geosc* 35:1540-1551.
- Bröcker M, Żelaźniewicz A, Enders M (1998) Rb–Sr and U–Pb geochronology of migmatitic gneisses from the Góry Sowie (West Sudetes, Poland): the importance of Mid–Late Devonian metamorphism. *J Geol Soc London* 155:1025-1036.
- Broska I, Siman P (1998) The breakdown of monazite in the West-Carpathian Veporic orthogneisses and Tatric granites. *Geol Carpathica* 49:161-167.
- Broska I, Williams CT, Janák M, Nagy G (2005) Alteration and breakdown of xenotime-(Y) and monazite-(Ce) in granitic rocks of the Western Carpathians, Slovakia. *Lithos* 82:71-83.
- Brouwer P (2010) THEORY OF XRF - Getting acquainted with the principles. 3rd edn. PANalytical B.V., Almelo.

- Budzikiewicz H, Schäfer M (2005) *Massenspektrometrie – Eine Einführung*. 5th edn. Wiley-VCH Verlag GmbH & Co. KGaA, Weinheim.
- Buschmann B, Nasdala L, Jonas P, Linnemann U, Gehmlich M (2001) SHRIMP U-Pb dating of tuff-derived and detrital zircons from Cadomian marginal basin fragments (Neoproterozoic) in the northeastern Saxothuringian Zone (Germany). *Neues Jahrb Geol P-M* 2001:321-342.
- Buschmann B, Elicki O, Jonas P (2006) The Cadomian unconformity in the Saxo-Thuringian Zone, Germany: Paleogeographic affinities of Ediacarian (terminal Neoproterozoic) and Cambrian strata. *Precambr Geol* 104:387-403.
- Caddick MJ, Kohn MJ (2013) Garnet: Witness to the evolution of destructive plate boundaries. *Elements* 9:427-432.
- Carswell DA (1990) *Eclogite Facies Rocks*. Springer Science + Business Media, New York.
- Catlos EJ, Harrison TM, Kohn MJ, Grove M, Ryerson FJ (2001) Geochronologic and thermobarometric constraints on the evolution of the Main Central Thrust, central Nepal Himalaya. *J Geophys Res* 106:16177-16204.
- Cawood PA, Kröner A, Collins WJ, Kusky TM, Mooney WD, Windley BF (2009) Accretionary orogens through Earth history. *Geol Soc London Spec Publ* 318:1-36.
- Cesare B, Acosta-Vigil A, Ferrero S, Bartoli O (2011) Melt inclusions in migmatites and granulites. *J Virtual Explorer* 38, paper 2. In: Forster MA, Fitzgerald JD (eds) *The Science of microstructure - Part II*.
- Connolly JAD (2005) Computation of phase equilibria by linear programming: a tool for geodynamic modeling and its application to subduction zone decarbonation. *Earth Planet Sc Lett* 236:524-541.
- Coward MP (1986) Heterogeneous stretching, simple shear and basin development. *Earth Planet Sc Lett* 80:325-336.
- Dallmeyer RD, Franke W, Weber K (1995) *Pre-Permian Geology of Central and Eastern Europe*. Springer-Verlag Berlin Heidelberg GmbH, Berlin.
- Deer WA, Howie RA, Zussman J (1992) *An Introduction to the Rock-Forming Minerals*. 2nd edn. Pearson, Edinburgh.
- Donovan JJ, Hanchar JM, Picolli PM, Schrier MD, Boatner LA, Jarosewich E (2003) A RE-EXAMINATION OF THE RARE-EARTH-ELEMENT ORTHOPHOSPHATE STANDARDS IN USE FOR ELECTRON-MICROPROBE ANALYSIS. *Canad Mineral* 41:221-232.

- Drost K, Kroner U (2003) Franz Kossmat – Originator of the Variscan orogenic zoning. *Geol Saxonica* 48-49:17-22.
- Dudek A (1995) Igneous Activity. In: Dallmeyer RD, Franke W, Weber K (eds) *Pre-Permian Geology of Central and Eastern Europe*. Springer-Verlag Berlin Heidelberg GmbH, Berlin, pp 398-402.
- Düll E (1902) Über die Eklogite des Münchberger Gneisgebietes – Ein Beitrag zur Kenntnis ihrer genetischen Verhältnisse. *Geognost Jahresh XV*:65-156.
- Egerton RF (2010) *Physical Principles of Electron Microscopy – An Introduction to TEM, SEM, and AEM*. Springer Science + Business Media, New York.
- Faryad SW (2012) High-pressure polymetamorphic garnet growth in eclogites from the Mariánské Lázně Complex (Bohemian Massif). *Eur J Mineral* 24:483-497.
- Ferry JM (2000) Patterns of mineral occurrence in metamorphic rocks. *Am Mineral* 85:1573-1588.
- Finger F, Broska I, Roberts MP, Schermaier A (1998) Replacement of primary monazite by apatite-allanite-epidote coronas in an amphibolite facies granite gneiss from the eastern Alps. *Am Mineral* 83:248-258.
- Floyd PA, Shail R, Leveridge BE, Franke W (1991) Geochemistry and provenance of Rhenohercynian synorogenic sandstones: implications for tectonic environment discrimination. *Geol Soc London Spec Publ* 57:173-188.
- Förster H-J, Romer RL (2010) Carboniferous magmatism. In: Linnemann U, Romer RL (eds) *Pre-Mesozoic Geology of Saxo-Thuringia - From the Cadomian Active Margin to the Variscan Orogen*. Schweizerbart, Stuttgart, pp 287-308.
- Franke W (1984) Variszischer Deckenbau im Raum der Münchberger Gneismasse - abgeleitet aus der Fazies, Deformation und Metamorphose im umgebenden Paläozoikum. *Geotektonische Forschungen* 68:1-253.
- Franke W (1989) Variscan plate tectonics in Central Europe – current ideas and open questions. *Tectonophys* 169:221-228.
- Franke W (2000) The mid-European segment of the Variscides: tectonostratigraphic units, terrane boundaries and plate tectonic evolution. In: Franke W, Haak V, Oncken O, Tanner D (eds) *Orogenic Processes: Quantification and Modelling in the Variscan Belt*. *Geol Soc London Spec Publ* 179:35-61.
- Franke W, Stein E (2000) Exhumation of high-grade rocks in the Saxo-Thuringian Belt: geological constraints and geodynamic concepts. In: Franke W, Haak V, Oncken O,

- Tanner D (eds) *Orogenic Processes: Quantification and Modelling in the Variscan Belt*. Geol Soc London Spec Publ 179:337-354.
- Franke W, Cocks LRM, Torsvik TH (2017) The Palaeozoic Variscan oceans revisited. *Gondwana Res* 48:257-284.
- Franz G, Thomas S, Smith DC (1986) High-pressure phengite decomposition in the Weissenstein eclogite, Münchberger Gneiss Massif, Germany. *Contrib Mineral Petrol* 92:71-85.
- Franz G, Andrehs G, Rhede D (1996) Crystal chemistry of monazite and xenotime from Saxothuringian-Moldanubian metapelites, NE Bavaria, Germany. *Eur J Mineral* 8:1097-1108.
- Fuhrman ML, Lindsley DH (1988) Ternary-feldspar modeling and thermometry. *Am Mineral* 73:201-215.
- Gasquet D, Bertrand J-M, Paquette J-L, Lehmann J, Ratzov G (2010) Miocene to Messinian deformation and hydrothermal activity in a pre-Alpine basement massif of the French western Alps: new U-Th-Pb and argon ages from the Lauzière massif. *Bull Soc géol Fr* 3:227-241.
- Gebauer D, Grünenfelder M (1979) U-Pb Zircon and Rb-Sr mineral dating of eclogites and their country rocks. Example: Münchberg Gneiss Massif, northeast Bavaria. *Earth Planet Sc Lett* 42:35-44.
- Gerdes A, Zeh A (2006) Combined U-Pb and Hf isotope LA-(MC-)ICP-MS analyses of detrital zircons: Comparison with SHRIMP and new constraints for the provenance and age of an Armorican metasediment in Central Germany. *Earth Planet Sc Lett* 249:47-61.
- Gerya TV, Stöckhert B (2002) Exhumation rates of high pressure metamorphic rocks in subduction channels: The effect of rheology. *Geophys Res Lett* 29:1261-1264.
- Gerya TV, Stöckhert B, Perchuk AL (2002) Exhumation of high-pressure metamorphic rocks in a subduction channel: A numerical simulation. *Tectonics* 6:1-15.
- Getty SR, Selverstone J, Wernicke BP, Jacobsen SB, Aliberti E, Lux DR (1993) Sm-Nd dating of multiple garnet growth events in an arc-continent collision zone, northwestern U.S. Cordillera. *Contrib Mineral Petrol* 115:45-57.
- Geyer G, Elicki O, Fatka O, Żylinska A (2008) Cambrian. In: McCann T (ed) *The Geology of Central Europe*. Geol Soc, London, pp 155-202.
- Gieré R, Sorensen SS (2004) Allanite and other REE-rich epidote-group minerals. *Rev Mineral Geochem* 56:431-493.

- Godard G (2001) Eclogites and their geodynamic interpretation: a history. *J Geodyn* 32:165-203.
- Goldstein J, Newbury D, Joy D, Lyman C, Echlin P, Lifshin E, Sawyer L, Michael J (2007) *Scanning Electron Microscopy and X-Ray Microanalysis*. 3rd edn. Springer Science + Business Media, New York.
- Goswami-Banerjee S, Robyr M (2015) Pressure and temperature conditions for crystallization of metamorphic allanite and monazite in metapelites: a case study from the Miyar Valley (high Himalayan Crystalline of Zaskar, NW India). *J Metamorph Geol* 33:535-556.
- Grieken RV, Markowicz A (2001) *Handbook of X-ray Spectrometry*. 2nd edn. Marcel Dekker, New York.
- Gross JH (2011) *Mass Spectrometry*. 2nd edn. Springer Science + Business Media, Heidelberg.
- Guy A, Edel J-B, Schulmann K, Tomek Č, Lexa O (2011) A geophysical model of the Variscan orogenic root (Bohemian Massif): Implications for modern collisional orogens. *Lithos* 124:144-157.
- Hammerschmidt K, Franz G (1992) Retrograde evolution of eclogites: evidences from microstructures and  $^{40}\text{Ar}/^{39}\text{Ar}$  white mica dates, Münchberg Massif, northern Bavaria. *Contrib Mineral Petrol* 111:113-125.
- Hanwen Z, Xianhua L, Ying L, Zhendong Y, Shutian S, Zengqiu Z (1999) Age of granulite from Huangtuling, Dabie Mountain: Pb-Pb dating of garnet by a stepwise dissolution technique. *Chinese Sci Bull* 10:941-944.
- Harley SL, Kelly NM (2007) Zircon - tiny but timely. *Elements* 3:13-18.
- Holland TJB, Powell R (1996) Thermodynamics of order-disorder in minerals. 2. Symmetric formalism applied to solid solutions. *Am Mineral* 81:1425-1437.
- Holland TJB, Baker JM, Powell R (1998) Mixing properties and activity-composition relationships of chlorites in the system  $\text{MgO-FeO-Al}_2\text{O}_3\text{-SiO}_2\text{-H}_2\text{O}$ . *Eur J Mineral* 10:395-406.
- Holland TJB, Powell R (1998) An internally consistent thermodynamic data set for phases of petrological interest. *J Metamorph Geol* 16:309-343.
- Hoskin PWO, Schaltegger U (2003) The Composition of Zircon and Igneous and Metamorphic Petrogenesis. *Rev Mineral Geochem* 53:27-62.
- Housecroft CE, Sharpe AG (2006) *Anorganische Chemie*. 2nd edn. Pearson Studium, München.

- Jackson MG, Hart SR, Saal AE, Shimizu N, Kurz MD, Blusztajn JS, Skovgaard AC (2008) Globally elevated titanium, tantalum, and niobium (TITAN) in ocean island basalts with high  $^3\text{He}/^4\text{He}$ . *Geochem Geophys Geosy* 9:1525-2027.
- Jahn B-M (1998) Geochemical and isotopic characteristics of UHP eclogites and ultramafic rocks of the Dabie orogen: Implications for continental subduction and collisional tectonics. In: Hacker BR, Liou JG (eds) *When continents collide: Geodynamics and geochemistry of ultrahigh-pressure rocks*. Kluwer Academic Publishers, Dordrecht, pp 203-239.
- Jahn B-M, Caby R, Monie P (2001) The oldest UHP eclogites of the World: age of UHP metamorphism, nature of protoliths and tectonic implications. *Chem Geol* 178:143-158.
- Janots E, Brunet F, Goffé B, Poinssot C, Burchard M, Cemic L (2007) Thermochemistry of monazite-(La) and dissakisite-(La): implications for monazite and allanite stability in metapelites. *Contrib Mineral Petrol* 154:1-14.
- Janots E, Engi M, Berger A, Allaz J, Schwarz J-O, Spandler C (2008) Prograde metamorphic sequence of REE minerals in pelitic rocks of the Central Alps: implications for allanite–monazite–xenotime phase relations from 250 to 610 °C. *J Metamorph Geol* 26:509-526.
- Jarosewich E (1991) Rare-Earth Element Reference Samples for Electron Microprobe Analysis. *Geostandard Newslett* 15:397-399.
- Jarosewich E (2002) Smithsonian Microbeam Standards. *J Res Natl Inst Stand Technol* 107:681-685.
- Jarosewich E, Nelen JA, Norberg JA (1980) Reference Samples for Electron Microprobe Analysis. *Geostandard Newslett* 4:43-47.
- Kachlík V (1993) The evidence for Late Variscan nappe thrusting of the Mariánské Lázně Complex over the Saxothuringian terrane (West Bohemia). *J Czech Geol Soc* 38:43-58.
- Kelsey DE, Clark C, Hand M (2008) Thermobarometric modelling of zircon and monazite growth in melt-bearing systems: examples using model metapelitic and metapsammitic granulites. *J Metamorph Geol* 26:199-212.
- Keppie JD, Nance RD, Murphy JB, Dostal J, Braid JA (2010) The high-pressure Iberian-Czech belt in the Variscan orogeny: extrusion into the upper (Gondwanan) plate? *Gondwana Res* 17:306-316.
- Klein C, Philpotts AR (2013) *Earth Materials – Introduction to Mineralogy and Petrology*. Cambridge University Press, New York.
- Klemd R (1989) P-T evolution and fluid inclusion characteristics of retrograded eclogites, Münchberg Gneiss Complex, Germany. *Contrib Mineral Petrol* 102:221-229.

- Klemm R (2010) Early Variscan allochthonous domains: the Münchberg Complex, Frankenberg, Wildenfels, and Góry Sowie. In: Linnemann U, Romer RL (eds) Pre-Mesozoic Geology of Saxo-Thuringia - From the Cadomian Active Margin to the Variscan Orogen. Schweizerbart, Stuttgart, pp 221-232.
- Klemm R, Matthes S, Okrusch M (1991) High-pressure relics in meta-sediments intercalated with the Weissenstein eclogite, Münchberg gneiss complex, Bavaria. *Contrib Mineral Petrol* 107:328-342.
- Klemm R, Matthes S, Schüssler U (1994) Reaction textures and fluid behaviour in very high-pressure calc-silicate rocks of the Münchberg gneiss complex, Bavaria, Germany. *J Metamorph Geol* 12:735-745.
- Kotková J, O'Brien PJ, Ziemann MA (2011) Diamond and coesite discovered in Saxony-type granulite: Solution to the Variscan garnet peridotite enigma. *Geology* 39:667-670.
- Krebs M, Schertl H-P, Maresch WV, Draper G (2011) Mass flow in serpentinite-hosted subduction channels:  $P$ - $T$ - $t$  path patterns of metamorphic blocks in the Rio San Juan mélangé (Dominican Republic). *J Asian Earth Sci* 42:569-595.
- Kreuzer H, Seidel E, Schüssler U, Okrusch M, Lenz K-L (1989) K-Ar geochronology of different tectonic units at the northwestern margin of the Bohemian Massif. *Tectonophysics* 157:149-178.
- Kreuzer H, Henjes-Kunst F, Seidel E, Bühn B (1993) Ar-Ar spectra on minerals from KTB and related medium-pressure units. *KTB Rep* 93-2:133-136.
- Krohe A (1996) Variscan tectonics of central Europe: Postaccretionary intraplate deformation of weak continental lithosphere. *Tectonics* 15:1364-1388.
- Kröner A, Hegner E (1998) Geochemistry, single zircon ages and Sm-Nd systematics of granitoid rocks from the Góry Sowie (Owl Mts), Polish West Sudetes: evidence for early Palaeozoic arc-related plutonism. *J Geol Soc London* 155:711-724.
- Kröner A, Willner AP (1998) Time of formation and peak of Variscan HP-HT metamorphism of quartzofeldspathic rocks in the central Erzgebirge, Saxony, Germany. *Contrib Mineral Petrol* 132:1-20.
- Kroner U, Hahn T, Romer RL, Linnemann U (2007) The Variscan orogeny in the Saxo-Thuringian zone – Heterogeneous overprint of Cadomian/Paleozoic Peri-Gondwana crust. In: Linnemann U, Nance RD, Kraft P, Zulauf G (eds) *The Evolution of the Rheic Ocean: From Avalonian-Cadomian Active Margin to Alleghenian-Variscan Collision*. *Geol Soc Am Spec Pap* 423:153-172.

- Kroner U, Mansy J-L, Mazur S, Aleksandrowski P, Hann HP, Huckriede H, Lacquement F, Lamarche J, Ledru P, Pharaoh TC, Zedler H, Zeh A, Zulauf G (2008) Variscan tectonics. In: McCann T (ed) *The Geology of Central Europe*. Geol Soc Lond, pp 599-664.
- Kroner U, Romer RL, Linnemann U (2010) The Saxo-Thuringian Zone of the Variscan Orogen as part of Pangea. In: Linnemann U, Romer RL (eds) *Pre-Mesozoic Geology of Saxo-Thuringia - From the Cadomian Active Margin to the Variscan Orogen*. Schweizerbart, Stuttgart, pp 3-16.
- Kroner U, Romer RL (2013) Two plates – Many subduction zones: The Variscan orogeny reconsidered. *Gondwana Res* 24:298-329.
- Kryza R, Pin C (2002) Mafic rocks in a deep-crustal segment of the Variscides (the Góry Sowie, SW Poland): evidence for crustal contamination in an extensional setting. *Int J Earth Sci* 91:1017-1029.
- Kryza R, Zalasiewicz JA, Charnley N, Milodowski AE, Kostylew J, Tyszka R (2004) In situ growth of monazite in anchizonal to epizonal mudrocks: first record from the Variscan accretionary prism of the Kaczawa Mountains, West Sudetes, SW Poland. *Geol Sud* 36:39-51.
- Kryza R, Fanning CM (2007) Devonian deep-crustal metamorphism and exhumation in the Variscan Orogen: evidence from SHRIMP zircon ages from the HT-HP granulites and migmatites of the Góry Sowie (Polish Sudetes). *Geodin Acta* 20/3:159-175.
- Lachance GR, Claisse F (1995) *Quantitative X-Ray Fluorescence Analysis: Theory and Application*. Wiley, Chichester.
- Langone A, Braga R, Massonne H-J, Tiepolo M (2011) Preservation of old (prograde metamorphic) U-Th-Pb ages in unshielded monazite from the high-pressure paragneisses of the Variscan Ulten Zone (Italy). *Lithos* 127:68-85.
- Li B, Massonne H-J (2016) Early Variscan *P-T* evolution of an eclogite body and its adjacent orthogneiss from the northern Malpica-Tuy shear-zone in NW Spain. *Eur J Mineral* 28:1131-1154.
- Li B, Massonne H-J, Opitz J (2017) Clockwise and anticlockwise *P-T* paths of high-pressure rocks from the 'La Pioza' eclogite body of the Malpica-Tuy zone, NW Spain. *J Petrol*, in press.
- Liebscher A, Franz G, Frei D, Dulski P (2007) High-pressure melting of eclogite and the *P-T-X* history of tonalitic to trondhjemitic zoisite-pegmatites, Münchberg Massif, Germany. *J Petrol* 48:1001-1019.
- Linnemann U (2003) The structural units of Saxo-Thuringia. *Geol Saxonica* 48-49:23-32.

- Linnemann U (2004) Das Saxothuringikum – Abriss der präkambrischen und paläozoischen Geologie von Sachsen und Thüringen. 2nd edn. Staatliche Naturhistorische Sammlungen, Dresden.
- Linnemann U, Gehmlich M, Tichomirowa M, Buschmann B, Nasdala L, Jonas P, Lützner H, Bombach K (2000) From Cadomian subduction to Early Paleozoic rifting: The evolution of Saxo-Thuringia at the margin of Gondwana in the light of single zircon geochronology and basin development (central European Variscides, Germany). *Geol Soc London Spec Publ* 179:131-153.
- Linnemann U, Romer RL (2002) The Cadomian orogeny in Saxo-Thuringia, Germany: Geochemical and Nd-Sr-Pb isotopic characterization of marginal basins with constraints to geotectonic setting and provenance. *Tectonophys* 352:33-64.
- Linnemann U, Romer RL, Gehmlich M, Drost K (2003) Paleogeography and provenance of Saxo-Thuringia under special consideration of pre-Variscan zircon ages and Nd-isotopic characteristics of sedimentary rocks. *Geol Saxonica* 48-49:125-136.
- Linnemann U, Gerdes A, Drost K, Buschmann B (2007) The continuum between Cadomian orogenesis and opening of the Rheic Ocean: Constraints from LA-ICP-MS U-Pb zircon dating and analysis of plate-tectonic setting (Saxo-Thuringian zone, northeastern Bohemian Massif, Germany). In: Linnemann U, Nance RD, Kraft P, Zulauf G (eds) *The evolution of the Rheic Ocean: From Avalonian-Cadomian active margin to Alleghenian-Variscan collision*. *Geol Soc Am Spec Pap* 423:61-96.
- Linnemann U, D'Lemos R, Drost K, Jeffries TE, Gerdes A, Romer RL, Samson SD, Strachan R (2008) The Cadomian Orogeny. In: McCann T (ed) *The Geology of Central Europe*. *Geol Soc, London*, pp 103-154.
- Linnemann U, Romer RL (2010) Pre-Mesozoic Geology of Saxo-Thuringia - From the Cadomian Active Margin to the Variscan Orogen. *Schweizerbart, Stuttgart*.
- Linnemann U, Schauer M, Hofmann M, Sagawe A (2010a) Geological mapping of the Saxo-Thuringian Zone: The historical perspective. In: Linnemann U, Romer RL (eds) *Pre-Mesozoic Geology of Saxo-Thuringia - From the Cadomian Active Margin to the Variscan Orogen*. *Schweizerbart, Stuttgart*, pp 17-28.
- Linnemann U, Romer RL, Gerdes A, Jeffries TE, Drost K, Ulrich J (2010b) The Cadomian Orogeny in the Saxo-Thuringian Zone. In: Linnemann U, Romer RL (eds) *Pre-Mesozoic Geology of Saxo-Thuringia - From the Cadomian Active Margin to the Variscan Orogen*. *Schweizerbart, Stuttgart*, pp 37-58.

- Linnemann U, Hofmann M, Romer RL, Gerdes A (2010c) Transitional stages between the Cadomian and Variscan orogenies: Basin development and tectono-magmatic evolution of the southern margin of the Rheic Ocean in the Saxo-Thuringian Zone (North Gondwana shelf). In: Linnemann U, Romer RL (eds) Pre-Mesozoic Geology of Saxo-Thuringia - From the Cadomian Active Margin to the Variscan Orogen. Schweizerbart, Stuttgart, pp 59-98.
- Liu Y, Siebel W, Theye T, Massonne H-J (2011) Isotopic and structural constraints on the late Miocene to Pliocene evolution of the Namche Barwa area, eastern Himalayan syntaxis, SE Tibet. *Gondwana Res* 19:894-909.
- Lo Pò D, Braga R, Massonne H-J, Molli G, Montanini A, Theye T (2016) Fluid-induced breakdown of monazite in medium-grade metasedimentary rocks of the Pontremoli basement (Northern Apennines, Italy). *J Metamorph Geol* 34:63-84.
- Ludwig KR (1999) Isoplot/Ex, Version 2.06: A Geochronological Tool-kit for Microsoft Excel. 1a. Berkeley Geochronology Center, Special Publications, pp 1-49.
- Martins L, Vlach SRF, Janasi VA (2009) Reaction microtextures of monazite: Correlation between chemical and age domains in the Nazaré Paulista migmatite, SE Brazil. *Chem Geol* 261:271-285.
- Massonne H-J (1993) High-pressure melting of eclogites from the Mid-European Variscides. *Terra Abstr*, 4<sup>th</sup> Int Eclogite Conf 5:16.
- Massonne H-J (1999) Experimental aspects of UHP metamorphism in pelitic systems. *Int Geol Rev* 41:623-638.
- Massonne H-J (2001) First find of coesite in the ultrahigh-pressure metamorphic region of the Central Erzgebirge, Germany. *Eur J Mineral* 13:565-570.
- Massonne H-J (2003) A comparison of the diamondiferous quartz-rich rocks from the Saxonian Erzgebirge and the Kokchetav Massif: are so-called diamondiferous gneisses magmatic rocks? *Earth Planet Sc Lett* 216:345-362.
- Massonne H-J (2005) Involvement of crustal material in delamination of the lithosphere after continent-continent collision. *Int Geol Rev* 47:792-804.
- Massonne H-J (2009) Hydration, dehydration, and melting of metamorphosed granitic and quartz-dioritic rocks at high and ultrahigh pressure conditions. *Earth Planet Sc Lett* 288:244-254.
- Massonne H-J (2010) Phase relations and dehydration behaviour of calcareous sediments at very-low to low grade metamorphic conditions. *Period Mineral* 79:21-43.

- Massonne H-J (2011) High-pressure/ultrahigh pressure rocks in the Bohemian Massif; Occurrences and PT conditions of high and ultrahigh pressure rocks in the Bohemian Massif. *Geolines* 23:18-26.
- Massonne H-J (2012) Formation of amphibole and clinozoisite-epidote during exhumation of eclogite in a subduction channel. *J Petrol* 53:1969-1998.
- Massonne H-J (2013) Constructing the pressure-temperature path of ultrahigh-pressure rocks. *Elements* 9:267-272.
- Massonne H-J (2014) Wealth of P–T–t information in medium-high grade metapelites: Example from the Jubrique Unit of the Betic Cordillera, S Spain. *Lithos* 208:137-157.
- Massonne H-J (2016a) Tertiary high-pressure metamorphism recorded in andalusite-bearing micaschist, southern Pirin Mts., SW Bulgaria. *Eur J Mineral* 28:1187-1202.
- Massonne H-J (2016b) Hydration of the lithospheric mantle by the descending plate in a continent-continent collisional setting and its geodynamic consequences. *J Geodyn* 96:50-61.
- Massonne H-J, O'Brien PJ (2003) The Bohemian Massif and the NW Himalaya. *EMU Notes in Mineral* 5:145-187.
- Massonne H-J, Czambor A (2007) Geochemical signatures of Variscan eclogites from the Saxonian Erzgebirge, central Europe. *Chem Erde* 67:69-83.
- Massonne H-J, Kennedy A, Nasdala L, Theye T (2007a) Dating of zircon and monazite from diamondiferous quartzofeldspathic rocks of the Saxonian Erzgebirge. *Mineral Mag* 71:407-425.
- Massonne H-J, Willner AP, Gerya TV (2007b) Densities of psammopelitic rocks at elevated temperatures and high to ultrahigh pressure conditions: what are the geodynamic consequences? *Earth Planet Sc Lett* 256:12-27.
- Massonne H-J, Willner AP (2008) Dehydration behaviour of metapelites and mid-ocean ridge basalt at very-low to low grade metamorphic conditions. *Eur J Mineral* 20:867-879.
- Massonne H-J, Dristas JA, Martínez JC (2012) Metamorphic evolution of the Río de la Plata craton in the Cinco Cerros area, Buenos Aires Province, Argentina. *J S Am Earth Sci* 38:57-70.
- Massonne H-J, Cruciani G, Franceschelli M, Musumeci G (2017) Anti-clockwise pressure-temperature paths record Variscan upper-plate exhumation: example from micaschists of the Porto Vecchio region, Corsica. *J Metamorph Geol*, in press.
- Matte P (1998) Continental subduction and exhumation of HP rocks in Paleozoic orogenic belts: Uralides and Variscides. *Geol Foren Stock For* 120:209-222.

- Matthes S (1978) The eclogites of Southern Germany – a summary. *N Jahrb Mineral - Monatshefte* 1978, Heft 3:93-109.
- Matthes S, Richter P, Schmidt K (1975) Die Eklogitvorkommen des kristallinen Grundgebirges in NE-Bayern IX. Petrographie, Geochemie und Petrogenese der Eklogite des Münchberger Gneisgebietes. *N Jahrb Mineral Abh* 126:45-86.
- McLennan SM (1993) Weathering and Global Denudation. *J Geol* 101:295-303.
- Meschede M (1986) A METHOD OF DISCRIMINATING BETWEEN DIFFERENT TYPES OF MID-OCEAN RIDGE BASALTS AND CONTINENTAL THOLEIITES WITH THE Nb-Zr-Y DIAGRAM. *Chem Geol* 56:207-218.
- Meschede M (2003) The Costa Rica convergent margin: a textbook example for the process of subduction erosion. *N Jahrb Geol P - Abhandl* 230:409-428.
- Moore DE, Blake MC Jr (1989) New evidence for polyphase metamorphism of glaucophane schist and eclogite exotic blocks in the Franciscan Complex, California and Oregon. *J Metamorph Geol* 7:211-228.
- Murphy DB (2001) *Fundamentals of Light Microscopy and Electronic Imaging*. Wiley-Liss, Danvers.
- Nance RD, Gutiérrez-Alonso G, Keppie JD, Linnemann U, Murphy JB, Quesada C, Strachan RA, Woodcock NH (2012) A brief history of the Rheic Ocean. *Geosci Front* 3:125-135.
- Nesse WD (2013) *Introduction to Optical Mineralogy*. 4th edn. Oxford University Press, New York.
- O'Brien PJ (1993) Partially retrograded eclogites of the Münchberg Massif, Germany: records of a multi-stage Variscan uplift history in the Bohemian Massif. *J Metamorph Geol* 11:241-260.
- O'Brien PJ (1997) Garnet zoning and reaction textures in overprinted eclogites, Bohemian Massif, European Variscides: A record of their thermal history during exhumation. *Lithos* 41:119-133.
- O'Brien PJ (2000) The fundamental Variscan problem: high-temperature metamorphism at different depths and high-pressure metamorphism at different temperatures. In: Franke W, Haak V, Oncken O, Tanner D (eds) *Orogenic Processes: Quantification and Modelling in the Variscan Belt*. *Geol Soc London Spec Publ* 179:369-386.
- O'Brien PJ, Kröner A, Jaeckel P, Hegner E, Żelaźniewicz A, Kryza R (1997) Petrological and isotopic studies on Palaeozoic high-pressure granulites, Góry Sowie Mts, Polish Sudetes. *J Petrol* 38:493-456.

- Oh CW, Liou JG (1990) Metamorphic evolution of two different eclogites in the Franciscan Complex, California, U.S.A. *Lithos* 25:41-53.
- Okrusch M, Matthes S, Schmidt K (1990) Eklogite des Münchberger Gneisgebietes. *Eur J Mineral* 2:55-84.
- Pavićević MK, Amthauer G (2000) *Physikalisch-chemische Untersuchungsmethoden in den Geowissenschaften*. E Schweizerbart'sche Verlagsbuchhandlung, Stuttgart.
- Pearce JA (1983) "Users Guide" to Basalt Discrimination Diagrams. Unpubl Rep, The Open University, Milton Keynes.
- Pearce JA, Cann JR (1973) Tectonic Setting of Basic Volcanic Rocks Determined Using Trace Element Analyses. *Earth Planet Sc Lett* 19:290-300.
- Petrie MB, Massonne H-J, Gilotti JA, McClelland WC, van Staal C (2016) The *P-T* path of eclogites in the St. Cyr klippe, Yukon, Canada: Permian metamorphism of a coherent high-pressure unit in an accreted terrane of the North American Cordillera. *Eur J Mineral* 28:1111-1130.
- Pitra P, Guiraud M (1996) Probable anticlockwise *P-T* evolution in extending crust: Hlinsko region, Bohemian Massif. *J Metamorph Geol* 14:49-60.
- Powell R, Holland TJB (1999) Relating formulations of the thermodynamics of mineral solid solutions: Activity modeling of pyroxenes, amphiboles, and micas. *Am Mineral* 84:1-14.
- Rasmussen B, Bengtson S, Fletcher IR, McNaughton NJ (2002) Discoidal impressions and trace-like fossils more than 1,200 million years old. *Science* 296:1112-1115.
- Romer RL, Schneider J, Linnemann U (2010) Post-Variscan deformation and hydrothermal mineralization in Saxo-Thuringia and beyond: a geochronologic review. In: Linnemann U, Romer RL (eds) *Pre-Mesozoic Geology of Saxo-Thuringia - From the Cadomian Active Margin to the Variscan Orogen*. Schweizerbart, Stuttgart, pp 347-360.
- Romer RL, Hahne K (2010) Baltica meets Gondwana – the isotope geochemical record. In: Linnemann U, Romer RL (eds) *Pre-Mesozoic Geology of Saxo-Thuringia - From the Cadomian Active Margin to the Variscan Orogen*. Schweizerbart, Stuttgart, pp 363-370.
- Rubatto D, Williams IS, Buick IS (2001) Zircon and monazite response to prograde metamorphism in the Reynolds Range, central Australia. *Contrib Mineral Petrol* 140:458-468.
- Rubatto D, Hermann J (2007) Zircon Behaviour in Deeply Subducted Rocks. *Elements* 3:31-35.

- Rudnick RL, Barth M, Horn I, McDonough WF (2000) Rutile-Bearing Refractory Eclogites: Missing Link Between Continents and Depleted Mantle. *Science* 287:278-281.
- Săbău G (2000) A possible UHP-eclogite in the Leaota Mts. (South Carpathians) and its history from high-pressure melting to retrograde inclusion in a subduction melange. *Lithos* 52:253-276.
- Schäfer J, Neuroth H, Ahrendt H, Dörr W, Franke W (1997) Accretion and exhumation at a Variscan active margin, recorded in the Saxothuringian flysch. *Geol Rundsch* 86:599-611.
- Schulmann K, Konopásek J, Janoušek V, Lexa O, Lardeaux J-M, Edel J-B, Štípská P, Ulrich S (2009) An Andean type Palaeozoic convergence in the Bohemian Massif. *Tectonics* 34:266-286.
- Shelley D, Bossière G (2000) A new model for the Hercynian Orogen of Gondwana France and Iberia. *J Structural Geol* 22:757-776.
- Spear FS (2017) Garnet growth after overstepping. *Chem Geol* 466:491-499.
- Spear FS, Pyle JM (2002) Apatite, monazite, and xenotime in metamorphic rocks. In: Kohn MJ, Rakovan J, Hughes JM (eds) *Phosphates: Geochemical, Geobiological, and Materials Importance*. *Rev Mineral Geochem* 48:293-335.
- Stettner G (1960a) Über Bau und Entwicklung der Münchberger Gneismasse. *Geol Rundsch* 49:350-375.
- Stettner G (1960b) Erläuterungen zur Geologischen Karte von Bayern 1:25000, Blatt Nr. 5836 Münchberg. Bayerisches Geologisches Landesamt, München, 162 pp.
- Štípská P, Pitra P, Powell R (2006) Separate or shared metamorphic histories of eclogites and surrounding rocks? An example from the Bohemian Massif. *J Metamorph Geol* 24:219-240.
- Štípská P, Schulmann K, Powell R (2008) Contrasting metamorphic histories of lenses of high-pressure rocks and host migmatites with a flat orogenic fabric (Bohemian Massif, Czech Republic): a result of tectonic mixing within horizontal crustal flow. *J Metamorph Geol* 26:623-646.
- Stosch H-G, Lugmair GW (1990) Geochemistry and evolution of MORB-type eclogites from the Münchberg Massif, southern Germany. *Earth Planet Sc Lett* 99:230-249.
- Straub SM, Layne GD (2003) Decoupling of fluids and fluid-mobile elements during shallow subduction: Evidence from halogen-rich andesite melt inclusions from the Izu arc volcanic front. *Geochem Geophys Geosy* 4:1525-2027.

- Suzuki K, Adachi M, Kajizuka I (1994) Electron microprobe observations of Pb diffusion in metamorphosed detrital monazites. *Earth Planet Sc Lett* 128:391-405.
- Taylor SR, McLennan SM (1985) *The Continental Crust: its Composition and Evolution*. Blackwell Scientific Publications, Oxford.
- Thomas R (2008) *Practical Guide to ICP-MS: a tutorial for beginners*. 2nd edn. CRC Press, Boca Raton.
- Tichomirowa M (2002) Die Gneise des Erzgebirges – hochmetamorphe Äquivalente von neoproterozoisch – frühpaläozoischen Grauwacken und Granitoiden der Cadomiden. *Freib Forschungshefte C* 495:1-222.
- Tichomirowa M, Sergeev S, Berger H-J, Leonhardt D (2012) Inferring protoliths of high-grade metamorphic gneisses of the Erzgebirge using zirconology, geochemistry and comparison with lower-grade rocks from Lusatia (Saxothuringia, Germany). *Contrib Mineral Petrol* 164:375-396.
- Timmermann H, Štědrá V, Gerdes A, Noble SR, Parrish RR, Dörr W (2004) The problem of dating high-pressure metamorphism: a U–Pb isotope and geochemical study on eclogites and related rocks of the Mariánské Lázně Complex, Czech Republic. *J Petrol* 45:1311-1338.
- Tomkins HS, Powell R, Ellis DJ (2007) The pressure dependence of the zirconium-in-rutile thermometer. *J Metamorph Geol* 25:703-713.
- Toulkeridis T, Clauer N, Kröner A, Reimer T, Todt W (1999) Characterization, provenance, and tectonic setting of Fig Tree greywackes from the Archaean Barberton Greenstone Belt, South Africa. *Sediment Geol* 124:113-129.
- Van Leeuwen T, Allen CM, Elburg M, Massonne H-J, Palin M, Hennig J (2016) The Palu Metamorphic Complex, NW Sulawesi, Indonesia: Origin and evolution of a young metamorphic terrane with links to Gondwana and Sundaland. *J Asian Earth Sci* 115:133-152.
- Vollbrecht A, Pawlowski J, Leiss B, Heinrichs T, Seidel M, Kronz A (2006) Ductile deformation of garnet in mylonitic gneisses from the Münchberg Massif (Germany). *Tectonophysics* 427:153-170.
- Walter R (2014) *Erdgeschichte – Die Geschichte der Kontinente, der Ozeane und des Lebens*. 6th edn. Schweizerbart, Stuttgart.
- Watson EB, Wark DA, Thomas JB (2006) Crystallization thermometers for zircon and rutile. *Contrib Mineral Petrol* 151:413-433.

- Wernicke B (1985) Uniform-sense normal simple shear of the continental lithosphere. *Can J Earth Sci* 22:108-125.
- White RW, Powell R, Holland TJB (2001) Calculation of partial melting equilibria in the system  $\text{Na}_2\text{O}-\text{CaO}-\text{K}_2\text{O}-\text{FeO}-\text{MgO}-\text{Al}_2\text{O}_3-\text{SiO}_2-\text{H}_2\text{O}$  (NCKFMASH). *J Metamorph Geol* 19:139-153.
- Williams ML, Jercinovic MJ, Hetherington CJ (2007) Microprobe monazite geochronology: understanding geologic processes by integrating composition and chronology. *Ann Rev Earth Planet Sci* 35:137-175.
- Williams ML, Jercinovic MJ, Harlov DE, Budzyń B, Hetherington CJ (2011) Resetting monazite ages during fluid-related alteration. *Chem Geol* 283:218-225.
- Willner AP, Krohe A, Maresch WV (2000) Interrelated P-T-t-d paths in the Variscan Erzgebirge dome (Saxony, Germany): Constraints on the rapid exhumation of high-pressure rocks from the root zone of a collisional orogen. *Int Geol Rev* 42:64-85.
- Willner AP, Sebazungu E, Gerya TV, Maresch WV, Krohe A (2002) Numerical modelling of PT-paths related to rapid exhumation of high-pressure rocks from the crustal root in the Variscan Erzgebirge Dome (Saxony/Germany). *J Geodyn* 33:281-314.
- Willner AP, Glodny J, Gerya TV, Godoy E, Massonne H-J (2004) A counterclockwise PTt-path in high pressure-low temperature rocks from the Coastal Cordillera accretionary complex of South Central Chile: constraints for the earliest stage of subduction mass flow. *Lithos* 75:283-310.
- Willner AP, Barr SM, Gerdes A, Massonne H-J, White CE (2013) Origin and evolution of Avalonia: evidence from U–Pb and Lu–Hf isotopes in zircon from the Mira terrane, Canada, and the Stavelot–Venn Massif, Belgium. *J Geol Soc* 170:769-784.
- Willner AP, Barr SM, Glondy J, Massonne H-J, Sudo M, Thomson SN, Van Staal CR, White CE (2015) Effects of fluid flow, cooling and deformation as recorded by  $^{40}\text{Ar}/^{39}\text{Ar}$ , Rb–Sr and zircon fission track ages in very low- to low-grade metamorphic rocks in Avalonian SE Cape Breton Island (Nova Scotia, Canada). *Geol Mag* 152:767-787.
- Winchester JA, Floyd PA, Awdankiewicz M, Piasecki MAJ, Awdankiewicz H, Gunia P, Gliwicz T (1998) Geochemistry and tectonic significance of metabasic suites in the Góry Sowie Block, SW Poland. *J Geol Soc London* 155:155-164.
- Wing BA, Ferry JM, Harrison TM (2003) Prograde destruction and formation of monazite and allanite during contact and regional metamorphism of pelites: petrology and geochronology. *Contrib Mineral Petrol* 145:228-250.

- Zack T, Moraes R, Kronz A (2004) Temperature dependence of Zr in rutile: empirical calibration of a rutile thermometer. *Contrib Mineral Petrol* 148:471-488.
- Zeh A, Williams IS, Brätz H, Millar IL (2003) Different age response of zircon and monazite during the tectono-metamorphic evolution of a high grade paragneiss from the Ruhla Crystalline Complex, central Germany. *Contrib Mineral Petrol* 145:691-706.
- Zeh A, Will TM (2010) The Mid-German Crystalline Zone. In: Linnemann U, Romer RL (eds) *Pre-Mesozoic Geology of Saxo-Thuringia - From the Cadomian Active Margin to the Variscan Orogen*. Schweizerbart, Stuttgart, pp 195-220.

## Danksagung

Bei all denjenigen, die zum Gelingen dieser Dissertation beigetragen haben, bedanke ich mich recht herzlich. Dies waren insbesondere die nachfolgend genannten Personen.

Zunächst ist hier *Herr Prof. Massonne* zu nennen, der mich freundlicherweise in das Institut für Mineralogie und Kristallchemie zum Anfertigen der Arbeit aufgenommen und meine zahllosen Fragen stets beantwortet hat.

Mein Dank gilt auch *Herrn Dr. Opitz*, der mich sowohl bei den ICP-MS-Messungen als auch den XRF-Messungen voller Tatendrang und wissenschaftlicher Neugier unterstützte.

*Herr Dr. Theye* hat mir wertvolle Hilfe bei den EMP-Messungen samt zugehörigen Auswertungen gegeben; auch dafür mein aufrichtiger Dank.

*Herr Prof. Willner* hat in zahlreichen Diskussionen die Arbeit vorangebracht, wofür ich ihm sehr dankbar bin.

Ich danke auch *Frau Kwiatkowski* für ihren unermüdlichen Einsatz bei den Schmelztabletten und den sauren Aufschlüssen.

*Herr Schmelz* hat sämtliche Dünnschliffe, die ich mit der EMP untersucht habe, hergestellt, wofür ich ihm sehr dankbar bin.

Ohne *Herrn Leiss* wären die Kohlenstoffbestimmungen der Gesteinspulver nicht ohne weiteres möglich gewesen.

Darüber hinaus danke ich *Herrn Dr. Viefhaus* für seine nützlichen Tipps während der Arbeit.

*Herrn Schopf* danke ich für seine Hilfe bei der SEM.

Meinen Zimmerkolleginnen *Botao Li* und *Gelareh Rahimi* danke ich für die angenehme Arbeitsatmosphäre.

Außerdem danke ich *Herrn Dr. Buchner* und *Herrn Prof. Gudat* für ihre Bereitschaft, Mitberichter und Mitprüfer dieser Arbeit zu sein.

Mein besonderer Dank gilt meiner *Mutter*, die mich sowohl moralisch als auch finanziell unterstützte.

## Erklärung über die Eigenständigkeit der Dissertation

Ich versichere, dass ich die vorliegende Arbeit mit dem Titel „Evolution of Rocks from the Münchberg Metamorphic Complex (NE Bavaria)“ selbständig verfasst und keine anderen als die angegebenen Quellen und Hilfsmittel benutzt habe; aus fremden Quellen entnommene Passagen und Gedanken sind als solche kenntlich gemacht.

## Declaration of Authorship

I hereby certify that the dissertation entitled “Evolution of Rocks from the Münchberg Metamorphic Complex (NE Bavaria)” is entirely my own work except where otherwise indicated. Passages and ideas from other sources have been clearly indicated.

Name / Name: Florian Waizenhöfer

Unterschrift / Signed: 

Datum / Date: 16.10.2017